

ABSTRACT

HILL, KEVIN A. Climate and Tropical Cyclones. (Under the direction of Dr. Gary Lackmann).

Part I of the work presented here investigates the impact of relative humidity on TC size in idealized WRF simulations. It is hypothesized that outer-core precipitation influences TC size, and therefore environmental factors that influence the amount of outer-core precipitation in turn influence TC size. Outer-core precipitation affects TC size through the diabatic generation of lower-tropospheric PV, which can amalgamate with the TC central PV tower or remain at radius. Four idealized high-resolution numerical simulations with the WRF model were performed in order to test the hypothesized sensitivity of TC size to environmental humidity. Differences in TC size between the runs were substantial, consistent with the hypothesis; several TC size metrics demonstrate this difference, including differences of a factor of 3 in the size of the RMW in the simulations.

During the simulation period, moisture fluxes led to similar moisture content in the boundary layer in all simulations, although large differences remained above the boundary layer and outside of the initial moist envelope. A close correspondence between the inward protrusion of the dry air and the formation of persistent precipitation was found, indicating that the presence of dry air was responsible for differences in simulated precipitation outside of the eyewall. PV budget analysis reveals that size differences can be linked to differences in precipitation in outer rainbands and associated diabatic production of lower tropospheric PV, which both were larger in the more moist simulations. Several feedback mechanisms serve to reinforce TC growth.

Part II of this research involved an investigation of climate change and its impact on TC intensity and structure. Previous work was extended in this study by utilizing a larger number of GCMs forced with 3 different greenhouse gas emissions scenarios to estimate climate change, which allowed for a detailed analysis of uncertainty. TC simulations featured higher resolution than in previous idealized downscaling studies, and the explicit convection simulations allowed for a more realistic representation of TC structure and

analysis of TC structure changes in a future climate. The high-resolution model output was used to investigate structural changes, and to explore the mechanism of future intensity changes.

A large sample of model simulations with 6-km grid spacing indicate an average increase in future TC maximum intensity of ~9%. A smaller sample of simulations with 2-km grid spacing indicate a slightly larger increase of 13%. Tropospheric stabilization, which varies largely in GCM projections, plays a key role in influencing future outflow temperature and structure. Simulations with no tropospheric stabilization had an average increase in central pressure deficit of 28%, slightly more than double that found with an identical SST increase along with projected tropospheric stabilization. Stratospheric cooling was found to not impact TC intensity in the model simulations. In addition to intensity increases being tied to warmer SSTs, it was also discovered that increases in rainfall lead to a stronger central PV tower, and that the increase in PV is highly correlated with intensity. Therefore, it is proposed that changes in both thermodynamic efficiency and in rainfall are responsible for future intensity increase.

Climate and Tropical Cyclones

by
Kevin Anthony Hill

A dissertation submitted to the Graduate Faculty of
North Carolina State University
in partial fulfillment of the
requirements for the degree of
Doctor of Philosophy

Marine, Earth, and Atmospheric Sciences

Raleigh, North Carolina

August 2010

APPROVED BY:

Gary M. Lackmann
Chair of Advisory Committee

Anantha R. Aiyyer

Fred Semazzi

Lian Xie

BIOGRAPHY

Kevin was born in Buffalo, NY on 11 November 1982, and graduated from Clarence High School in 2000. Kevin's first fascination with meteorology was lake effect snow storms, which dump large amounts of snow in very isolated areas. During high school, Kevin learned that he had an aptitude for math and science, and upon arriving at The State University of New York at Brockport, he chose to major in meteorology and minor in math and statistics, while taking additional courses in physics and computer science in order to prepare for graduate school. Upon graduating from Brockport with a B.S. in Meteorology and a minor in mathematics and statistics, Kevin began graduate school in Atmospheric Science at NCSU under the advisement of Dr. Gary. M. Lackmann.

Kevin's Master's research focused on tropical cyclone simulations with the WRF model and the sensitivity of the results to turbulence parameterization and model resolution. His PhD research consisted of two major parts, the first of which was motivated by this earlier work. This research consisted of studying the impact of environmental moisture on tropical cyclone size, and also the influence of climate change on tropical cyclone intensity and structure. During his graduate school years, Kevin taught several semesters of an introduction to meteorology laboratory class, and was awarded the North Carolina State University Outstanding Teaching Assistant Award. Kevin also remained active in the Graduate Student Association, took an internship course at the National Weather Service office in Raleigh, NC, and participated in the University of Oklahoma forecast competition.

ACKNOWLEDGEMENTS

Support for this research was received from the Department of Energy (DOE grant ER64448) and the National Science Foundation (NSF grant ATM-0334427) both awarded to North Carolina State University.

I would like to thank the members of my advisory committee, Drs. Gary Lackmann, Anantha Aiyyer, Frederick Semazzi, and Lian Xie for their insights and helpful suggestions. I would especially like to thank Dr. Gary Lackmann for his support, patience, and advisement over the years. I am very fortunate to have worked with him throughout my graduate education. I would also like to thank other members of the MEAS faculty, I cannot believe how much I have learned over the last 6 years and your courses have been a large part of that.

I have been fortunate to work with a great group of people in the Forecasting Lab (or whatever it is called now?), and I acknowledge its members (both past and present) for everything from collaboration on research and technical support to laughter and friendship.

Finally, I would like to express my gratitude to my family and friends. First, thank you to my parents, David and Phyllis, and to my brother Brian for love and support throughout the years. Your visits to Raleigh have always been a pleasure and I hope you have enjoyed them as well. Thank you to my friends throughout the years, including several classes of students who have come and gone. North Carolina State always seems to attract a great group of intelligent, hard working, and fun students, and meeting and interacting with many of you over the course of my education has been incredibly rewarding.

TABLE OF CONTENTS

List of Tables	ix
List of Figures	x
1. Introduction and background	
1.1 Overall motivation behind TC research.....	1
1.2 TCs and climate change.....	2
1.2.1 Evidence	2
1.2.2 Research Objectives.....	3
1.2.3 Previous research.....	5
1.2.3.1 TC maximum intensity.....	5
1.2.3.2 The tropospheric response to increased greenhouse gas concentrations.....	7
1.2.3.3 Greenhouse gas induced temperature changes in GCMs.....	9
1.2.3.4 Tropical cyclone intensity studies.....	12
1.2.4 Summary.....	15
1.3 TC Size.....	15
1.3.1 Motivation.....	15
1.3.2 Research objectives and hypothesis.....	16
1.3.3 Observed sizes.....	16
1.3.4 Controls on TC size.....	17
1.3.5 Potential vorticity (PV), TC rainbands, and TC size.....	19

2. Methodology

2.1 Tropical cyclone size.....	23
2.1.1 Model set-up and initial conditions.....	23
2.1.2 Potential vorticity techniques.....	26
2.1.3 Analysis techniques.....	27
2.1.3.1 Wind radii.....	27
2.2 Future TC intensity, rainfall, and structure.....	28
2.2.1 Current climate conditions.....	28
2.2.2 Creation of future climate environment.....	29
2.2.3 Idealized tropical cyclone characteristics.....	30
2.2.4 Numerical model TC simulations.....	30
2.2.4.1 Simulations with 6-km grid spacing.....	31
2.2.4.2 Simulations with 2-km grid spacing.....	32
2.2.5 Analysis techniques.....	33
2.2.5.1 Computation of mass weighted inflow, outflow.....	33
2.2.5.2 Comparison with MPI estimates.....	34

3. Tropical cyclone size

3.1 Simulated TC Intensity.....	41
3.2 Simulated TC Size.....	41
3.3 Precipitation structure.....	43

3.4 Time evolution of water vapor fields.....	45
3.4.1 Simulation day 2 (hours 24 – 48).....	45
3.4.2 Simulation day 8 (hours 168 – 192).....	46
3.4.3 Summary of moisture changes.....	47
3.5 Physical mechanisms.....	48
3.5.1 Angular momentum import.....	48
3.5.2 Outer core precipitation, diabatic heating, and pressure gradient.....	49
3.5.3 Azimuthally averaged PV diagnostics.....	50
3.5.4 PV tower growth, eye and wind-field expansion.....	54
3.5.5 Spiral band structure.....	55
3.5.6 Feedback mechanisms.....	57
3.6 Summary.....	58
4. Future climate change and tropical cyclones	
4.1 Future projections - TC environment.....	100
4.1.1 Environmental temperature.....	100
4.1.2 Environmental moisture.....	102
4.1.3 Large-scale conditions in sensitivity experiments.....	103
4.1.4 Freezing level and tropopause height.....	105
4.2 TC Intensity; thermodynamic efficiency and dynamical changes.....	106
4.2.1 Simulations with 2-km grid spacing.....	106

4.2.1.1 TC intensity.....	106
4.2.1.2 Thermodynamic efficiency.....	108
4.2.1.3 Dynamical influences: rainfall and PV.....	112
4.2.2 Simulations with 6-km grid spacing.....	116
4.2.2.1 TC intensity.....	116
4.2.2.2 Thermodynamic efficiency.....	117
4.2.2.3 Dynamical influences: rainfall.....	119
4.3 Structural analysis (2-km simulations).....	120
4.3.1 Vertical velocity.....	121
4.3.2 Inflow.....	122
4.3.3 Outflow.....	123
4.3.4 Eye structure.....	123
4.4 TC Size.....	125
4.4.1 6-km Simulations.....	126
4.4.2 2-km simulations.....	126
4.5 Summary.....	127
5. Discussion and concluding remarks	
5.1 TC Size.....	195
5.1.1 Additional implications and future research directions.....	198
5.2 Climate change and TCs.....	200

5.2.1 Additional implications and future research directions.....	204
---	-----

LIST OF TABLES

Table 2.1	Global climate models utilized in this study, along with the institution and agencies responsible for their development. In order to be used in this study, GCM output from the 20c3m, SRESA1B, SRESA2, and SRESB1 runs must have been available.....	36
Table 2.2	Summary of sensitivity experiments, and names that will be used to describe them in subsequent chapters.....	37
Table 4.1	Summary of projected changes in SST from the different emissions scenarios.....	130
Table 4.2	Summary of simulated maximum intensity in 2-km simulations with ensemble mean projected climate changes, and MPI estimates. For the WRF simulations, the minimum values shown are the average of the minimum values in the MYJ and YSU runs.....	131
Table 4.3	Summary of maximum intensity in 2-km simulations and sensitivity experiments.....	132
Table 4.4	Mass weighted inflow and outflow temperature (C), and relative to control. Thermodynamic efficiency multiplied by SST, and increase relative to control (%).....	133
Table 4.5	Summary of intensity statistics for 6-km simulations.....	134

LIST OF FIGURES

Figure 1.1	Schematic of GCM ensemble mean temperature change profile (blue curve) and the associated physical processes responsible for the change.....	22
Figure 2.1	Outline of region used for the averaging of environmental conditions in TC size and future TC experiments. The region encompasses 8.5 – 15° North, and 60 – 40° West.	38
Figure 2.2	Global GHG emissions (in GtCO ₂ -eq per year) in the absence of additional climate policies six illustrative SRES marker scenarios (colored lines) and 80 th percentile range of recent scenarios published since SRES (post-SRES) (gray shaded area). Dashed lines show the full range of post SRES scenarios. The emissions include CO ₂ , CH ₄ , N ₂ O, and F-gases. {WGIII 1.3, 3.2, Figure SPM.4]	39
Figure 2.3	Time-series of minimum central pressure from WRF model simulations utilizing initial vortices of different strength blue (15 m s ⁻¹), red (20 m s ⁻¹), yellow (25 m s ⁻¹) and green (30 m s ⁻¹). 24-hour mean minimum central pressure values are 907, 907, 908, and 906 hPa for simulations with initial maximum winds of 15, 20, 25, and 30 m s ⁻¹ , respectively.....	40
Figure 3.1	Time-series of simulated minimum central pressure (hPa).....	61
Figure 3.2	As in Fig. 3.1 except maximum 10-m wind speed (m s ⁻¹).....	62
Figure 3.3	Time-series of TC wind field parameters for each simulation as specified in legend, with application of a 1-2-1 smoother (a) radius of maximum 10-m wind speed (km); (b) maximum radius of hurricane-force 10-m wind speed. Values computed from azimuthally averaged model 10-m wind speed.....	63
Figure 3.4	Hovmöller diagram (with time on the ordinate and radius from TC center on the abscissa) of azimuthally averaged 10-m wind speed (shaded; m s ⁻¹) for simulations (a) 20RH, (b) 40RH, (c) 60RH, (d) 80RH.....	64
Figure 3.5	Hovmöller diagram of the time rate of change of the azimuthally averaged 10-m wind speed (shaded; m s ⁻¹ hr ⁻¹), the hurricane and tropical storm force wind values (black contours), and the 20 dBz simulated composite reflectivity contour (red) for simulations (a) 80RH, (b) 60RH, (c) 40RH, (d) 20RH simulation.....	65
Figure 3.6	Model simulated composite reflectivity at hour 24 for (a) 20RH, (b) 40RH, (c) 60RH, (d) 80RH simulations. The composite reflectivity includes all model vertical levels.....	66

Figure 3.7	As in Fig. 3.6, but for simulation hour 126.....	67
Figure 3.8	As in Fig. 3.6, but for simulation hour 180.....	68
Figure 3.9	As in Fig. 3.4 except for composite simulated radar reflectivity (dBz, shaded as in legend at bottom of panels). The radius of maximum 10-m wind speed, hurricane force wind, and tropical storm force wind are indicated by the black contours.....	69
Figure 3.10	Cross-section of azimuthally averaged change (relative to initialization) in specific humidity (shaded; g kg ⁻¹) and specific humidity (contoured; g kg ⁻¹) time averaged between simulation hours 24 and 48.....	70
Figure 3.11	Cross-section of azimuthally averaged change (relative to initialization) in relative humidity (shaded; %) and relative humidity (contoured; %) time averaged between simulation hours 24 and 48.....	71
Figure 3.12	Cross-section of difference (relative to the 80RH simulation) in relative humidity (shaded; %), relative humidity (black contours; %), and the 15 dBz simulated radar reflectivity contour (red contour) time averaged between simulation hours 24 and 48.....	72
Figure 3.13	Cross-section of equivalent potential temperature (K; contoured) and the equivalent potential temperature lapse rate (K/km; shaded) time averaged between simulation hours 24 and 48.....	73
Figure 3.14	As in Fig. 3.10 except for between simulation hours 168 and 192.....	74
Figure 3.15	As in Fig. 3.11 except for between simulation hours 168 and 192.....	75
Figure 3.16	As in Fig. 3.12 except for between simulation hours 168 and 192.....	76
Figure 3.17	As in Fig. 3.13 except for between simulation hours 168 and 192.....	77
Figure 3.18	Cross-section of azimuthally averaged angular momentum (shaded; m ² s ⁻²) and radial inflow (contoured; m s ⁻¹) time averaged between simulation hours 24 and 48.....	78
Figure 3.19	Cross-section of azimuthally averaged angular momentum multiplied by radial inflow (shaded; m ³ s ⁻³) and the value in the 80RH simulation divided by the value in that simulation (contoured), time averaged between simulation hours 24 and 48.....	79
Figure 3.20	As in Fig. 3.18 except for between simulation hours 168 and 192.....	80
Figure 3.21	As in Fig. 3.19 except for between simulation hours 168 and 192.....	81

Figure 3.22	Tangential wind tendency (shaded; $\text{m s}^{-1} \text{hr}^{-1}$) and angular momentum import (contoured). Data averaged over the lowest 2-km of the troposphere.	82
Figure 3.23	850 – 700 hPa layer average latent heating (shaded; K hr^{-1}) and composite simulated reflectivity (contoured).....	83
Figure 3.24	850 – 700 hPa layer average latent heating (shaded; K hr^{-1}) and surface pressure gradient (contoured).....	84
Figure 3.25	Cross-section of azimuthally averaged potential vorticity (shaded; PVU), simulated radar reflectivity (red contour; dBz) and potential temperature (black contours; K) time averaged between simulation hours 0 and 24.....	85
Figure 3.26	As in Fig. 3.25, except for time averaged between simulation hours 72 and 96.....	86
Figure 3.27	As in Fig. 3.25, except for time averaged between simulation hours 144 and 168.....	87
Figure 3.28	Azimuthally and layer-averaged 850-700 hPa PV (PVU, $1 \text{ PVU} = 10^{-6} \text{ m}^2 \text{s}^{-1} \text{K kg}^{-1}$, shaded as in legend at bottom of panels, extending to 150-km radius). The radius of maximum 10-m wind speed is shown by the thick black line and 30 and 60 km radii are highlighted for reference.....	88
Figure 3.29	Azimuthally averaged composite reflectivity (shaded greater than 40 dBZ, as in legends) and average 850-700 hPa PV (contoured, PVU) after 1 pass with a 9-pt smoother. The radius of maximum 10-m wind speed is shown by the thick black line and radii of 45 and 90 km are highlighted.....	89
Figure 3.30	Azimuthally and layer averaged 850-700 hPa diabatic PV tendency (shaded, PVU hr^{-1}) and PV (PVU, solid black contours). The radius of maximum 10-m wind speed is shown by the thick blue line and radii of 45 and 90 km are highlighted.....	90
Figure 3.31	As in Fig. 3.28, except extending to 500-km radius and highlighting smaller PV values. Also, the radius of hurricane and tropical storm force wind are indicated by the thick black lines.....	91
Figure 3.32	As in Fig. 3.30, except extending to 500-km radius and highlighting smaller PV values. Also, the radius of hurricane and tropical storm force wind are indicated by the thick blue lines.....	92
Figure 3.33	(a) Azimuthally averaged, model-output net moist diabatic tendency from 80RH_Fix simulation at 120 h (K hour^{-1}), (b) as in (a) except for positive	

diabatic tendency; (c) as in (a) except for negative diabatic tendency; (d) non-advection PV tendency due to moist diabatic processes.....	93
Figure 3.34 24-hour mean volume-average (0-80km, surface-250 hPa) mass-weighted PV for the 80RH simulation (a) and 20RH simulation (b), and the corresponding hourly rate of change of average PV for the 80RH simulation (c) and 20RH simulation (d).....	94
Figure 3.35 24-hour averages of eddy PV flux (m PVU s^{-1}) in the 80-km radius ring for the 80RH simulation (black) and 20RH simulation (gray).....	95
Figure 3.36 Horizontal plots of model instantaneous rainfall rate (shaded, in hr^{-1}) and distance from TC center (contoured) for the 80RH simulation valid at simulation time a) hour 84, b) hour 109, c) hour 116 minute 50, d) hour 134.....	96
Figure 3.37 850 hPa PV (solid contours every 2 PVU) and model simulated composite reflectivity (shaded as in legend at left of figure) at hours 72 (a), and 102 (b) 80RH_Fix simulation.....	97
Figure 3.38 Zonal cross-section plots through band indicated in Fig. 3.37a (a) model-output diabatic tendency ($\times 10^3 \text{ K s}^{-1}$, shaded as in legend), radial circulation (vector, vertical component scaled by 25 ub s^{-1}), 0°C isotherm (red line), and simulated radar reflectivity (light blue contours); (b) as in (a) except with absolute vorticity vectors instead of circulation, and PV (PVU, blue contours) instead of reflectivity. (c) PV (PVU, blue contours), diabatic PV flux vectors, moist diabatic PV tendency (shaded as in legend), and 0°C isotherm.....	98
Figure 3.39 Azimuthally averaged 850-hPa absolute vorticity (shaded) and surface latent heat flux (W m^{-2} , solid black contours).....	99
Figure 4.1 Ensemble mean projected change in temperature (K) for each emissions scenario.....	135
Figure 4.2 Projected change in temperature (K) for each of the 13 GCMs used from the SRESA1B emissions scenario. Data table on the right provides mean, minimum, maximum, and standard deviation values at each pressure level.....	136
Figure 4.3 As in Fig. 4.2, except for the SRESA2 emissions scenario.....	137
Figure 4.4 As in Fig. 4.2, except for the SRESB1 emissions scenario.....	138
Figure 4.5 Projected SST increase (K) versus maximum tropospheric warming (K) for each of the GCMs.....	139

Figure 4.6	Ensemble mean projected change in relative humidity (%) for each emissions scenario.....	140
Figure 4.7	Ensemble mean projected change in mixing ratio (g kg^{-1}) for each emissions scenario.....	141
Figure 4.8	Projected change in mixing ratio (g kg^{-1}) for each of the 13 GCMs used from the SRESA1B emissions scenario. Data table on the right provides mean, minimum, maximum, and standard deviation values at each pressure level.....	142
Figure 4.9	As in Fig. 4.8, except for the SRESA2 emissions scenario.....	143
Figure 4.10	As in Fig. 4.8, except for the SRESB1 emissions scenario.....	144
Figure 4.11	Projected SST increase (K) versus maximum tropospheric moistening (g kg^{-1}) for each of the GCMs.....	145
Figure 4.12	Projected temperature (K) changes in sensitivity experiments. Although SST changes are not listed, they follow closely the projected temperature change at the 1000-mb level.....	146
Fig. 4.13	As in Fig. 4.12, except for mixing ratio (g kg^{-1}).....	147
Figure 4.14	Freezing level (left) and lapse-rate tropopause (identified as the height at which the lapse rate becomes less than 2 K km^{-1}) at simulation hour 0.....	148
Figure 4.15	Time-series of simulated minimum central pressure (hPa) in the control (black) and with ensemble mean projected future climate changes (see legend).....	149
Figure 4.16	As in Fig. 4.15, except for the SRESA1B future simulation and the sensitivity experiments (see legend).....	150
Figure 4.17	Cross sections of temperature difference between the future environment and the control (K; shaded), future radial flow (m s^{-1} ; black contours), and current radial flow (contoured at 5 m s^{-1} ; red contour). Vertical axis extends from the surface to 20-km.....	151
Figure 4.18	As in Fig. 4.17, except covering the lower troposphere (0 – 3 km).....	152
Figure 4.19	As in Fig. 4.17, except covering the upper troposphere (10 – 20 km).....	153
Figure 4.20	Outward mass flux as a function of temperature in the control simulation and in simulations with ensemble mean projected changes. Outward mass flux placed into temperature bins that were 5° C wide.....	154

Figure 4.21	Outward mass flux as a function of temperature in the control, the SRESA1B, and the sensitivity experiments.....	155
Figure 4.22	Rain-rate (in hr^{-1}) averaged between simulation hours 216 and 240, for the control and future simulations with ensemble mean projected changes (emissions scenario indicated in each image).....	156
Figure 4.23	As in Fig. 4.22, except for the simulation with projected changes from the SRESA1B ensemble, and in tropospheric stabilization sensitivity experiments.....	157
Figure 4.24	Percentage increase in average rainfall in future climate experiments relative to the control simulation within 250-km of the TC center. Values were averaged between simulation hours 216 and 240.....	158
Figure 4.25	Area averaged (within 250-km of the TC center) percentage increases (relative to the control simulation) of various quantities (indicated by legend). Parameters other than rainfall were computed at the 700-hPa pressure level. Values were averaged between simulation hours 216 and 240.....	159
Figure 4.26	Contoured frequency diagram of hourly rainfall rate (in hr^{-1}) as a function of time in the control simulation and future simulations with ensemble mean projected changes. Grid cells within 500-km of the objectively determined TC center were used. In future simulations, contours from the control simulation are shown for reference.....	160
Figure 4.27	As in Fig. 4.26, except for in the SRESA1B future simulation and in the sensitivity experiments.....	161
Figure 4.28	Cross sections of time-averaged (simulation hours 216 – 240) potential vorticity (PVU; shaded), potential temperature (K; black contours), and the 0-C isotherm (blue contour) for the following simulations control (upper left), SRESA1B (upper right), SRESA2 (lower left), and SRESB1 (lower right).....	162
Figure 4.29	As in Fig. 4.28, except for the SRESA1B and sensitivity experiments.....	163
Figure 4.30	Scatter plot of (top left panel) percentage increase in area-averaged (within 200-km of center) 850 – 700 hPa PV versus increase in precipitation averaged between simulation hours 216 – 240 for all future simulations with 2-km grid spacing, (top right) as in top left but excluding no-stable future simulations, (bottom left) as in top left panel except PV versus increase in SLP deficit, and (bottom right) as in bottom left except excluding no-stable future simulations.....	164

Figure 4.31	Central pressure reduction in future simulations (relative to control; central pressure deficit defined relative to the ambient environment) for future simulations with projected changes from individual GCMs driven by the SRESA1B emissions scenario.....	165
Figure 4.32	As in Fig. 4.31, except for projected changes from the SRESA2 emissions scenario.....	166
Figure 4.33	As in Fig. 4.31, except for projected changes from the SRESB1 emissions scenario.....	167
Figure 4.34	As in Fig. 4.31, except for projected changes from all emissions scenarios.....	168
Figure 4.35	Simulated minimum central pressure versus MPI estimates (hPa). Simulations with the YSU (red) and MYJ (blue) parameterization schemes are shown separately in order to highlight the differences. Separate linear regression lines and best fit parameters are also indicated.....	169
Figure 4.36	Left minimum central pressure (hPa) versus thermodynamic efficiency in all 78 future simulations with 6-km grid spacing. Right as in the left panel, but y-axis displays the thermodynamic efficiency multiplied by the SST.....	170
Figure 4.37	Left relationship between SST and mass-weighted inflow temperature ($^{\circ}$ C) in all 78 future simulations with 6-km grid spacing. Right relationship between the increases (relative to control) in SST and inflow temperature ($^{\circ}$ C).....	171
Figure 4.38	Left relationship between SST and mass-weighted outflow temperature ($^{\circ}$ C) in all 78 future simulations with 6-km grid spacing. Right relationship between the increases (relative to control) in SST and inflow temperature ($^{\circ}$ C).....	172
Figure 4.39	Percentage increase in area averaged rainfall in future simulations (relative to control) all 78 future simulations with 6-km grid spacing.....	173
Figure 4.40	As in Fig. 4.39, except separated for each PBL scheme.....	174
Figure 4.41	Contoured frequency by altitude diagram of vertical velocity ($m s^{-1}$) in the control simulation and future simulations with ensemble mean projected changes.....	175
Figure 4.42	As in Fig. 4.41, except for the SRESA1B future simulation and the sensitivity experiments.....	176

Figure 4.43	Contoured frequency by altitude diagram of inflow velocity (m s^{-1}) in the control simulation and future simulations with ensemble mean projected changes.....	177
Figure 4.44	As in Fig. 4.43, except for the SRESA1B future simulation and the sensitivity experiments.....	178
Figure 4.45	Contoured frequency by altitude diagram of outflow velocity (m s^{-1}) in the control simulation and future simulations with ensemble mean projected changes.....	179
Figure 4.46	As in Fig. 4.45, except for the SRESA1B future simulation and the sensitivity experiments.....	180
Figure 4.47	Time (ordinate) – height (abscissa) plot of eye temperature anomaly (shaded; $^{\circ}\text{C}$) and vertical velocity (black contours; cm s^{-1}). The dashed black contours indicate the eye subsidence (cm s^{-1}) and the dashed line represents the thermal tropopause, where the lapse rate becomes less than 2 K km^{-1} . The “eye” is defined as the 5 grid cells located within 2-km of the TC center, although the results are not sensitive to this choice.....	181
Figure 4.48	As in Fig. 4.47, except for the SRESA1B simulation and the sensitivity experiments.....	182
Figure 4.49	Time-height plot of eye temperature anomaly difference ($^{\circ}\text{C}$; shaded, relative to the control simulation). The thermal tropopause, where the lapse rate becomes less than 2 K km^{-1} , is dashed black in the control and red in the future simulation.....	183
Figure 4.50	Average maximum radius of TS force wind (km). For each simulation within each large-scale environment, the maximum radius of TS force wind was averaged over simulation hours 96 – 120.....	184
Figure 4.51	Left panel relative to the control simulation, the change in hourly rain rate (in hr^{-1} ; shaded, positive denotes heavier rainfall in control simulation). Tropical storm and hurricane force wind contours for the control simulation (blue) and SRESA1B simulation (red). Right panel relative to the control simulation, the percentage change in surface pressure gradient (shaded; positive denotes larger gradient in control simulation). Wind contours as in left panel. Future climate values averaged over all 26 future simulations with projected changes from SRESA1B GCMs.....	185
Figure 4.52	As in Fig. 4.51, except for the SRESA2 simulations.....	186
Figure 4.53	As in Fig. 4.51, except for the SRESA2 simulations.....	187

Figure 4.54	Tropical storm force wind radii (km) in simulations with 2-km grid spacing.....	188
Figure 4.55	As in Fig. 4.51, except for the SRESA1B simulations with 2-km grid spacing.....	189
Figure 4.56	As in Fig. 4.51, except for the SRESA2 simulations with 2-km grid spacing.....	190
Figure 4.57	As in Fig. 4.51, except for the SRESB1 simulations with 2-km grid spacing.....	191
Figure 4.58	As in Fig. 4.51, except for the no-stable simulations with 2-km grid spacing.....	192
Figure 4.59	As in Fig. 4.51, except for the least-stable simulations with 2-km grid spacing.....	193
Figure 4.60	As in Fig. 4.51, except for the most-stable simulations with 2-km grid spacing.....	194

Chapter 1

Introduction and Background

1.1 Overall motivation behind TC research

According to studies of hurricane damage, tropical cyclones (TCs) are the costliest natural disasters in the United States (Pielke and Landsea, 1998). The cost associated damage from TCs has been enhanced in the last few decades by a significant increase in population growth in coastal and near coastal regions, and as a result the United States is now more vulnerable to TCs than ever before (e.g., Sheets 1990; Marks et al. 1998; Pielke et al. 2008). The 2004 and 2005 Atlantic hurricane seasons illustrate this vulnerability, with both seasons setting numerous records for TC damage (Franklin et al. 2006, Beven et al. 2008). The 2004 Atlantic hurricane season was among the most damaging on record, with the United States suffering a record \$45 billion in property damage, enduring landfalls from five hurricanes. The 2005 season broke many of the records set during 2004, with property damage from one storm alone (Katrina, with a damage estimate of \$81 billion) almost doubling that of the entire 2004 season.

The particular investigation presented here aims to improve the understanding of two separate but somewhat related questions pertaining to TCs. First, the impact of environmental relative humidity on TC size and structure will be analyzed. As will be discussed, the size of a TC plays a large role in determining the damage, and therefore an understanding of what controls TC size is of critical importance. Second, the impact of anthropogenic climate change on TC intensity and structure will be investigated. Anthropogenic climate change also has the potential to impact TC size, which will be discussed in further detail in chapter 3.

1.2 TCs and climate change

1.2.1 Evidence

An increase in Atlantic TC activity since 1995 has been observed (Goldenberg et al. 2001; Klotzbach 2006), and studies by Emanuel (2005) and Webster et al. (2005) have suggested that there has been an increase in global TC intensity since the 1970s. While others have questioned the interpretation and quality of the data (Landsea et al. 2006), the observed increase in Atlantic main development region (MDR) sea surface temperature (SST) during the 21st century (e.g. Vecchi 2008) suggests the potential for more intense TCs, given the close association between observations of SST and maximum TC intensity in the North Atlantic basin (Demaria and Kaplan 1994).

While multidecadal fluctuations in North Atlantic SST have been observed (Goldenberg et al. 2001), Santer et al. (2006) have presented model-based evidence that the rising trend in the Atlantic MDR SST is too large to be explained by internal climate variability alone and that human-caused changes in greenhouse gases are the main driver of the 20th-century SST increase. The Intergovernmental Panel on Climate Change's (IPCC's) Fourth Assessment Report (AR4; Solomon et al. 2007) concluded that most of the observed global mean temperature increase since the mid-twentieth century is very likely (defined as a probability of >90%) due to anthropogenic increases in greenhouse gas concentrations. Both of these findings suggest that the observed SST increase is due at least in part to increases in greenhouse gases, and a continued increase in surface temperature (and SST) is projected by all general circulation models (GCMs) that employ increasing concentrations of carbon dioxide (CO_2) in the 21st century (Solomon et al. 2007).

Due to the proportionality between monetary loss and the cube of the maximum wind speed (e.g. Southern 1979; Emanuel 2005), even relatively modest increases in the intensity of strong TCs could significantly increase the damage potential. Increased TC rainfall in a warmed climate also could potentially increase damage potential. Regardless of changes in TCs themselves, increasing coastal populations and potential rises in sea level due to global

warming may leave coastal communities even more vulnerable to TC impacts in the coming years. Therefore, TC-associated damage and fatalities throughout the globe have the potential to increase during the 21st century as anthropogenic global warming and coastal vulnerability both increase. Based on this threat, it is imperative that the impact of future climate change on TCs be investigated using the best analysis tools currently available; this is the main goal of the present study, which will be described in further detail in subsequent sections.

1.2.2 Research Objectives

In a recent review paper, Knutson et al. (2010) succinctly summarized previous studies that investigated the impact of climate change on TCs. Several of these studies will be summarized in future sections, but first it is important to outline the current state of relevant research in order to understand the uniqueness of this study. Previous studies indicate a likely increase in TC intensity, although a large number of these previous studies were conducted with resolution that was too coarse to realistically simulated observed TC intensity. Mechanisms responsible for the increase in intensity were generally not identified, and few studies sought to analyze changes in TC structure.

The goal of this study is to assess the potential for the most intense TCs to increase in intensity due to global warming. We also seek to gain insight into the physical processes that are responsible for global warming induced changes in TC intensity and structure. Specifically, here we address global warming-induced changes in the thermodynamic environment (e.g. SST, atmospheric temperature, moisture) within which strong TCs form, with the ultimate goal of determining how these changes will impact the intensity, structure, and rainfall associated with strong TCs in a warmed climate. GCM projections play a role in this study, as we utilize their output to assess likely changes in the thermodynamic environment due to anthropogenic climate change. The impact of changes in wind shear will not be addressed here; the most intense TCs tend to form in regions and at times of low wind

shear, and we assume that even if there were a modest increase in monthly-mean wind shear (e.g. Vecchi and Soden, 2007), low shear periods would still occur.

Previous studies have sought to address some of the questions we pose, but this study will advance previous research in a number of ways:

1. A larger sample of current state-of-the-art GCM projections will be utilized to provide estimates of changes in environmental SST and tropospheric temperature and moisture due to global warming, and this larger ensemble should provide a more robust prediction of these changes. Individual GCM projections that depart considerably from the ensemble mean will also be utilized, and the role of tropospheric stabilization in altering TC intensity will be isolated with specifically designed model experiments.
2. This study will place an increased emphasis on the physical processes responsible for changes in TC intensity, structure and rainfall.
3. TCs will be simulated using higher resolution than in previous studies, allowing for the omission of cumulus parameterization (CP), which is required at larger grid lengths. This improved resolution and lack of CP will allow for more realistic simulation of TC intensity and structure, aiding in our goal to make a more direct link to TC processes, structural changes, and theory in order to better understand the physical mechanisms responsible for intensity change.
4. An attempt to quantify and identify sources of uncertainty in projections of TC intensity change will be made, with the goal of identifying future research avenues that will reduce the uncertainty.

1.2.3 Previous research

To form the basis for studying climate change and TCs, it is necessary to understand the environmental factors that impact TC intensity, and also the physical basis behind greenhouse gases altering tropospheric and stratospheric temperature and their representation in GCMs. Also required, of course, is an examination of previous studies that have investigated this topic.

1.2.3.1 TC maximum intensity

In order to examine how climate change may alter TC intensity, it is first necessary to understand what controls maximum TC intensity. Numerous attempts (e.g. Miller 1958, Malkus and Riehl 1960, Emanuel 1986, 1988, 1995, and Holland 1997) have been made to compute an upper bound on TC intensity for given atmospheric and oceanic conditions; this upper bound is usually stated as either the minimum surface pressure or maximum near-surface wind speed that a TC could attain a given environment. Assumed in most these derivations is the absence of environmental factors known to inhibit TC intensification, including wind shear, upwelling, and land interactions. Due to the presence of these detrimental factors, in nature only a fraction of TCs reach their maximum potential intensity (MPI)¹ (Emanuel 2000). At first glance the relatively small number of observed TCs attaining their MPI may call into question the usefulness of utilizing MPI in the context of climate change. However, Emanuel (2000) showed that the cumulative distribution functions (CDFs) of storm lifetime maximum intensity, normalized by climatological potential intensity, were nearly linear, but storms achieving hurricane strength have CDFs of smaller slope than those achieving only tropical storm strength. This suggests that there is a nearly uniform probability that a TC will achieve any given intensity up to marginal hurricane strength, and a uniform but lower probability that it will achieve any intensity between

¹Also of note is the fact that some observed TCs have *exceeded* the MPI (Montgomery et al. 2006), possibly due to the neglect of certain physical processes in MPI derivations.

marginal hurricane intensity and the potential intensity. In other words, based on current observations if global warming were to result in a 10 – 20% increase in MPI, the intensity of observed events would rise on average by the same percentage, including those TCs that do not attain their MPI. Therefore, an understanding of how MPI will change due to anthropogenic climate change may provide insight into how actual TC intensity will change as well.

Relatively recent analysis of different techniques for estimating MPI has revealed that the theory debuted in Emanuel (1986, hereafter referred to as EMPI), is the closest to providing a useful calculation of maximum intensity and that it also predicts a structure similar to that of observed TCs (Camp and Montgomery, 2001). Emanuel (1986) advanced the hypothesis that the intensification and maintenance of TCs depends exclusively on self-induced heat transfer from the ocean, and derived a relation between environmental parameters and TC maximum intensity. Two separate derivations were presented, the first based on a balance between frictional dissipation and energy production in the inflowing boundary layer, and the second in which TC energetic processes were described as a simple Carnot heat engine in which latent and sensible heat are extracted from the ocean at a temperature T_{in} and ultimately given up in the outflow at a temperature T_{out} . The EMPI is proportional to the thermodynamic efficiency, $(T_{in} - T_{out})/T_{in}$. This efficiency, multiplied by the oceanic heat source, represents the production of energy that is used to overcome frictional dissipation. The results suggest that extremely intense cyclones would occur with SSTs substantially warmer or upper tropospheric temperatures much colder than at present. Anthropogenic climate change leads to changes in both SSTs and upper tropospheric temperatures in the tropics, and therefore an understanding of both is required to assess potential changes in TCs intensity.

Shen et al. (2000) studied the effect of thermodynamic environmental changes on hurricane intensity and applied their results to the global warming problem. Idealized simulations utilized large-scale values of temperature and moisture based on observations, and the impact of changes in the SST and/or vertical temperature profile on simulated TC

intensity was investigated. Increasing the SST while maintaining a fixed vertical temperature profile always led to more intense TCs, as anticipated; this is consistent with MPI theory, as increased SSTs lead to warmer inflow and increased thermodynamic efficiency. Model simulations indicated that stabilization in the upper troposphere led to a reduction in TC intensity; this again is consistent with MPI theory, as upper tropospheric warming leads to a warmer outflow temperature and lower thermodynamic efficiency. Specifically, they found that without stabilization aloft the intensity increase associated with an SST increase of 2° C would double, while the intensity increase associated with a more modest SST increase (1.5° C) could be completely offset by an increase in upper-tropospheric temperature of 3 - 4° C. As stated by the authors and will be described subsequently, in the tropics SST and tropospheric stability are related, with GCM output indicating increases in both tropical SST and tropospheric stability in future climate projections. Increases in SST and tropospheric stabilization consistent with the GCM output led to model-attained TC intensity increases of 7–8 hPa. In the absence of the tropospheric stabilization, however, the same SST increase led to an intensity increase of approximately double this amount, indicating that stabilization of the troposphere partially offsets the increase in TC intensity that would occur due to SST increase alone. Therefore, based on the results of this study and also MPI theory, it is not only increases in SST that will impact future TC intensity changes but also warming of the upper troposphere.

1.2.3.2 The tropospheric response to increased greenhouse gas concentrations

Figure 1.1 presents a typical profile of projected 21st century temperature change in the tropics (blue curve) along with a summary of the physical processes responsible for these temperature changes, based upon previous research involving observational and model data. As indicated by the figure, temperatures in the troposphere are impacted by both tropospheric processes (convective) and stratospheric processes (radiative), as will be described in further detail in subsequent sections.

In an atmosphere with higher CO₂ concentrations, downwelling infrared radiation to the surface increases, leading to increases in surface temperature (or over the ocean, SST). Changes in the SST over the tropics subsequently lead to tropospheric lapse rate changes. The principle mechanism by which the tropospheric lapse rate is modified by surface temperature change in the tropics is the vertical transfer of heat by convective processes (e.g. Rennick 1977). In the absence of large-scale circulations, the tropical atmosphere tends to adjust toward an equilibrium that results when the loss of energy to space by long-wave radiation is balanced by the transfer of latent and sensible energy from the surface to the boundary layer, and its redistribution throughout the atmosphere by deep moist convection. The upper tropospheric temperature structure that results from convective adjustment is sensitive to the surface temperature, and in the tropics as the surface temperature increases moist convection produces an increasingly stable temperature stratification. Convective adjustment can act directly only in regions of frequent precipitation, which also tend to be regions of high SST (e.g. Zhang 1993; Fu et al. 1994), although advection and dynamical adjustment (e.g. Sobel et al. 2002) spread the convective heating to convectively inactive regions as well.

Complicating this relatively simple picture is the feedback between tropospheric water vapor and surface temperature (hereafter referred to as the water vapor feedback). Water vapor is a greenhouse gas, and as such increases in its concentration in the troposphere lead to an increase in downwelling infrared radiation, which leads to subsequent changes in surface temperature. Model experiments designed to isolate the impact of this feedback indicate that a strongly positive water vapor feedback amplifies greenhouse warming by a factor of 1.6 relative to an experiment with this feedback disabled (Houghton et al. 1990).

The region between typical convective outflow and the cold-point tropopause (the region where the coldest temperatures are found) has been referred to as the Tropical Tropopause Layer. This region, also referred to as the “sub-stratosphere/upper troposphere”, is around 150 – 70 hPa, and temperatures there are theorized to be mainly controlled by radiative processes. Forster et al. (2007), utilizing a radiative fixed dynamical heating model,

found that cooling in the stratosphere (70 – 30 hPa) due to ozone depletion leads to reduced downwelling longwave radiation, and subsequently leads to cooling that extends to the upper troposphere (150 – 70 hPa). Regardless of future changes in stratospheric ozone concentrations, cooling of the stratosphere is likely to continue as greenhouse gas concentrations increase. In a review paper discussing stratospheric temperature trends, Ramaswamy et al. (2001), found that increases in greenhouse gases accounted for ~1/4th of the observed 1979 – 1990 cooling trend in the lower stratosphere. In the stratosphere an increase in greenhouse gas concentration enhances the thermal emissivity. Due to the increase in emissivity, assuming that the radiation absorbed by this layer remains fixed, to achieve equilibrium the same amount of energy has to be emitted at a lower temperature and the layer cools. The increase in thermal infrared absorptivity, conversely, leads to enhanced absorption of radiation emitted by the troposphere, leading to a warming tendency. The net result is a balance involving these processes that depends heavily on the absorption spectrum. For CO₂ the main 15-μm absorption band is saturated over quite short distances, and therefore the absorbed radiation originates from the cold upper troposphere. When the CO₂ concentration is increased, the increase in absorbed radiation is quite small and the effect of the increased emission dominates, leading to a cooling at all heights in the stratosphere. To summarize, temperature changes in the stratosphere impact the upper troposphere, and therefore model representation of stratospheric processes is important as it could potentially impact TC outflow and thermodynamic efficiency.

1.2.3.3 Greenhouse gas induced temperature changes in GCMs

Based on the previous discussion, it is evident that heating due to convection plays an integral role in determining the vertical profile of temperature in the tropics, and that the upward transport of water vapor by convection and evaporation of hydrometeors can impact tropospheric water vapor and play an important role in radiative processes that determine the surface temperature. GCMs, owing to their coarse grid spacing, employ parameterization schemes in order to represent the effects of clouds that cannot be resolved on the model grid.

Cumulus parameterization (CP) schemes are generally classified as being either an adjustment scheme or a mass flux scheme. Adjustment schemes are active if a grid point is conditionally unstable and serve to relax the temperature profile to that of a reference profile, immediately precipitating out any water mass condensed by this procedure. Mass flux schemes are triggered by the presence of grid convective instability at a grid point, the existence of grid-scale mass convergence beyond some threshold, or exceedance of a threshold rate of destabilization at a grid point, and attempt to explicitly model feedback processes in each grid cell. Mass flux schemes generally provide a more accurate parameterization, including the magnitude of the vertical motion inside the clouds and the precipitation type and distribution. Grid length also plays a role in the accuracy of CP.

GCM projections are sensitive to the type of CP scheme employed, as described in Allan et al. (2002). A comparison of climate models revealed that the use of an adjustment scheme led to an upper troposphere that was too cold and dry, a common characteristic of adjustment schemes (e.g., Hack 1994), while temperature and moisture in the upper troposphere were more realistically simulated with a mass flux scheme. Specifically, Hack (1994) attributes the improvement in upper tropospheric temperature and moisture in models using mass flux schemes to the explicit vertical eddy heat transport term, which is not accounted for in adjustment schemes. The choice of scheme impacts the water vapor feedback, with mass flux schemes tending to transport water vapor more efficiently into the upper atmosphere, leading to a stronger dependence of temperature and moisture on changes in the surface temperature in models with mass flux schemes. Vertical resolution also impacts the performance of a CP scheme, as demonstrated by Tompkins and Emanuel (2000). In this study column models were run to an equilibrium state and the sensitivity to vertical resolution was analyzed. Convergence of the results was found with a uniform vertical resolution of 25 hPa, while coarser resolution led to significant errors in both the water vapor and temperature profiles (relative to the high resolution results).

CP scheme is but one factor that can impact climate change projections in GCMs. Cordero and Forster (2006) describe the impact of tropospheric and stratospheric processes

on upper tropospheric temperatures, and compare 20th century temperature trends from GCMs utilized in the IPCC AR4 to both observations and the NCEP reanalysis. Near the surface and through the middle troposphere the models agree reasonably well with each other and were generally within 2-3° C of the NCEP reanalysis. The model spread increases with height, as does the disagreement between observations and the models. Observations indicate a cooling trend in radiosonde observations down to 200 hPa, while the models exhibit a moist-adiabatic response in this region, indicating that convective processes have a dominant influence on temperatures at this level. Of the 19 models that were studied, all include well-mixed greenhouse gas forcing while only 11 include stratospheric ozone depletion. Models that include ozone depletion were found to be significantly closer to observations than the models that omit ozone variations. From the surface to 200 hPa, models including ozone depletion were found to be within the range of uncertainty for the radiosonde observations, while in the models without ozone depletion temperatures were within the range of uncertainty from the surface to only the 500-hPa level. These results indicate that model ozone concentrations impact temperature values into the troposphere, and that realistic ozone concentrations and representation of stratospheric processes are required to realistically simulate temperatures in the mid-upper troposphere.

To summarize, temperature changes in the upper troposphere may impact future TC intensity by altering TC outflow structure and temperature, and subsequently the thermodynamic efficiency. Changes in upper tropospheric temperatures due to global warming modeled by GCMs will be sensitive to a number of model attributes, including the CP scheme, the vertical resolution, and the representation of radiative processes linked to the distribution of ozone. Therefore, projected temperature changes in the upper troposphere are more uncertain than those at a lower altitude, and are important because they play a role in altering TC outflow and thermodynamic efficiency. Thorough analysis of the representation of these physical processes in the different GCMs may allow for a more informed decision to be made concerning which GCMs to trust in forecasts of climate change, which in turn could increase confidence in projections of TC intensity change. At this time, we have utilized ensemble mean projections and projections from individual GCMs that depart most from the

mean (as described in chapter 2), in order to provide a projection of the most likely change in TC intensity along with a measure of the uncertainty.

1.2.3.4 Tropical cyclone intensity studies

Studies investigating the impact of global warming on TC intensity have employed several different strategies. The most basic type utilizes a GCM to simulate past TC activity using observed SSTs (varying in time or based on a long-term climatology), and compares the results to TC activity in a future projection. By comparing TC activity from the future and current periods, changes in intensity, frequency, and other characteristics can be studied, and generally speaking systematic biases in the GCM should ideally cancel out. Due to the large computational expense associated with long-term integrations, GCMs are required to use horizontal resolution that is unable to realistically simulate important storm-scale physical processes that determine TC intensity (e.g., storm-scale variations in turbulent fluxes, secondary circulation, and eye-eyewall processes), in part stemming from the need to parameterize sub-grid scale convection. The CP scheme degrades the realism of the TC secondary circulation, impacting TC intensity as well (e.g., Davis and Bosart 2002). Due to these limitations, tropical disturbances in these models are often referred to as being “TC-like” in that the modeled storms are larger in size and weaker than those observed. Recently, GCM projections with grid spacing of less than 30 km have provided evidence for increasing TC intensity in a warmed climate (e.g., Oouchi et al. 2006; Bengtsson et al. 2007); however still higher resolution is required to reproduce observed TC intensities. Bengtsson et al. (2007) specifically found that model projections with increased resolution predicted a larger increase in the frequency of intense TCs in the future climate, highlighting the need for high-resolution models, with explicit convection, in studies of TC intensity change in future climates.

In order to simulate future TC activity at high resolution, a procedure hereafter referred to as idealized downscaling was developed (e.g., Knutson and Tuleya 1999, 2001,

2004; Shen et al. 2000). In this approach, model simulations of an individual idealized TC embedded in a simplified large-scale environment with no other disturbances and no land are performed. Large-scale conditions, including SST, atmospheric moisture, temperature, and wind, can be based on observational analyses or model data. These large-scale conditions are typically averaged over time and space to represent the average conditions that support strong TCs. By utilizing large-scale conditions from a GCM projection, the impact of climate change on TCs can be determined. Due to the absence of external factors detrimental to TC intensity, this approach is better suited for the study of maximum TC intensity, and allows for the impact of specific changes in assumed parameters or in the large-scale environment to be analyzed in isolation. Knutson and Tuleya (1999) demonstrated the viability of this methodology by showing that simulated TC intensification in the future climate was similar using either high-resolution regional model simulations or the idealized downscaling technique.

Using the idealized downscaling technique, Knutson and Tuleya (1999) found a simulated increase in surface wind speed of $3\text{--}7 \text{ m s}^{-1}$ (5–11%), a decrease in central pressure of 7 to 24 hPa, and an increase in near-storm precipitation of 28% in future storms. The impact of ocean coupling on simulated TC intensity change was found to be minimal by Knutson and Tuleya (2001), who identified statistically significant increases in maximum surface wind speed of 5–6% along with a 20% increase in rainfall within 100-km of TC center. The robustness of previous results was examined in Knutson et al. (2004) by testing the sensitivity of the results to the choice of climate model large-scale conditions and the CP scheme used in the TC simulations. Large-scale conditions from nine different climate models from the World Climate Research Program (WCRP) Coupled Model Intercomparison Project (CMIP2+) experiment were compared, and four different CP schemes for the hurricane model were tested, including the omission of CP in on the highest resolution inner grid. Nearly all combinations of large-scale conditions and CP schemes produced an increase in both simulated storm intensity and near-storm precipitation rates in future TCs. Averaged over all simulations, a 14% increase in central pressure fall, a 6% increase in maximum surface wind speed, and an 18% increase in averaged precipitation rate within

100-km of TC center was found in high-CO₂ experiments relative to the control. Overall, the simulated intensity increases in these studies were found to be fairly similar and robust, and large increases in TC rainfall were also noted.

Using dynamical downscaling approaches, numerical models utilizing observed SSTs and atmospheric reanalyses have been able to reproduce year-to-year variability in Atlantic hurricane counts for 1980–2006 (Knutson et al. 2007). In these simulations, the interior solution is nudged towards atmospheric reanalyses on larger spatial scales. Due to shorter integration lengths and a smaller domain, these simulations were run with substantially higher resolution (18-km grid spacing) than full GCM projections, but still contained a larger number of TCs and transient synoptic-scale conditions. A similar approach was later adopted by Knutson et al. (2008) to study the impact of climate change on Atlantic TC activity, with the mean atmospheric state (used by the interior nudging) and SSTs altered according to late twenty-first-century changes simulated by an ensemble of the WCRP CMIP3 models, under Intergovernmental Panel on Climate Change (IPCC) emissions scenario A1B. Although finding a reduction in the total number of tropical storms and hurricanes, these simulations indicate an increase in the frequency and intensity of the strongest hurricanes, and an increase in near-hurricane rainfall rates. Although these simulations were performed at fairly high resolution, Bender et al. (2010) extended the modeling approach by downscaling each individual model storm from the 18-km simulations, noting that the 18-km simulations are unable to reproduce the observed frequency of intense hurricanes. These higher resolution simulations indicate an increase in the number of category 4 and 5 hurricanes in the future climate. The authors note that the results are sensitive to the manner in which the late 21st century changes were calculated, and whether or not ensemble-mean or individual GCM data are utilized.

Lynn et al. (2009) conducted model simulations of hurricane Katrina, but with the addition of GCM projected mean climate change values from various points of the 21st century. An increase in future intensity was noted, along with a decrease in size. The authors speculated that the decrease in size was due to an increase in tropospheric stability;

this possible change will also be investigated here. Also, the increase in intensity was attributed to warming SST, while a reduction in intensity due to tropospheric stabilization and outflow warming was also noted. The authors did not attempt to assess the sensitivity of the results to the GCM chosen for projected climate changes.

1.2.4 Summary

To summarize, previous studies that investigated the impact of climate change on TCs have typically noted an increase in maximum TC intensity, along with an increase in rainfall. While several studies have described the sensitivity of the results to the GCM projected tropospheric warming (e.g., Knutson et al. 2004; Bender et al. 2010), in general this has not been a main focus.

1.3 TC Size

1.3.1 Motivation

The size of a TC is important for a number of reasons, including its role in influencing TC impacts, environmental interaction, and also track. Specifically, the size of a TC, in addition to intensity, has a direct influence on the extent of evacuations, ship re-routing, along-track timing of the arrival of storm conditions, and the duration of high winds and storm total rainfall at a given location. After landfall, the area under threat of TC-spawned tornadoes and high precipitation totals is in part dependent on storm size. Furthermore, a recent study by Irish et al. (2008) found that for a given TC intensity, storm surge variations of up to 30% could be explained by the size of the storm. Hurricane Katrina, which caused unprecedented storm surge damage to portions of the Gulf coast, was only rated a category 3 on the Saffir-Simpson hurricane scale at landfall, but its large size, at least in part, led to the large surge. Recently, a scale designed to take into account the role of TC size in damage potential has been developed (MaClay et al. 2008), which utilizes wind

speeds within 200-km of the center. Dynamically, the vulnerability of a storm to vertical wind shear and dry environmental air may be related to its size, and the movement of large storms may differ from that of smaller ones due to more pronounced beta drift. Fovell et al. (2009) document sensitivity in the track of simulated TCs to choice of model microphysics scheme, and relate this to differences in the lateral extent of the wind field. Climate change may also lead to changes in TC size. Therefore, knowledge of the environmental and dynamical factors that determine TC size is relevant to the prediction of TC track, intensity, and impacts. Despite the importance of TC size, the physical mechanisms determining this have received limited attention in the scientific literature (e.g., Liu and Chan 2002).

1.3.2 Research objectives and hypothesis

The purpose of this research is to investigate the influence of environmental humidity on the lateral extent of the TC wind field. We hypothesize that the size of the TC wind field is related to the extent and intensity of outer spiral rainbands, which are in turn related to the environmental relative humidity. More moist environments support a larger amount of precipitation outside of the TC core, which leads to greater diabatic PV production there and a larger wind field. This PV, if given a favorable geometric structure, may amalgamate with the TC core, although its mere presence outside of the TC core leads to a larger wind field (e.g., Hill and Lackmann 2009). Dry environments lead to suppressed rainfall outside of the TC core, and a narrower PV distribution and wind field. This hypothesis was tested by conducting idealized experiments with the WRF model, which are designed to isolate the sensitivity of size to environmental moisture.

1.3.3 Observed sizes

TC size can be measured in several ways, including distance from the TC center to outermost closed sea-level isobar, radius of gale, tropical-storm, or hurricane-force winds,

radius of maximum wind (RMW), and breadth of satellite-observed cloud shield. Tropical cyclones (TCs) are observed to vary considerably in size (e.g., Frank and Gray 1980; Merrill 1984; Weatherford and Gray 1988; Cocks and Gray 2002; Kimball and Mulekar 2004). Notable differences in size between basins have been noted, such as those between the northwest Pacific and West Indies (Frank and Gray 1980), and between the Western North Pacific and North Atlantic (Merrill 1984). Well-documented extremes range from Supertyphoon Tip (October 1979), which was characterized by a radial extent of gale-force winds (17 m/s) of ~1100 km (Dunnavan and Diercks, 1980), to Tropical Cyclone Tracy (December 1974), which featured peak winds near 65 m/s, yet gale-force winds extending only 50 km from the center (Bureau of Meteorology 1977). The corresponding area experiencing gale-force winds was less than 8,000 km² for Tracy and over 3,800,000 km² for Tip. Within the Atlantic basin TC size varies substantially as well, with an order of magnitude differences noted in the radius of tropical storm force wind in extreme cases (e.g., Kimball and Mulekar 2004; their Table 2).

1.3.4 Controls on TC size

In general, previous studies have found little correlation between TC intensity and size. Frank and Gray (1980) noted that the extent of the 15 m s⁻¹ wind speed radius was quite variable for TCs of similar maximum intensity. Merrill (1984) calculated a correlation coefficient of only 0.28 between storm size (measured as the radius of outermost closed isobar) and intensity (defined as the maximum wind speed) using a large sample of storms for the North Atlantic and Pacific basins. Weatherford and Gray (1988) found a weak relationship ($R^2 = 0.23$) between minimum central pressure and the radius of 15 m s⁻¹ wind. Cocks and Gray (2002) did note an increase in the variance explained between these two parameters after removal of what they termed “gyre” TCs, with R^2 increasing to 0.40. From an analytical standpoint, Emanuel (1986) suggested that the wind speeds in the outer core of a TC are not directly related to intensity.

Previous studies have also sought to correlate differences in TC size with environmental parameters. Observational data indicates that storm size varies with latitude (e.g., Merrill 1984; Cocks and Gray 2002; Kimball and Mulekar 2004) with a tendency for size increases as a TC moves poleward. Changes in angular momentum import with latitude were hypothesized by Merrill (1984) to account for changes in TC size resulting from latitudinal changes or changes in synoptic environment. Studies of the extratropical transition of TCs have noted, as did Merrill (1984), that the size of the TC wind field often increases during recurvature (e.g., Jones et al. 2003). A tendency for TC to peak in size during the month of September was noted by Kimball and Mulekar (2004), while a peak was found during late season storms in the Western North Pacific (Cocks and Gray 2002).

Emanuel (1986) and Rotunno and Emanuel (1987) investigated TC size as well, and emphasized the size of the initial disturbance as a determining factor. Cocks and Gray (2002) highlighted initial disturbance size as well, classifying observed systems into size groups. They noted that small TCs were small throughout their lifecycles, and large TCs were significantly larger than medium and small TCs by the 25% point of their composite life cycles. Xu and Wang (2010) emphasize the role of initial vortex size in determining mature TC size, but acknowledge that environmental moisture also plays a role. Very recently, Matyas and Cartaya (2009) analyzed Hurricanes Frances and Jeanne (2004), and determined that the precipitation distribution was influenced by the degree of outer rainband activity, which was in turn related to environmental humidity. Kimball (2006) noted that increasing moisture in the near-TC environment enhanced the formation of rainbands and led to a larger storm, although the physical mechanisms responsible for this size increase was not investigated in detail. Hill and Lackmann (2009) emphasized the importance of environmental relative humidity in controlling TC size in idealized model simulations with the WRF model.

1.3.5 Potential vorticity (PV), TC rainbands, and TC size

Following the papers of Hoskins et al. (1985) and Davis and Emanuel (1991), numerous studies have utilized the PV framework for the study of tropical cyclones (e.g., Jones et al. 2003, section 3b). These include studies of TC motion (e.g., Wu and Emanuel 1995a,b; Shapiro and Franklin 1999), formation and intensification (e.g., Molinari et al. 1998; Davis and Bosart 2001, 2002; Möller and Shapiro 2002), and circulation dynamics (Wang and Zhang 2003). Using a nonlinear balance relation, Wang and Zhang (2003) demonstrated that a large fraction of the TC circulation could be recovered from a PV inversion, with notable unbalanced flow in the lower inflow and upper-level outflow layers. In the study of TCs, important principles from a PV perspective are superposition and diabatic generation, as illustrated in Davis and Emanuel (1991, their Fig. 1). The superposition principle states that the net balanced circulation associated with multiple PV anomalies is the arithmetic addition of the individual balanced circulations. For example, Molinari et al. (1998) used this framework to examine trough interactions with Hurricane Opal, and Möller and Shapiro (2002) and Shapiro and Möller (2003) utilized this framework to investigate the role of asymmetries in the intensification of Hurricane Opal. Davis and Bosart (2001, 2002) appealed to a combination of diabatic PV production and superposition to explain the genesis of Hurricane Diana (1984).

From a PV perspective, the size of the balanced primary circulation in a TC is linked to the size and strength of three cyclonic PV anomalies associated with the storm. The most prominent PV feature is the interior cyclonic PV tower; in high-resolution simulations of strong TCs, this PV anomaly can exceed 100 PVU² (e.g., Hausman et al. 2006). These extreme PV values, more typical of those found far above the tropopause, are attributable to intense latent-heating gradients in the presence of very large cyclonic vorticity in the TC eyewall. Diabatic PV growth due to condensational heating is responsible for the aforementioned interior cyclonic PV maxima. As shown by Raymond (1992), Stoelinga

² 1 Potential vorticity unit (PVU) is defined as $10^{-6} \text{ K m}^2 \text{ kg}^{-1} \text{ s}^{-1}$.

(1996) and others, the rate of diabatic PV generation is related to the projection of the heating gradient onto the absolute vorticity vector. Due to the decrease in cyclonic circulation with height in a warm-core vortex, the absolute vorticity vectors tilt outward with height, meaning that the maximum diabatic PV production should be found radially inward and beneath the location of maximum heating.

Additionally, the TC core is associated with an equivalent cyclonic PV anomaly due to the warm potential temperature anomaly at the surface in the center of the storm, which also contributes to the storm circulation. Even with constant surface air temperatures, the lower surface pressure in a TC core yields larger potential temperature values there. Warm surface potential temperature anomalies are equivalent to cyclonic PV anomalies (Bretherton 1966), and thus contribute to the cyclonic TC wind field.

Cyclonic PV is generated by latent heat release in outer spiral bands, and here it is hypothesized that more moist environments support more intense and widespread spiral bands, which produce larger amounts of PV, and subsequently play a role in determining TC size. PV generated in spiral bands outside the storm core contributes to the overall cyclonic PV distribution as cyclonic PV wraps into the core PV tower, and also due to the presence of cyclonic PV that has not amalgamated with the central tower. Inversion of a broader or stronger PV distribution is consistent with a broader balanced TC primary circulation. Previous studies have examined the development of diabatic PV maxima associated with spiral bands (e.g., Guinn and Schubert 1993; May and Holland 1999; Chen and Yau 2001; Wang 2002a; Chen et al. 2003; Hence and Houze 2008). These studies point to the role of spiral bands as a potentially important source of PV and momentum that could affect storm intensity, and Guinn and Schubert (1993) also mention the possible linkage between storm size and spiral band activity. Hence and Houze (2008) indicate that diabatic PV production is associated with the development of a secondary wind maximum. Growth of the lower-tropospheric cyclonic PV distribution is associated with latent heat release in the eyewall as well as in outer rainbands. As described in chapter 2, we utilize a PV budget to study the

impact of diabatic PV production in spiral rainbands on TC size in the different WRF experiments.

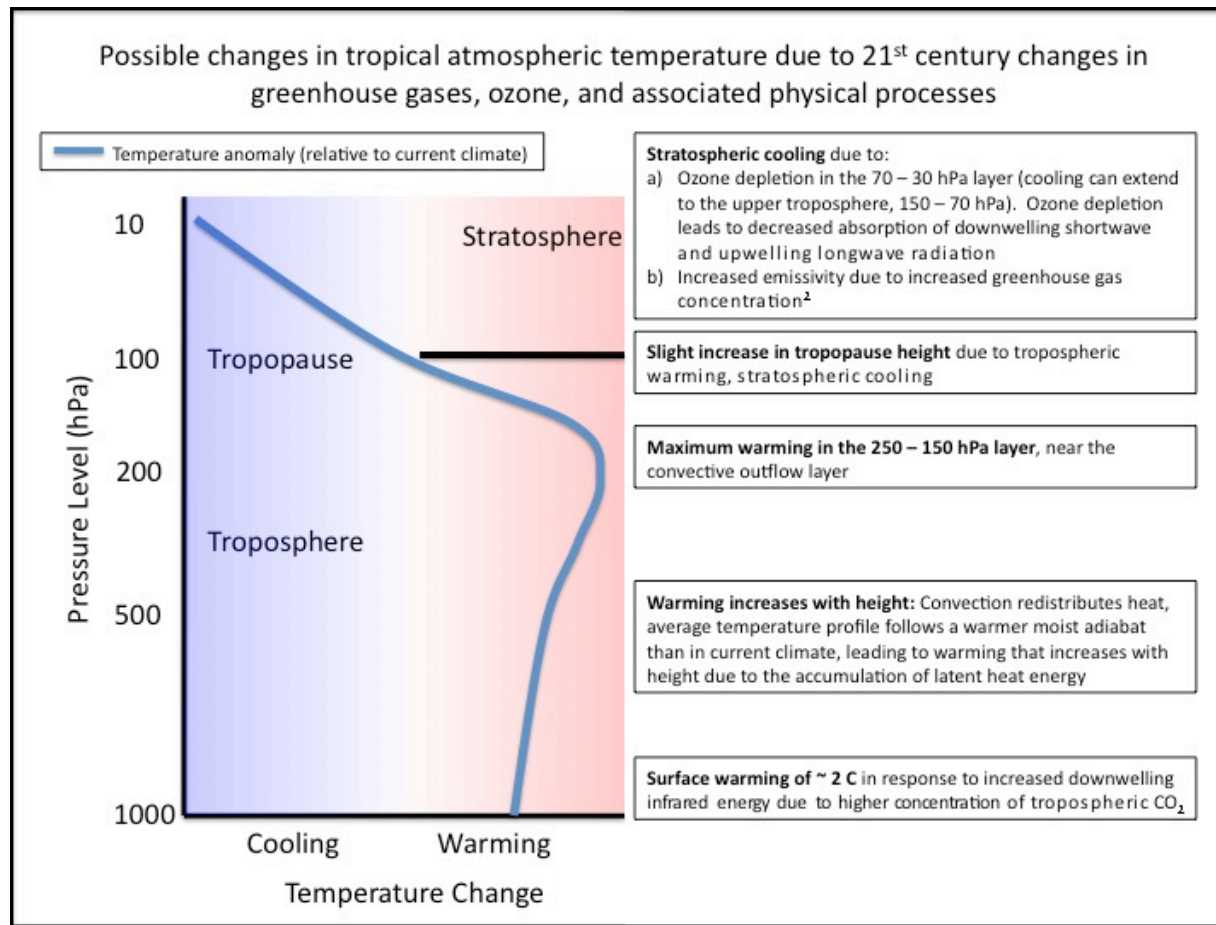


Figure 1.1: Schematic of GCM ensemble mean temperature change profile (blue curve) and the associated physical processes responsible for the change.

Chapter 2

Methodology

2.1 Tropical cyclone size

2.1.1 Model set-up and initial conditions

In order to investigate the impact of relative humidity on TC size, a set of model experiments designed to isolate this parameter was required. A method designed by the author was created to initialize a TC-like vortex within a tranquil ambient environment. This initialization procedure, referred to as a “quasi-idealized” approach, has the advantage over real-case simulations in that the role of moisture on TC size can be isolated. Four idealized simulations designed to investigate the sensitivity of TC size to environmental humidity were performed using version 2.2 of the Weather Research and Forecasting (WRF-ARW) model). In each simulation, the environmental temperature profile and SST were specified as the mean for the region 8.5–15°N, 40–60°W, during the month of September 2005 (region shown in Fig. 2.1). Atmospheric variables were computed from Global Forecast System (GFS) analysis data, and the SST was derived from the Reynolds 0.5° analysis. The moisture field, which is a function of distance from TC center, will be described in a subsequent section. The average SST in this region was 29.2°C, favorable for intense TC development. This region and time were chosen in order to be consistent with conditions that are favorable for TC development, but experiments with other environmental soundings, such as that of Jordan (1958) produced similar results (not shown).

An axisymmetric initial vortex, similar to that of Kwok and Chan (2005), was superimposed on the horizontally uniform temperature field. The maximum wind speed was initially 20 m s^{-1} at a radius of 50 km, with a minimum sea level pressure of $\sim 1000 \text{ hPa}$. The horizontal wind field $V_T(r)$ was specified following Chan and Williams (1987):

$$V_T(r) = V_{\max} \left(\frac{r}{r_{\max}} \right) \exp \left\{ \frac{1}{b} \left[1 - \left(\frac{r}{r_{\max}} \right)^b \right] \right\}, \quad (1)$$

where r is the radius, r_{\max} the radius of maximum wind, and V_{\max} the maximum wind. The parameter b is related to the size of the vortex, and $b = 0.33$ in all experiments. Vertical structure is introduced to the horizontal wind field by multiplying $V_t(r)$ by a function $w(p)$ that decreases with pressure above 850 hPa:

$$w(p) = \left[\frac{3(p/p_m)}{2 + (p/p_m)^3} \right], \quad (2)$$

where p_m is the vertical level of maximum tangential wind, set to 850 hPa. The initial vortex was centered at 11°N, although additional experiments reveal that the results are not sensitive to this choice (not shown). Based on the specified wind profile, temperature anomalies in the TC were computed assuming gradient thermal wind balance. Next, surface pressure was recomputed with the addition of the TC temperature anomalies, and finally the full height field was recomputed utilizing the surface pressure field along with the temperature field.

In all experiments, 80% relative humidity is specified within 100 km of the TC center (referred to as the moist envelope), adjusting linearly to 20, 40, 60 or 80% between 100 and 150 km radius, with uniform values outside 150 km. Hereafter, simulations will be referenced according to the relative humidity value found beyond 150 km (e.g., 20RH refers to the simulation with 20% relative humidity outside of 150 km). Although these specifications are somewhat arbitrary, these specific choices were made after careful consideration. Regarding the inner-core moisture specification, the unsaturated TC core leads to slow initial intensification in all simulations, as some time is required to reach saturation, commence diabatic heating, and begin the intensification process. The specification of the unsaturated core is, however, in our view superior to arbitrarily specifying 100% relative humidity within some radius, as it allows for the model to develop the TC inner-core moisture structure in a physically realistic manner. The 100-km radius for

the moist envelope was based upon the assumption that a typical TC would contain substantial water vapor out to a distance of approximately double the radius of maximum wind. Several additional experiments were performed in order to examine the sensitivity of the results to the inclusion and radius of the moist envelope. An experiment with 20% ambient relative humidity and a moist envelope radius of 50-km was also performed. The results were found to not be very sensitive to the radius of the moist envelope, although the smaller moist envelope did reduce the TC size slightly. Experiments in which relative humidity was initially set to 80, 60, 40 or 20% everywhere (including inside the vortex) were also performed, and the results are highly similar to those with a moist envelope surrounding the initial vortex. The main difference is that the dryer simulations take longer to intensify due to the time required for moistening of the inner core. Finally, the wide range in ambient relative humidity values was imposed in order to provide a robust test of sensitivity to this parameter rather than to specifically reflect conditions in nature; however, the 20RH simulation could be analogous to conditions near the Saharan air layer in the North Atlantic (e.g., Dunion and Velden 2004, their Fig. 2, Dunion and Marron 2008).

The idealized experiments were conducted using the full-physics advanced-research WRF (ARW) on an actual geophysical domain, but with the domain set to include only water. Model simulations were run for 10 days, which allowed the storm size to evolve sufficiently for the purposes of this study. These simulations utilized a high-resolution vortex tracking inner domain (508×508 grid points with 2-km grid spacing) one-way nested within an outer domain (400×400 points with 6-km grid spacing). The 1016×1016 km inner domain dimension is sufficiently large to accommodate most observed TCs, but is run with grid spacing that can resolve spiral bands, which are important to TC size. Lateral boundary conditions on the outer 6-km domain were set to the constant environmental values, whereas the lateral boundaries of the mobile inner nest were obtained from the (time varying) 6-km simulation. Simulations on both domains included 47 vertical layers, and a model top of 50 hPa.

Model experiments were performed on both an f-plane and with full Coriolis force. The sensitivity of TC size to environmental moisture was consistent in both sets of experiments, although in model simulations with full Coriolis the TCs approached the NW edge of the outer 6-km domain towards the end of the simulation due to beta drift. By utilizing an f-plane valid at 11°N the TCs moved little during the 10-day simulation, assuring that the nested domain remained nearly centered in the outer domain and reducing the possible impact of the lateral boundaries. Therefore, results shown here are from the f-plane simulations, although the results are similar with each set of simulations.

Cumulus parameterization was omitted on both domains. The WSM 6-class scheme was used for the parameterization of microphysical processes (Hong and Lim 2006). The Mellor-Yamada-Janjić (MYJ) surface layer scheme (Janjić 2002), based on Monin-Obukhov similarity theory, was used with the MYJ boundary layer parameterization, based on Mellor-Yamada 2.5-level turbulence closure.

2.1.2 Potential vorticity techniques

Central to our hypothesis is the production of PV in TC spiral rain bands. In order to examine the PV distribution and production in the idealized experiments, we utilize the isobaric PV-tendency equation of Lackmann (2002):

$$\frac{\partial q}{\partial t} = -\nabla_p \cdot (q \vec{V}_h) - \frac{\partial}{\partial p} (\omega q) - g \cdot \nabla_3 \vec{y} \quad (3)$$

where q is the Ertel PV, $\vec{y} = -\dot{\theta}(\hat{k} + \nabla_3 \times \vec{V}_h) + \nabla_3 \theta \times \vec{F}$ is the nonadvective PV flux, $\vec{\nabla}_3$ and $\vec{\nabla}_p$ are the three- and two-dimensional gradient operators, respectively, \vec{F} is the frictional force vector, and $\dot{\theta}$ is the Lagrangian potential temperature tendency. The terms in (1) were evaluated locally, and in order to assess the impact of rainbands and asymmetric TC

features, the horizontal flux term was divided into azimuthal mean and perturbation components.

The diabatic PV tendency computation employs two different forms of $\dot{\theta}$: for fixed domains, the model-output diabatic temperature tendency from the microphysics scheme was used. Output from moving nests in WRF version 2.2 does not include the model-derived diabatic tendencies, necessitating the use of a parameterization from Emanuel et al. (1987) for condensational heating in the moving-nest simulations:

$$\dot{\theta} = \omega \left(\frac{\partial \theta}{\partial p} - \frac{\gamma_m}{\gamma_d} \frac{\theta}{\theta_e} \frac{\partial \theta_e}{\partial p} \right) \quad (4)$$

where γ_d and γ_m are the dry and moist-adiabatic lapse rates, respectively. The model-output diabatic tendency is more complete, as it includes latent cooling as well as heating, but comparisons of PV budget terms using both diabatic formulations were qualitatively similar (not shown). The frictional contribution to the PV tendency is treated as a residual.

2.1.3 Analysis techniques

2.1.3.1 Wind radii

In order to examine the size of the TC wind field, the radius of maximum wind (RMW), radius of tropical storm force wind (RTS), and radius of hurricane force wind (RHW) were computed. In order to compute these size metrics, the model 10-m wind speeds were azimuthally averaged around the TC center. The TC center at each output time was located by objectively analyzing the grid cell with the lowest smoothed sea level pressure. Different smoothing techniques were tested, and the resulting center fixes were not highly sensitive to the details of the smoothing; ultimately, a 40-pass Gaussian filter was employed. Once the center fixes were obtained, the azimuthally averaged wind speeds were computed. Finally, the RMW was then determined to be the distance where the azimuthally averaged

winds were maximized, while the RHW and RTS were computed as the maximum distance at which the azimuthally averaged wind speed exceeded the hurricane and tropical storm force criteria, respectively.

2.2 Future TC intensity, rainfall, and structure

In order to examine changes in future TCs, simulations of idealized TCs in large-scale conditions consistent with current observed conditions and projected future conditions were performed, and the climate sensitivity was investigated. To this end, this research combines reanalysis and analysis data for current climate conditions, GCM projections for estimates of climate change, and high-resolution TC simulations in an attempt to quantify the impact of global warming on maximum TC intensity and TC structure. Each component of the methodology will be addressed in subsequent sections.

2.2.1 Current climate conditions

The first step in this study is to identify the typical large-scale conditions (SST, atmospheric temperature and moisture) within which strong TCs develop and intensify. Previous studies of this type have utilized GCM integrations with fixed (based on observations) CO₂ values for current climate conditions. In this study, current climate conditions are observationally based in order to avoid any systematic biases between GCMs and actual conditions. Atmospheric temperature and moisture were computed using monthly-mean 2.5 degree NCEP/NCAR (Kalnay et al. 1996) reanalysis data, while 0.5° Real-time global (RTG) SST data were used. Conditions were averaged during the month of September and over the years 1990 – 1999, in order to smooth diurnal variations and transient weather disturbances. Spatial averaging was performed over the region shown in Fig. 2.1, which encompasses the western half of the Atlantic “Main Development Region”

(MDR) as specified in Vecchi and Soden (2007). Simulations utilizing the large-scale conditions from the reanalysis data will hereafter be referred to as the “control” experiments.

2.2.2 Creation of future climate environment

In order to construct future climate values, future changes were calculated using GCM output. GCM output used here is a subset of that produced in aid of the most recent report of the IPCC. These GCMs were run with greenhouse gas concentrations specified in accordance with a number of different scenarios, described in detail in the IPCC Special Report on Emissions Scenarios (SRES; 2002). These scenarios are designed to span a range of demographic, economic and technological driving forces of greenhouse gas emissions. As such, each emissions scenario is considered to be equally plausible, and for this study we will utilize 3 commonly used future greenhouse gas emissions scenarios: SRESA1B, SRESA2, and SRESB1. In order to maintain consistency, GCMs utilized in his study must contain all necessary data fields from these three future scenarios and also from the 20C3M experiment, which is designed to replicate 20th century conditions. The SRESA1B scenario follows the A1 storyline, which describes a future world of very rapid economic growth, global population that peaks in mid-century and declines thereafter, and the rapid introduction of new and more efficient technologies. The A1B scenario assumes a balance across increases in both fossil intensive and non-fossil energy sources. The A2 storyline and scenario describe a very heterogeneous world, with continuously increasing global population, regionally oriented economic development, and fragmented technological change. Finally, the B1 scenario describes a convergent world with a global population that peaks in mid-century and declines thereafter, with rapid changes in economic structures towards a service and information economy, with the introduction of clean and resource-efficient technologies. The resulting estimates of greenhouse gas emissions are displayed in Fig. 2.2; to summarize, the scenarios listed in order of increasing emissions (and concentrations) are SRESB1, SRESA1B, and SRESA2.

In total, the necessary data fields from the three emissions scenarios were available

from 13 GCMs; see Table 2.1 for a list of the models and the agencies responsible for their development. Monthly-mean atmospheric temperature and moisture, along with surface pressure and sea surface temperature data were obtained from the World Climate Research Program (WCRP) third Climate Model Intercomparison Project (CMIP3) multimodel dataset¹. To facilitate further analysis, model output initially in the network common data format (NetCDF) was converted to the GEMPAK file format using a Fortran conversion utility written by the author. The future change in a variable was calculated as the difference between the September 1990 – 1999 and September 2090 – 2099 mean. The 1990 – 1999 September mean was computed using data from the 20C3M runs, while the 2090 – 2099 September mean was calculated using output from projections forced with either the SRESA1B, SRESA2, or SRESB1 emissions scenario. In total, 39 sets of projected changes were computed; 13 from each of the 3 emissions scenarios considered. These projected changes and their uncertainty will be described in detail in chapter 4.

2.2.3 Idealized tropical cyclone characteristics

An axisymmetric TC-like vortex, similar to that utilized in the TC size investigation was inserted within the previously described horizontally uniform environments. The initial vortex utilized the same analytic expression for wind speed as described previously, although in this case r_{\max} was set to be 70 km, and V_{\max} 30 m s⁻¹. Additional model experiments revealed that the maximum intensity after a sufficiently long integration period was not sensitive to the strength of the initial vortex (Fig. 2.3).

2.2.4 Numerical model TC simulations

The WRF model version 2.2 (Skamarock et al. 2007) was used to simulate TC intensification in the current and future climate environments. The model was run on an

¹ GCM data is available at: <https://esgcet.llnl.gov:8443/index.jsp>

actual geophysical domain without land (TC initially centered at 10° N) and with full model physics. An f-plane, valid at 10° N, was utilized in order to minimize TC movement and interaction with domain boundaries. The SST remained constant during the model integrations. Simulations featured 47 vertical layers, with a higher concentration in the boundary layer and a model top of 10-hPa (distribution based on the results of Zhang et al. 2003).

Model simulated TC intensity is sensitive to many aspects of the model configuration, including grid spacing, and the parameterization of microphysical processes and turbulent mixing (e.g. Braun and Tao 2000; Davis and Bosart 2002; Hill and Lackmann 2009). Preliminary model experiments utilizing one of the following microphysics schemes (Kessler, Purdue-Lin, WSM6) along with either the YSU or MJY surface layer/PBL parameterization schemes were performed. The results indicated that the Purdue-Lin scheme tended to produce TC intensity that far exceeded the maximum potential intensity (MPI) and the intensity in the other model simulations. The Kessler scheme produced reasonable TC intensity, but due to the lack of frozen hydrometeors did not produce a highly realistic TC structure. The WSM6 scheme produced realistic TC structure, and intensity that was fairly close to the MPI, and was therefore used in the large-sample of model simulations. Model simulations were performed with either the MJY or YSU parameterization schemes, as both produced realistic results and by utilizing both the larger number of simulations provides for potentially more robust results.

2.2.4.1 Simulations with 6-km grid spacing

A large number of simulations with 6-km grid spacing (400 x 400 grid points) were performed in order to assess the sensitivity of the results to individual GCM choice. In each of the future simulations, projected changes were computed using an individual GCM. 78 future simulations were performed, utilizing the 39 future projections (13 GCMs, and 3 different emissions scenarios) and the 2 different PBL parameterization schemes (MJY or

YSU). A control simulation utilizing the current climate conditions was also performed in order to form the basis for comparison. Model simulations were integrated for 5 days, allowing sufficient time for TCs to reach a maximum intensity while minimizing computational expense. Model output was saved every 3 hours, with the assumption that this interval is sufficiently frequent to capture the maximum intensity.

2.2.4.2 Simulations with 2-km grid spacing

Simulations with a high-resolution nested domain (2-km grid spacing, 508 x 508 grid points) were also performed in order to more realistically simulate TC structure. Ideally, all 78 of the previously described experiments would have been performed with 2-km grid spacing, but computational limitations rendered this large number intractable. Instead, future simulations that utilized the ensemble mean (averaged over the 13 individual GCMs) projected change from each emissions scenario were performed, along with a control simulation. These future simulations will be referred to by the emissions scenario that was used to produce the ensemble average climate change projection; e.g., the SRESA1B simulation will refer to the one performed using future climate change averaged over the 13 GCMs forced with the SRESA1B emissions scenario. Model output was saved every hour, in order to allow for construction of time-averaged quantities for analysis of TC structure. The simulations were integrated for 240 hours in order to capture peak intensity in the simulations.

In order to further examine the impact of anthropogenic thermodynamic changes on TC intensity and structure, a series of sensitivity experiments designed to isolate the impact of upper-tropospheric warming were performed. An additional experiment, designed to investigate the impact of stratospheric cooling, was also performed. These studies, along with the names by which they will be referred to subsequently, are summarized in Table 2.2. These experiments will briefly be described below, with further description and analysis being found in chapter 4.

The least-stable and most-stable experiments utilized the projected changes from the SRESA1B GCMs that featured the least and most tropospheric stabilization. The tropospheric stabilization was computed as the difference between the maximum warming in the troposphere and the warming at the 1000-hPa level. The GCMs that projected these large differences in tropospheric stabilization are listed in Table 2.2. An additional experiment designed to examine the role of tropospheric stabilization is the no-stable experiment. These simulations featured uniform warming throughout the troposphere, set as the value of warming at the 1000-hPa level averaged over the SRESA1B ensemble, and the projected changes in moisture, SST, and stratospheric temperature averaged over the SRESA1B ensemble. Finally, a fourth experiment designed to investigate the potential impact of stratospheric cooling was also performed. In these simulations, projected changes from the SRESA1B ensemble were utilized, but with no projected temperature change in the stratosphere.

2.2.5 Analysis techniques

2.2.5.1 Computation of mass weighted inflow, outflow

In order to quantitatively assess the impact of climate change on TC intensity, the mass weighted inflow and outflow temperatures were computed. In order to compute these quantities, several steps were required. First, the TC center was objectively determined using a procedure identical to that described in section 2.1.3.1, where the center was specified as the grid cell with minimum smoothed sea level pressure. Next, the total wind was decomposed into tangential and radial components using the GEMPAK analysis, display, and product generation package. The total mass in each grid cell was computed by multiplying the cell volume by the average cell density. The mass-flux at each grid cell was then computed as the radial component of the wind multiplied by the grid cell mass. The total inward and outward mass-flux was then computed. Finally, at each grid cell, the fractional mass-flux (the grid cell value divided by the total value) was computed, and the temperature

of that grid cell was weighted accordingly. The mass-weighted inflow or outflow temperature was then computed as the sum of the mass-weighted temperature contributions of each grid cell.

Some ambiguity existed in the specification of what vertical levels should be analyzed for the mass flux. Several different specifications were considered; in the end, inward flux at an altitude of less than 1.5 km was considered, while outward mass flux above 12-km was considered. Inward mass flux above, or outward mass flux below, these specified values was not utilized in these computations, although their contribution was found to be fairly small in comparison with the total values.

2.2.5.2 Comparison with MPI estimates

Model simulated intensity will be analyzed in subsequent sections and forms the basis for evaluating the impact of climate change on TC intensity. Estimates of MPI also will be described, in order to provide further insight into the possible impact of climate change on TC intensity. In this case, the MPI estimate will be made using a subroutine written by Prof. Kerry Emanuel². This subroutine, which requires values of SST and surface pressure, along with 1-d soundings of atmospheric temperature and moisture, provides estimates of the maximum near-surface wind speed and minimum central pressure that a TC could attain in the input environment. This procedure is used operationally to provide real-time MPI estimates³, and has been shown to fairly realistically replicate the observed distribution⁴ of global maximum intensity. Although providing a useful secondary estimate of the impact of climate change on TC intensity, a large amount of uncertainty exists in the MPI estimates. Several tunable parameters, including the inclusion/exclusion of dissipative heating, and the ratio of the exchange coefficient for enthalpy to the exchange coefficient for momentum, are

² This subroutine is available at: <ftp://texmex.mit.edu/pub/emanuel/TCMAX/>

³ Real-time MPI estimates are available at: <http://wxmaps.org/pix/hurpot.html>

⁴ A comparison between estimated and observed maximum TC intensity is available at: <http://wind.mit.edu/~emanuel/holem/hurmap2.gif>

required in order to produce the MPI estimates. The values shown subsequently were produced using the subroutine with the inclusion of dissipative heating, and the default ratio of the exchange coefficients (0.9).

Table 2.1: Global climate models utilized in this study, along with the institution and agencies responsible for their development. In order to be used in this study, GCM output from the 20c3m, SRESA1B, SRESA2, and SRESB1 runs must have been available.

Model Abbreviation	Institution	Sponsoring Agency
bccr_bcm2_0		
cnrm_cm3	Centre National de Recherches Meteorlogiques	Meteo France
csiro_mk3_0		
csiro_mk3_5		
gfdl_cm2_0	Geophysical Fluid Dynamics Laboratory	NOAA
gfdl_cm2_1	Geophysical Fluid Dynamics Laboratory	NOAA
inmcm3_0	Institute of Numerical Mathematics	Russian Academy of Science
ipsl_cm4	Institut Pierre Simon Laplace (IPSL)	CNRS, CEA
miroc3_2_medres	Center for Climate System Research, University of Tokyo	National Institute for Environmental Studies
mpi_echam5		
mri_cgcm2_3_2a	Meteorological Research Institute	Japan Meteorological Agency
ncar_ccsm3_0	National Center for Atmospheric Research (NCAR)	NSF (a primary sponsor), DOE (a primary sponsor), NASA, and NOAA
ukmo_hadcm3	Hadley Centre for Climate Prediction and Research	Met Office, United Kingdom

Table 2.2: Summary of sensitivity experiments, and names that will be used to describe them in subsequent chapters.

Simulation Name	Description
Least-stable	Thermodynamic changes taken from SRES A1B projection of the CSIRO model
Most-stable	Thermodynamic changes taken from SRES A1B projection of the IPSL model
No-stable	SST increase, stratospheric cooling taken from SRES A1B ensemble. Tropospheric warming fixed at value from SRES A1B ensemble at the 1000-mb level.
No-strat-cooling	SST increase, tropospheric warming from SRES A1B ensemble. No change in stratospheric temperature.

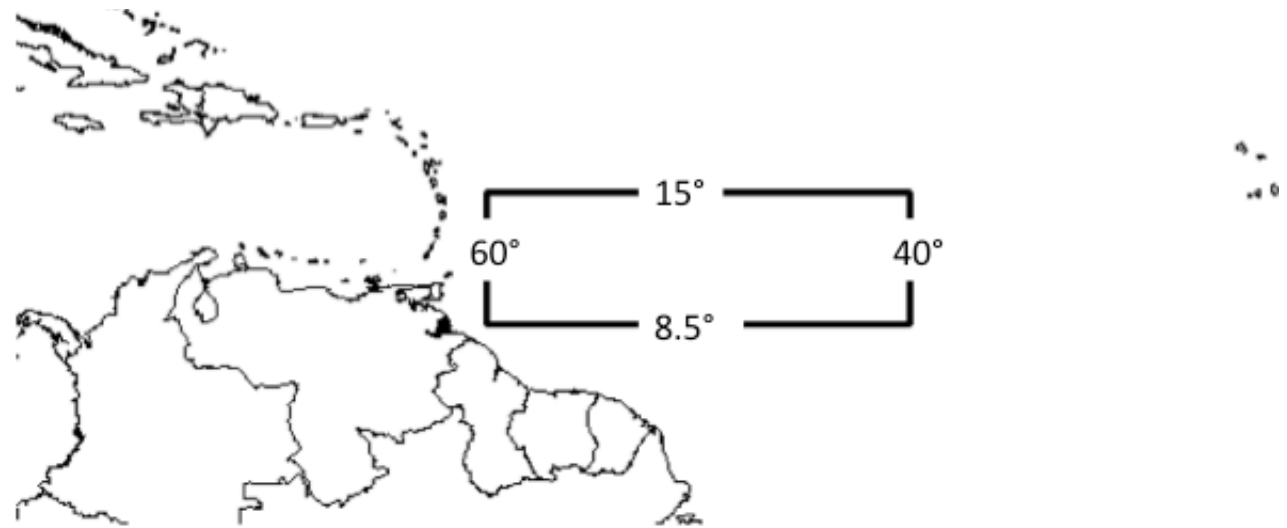


Figure 2.1: Outline of region used for the averaging of environmental conditions in TC size and future TC experiments. The region encompasses $8.5 - 15^{\circ}$ North, and $60 - 40^{\circ}$ West.

Scenarios for GHG emissions from 2000 to 2100 in the absence of additional climate policies

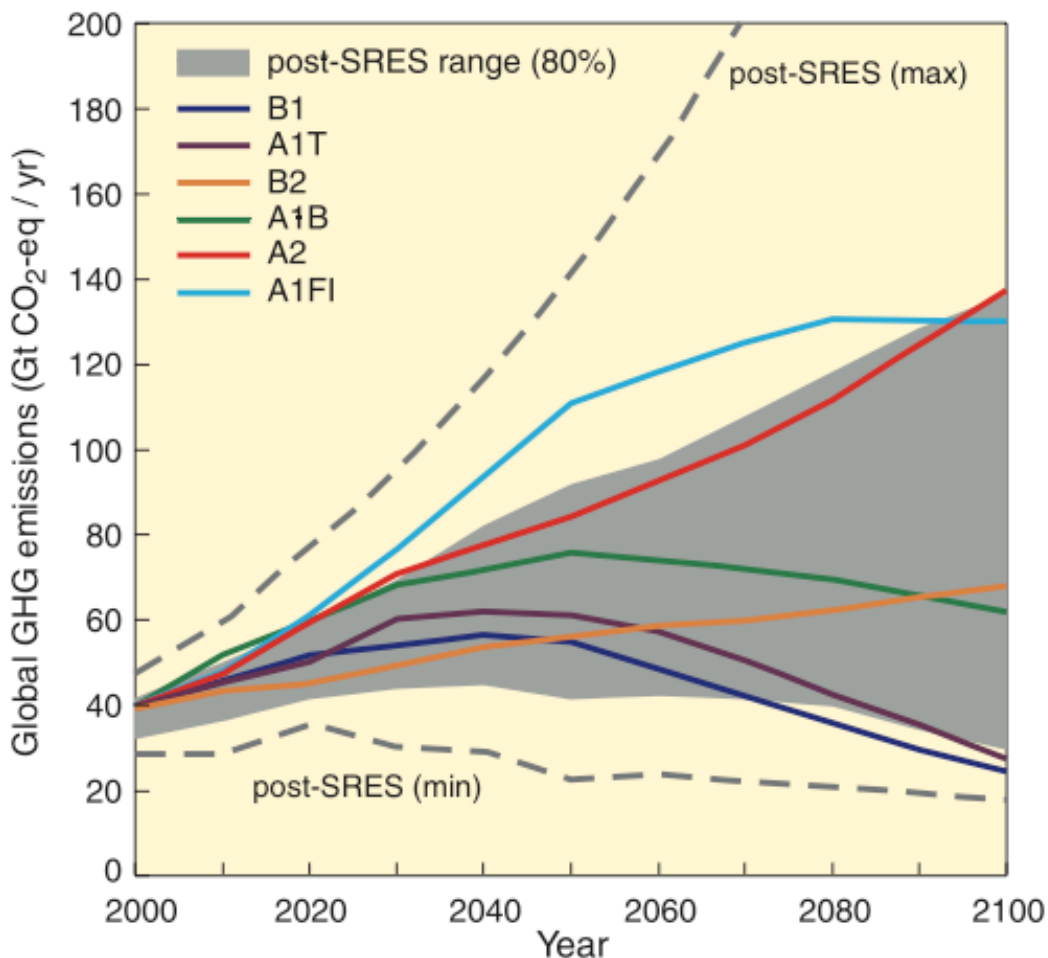


Figure 2.2: Global GHG emissions (in GtCO₂-eq per year) in the absence of additional climate policies: six illustrative SRES marker scenarios (colored lines) and 80th percentile range of recent scenarios published since SRES (post-SRES) (gray shaded area). Dashed lines show the full range of post SRES scenarios. The emissions include CO₂, CH₄, N₂O, and F-gases. [WGIII 1.3, 3.2, Figure SPM.4]

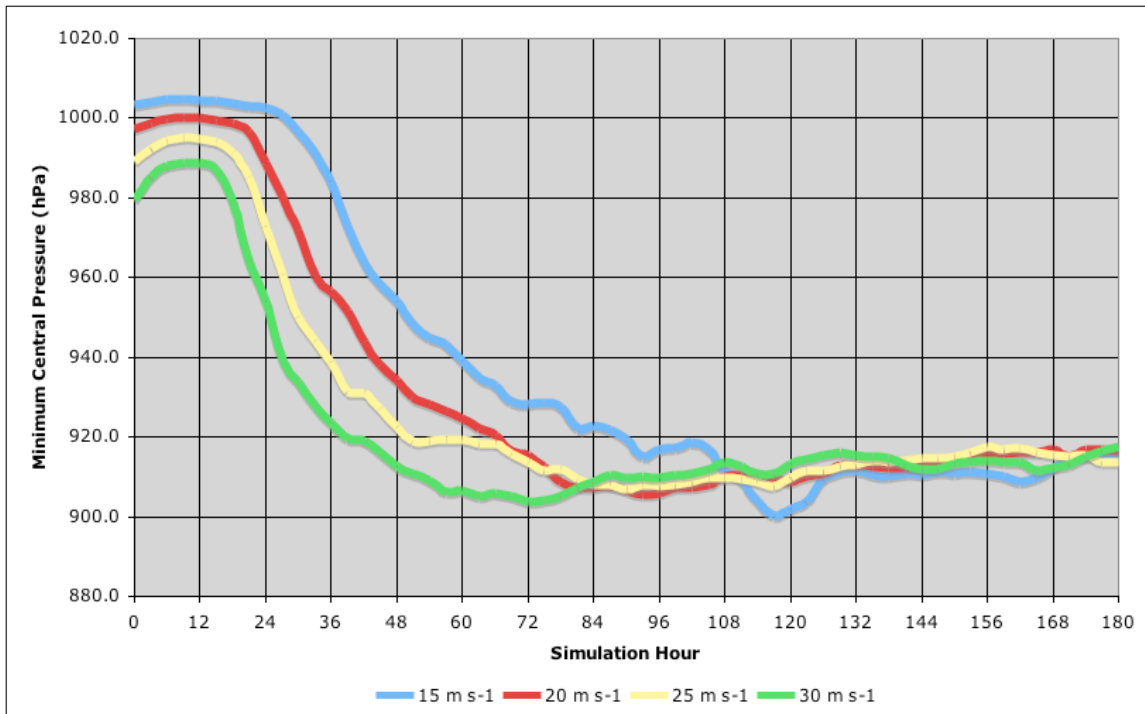


Figure 2.3: Time-series of minimum central pressure from WRF model simulations utilizing initial vortices of different strength: blue (15 m s^{-1}), red (20 m s^{-1}), yellow (25 m s^{-1}) and green (30 m s^{-1}). 24-hour mean minimum central pressure values are 907, 907, 908, and 906 hPa for simulations with initial maximum winds of 15, 20, 25, and 30 m s^{-1} , respectively.

Chapter 3

Tropical cyclone size

As previously discussed in chapter 1, we hypothesize that rainband activity leads to larger TCs, through the diabatic generation of PV. In order to test this hypothesis, model simulations with different initial moisture profiles outside of the TC core were conducted, the results of which will be discussed in this chapter.

3.1 Simulated TC Intensity

The simulated TCs in the 20RH, 40RH and 60RH runs each attain a MCP of ~ 900 hPa, while the TC in the 80RH run reaches ~ 880 hPa (Fig. 3.1). The MCP in the 80RH TC reaches a minimum at ~ 120 h, followed by a gradual increase in pressure. The 20, 40, and 60RH TCs exhibit gradual intensification through day 9, and reach a quasi-steady intensity thereafter. The maximum 10-m wind speed is quasi steady ($\pm 10 \text{ m s}^{-1}$) in all simulations after hour 48 (Fig. 3.2). The similarity in maximum wind speeds after hour 72 between the different simulations contrasts with the relatively large differences in MCP. As discussed subsequently, the pressure gradient is actually less in the 80RH simulation than in the others due to its large size, especially after simulation hour 72. The combination of a larger eyewall and a smaller pressure gradient leads to similar gradient wind speeds. Also, very strong turbulent momentum exchange coefficients in the model surface layer scheme (e.g., Hill and Lackmann 2009) tend to equalize the 10-m wind speed values. Despite the similarities in maximum intensity, large structural differences are present in the different simulations, as will be discussed in subsequent sections.

3.2 Simulated TC Size

Consistent with our hypothesis, the size of the simulated TCs exhibited considerable variation with environmental humidity, with more moist environments associated with larger storms (Fig. 3.3). The size differences were consistent throughout the model integrations, but generally increased with time. During the first 24 hours of model integration, the RMW in all four simulations decreases from the $\sim 50\text{-km}$ initial value to $\sim 20\text{-km}$ or less as

convection became organized and the TC secondary circulation became established (Fig. 3.3a). After this initial contraction, the RMW gradually increased in size in the 20RH, 40RH and 60RH TCs, ranging from ~ 30 km in the 20RH run to ~ 50 km in the 60RH run by hour 240. The RMW in the 80RH simulation slowly increased in size through the end of the simulation, with the exception of two periods of rapid growth (between hours 108 – 120 and 165 – 171). During the last 24 hours of the 80RH run the simulated TC grew to the point where it appears to have interacted with the domain boundaries, and therefore analysis will mainly focus on the first 9 days of integration. The peak RMW was ~ 80 km in the 80RH simulation (prior to hour 216), approximately 3 times larger than in the 20RH simulation. Higher environmental humidity was also associated with a larger maximum radius of hurricane force wind (hereafter RHW), which by the end of the simulations ranged from peak values of greater than 250 km in the 80RH run to a peak value of only ~ 100 km in the 20RH run. The RHW was characterized by less abrupt changes in size than that of the RMW; specifically, the RHW does increase during the two periods of rapid RMW growth but not in as drastic of a fashion. As shown subsequently, these abrupt increases in the RMW are associated with eyewall replacement cycles, during which time a secondary eyewall becomes dominant and the eye size increases. The outer core wind field does tend to increase during these replacement cycles, but is likely more related to the outer core precipitation, pressure gradient, and potential vorticity structure than inner-core processes. The similarity in size early in the simulation may be related to the identical relative humidity values inside 100-km radius at the initial time, which likely delays the influence of the outer-core environment on TC size evolution. However, similar results were obtained by a set of simulations that did not use the initial moist envelope (Hill and Lackmann 2008a).

Hovmöller diagrams of 10-m wind speed reveal steady wind field expansion in each model run (Fig. 3.4); this behavior is consistent with moistening of the outer-core environment due to surface fluxes and convection. Note that the lateral boundary conditions on the inner 2-km moving nest are obtained from the 6-km domain, which is characterized by moistening due to the aforementioned processes. In order to further assess changes in the TC wind field with time, Fig. 3.5 displays the time rate of change of tangential wind speed

(shaded) along with the RTS, RHURR, and 20 dBz simulated composite reflectivity contours. Outside of the initial moist envelope ($R > 100$ -km), winds begin increasing in the 80RH simulation almost immediately while growth is systematically delayed in the progressively dryer simulations (Fig. 3.5). Outside of 150 km, in the 80RH run the bulk of the increase in outer core wind speed occurs between simulation hours 48 and 144, during which time accelerations of $> 0.3 \text{ m s}^{-1} \text{ h}^{-1}$ occur. In the other simulations growth occurs in episodic bursts, which could be related to times of enhanced rainband activity, as many of these bursts are preceded by outward expansion of the composite simulated reflectivity. The close correspondence between the wind field growth (specifically the tropical storm force wind contour) and the 20 dBz simulated composite reflectivity contour qualitatively illustrates the link between rainband activity and the size of the wind field; this link is further analyzed in subsequent sections.

3.3 Precipitation structure

Central to our hypothesis is the evolution of the radial latent heating distribution, which in turn impacts the size and strength of the cyclonic PV distribution, and thus the size of the balanced TC wind field. Before examining the heating distribution itself, the simulated composite radar will be presented to provide information about the character and intensity of the radial rainfall distribution. In order to provide a sense of the typical precipitation distribution in each simulated TC, 3 snapshots of model-simulated composite reflectivity are next provided (Figs. 3.6 – 3.8). These images are from simulation hour 24, 126, or 180; these times were chosen in order to demonstrate size differences early in the simulation, or during two periods of quasi-steady size in the 80RH simulation.

By simulation hour 24, differences in the precipitation structure and rainband activity have developed (Fig. 3.6). As environmental moisture is increased in the simulations, there is an increase in the simulated rainband activity, with little-to-no rainbands in 20RH and extensive rainband activity in 80RH. Between simulation hour 24 and 126 there is steady growth in 20RH, 40RH, and 60RH, and significant growth in 80RH, which is clearly evident in the precipitation structure (Fig. 3.7). By this time all simulated TCs appear to have a well-

organized structure, with a well-defined eye and eye wall. A wider eye and broader eye wall are evident in the 80RH run, along with a larger coverage of precipitation in the outer spiral rainbands relative to the drier simulations. Some outer rainband activity is evident in the dryer simulations, as moisture fluxes have increased the tropospheric water vapor content sufficiently to allow for precipitation. Despite the size differences, peak simulated radar reflectivity values within the eyewall are comparable in each simulation, exceeding 55 dBZ. Finally, at simulation hour 180 it is evident that simulated TCs in the 20RH, 40RH, and 60RH simulations have continued to grow, with rainband activity increasing as well. The 80RH simulation has increased in size, with the most notable difference being a wider eye and broader eye wall than at simulation hour 126.

Another way of analyzing the simulated precipitation structure is provided in Fig. 3.9, a hovmoller diagram of simulated composite reflectivity. In each simulation, the RMW (indicated by the thick black line) is located radially inward of the narrow zone of highest simulated composite reflectivity in the eyewall. The 80RH run is characterized by persistent strong reflectivity outside of the initial moist envelope (100-km), while in the dryer simulations development of precipitation in this region is systematically delayed and less intense (in an azimuthally averaged sense). The eyewall, identified as the zone of highest reflectivity, is observed to expand to near 120 km in the 80RH run, while remaining closer to 40 km in the 20RH run. Both inward and outward propagating rainbands are evident in the 80RH simulation, while outward propagating features are more prevalent in the other simulations. Rainbands are more numerous and extend to larger radii in the more moist simulations. The TC in the 80RH simulation is unique among the experiments in that it exhibits two eyewall replacement cycles beginning around hour 96 and hour 144. In each of these cycles, a secondary band of higher reflectivity develops outside of the eyewall, while the inner eyewall reflectivity maximum dissipates. An abrupt increase in the RMW, as opposed to the steady increase in size outside of these periods, is associated with these replacement cycles. A close correspondence between the simulated composite reflectivity and the expansion of the hurricane and tropical storm force wind is again evident (Fig. 3.9).

3.4 Time evolution of water vapor fields

As previously shown, rainbands were able to develop in the dryer simulations; next, the time evolution of the water vapor fields will be analyzed in order to assess the role of the initial moisture specification in the mature TC structure. The analysis will focus on time-averaged quantities during two separate 24-h periods: simulation hours 24 – 48 or 168 – 192. These periods were chosen in order to represent the TC after the initial organizational phase but before large size changes (24 – 48) and a mature, quasi-steady mature structure (168 – 192).

3.4.1 Simulation day 2 (hours 24 – 48)

Relative to the initialization, increases in specific and relative humidity occur during the early stages of the simulation, as indicated in Figs. 3.10 – 3.11, cross sections of moisture changes averaged during day 2 of the simulations. Specifically, moistening of up to ~ 10 , 8, and 4 g kg $^{-1}$ in the lowest 1-km of the troposphere outside of the moist envelope is present in the 20RH, 40RH, and 60RH simulations, respectively. An increase in near-surface moisture content near the TC center is also found, with similar moistening in all simulations of ~ 6 g kg $^{-1}$. Focusing instead on relative humidity (Fig. 3.11), larger near-surface moistening is again found in the initially dryer simulations, while a decrease in relative humidity near the TC center is indicated, likely due to both increased temperature and decreased water vapor content. A general decrease in relative humidity in the upper levels is also likely due to the fact that these regions were saturated with respect to ice at the initialization time. Focusing on the extreme cases, increases in relative humidity of greater than 60% are present in the 20RH simulation, yielding relative humidity values of $\sim 80\%$ in the boundary layer, while some modest moistening is present in the 80RH simulation, with boundary layer values now exceeding 80%.

Despite the moistening in the initially dry simulations, large differences in relative humidity are still present during day 2 of the simulations (Fig. 3.12). Most notably, the dryer simulations feature lower relative humidity between ~ 1 – 10 km altitude outside of the initial

moist envelope where surface moisture fluxes have not led to moistening; hereafter this region of dry air will be referred to as the dry tongue. The depth and magnitude of this relative dryness is also larger in the dryer simulations; in 20RH, relative humidity is more than 60% less than in 80RH in this region, with values of less than ~20% still inhibiting the formation of precipitation. Focusing on the lowest 1-km of the troposphere outside of the moist envelope, relative humidity is still ~20 – 30 % less in 20RH than in 80RH, as the turbulent moisture fluxes from the surface have not yet equalized the moisture content. The 40RH simulation still possesses relative humidity values of ~10 – 20% less than 80RH in this region, while relative humidity in 60RH is similar to that found in 80RH. Examination of the 15 dBZ simulated radar reflectivity contour reveals greater radial extent in the initially more-moist simulations. Also, the radial extent of the reflectivity contour appears to be closely tied to the inward penetration of the dry tongue, although it is difficult to assess if the dry tongue is controlling the radial extent of simulated hydrometeors.

The moisture differences are evident in a plot of equivalent potential temperature (Fig. 3.13) and its rate of change with height. Convective instability, which is a decrease in equivalent potential temperature with height, is present in the lowest ~3-km of the troposphere in all simulations due to the presence of a moist boundary layer with dryer air above. The depth of the convectively unstable layer is actually larger in the initially dryer simulations, owing to increased depth and intensity of the dry tongue. Despite the presence of the convectively unstable layer, rainband development in the initially dryer simulations is suppressed. Since the boundary layer air is dryer, a larger amount of lift would be required to reach saturation, and therefore the instability cannot be realized as easily in the dryer simulations.

3.4.2 Simulation day 8 (hours 168 – 192)

Averaged over simulation hours 168 – 192, the moisture content in the initially dryer simulations has continued to increase (Figs. 3.14 – 3.15). Increased moisture in the low-level eye (below ~4 km) is evident, due to surface fluxes. The largest moisture increases are again found in the boundary layer outside of the moist envelope, with increases exceeding 11 g kg^{-1}

in the 20RH simulation, and more modest increases in the other simulations. The 80RH simulation has also experienced moistening, most notably within \sim 300 km of the TC center. Relative humidity changes are again largest in the initially dryer simulations (Fig. 3.15), with the largest increases outside of the moist envelope.

Relative humidity differences between the 80RH and other simulations are much reduced by day 8, although the influence of the initial conditions is still present (Fig. 3.16). Relative humidity near the surface (< 1 km altitude) is generally comparable in all simulations due to moisture fluxes, reaching $>$ 90% in the TC core and $>$ 80% through 500-km radius. The largest difference in relative humidity remains in the mid levels outside of the moist envelope; although significant moistening has occurred in the initially dryer simulations, relative humidity values are still up to \sim 60% less in the 20RH simulation and up to 40 – 50% less in 40RH and 60RH. The inward protrusion of the dry tongue remains larger in the initially dryer simulations, with relative dryness reaching to within 100-km of the TC center in 20RH, 150-km in 40RH, and 300-km in 60RH. A close correspondence between the decreased relative humidity and the 15 dBZ simulated reflectivity contour is again found at this time. Convective instability is still present in all the simulations in the lowest \sim 4 km of the troposphere, with the largest depth of instability outside of 300 km radius again found in the 20RH and 40RH simulations where dryer air is located closer to the surface (Fig. 3.17). The increase in low-level moisture content and the presence of convective instability has allowed for some rainbands to form in the initially dry simulations by this time (e.g., Figs. 3.8, 3.9) although to a much lesser extent than in the 80RH simulation. The presence of dryer mid-level air (\sim 5 – 10 km), however, still reduces the rainband activity in the dryer simulations.

3.4.3 Summary of moisture changes

Overall, significant moistening occurs in all simulations, with the largest moistening occurring in the initially dryer simulations and outside of the initial moist envelope. This moistening reduces the differences in moisture content between the simulations, although the initially dryer simulations remain dryer in a region referred to as the “dry tongue”, which

occurs in the mid levels of the troposphere and extends inward toward the TC center. This region of dry air appears to be collocated with the edge of high simulated radar reflectivity, and thus is hypothesized to limit the outward expansion of precipitation in the dryer simulations. Convective instability is present in the lowest several km in all the simulations, owing to a moist boundary layer, although the presence of dry air in the mid-levels has a tendency to reduce the amount of rainband activity in the dryer simulations.

3.5 Physical mechanisms

The sensitivity of simulated TC size to environmental humidity presented in the previous section is consistent with our initial hypothesis, but we have yet to examine the physical processes responsible for these differences. In this section we will investigate the manner in which changes to the size of the TC wind field, precipitation, and PV distribution come about during the evolution of the simulated TCs.

3.5.1 Angular momentum import

Angular momentum import is one process by which the wind field can be increased; Wang (2010) cited this as the dominant growth mechanisms in idealized simulations. Next, the simulated angular momentum and radial flow will be analyzed. By day 2 of the simulations, differences in the angular momentum and radial inflow are present in the simulations (Fig. 3.18). Specifically, higher values of angular momentum are present outside of 50-km in the more moist simulations, and also the radial extent of inflow exceeding 2 m s^{-1} is also larger. These differences are likely due to differences in precipitation outside of the TC core; as shown in Fig. 3.6, at this time the more moist simulations are already producing more precipitation outside of the core. This precipitation increases the angular momentum and also leads to an increase in the radial extent of inflow. The inward import of angular momentum, not surprisingly, is also larger in the more moist simulations at this time (Fig. 3.19). Specifically, angular momentum import in the lowest 2-km of the troposphere is up $\sim 2 \times$ larger in 80RH than in 20RH, with the largest differences outside of the initial moist envelope. By day 7 of the simulations the differences in angular momentum and radial

inflow are even more striking (Fig. 3.20), with much larger values of angular momentum in the more moist simulations and also a broader radial extent of inflow. By this time, angular momentum import is up to 10x larger in the 80RH simulation than in 20RH in the lowest 2-km of the troposphere (Fig. 3.21). Averaged over the lowest 2-km of the troposphere, a hovmoller diagram of the time rate of change of the tangential wind speed and the radial angular momentum import illustrates differences in the simulations (Fig. 3.22). Angular momentum import values are much smaller in the dryer simulations, and this is consistent with the lack of increase in the outer core tangential wind speeds in those simulations.

Overall, it is evident that both the outer-core angular momentum and radial inflow are stronger in the initially more-moist simulations, despite the fact that the initial wind field was identical in all the simulations. Therefore, these differences must be tied in some way to the specified differences in environmental moisture. Wang (2010) studied the influence of the initial vortex size on the mature structure in idealized numerical simulations, and found that larger initial disturbances resulted in a larger mature size. His analysis revealed that the differences in mature size could be tied to larger angular momentum import in simulations with a larger initial vortex, which was larger due to the presence of more active spiral rainbands. The results of these idealized experiments agree with Wang (2010), although here the differences in angular momentum import are tied to outer core precipitation and thus the initial moisture specification. The more-moist simulations feature more active spiral rainbands, which drives strong boundary layer inflow outside the eyewall and increased angular momentum import. As the angular momentum import increases so do the outer core winds and the moisture flux, which subsequently leads to more intense rainbands and a positive feedback.

3.5.2 Outer core precipitation, diabatic heating, and pressure gradient

Wang (2009) postulated that the impact of diabatic heating in outer spiral rainbands on the storm structure mainly results from hydrostatic adjustment. Heating in outer spiral rainbands leads to a hydrostatic reduction in surface pressure, especially on the inward side as inertial stability is generally high there, whereas on the outer side inertial stability may be

lower and the heating could be lost to gravity wave radiation. As previously shown, the more moist simulations feature a greater amount of precipitation at radius, and the diabatic heating at large radius plays a role in influencing the simulated TC size.

As anticipated, there is a close correspondence between precipitation (as represented by the simulated composite radar reflectivity) and the lower tropospheric diabatic heating (Fig. 3.23). The largest heating rates are in the eyewall region, although average heating rates of $> 1 \text{ K hr}^{-1}$ extend radially outward well away from the TC center. The simulated radar and precipitation are larger at radius in the more moist simulations, as precipitation is able to form in the more-moist outer core region. Based on the results of Wang (2009) it would be anticipated that this additional heating at large radius in the more moist simulations would serve to broaden the surface pressure gradient; this indeed is the case in the simulations, as there is a close correspondence between the broadening of the diabatic heating and the surface pressure gradient in the simulations (Fig. 3.24). At large radius the pressure gradient is larger in the more moist simulations, consistent with the increased size of the TC wind field found there.

3.5.3 Azimuthally averaged PV diagnostics

From a PV perspective, the broader wind field seen in the more moist simulations could be associated with stronger cyclonic PV anomalies, a larger spatial extent of these anomalies, or both. During the first day of the simulations, the azimuthally averaged PV distribution is fairly similar (Fig. 3.25). The 15 dBz simulated reflectivity contour extends to $\sim 50\text{-km}$ in all the simulations, and inside of this zone (more specifically within $\sim 25\text{-km}$ of center) is the main cyclonic PV tower, where values exceed 20 PVU in all the simulations. PV values of $> 0.5 \text{ PVU}$ extend to $\sim 150\text{-km}$ radius in all the simulations. By simulation hour 96, large differences in the PV (and precipitation) structure are evident (Fig. 3.26). The central PV towers in all the simulations feature PV values exceeding 60 PVU, and extend to a similar radius. The central PV tower is not more intense in 80RH than in the other simulations. Outside of the central PV tower, however, large differences are present. Vertically coherent PV values exceeding 0.5 PVU have expanded to $> 250\text{-km}$ in the 80RH

run, \sim 125 km in the 60RH run, and $<$ 100-km in the 20RH run. This growth of outer-core PV appears (as will be confirmed later) to be diabatic in nature, as demonstrated by the close correspondence between the 15 dBZ simulated reflectivity contour and the lateral extent of the PV. By simulation hour 168, all simulations to some extent feature growth in the radial extent of the central PV tower and also outer-core PV exceeding 0.5 PVU (Fig. 3.27). Again, the close correspondence between the PV expansion and the simulated reflectivity contours illustrates the importance of the diabatic PV generation, which is tied to the amount of precipitation and environmental moisture content. In the 80RH simulation numerous changes have occurred since the previous 24-h period; most notably the central PV tower has broadened and weakened, and now features PV values exceeding 20 PVU out to \sim 50-km radius. A diabatically generated PV maxima also extends radially outward with height in the 80RH simulation, emanating from near the surface at 50-km radius. The other simulations still feature a fairly compact central PV tower, with expanding PV outside of this region. Overall, the simulations featured a fairly similar PV structure during the first 24-h, owing to similar initializations. Differences in the radial extent of precipitation, however, lead to an increased lateral extent of PV in the more-moist simulations due to increased rainband activity.

Further examination of the azimuthally averaged lower tropospheric PV (in the 850–700-hPa layer) within 150-km radius confirms differences revealed in cross-sections (Fig. 3.28). The inner PV tower in the 80RH run is comparable in strength to that in the other simulations prior to 96 h, but after storm expansion, the PV distribution is broader and weaker relative to that in the drier simulations. The radius of maximum PV expands to \sim 60 km in the 80RH run, compared to \sim 25 km in the 20RH simulation. Average PV values of $>$ 5 PVU are present in the 80RH simulation out to \sim 100-km in 80RH and only \sim 45 km in 20RH by the end of the simulations. Relative to the drier simulations, the broader, less-concentrated precipitation distribution (in an azimuthally averaged sense) along with the greater precipitation at large radius in the 80RH run is consistent with the more diffuse PV distribution evident after \sim 120 h in this simulation and also the larger radial extent of high PV. The radius of maximum wind is located on the outer edge of the intense inner-core PV

tower and, especially in the 80RH simulation, responds quickly to changes in the radial extent of the high PV values.

Focusing on the inner-core precipitation and PV structure more closely, Fig. 3.29 shows the 850-700 hPa average PV and the composite simulated reflectivity. A close correspondence between the zone of highest simulated reflectivity and the outer fringe of the PV tower is apparent in each simulation; lateral PV expansion is observed to occur simultaneously or shortly after the lateral expansion of the region of highest reflectivity. Also, it is evident that the expansion of the outer-core PV is associated with expanding precipitation. The expansion of the PV tower is associated with strong diabatic PV generation near the outside edge of the PV tower (Fig. 3.30). The diabatic PV generation is stronger in the 45-90 km radial band in the 80RH simulation, especially after simulation hour 96, consistent with higher reflectivity values in spiral rainbands outside of the eyewall in this simulation. The diabatic PV generation in the vicinity of the eyewall is the least in the 80RH simulation, consistent with the more diffuse nature of the eyewall precipitation. Comparison of Figs. 3.29 and 3.30 demonstrates that the zone of maximum inner-core diabatic PV production lies radially inward from the location of highest reflectivity; this offset is consistent with the outward slope of absolute vorticity vectors, and also with larger vorticity vector magnitude at smaller radii.

Focusing on a wider perspective and highlighting lower average PV values, it is evident that differences are also present in the lower-tropospheric PV distribution outside of 150-km radius (Fig. 3.31). A close correspondence between the outer-core PV and the RHW and RTS is evident, as expected based on previous analysis of precipitation, latent heating, and the wind radii. Changes in the RMW and the RHW or RTS tend to occur at the same time but this is not always the case, as expansion of the RHW and especially the RTS closely match outer-core PV growth. As previously shown, the main outer-core wind field growth in the 80RH simulation occurs between simulation hours 72 and 144; this period also features a rapid increase in the PV outside of 100-km, which is likely driven by diabatic production in spiral rainbands. By the end of the this main growth period, simulation hour 144, the radial extent of layer-averaged PV exceeding 1 PVU has reached a quasi-maximum. Simulations

other than 80RH feature much lower values of PV outside of 150-km, with episodic increases in PV occurring at or just prior to increases in the wind field. Overall, it is evident that there is higher PV outside of 150-km radius in the more-moist simulations, consistent with the greater rainband activity and larger diabatic PV production there (Fig. 3.32). In the 20RH simulation, average diabatic PV generation $> 1 \text{ PVU hr}^{-1}$ outside of 150-km begins after simulation hour 24; this delay is less in the more-moist simulations, which feature earlier formation of precipitation in this region. Although there clearly exists diabatic PV generation at large radii in the dryer simulations, it is much smaller than in the more-moist simulations and specifically than in the 80RH run.

The 80RH simulation exhibits the most pronounced wind-field expansion and lateral PV growth, and so this experiment will be utilized to further diagnose the processes at work. Although parameterized condensational heating allowed computation of the diabatic tendency, a more accurate PV budget requires output of diabatic heating from the model cloud microphysics scheme. The parameterization does not account for cooling due to evaporation and melting; May and Holland (1999) demonstrate that these cooling processes contribute to the heating gradient and are important to the PV budget in spiral bands. As previously discussed, output of the model-generated heating tendency was not possible for moving nest runs; therefore an additional experiment was conducted that was identical to the 80RH simulation, except using a fixed inner 2-km nest. The evolution of the simulated TC in this experiment, referred to as 80RH_Fix, was very similar to that in the original 80RH run until the last few days of the simulation when the fixed-domain storm drifted closer to the domain boundaries (not shown).

The azimuthally averaged diabatic tendency at hour 120 reveals strong net heating in the TC cross section, with the exception of small zones of net cooling within the melting layer immediately outside the primary and secondary eyewalls (Fig. 3.33a). The heating-only cross section exhibits consistent heating from cloud base to an altitude of $\sim 12 \text{ km}$ at least out to a radial distance of 400 km (Fig. 3.33b). Evaporation and melting largely cancel this heating tendency below the melting level outside of $\sim 200 \text{ km}$ radius. When negative diabatic tendencies are averaged separately (Fig. 3.33c), the dominant contribution is found

beneath the freezing level, and a local maximum corresponding to the melting layer can be identified. The azimuthally averaged moist diabatic PV tendency exhibits strongest tendencies in and near the eyewall, but with strong cancellation evident even in the azimuthal average (Fig. 3.33d). Farther from the inner core, a consistent net positive PV tendency is evident below the melting level, presumably due to diabatic generation in spiral rainbands.

The presence of large diabatic PV generation in the outer-core region is consistent with a broadening of the PV distribution, and contributes to wind field expansion even if it is not amalgamated with the central PV tower. Given a favorable rainband configuration, however, inward radial transport of diabatically produced outer-core PV could contribute significantly to the strength of the inner-core PV.

3.5.4 PV tower growth, eye and wind-field expansion

As previously shown, diabatic PV production in the spiral rainbands was present in the 80RH simulation; next, the impact of inward PV flux on the volume-averaged PV structure will be investigated. Although a budget analysis of this type is enlightening, it is noted that PV generated in spiral bands need not flux into the TC core to influence the TC circulation; its very presence at radius leads to a broadening of the cyclonic wind field. In order to quantify the role of inward PV flux on the PV tower growth, volume-averaged (0 – 80 km radius, and surface – 250 hPa) PV diagnostics are now presented for the 80RH and 20RH simulations. In the 80RH simulation there is an increase in volume averaged PV through \sim 132 hours of the simulation, and thereafter the average is quasi-steady (Fig. 3.34). The cutoff in PV growth in the 80RH simulation is partially attributable to the outward radial expansion of the PV tower to the 80-km averaging volume boundary. In the 20RH simulation there is steady growth throughout the entire simulation period, although the growth rate is much lower than in the 80RH simulation.

The horizontal advection of diabatically generated PV can be separated into symmetric and perturbation (eddy) contributions, defined relative to an azimuthal mean. The eddy PV advection at 80-km radius averaged between hours 84 and 132 (the peak growth period in the 80RH run) is \sim 5 times greater in the 80RH simulation relative to the 20RH

simulation (Fig. 3.35), consistent with the paucity of spiral rainbands in the 20RH simulation relative to the 80RH simulation. After hour 132, the 80-km radius is too small to fully contain the inner PV tower in the 80RH simulation, but in the 20RH simulation the inner PV tower remains inside the 80-km radius. In the 20RH simulation, the largest eddy PV flux occurs after simulation hour 192; this increase occurs at a time when the composite reflectivity in the outer core is increasing, and also matches the onset of a period of expansion of the RHW. By the end of the simulation, the eddy PV flux in the 20RH simulation is approaching that found during the main growth period (hours 96 – 144) of the 80RH simulation.

Focusing on the 80RH simulation, the most rapid PV growth occurs between hours 84 and 120. At the beginning of this period, the TC inner-core is fairly compact, with an eyewall, evident as a band of maximum rain rate, at a radial distance of \sim 30-km (Fig. 3.36a). Growth occurs throughout the period but is more abrupt during an eyewall replacement cycle, which is evident at simulation hour 109 (Fig. 3.36b) at which time an outer eyewall of \sim 75-km radius is beginning to form. Mixing by what appear to be breaking vortex Rossby waves in the eyewall may also contribute to the expansion of the TC inner core. These waves are visible in Fig. 3.36c as regions of high rainfall rate on the eye-eyewall interface, and their presence was also evident during animations of lower-tropospheric PV, instantaneous rain rate, and other fields (not shown). These wave-breaking events appear similar in scale and character to the mesovortices discussed by Schubert et al. (1999) and Kossin and Schubert (2001). After this growth period, the TC structure takes on a new quasi-steady configuration, with a larger eye and coherent single eyewall at \sim 60-km (Fig. 3.36d). In contrast, during this same time period, there is much less spiral band activity in the 20RH simulation, no eyewall replacement cycles and also little evidence of mixing due to vortex Rossby waves (not shown).

3.5.5 Spiral band structure

The azimuthally averaged PV, simulated reflectivity, and diabatic PV tendency demonstrate that moist environments favor diabatic broadening of the cyclonic PV tower.

However the azimuthal averaging obscures the details of this process. While a detailed investigation of the spiral bands is beyond the scope of the current study, it is evident that these bands play a fundamental role in the generation and import of PV into the cyclonic inner core PV tower, and also the breadth of the PV distribution (and thus the lateral extent of the TC wind field). The strength and extent of the spiral banding is clearly sensitive to the environmental humidity, as illustrated here. The instantaneous 850 hPa PV superimposed with the simulated reflectivity at hours 72 and 102 of the 80RH_Fix simulation (Fig. 3.37) is characterized by collocated bands of heavy precipitation and cyclonic PV outside the eyewall, consistent with findings of May and Holland (1999), Chen and Yau (2001), and Hence and Houze (2008). At the 850-hPa level, the cyclonic PV maxima are cellular in nature, organized along spiral bands. The coarser 6-km grid spacing used in the Chen and Yau (2001) study may explain the more continuous banded PV features of that study relative to what is shown in Fig. 3.37.

Instantaneous cross-sectional plots of the moist diabatic PV tendency were generated for a number of spiral bands; a representative example for section A-B indicated in Fig. 3.37a is presented in Fig. 3.38. Strongest latent heat release closely corresponds to localized cores of strong upward motion, located radially inward from the highest reflectivity (Fig. 3.38a). Diabatic cooling is mainly confined to the melting layer. The radial flow suggests the interception of low-level inflow by the spiral band (Fig. 3.38a), analogous to the observational findings of May (1996) and Hence and Houze (2008). The core of largest PV (in excess of 20 PVU) in this band is found close to the diabatic heating maximum, and also slopes radially outward with height (Fig. 3.38b). Strong positive PV tendencies are collocated with the band of large PV, and are largely confined below the freezing level (Fig. 3.38c). This PV generation pattern differs in some respects from that discussed by May and Holland (1999), in that the strongest PV generation is observed in association with intense updraft cores, rather than in regions of stratiform precipitation. However, the recent observational spiral band study of Hence and Houze (2008) also found that the updraft cores exerted the strongest influence on the larger-scale circulation. The significance of melting in the PV budget is important, consistent with the May and Holland (1999) study. It appears

that enhanced diabatic PV production is localized in the region of intense vertical heating gradients beneath the updraft cores, leading to the cellular PV structure seen in Fig. 3.38. Owing to local values of absolute vorticity on the order of 10^{-3} s^{-1} outside the inner core, the local Rossby radius is diminished, supporting the generation of small-scale PV maxima even within the relatively narrow spiral bands. This interpretation is consistent with that of Wang (2008) and Hence and Houze (2008) in recognition of the inertially stable inside portion of the spiral band as being dynamically favorable for a balanced response to heating in spiral bands.

3.5.6 Feedback mechanisms

As the wind field and zone of diabatically generated lower-tropospheric PV expands, the radial annulus that exhibits a favorable PV gradient for Rossby wave propagation may also broaden, which we speculate could allow further outward radial expansion of spiral bands. Wang (2002a) found that the favorable zone of PV gradient in numerical TC simulations was confined to within about 60 km of the storm center. Here, in simulations with higher environmental humidity, enhanced diabatic PV generation in spiral bands contributes to a broadening zone favorable to Rossby wave activity, which may feed back to the strength of influence that convectively coupled vortex Rossby waves have on storm structure and intensity. Both inward and outward propagating waves are suggested in reflectivity patterns out to radial distances of several hundred kilometers in the 80RH simulation, consistent with a broader zone of favorable wave activity in the more moist simulations.

As the cyclonic PV distribution grows in size, the strengthening outer wind field leads to enhanced upward heat and moisture flux over a larger area (Fig. 3.39), which could serve to further enhance precipitation and diabatic PV generation in outer spiral bands in a positive feedback. Due to the obvious linkage between the wind field and the strength of turbulent fluxes in the surface layer, it is difficult to isolate this feedback without additional model experiments. Another feedback associated with the expanding cyclonic wind field relates to the fact that the diabatic PV tendency is proportional to the magnitude of the absolute

vorticity vector itself. Therefore as the cyclonic wind field expands, subsequent heating in the spiral bands is more effective in lower tropospheric PV generation. As the cyclonic vorticity and inertial stability increase, the local Rossby radius decreases, leading to a stronger balanced response to heating at an increasingly large radius (e.g., Bister 2001). The expansion of cyclonic vorticity evident in Fig. 3.39 supports this speculation, although additional analysis is required to investigate this feedback.

3.6 Summary

The size of a TC has important implications for the severity and duration of many TC impacts, affecting evacuations, storm surge, duration and amount of precipitation and timing of the arrival of adverse conditions. Despite these impacts, forecasts most often emphasize TC track and intensity, and relatively little research has been conducted concerning the physical processes or environmental factors that control TC size. Here, we hypothesize that TC size is sensitive to the extent and intensity of spiral bands. Many factors influence the amount and extent of TC rainbands; one factor, relative humidity, was investigated in order to test this hypothesis. Four idealized high-resolution numerical simulations with the WRF model were performed in order to test the hypothesized sensitivity of TC size to environmental humidity. Identical vortices, placed within a moist envelope, were allowed to evolve in environments with initial relative humidity varying between 20 and 80% outside of the TC core. Inner grid spacing of 2 km allowed explicit resolution of spiral bands, which played an integral role in the evolution of cyclonic PV anomalies for the simulated storms.

Results are consistent with the hypothesis that moist environments favor the development of larger TCs, with progressively larger storms evident with each incremental RH increase. The 80RH simulation was much larger than the other 3, possibly due to the quicker size growth during the early portion of the simulation and subsequent feedback mechanisms. Differences in TC size between the runs were substantial, with the TC in the 80RH run exhibiting a RMW that was triple that in the 20RH run by hour 240. The more moist runs did not exhibit heavier eyewall precipitation or a more intense cyclonic PV tower. However, more precipitation in outer rainbands occurred in the more moist simulations,

which led to diabatic broadening of the PV distribution and lateral expansion of the TC wind field. Lower-tropospheric diabatic PV production in spiral bands led to a broadening of the cyclonic PV distribution both through the contribution to a broadening of the central PV tower as PV filaments spiraled inwards, and also through the presence of enhanced cyclonic PV near the spiral bands at larger radial distances from the core. Angular momentum import, aided by the presence of greater spiral band activity in the more moist simulations, is also implicated for the size differences.

The TC in the 80RH simulation exhibited stronger spiral banding relative to the other experiments, and also exhibited eyewall replacement cycles, unlike the TCs in drier simulations. The eyewall replacement cycles were accompanied by an increase in RMW, although considerable growth of RHW and RMW occurred outside of these cycles as well. The eye diameter increased during a time period when vortex Rossby waves appeared to break in the eyewall region. The PV evolution in the 80RH simulation, which is characterized by a broader but more diffuse PV tower after storm expansion, appears to be consistent with processes of the type described by Guinn and Schubert (1993) and Schubert et al. (1999), who implicate vortex Rossby wave breaking as a means of diluting PV in the inner core of the storm while broadening the PV distribution. Animations of lower tropospheric vorticity and PV are suggestive of vortex Rossby wave breaking between hours 96 and 120, during which time the PV tower expands and weakens. The enhanced spiral banding and eyewall replacement evident in the 80RH simulation is also consistent with the speculation of May and Holland (1999), who suggested that vorticity production in spiral bands could influence the development of secondary eyewalls in the presence of inward radial vorticity advection. The recent Hence and Houze (2008) and Wang (2008) studies provide additional support for this hypothesis.

Emanuel (1986) derived an analytical expression for the ratio of the RMW and extent of the outer wind field (his eq. 46) and notes that compensation will occur with changes in latitude or sea-surface temperature. Rotunno and Emanuel (1987) test these ideas with a numerical model, and conclude that the horizontal size of a TC is determined by the size of the initial disturbance. Recently, Wang (2010) also concluded that the initial vortex size

influences the TC size, although even with the same initial vortex the relative humidity did influence the mature size. We concur that the size of the initial disturbance is an important factor in determining TC size, although it is difficult to separate the influences of initial vortex size and environmental moisture content as the two are closely related.

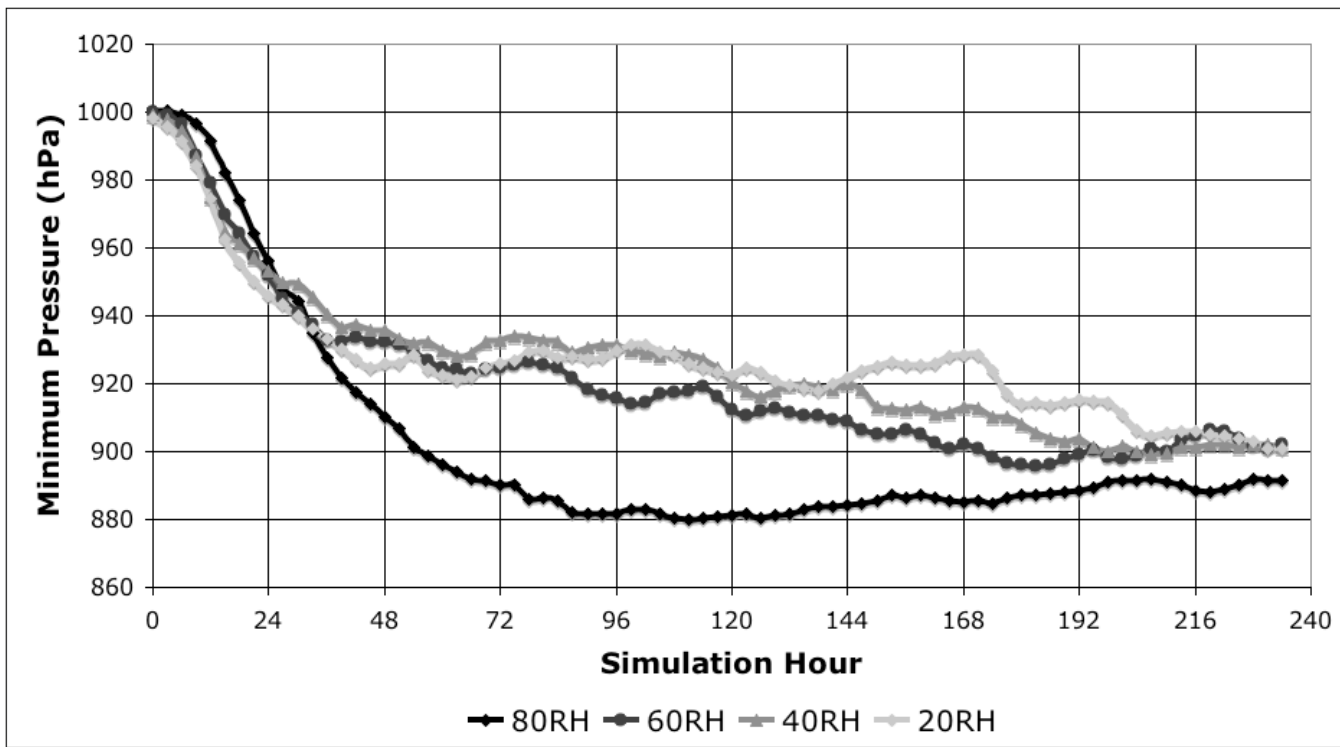


Figure 3.1: Time-series of simulated minimum central pressure (hPa).

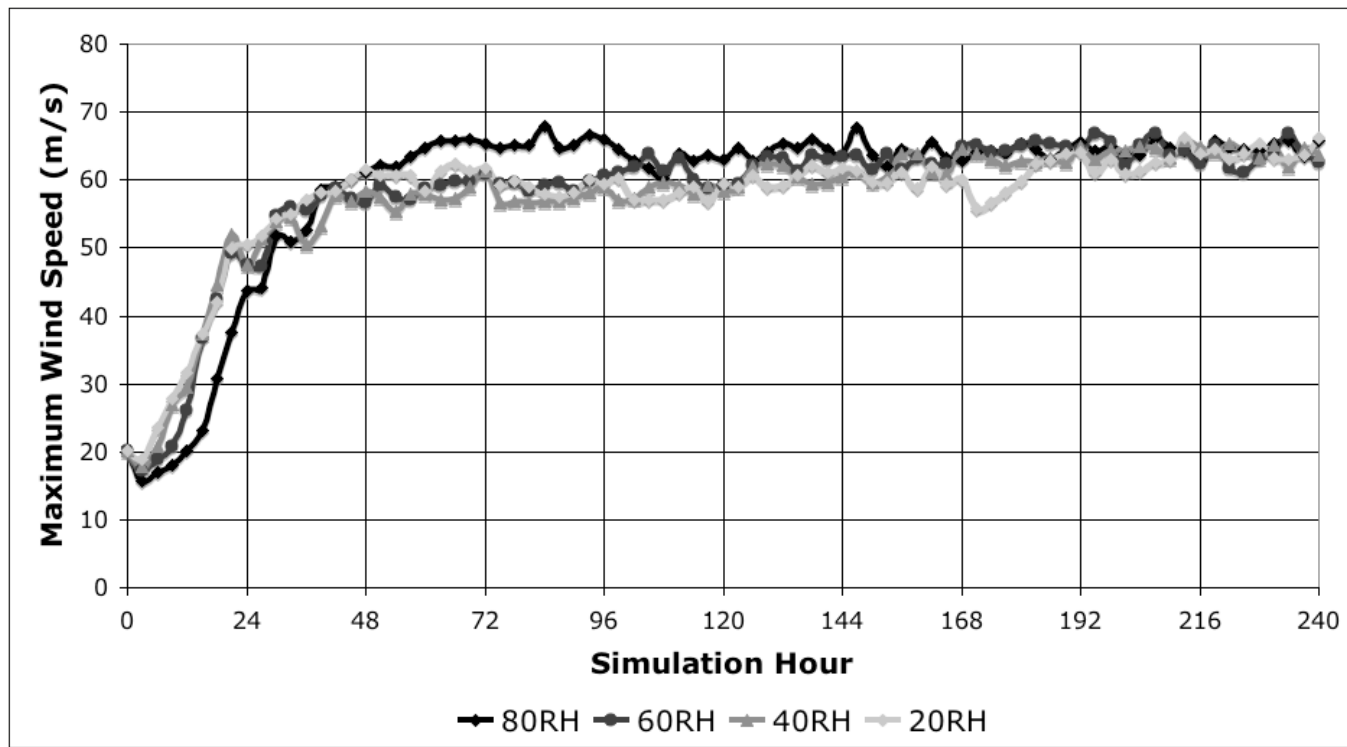


Figure 3.2: As in Fig. 3.1 except maximum 10-m wind speed (m s^{-1}).

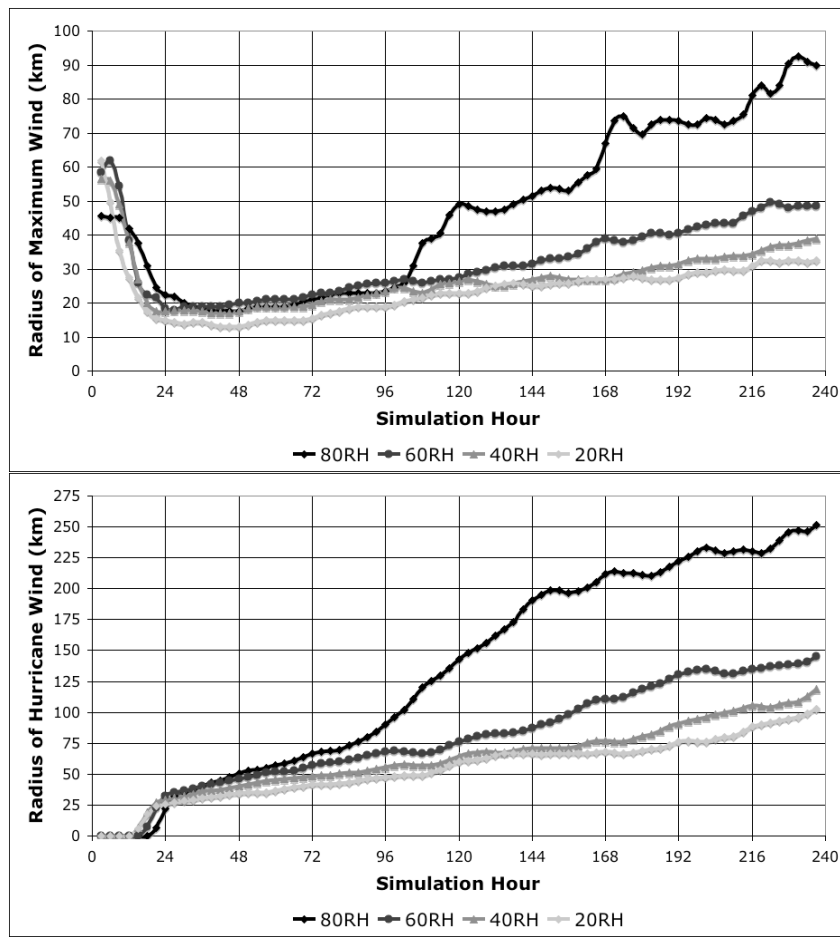


Figure 3.3: Time-series of TC wind field parameters for each simulation as specified in legend, with application of a 1-2-1 smoother: (top) radius of maximum 10-m wind speed (km); (bottom) maximum radius of hurricane-force 10-m wind speed. Values computed from azimuthally averaged model 10-m wind speed.

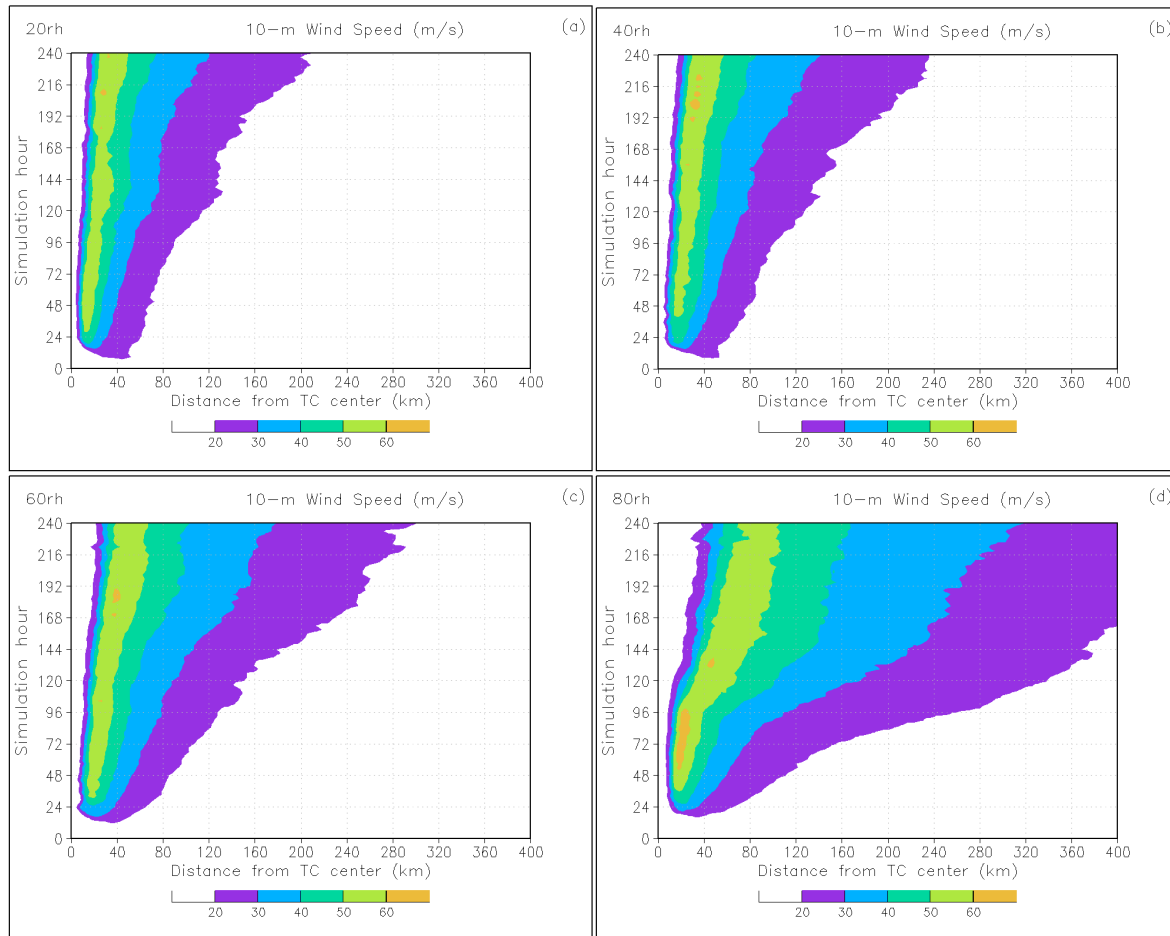


Figure 3.4: Hovmöller diagram (with time on the ordinate and radius from TC center on the abscissa) of azimuthally averaged 10-m wind speed (shaded; m s^{-1}) for simulations: (a) 20RH, (b) 40RH, (c) 60RH, (d) 80RH.

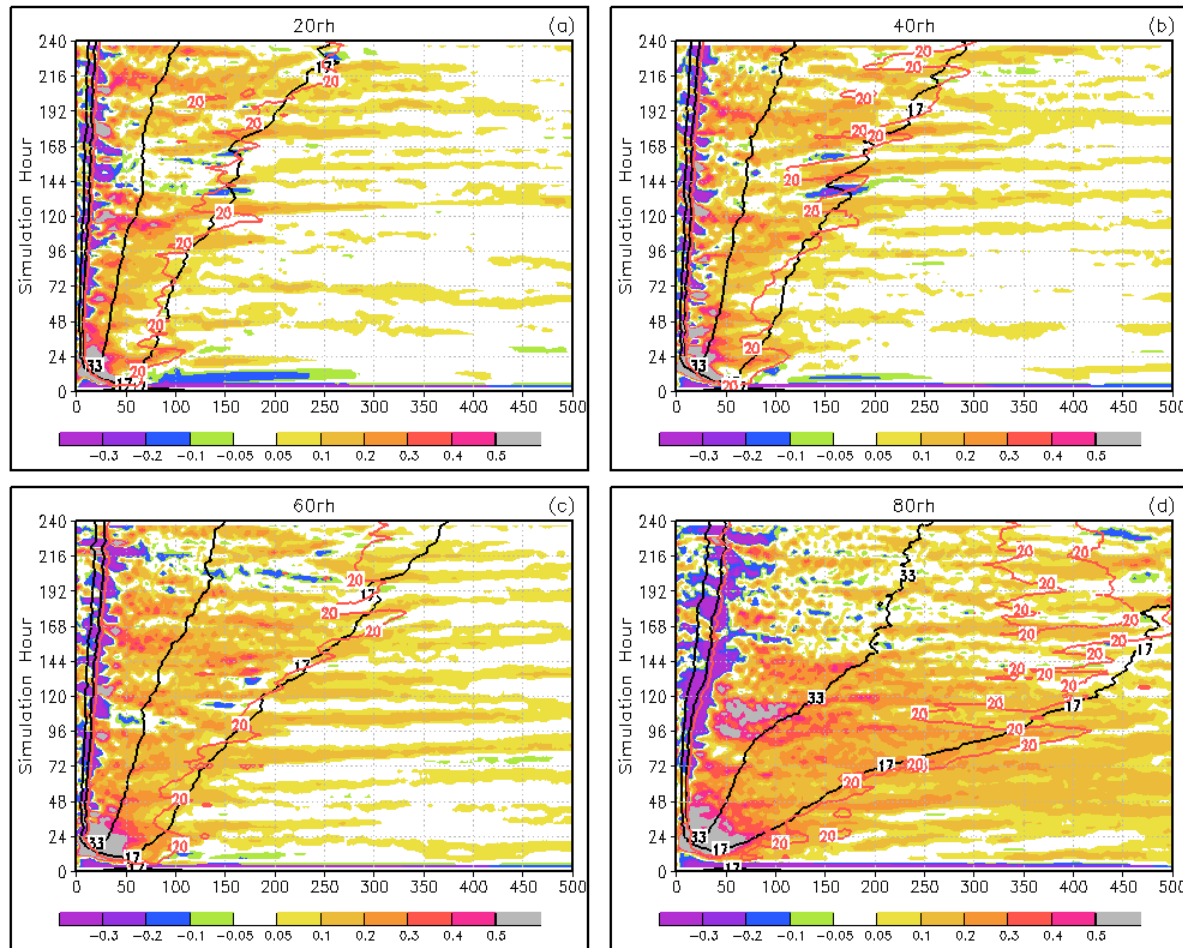


Figure 3.5: Hovmöller diagram of the time rate of change of the azimuthally averaged 10-m wind speed (shaded; $\text{m s}^{-1} \text{ hr}^{-1}$), the hurricane and tropical storm force wind values (black contours), and the 20 dBZ simulated composite reflectivity contour (red) for simulations: (a) 80RH, (b) 60RH, (c) 40RH, (d) 20RH simulation.

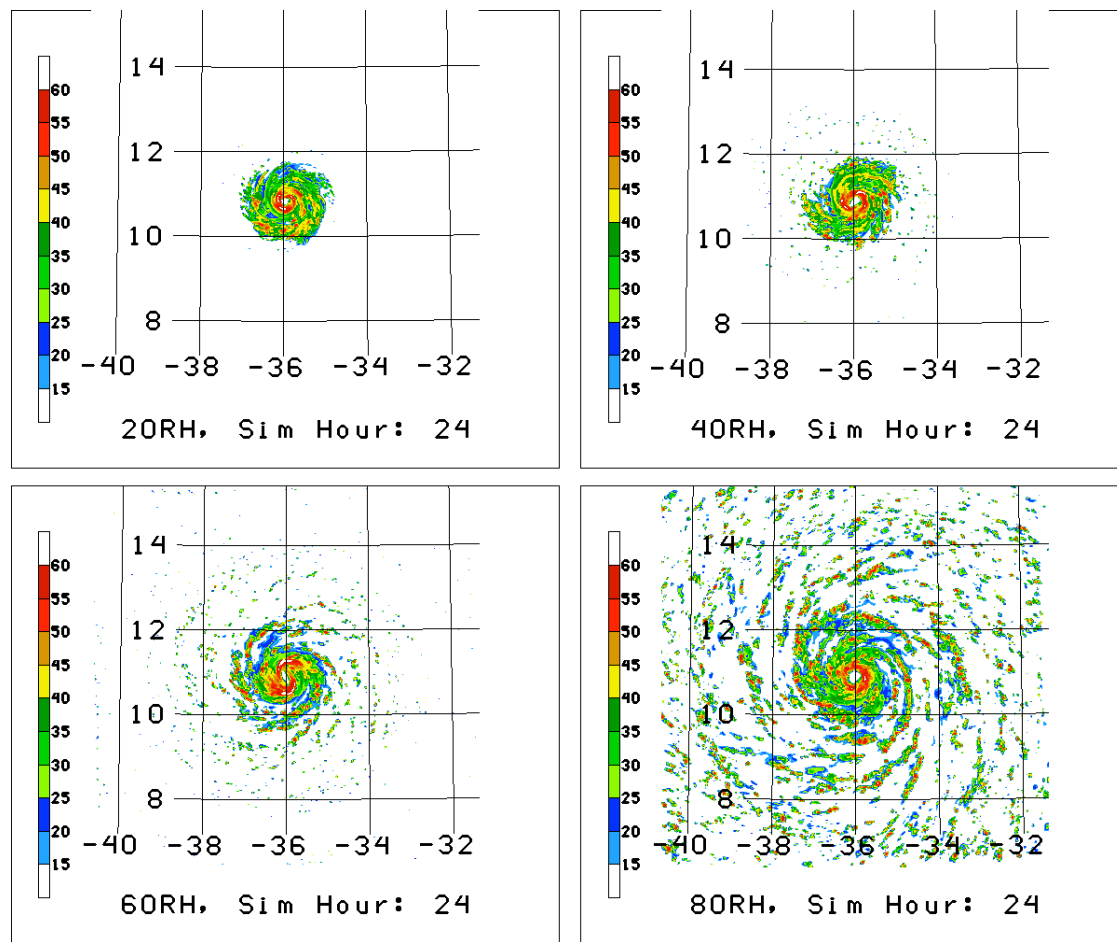


Figure 3.6: Model simulated composite reflectivity at hour 24 for (top left) 20RH, (top right) 40RH, (bottom left) 60RH, (bottom right) 80RH simulations. The composite reflectivity includes all model vertical levels.

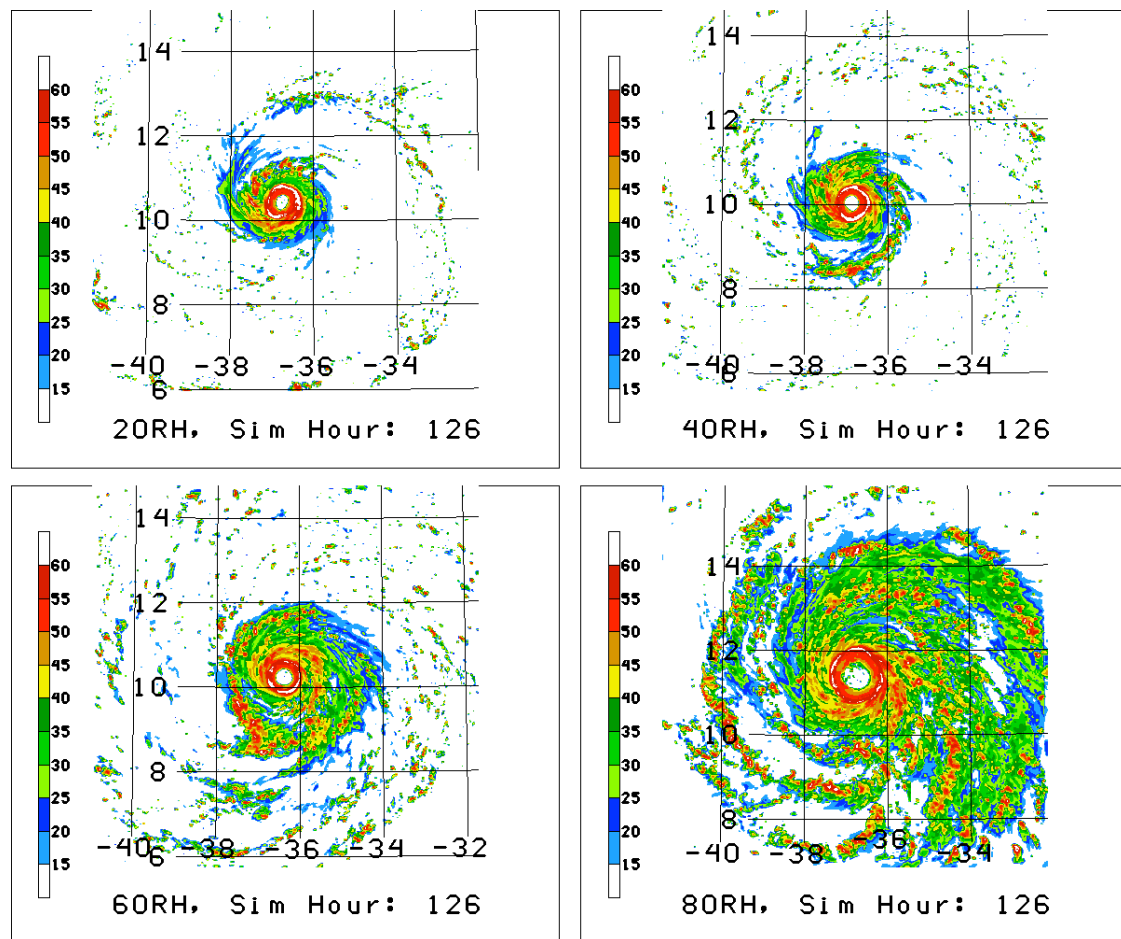


Figure 3.7: As in Fig. 3.6, but for simulation hour 126.

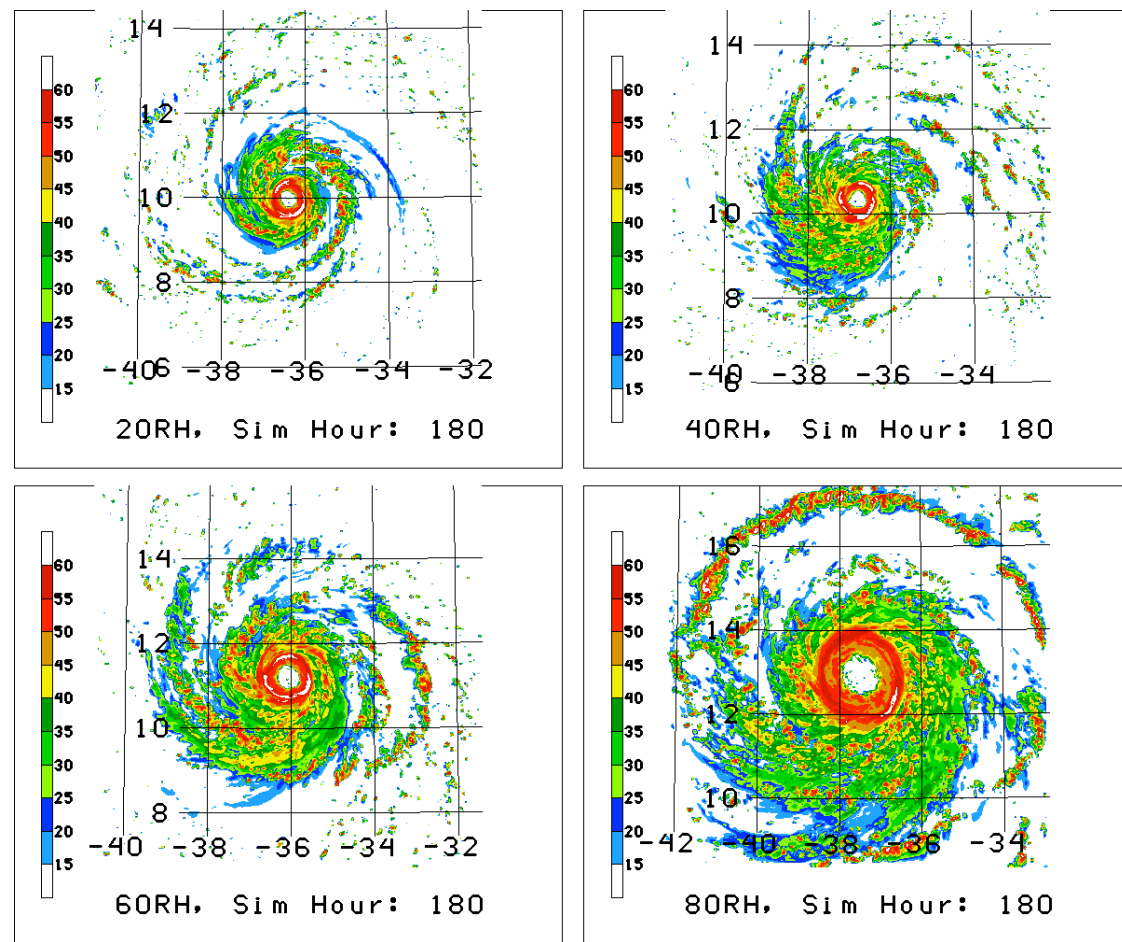


Figure 3.8: As in Fig. 3.6, but for simulation hour 180.

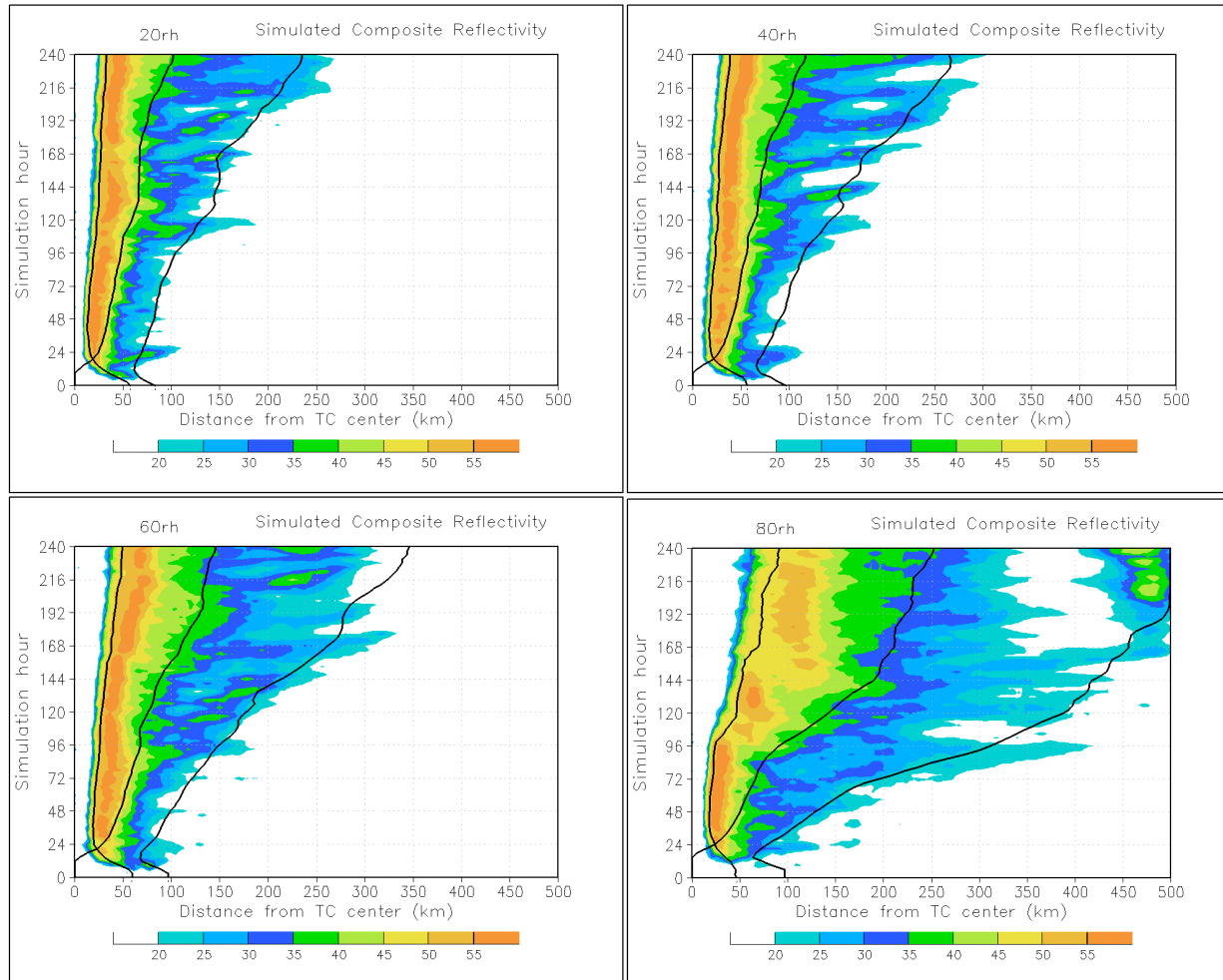


Figure 3.9: As in Fig. 3.4 except for composite simulated radar reflectivity (dBZ, shaded as in legend at bottom of panels). The radius of maximum 10-m wind speed, hurricane force wind, and tropical storm force wind are indicated by the black contours.

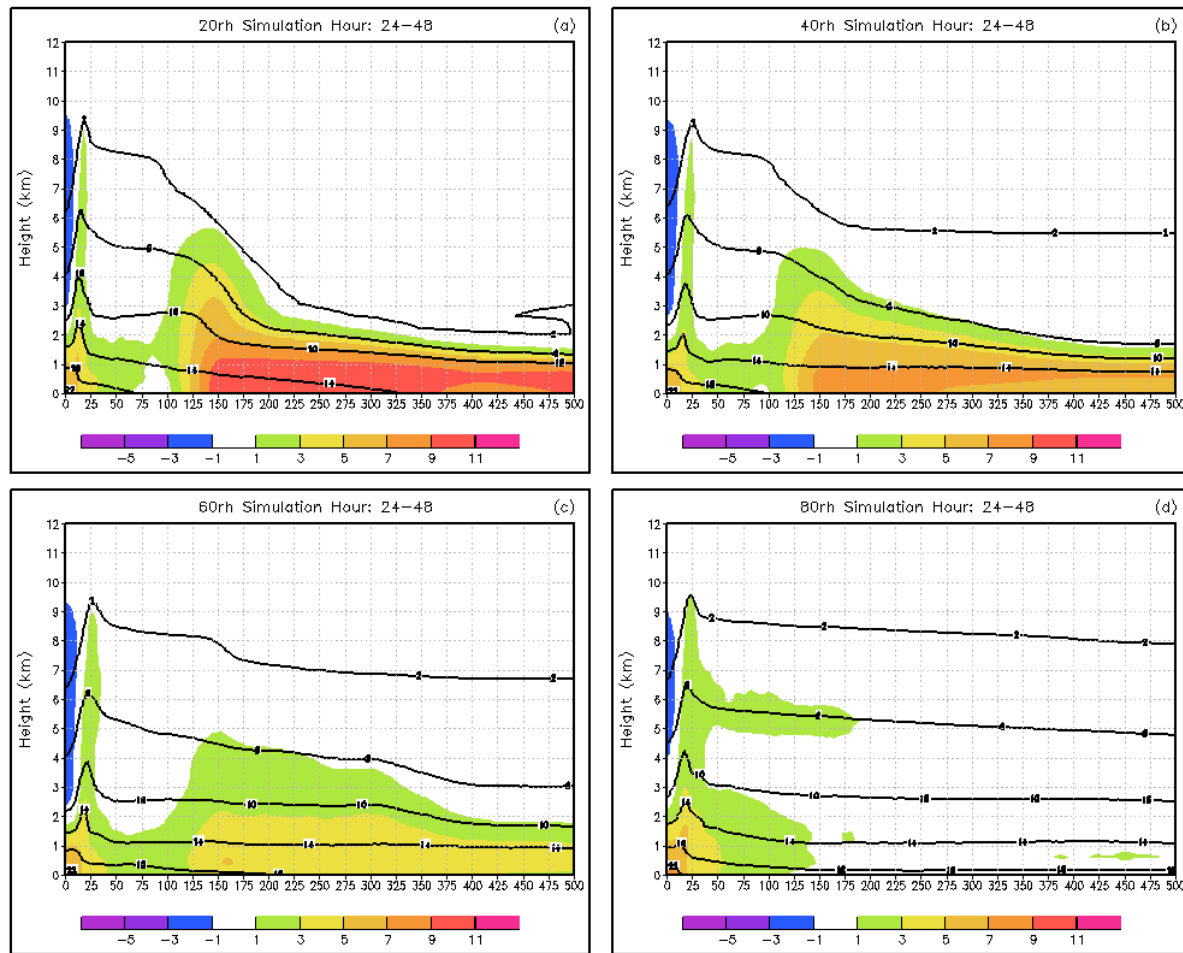


Figure 3.10: Cross-section of azimuthally averaged change (relative to initialization) in specific humidity (shaded; g kg^{-1}) and specific humidity (contoured; g kg^{-1}) time averaged between simulation hours 24 and 48.

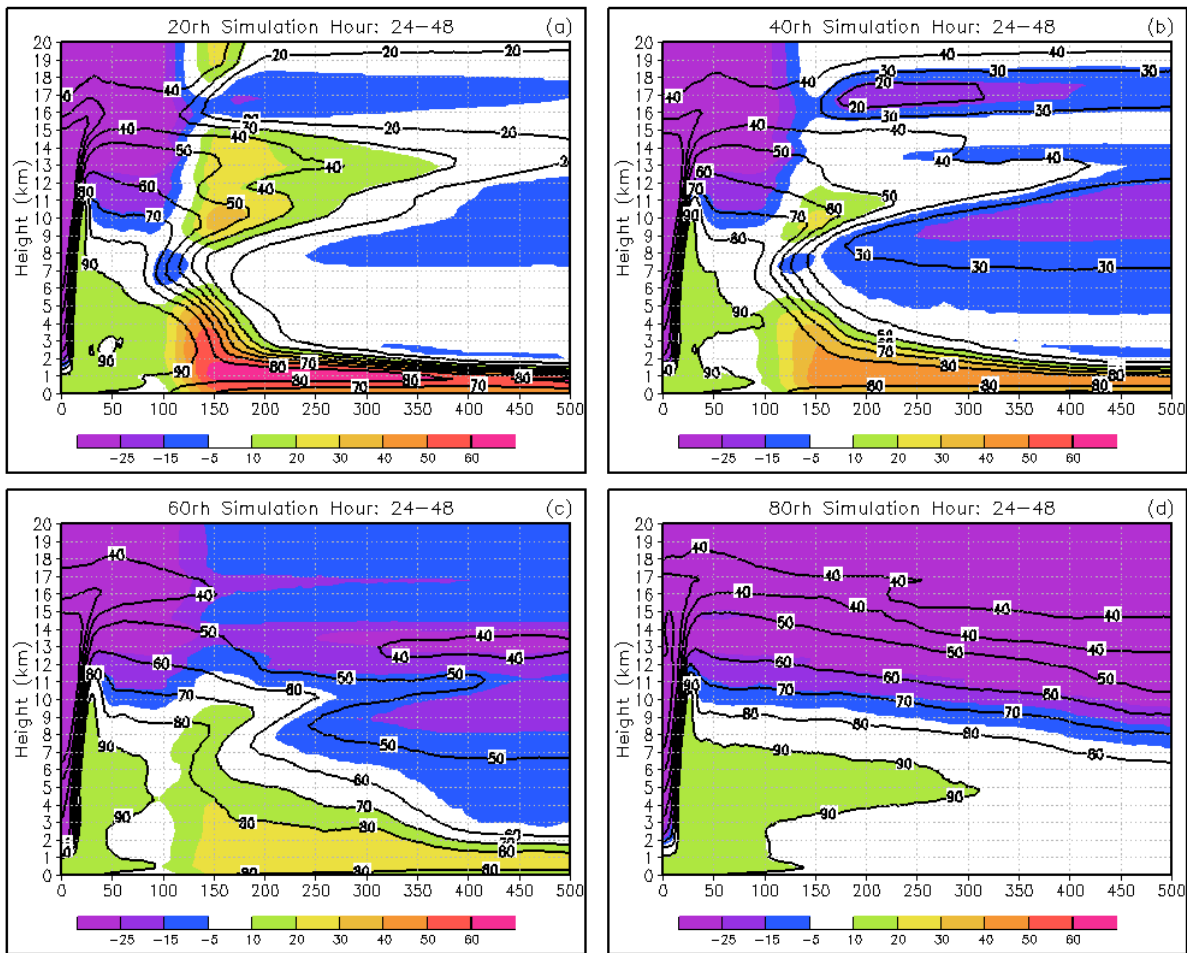


Figure 3.11: Cross-section of azimuthally averaged change (relative to initialization) in relative humidity (shaded; %) and relative humidity (contoured; %) time averaged between simulation hours 24 and 48.

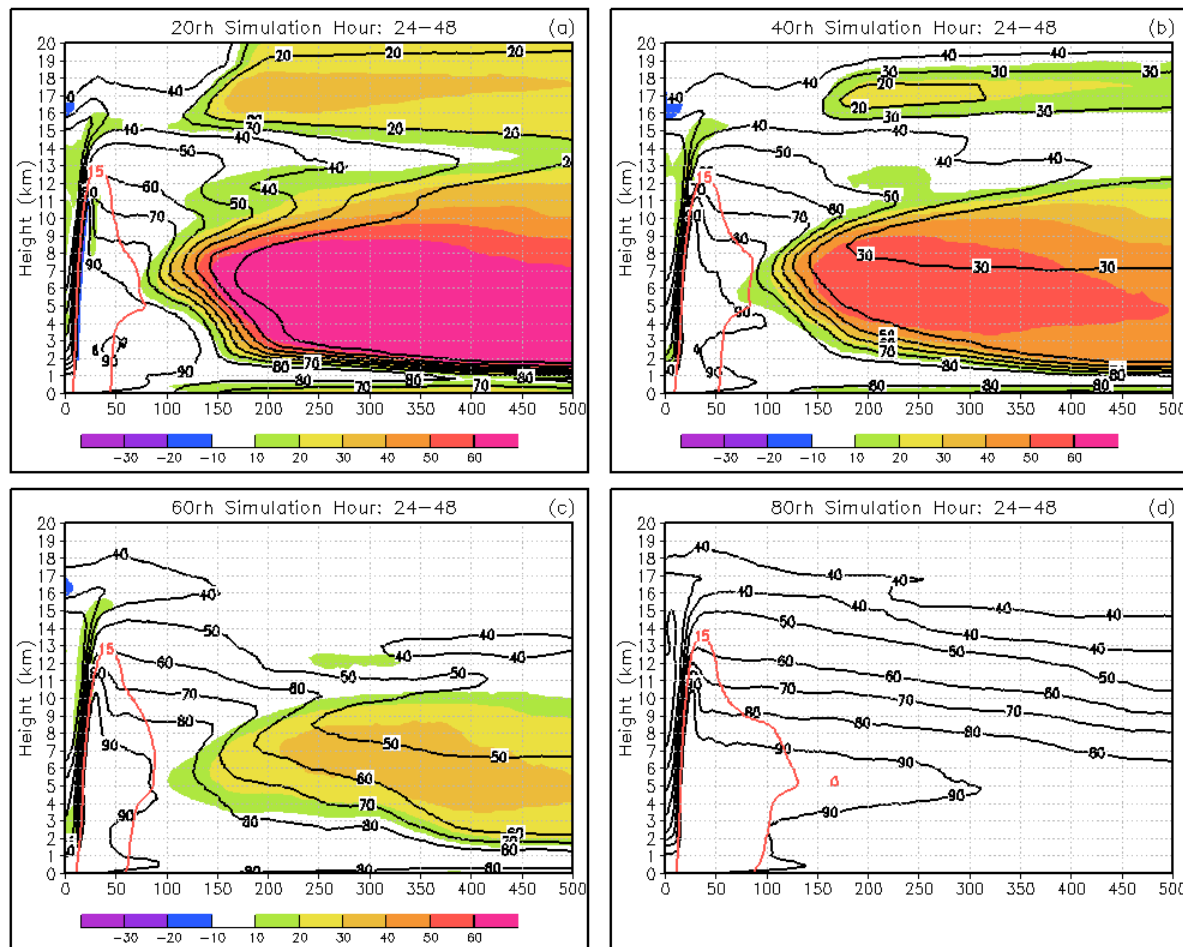


Figure 3.12: Cross-section of difference (relative to the 80RH simulation) in relative humidity (shaded; %), relative humidity (black contours; %), and the 15 dBz simulated radar reflectivity contour (red contour) time averaged between simulation hours 24 and 48.

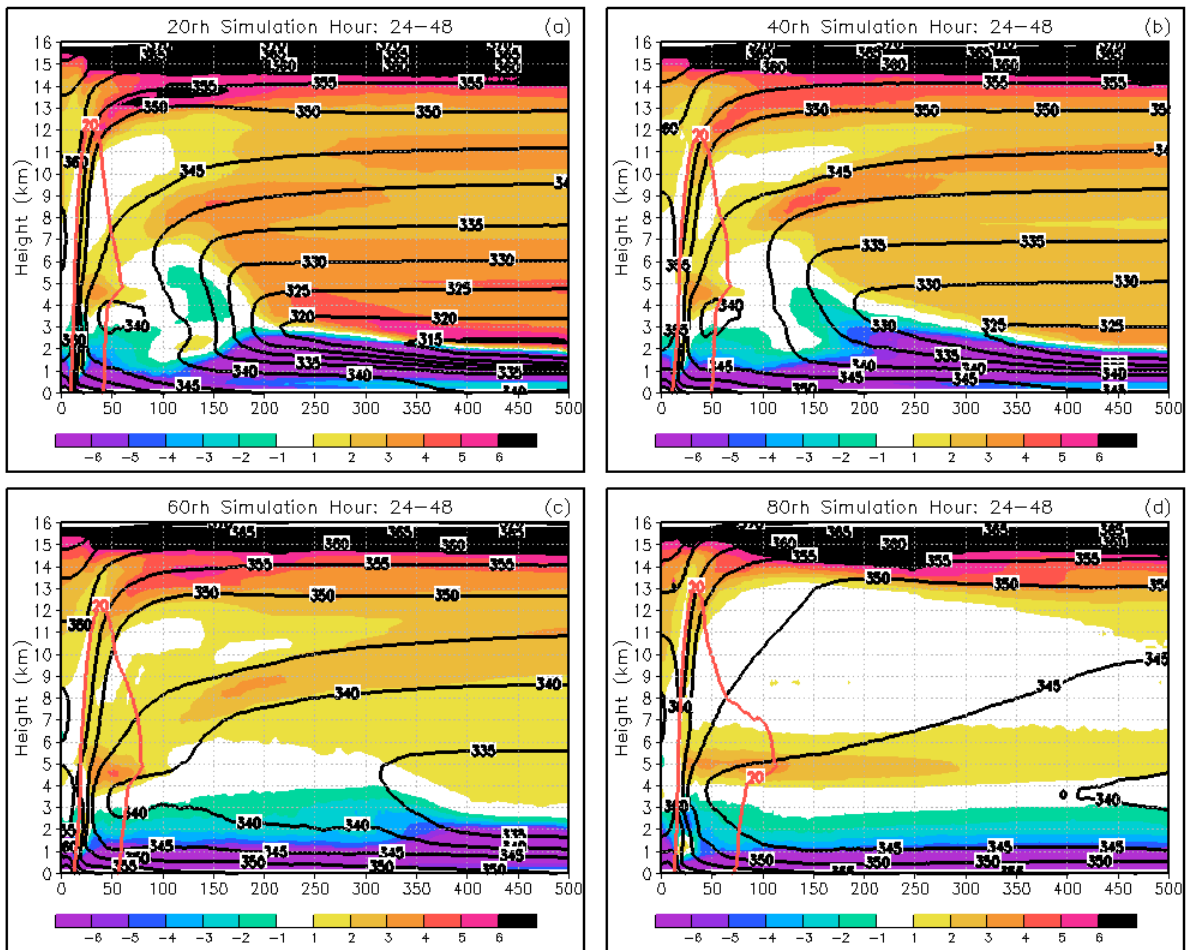


Figure 3.13: Cross-section of equivalent potential temperature (K; contoured) and the equivalent potential temperature lapse rate (K/km; shaded) time averaged between simulation hours 24 and 48.

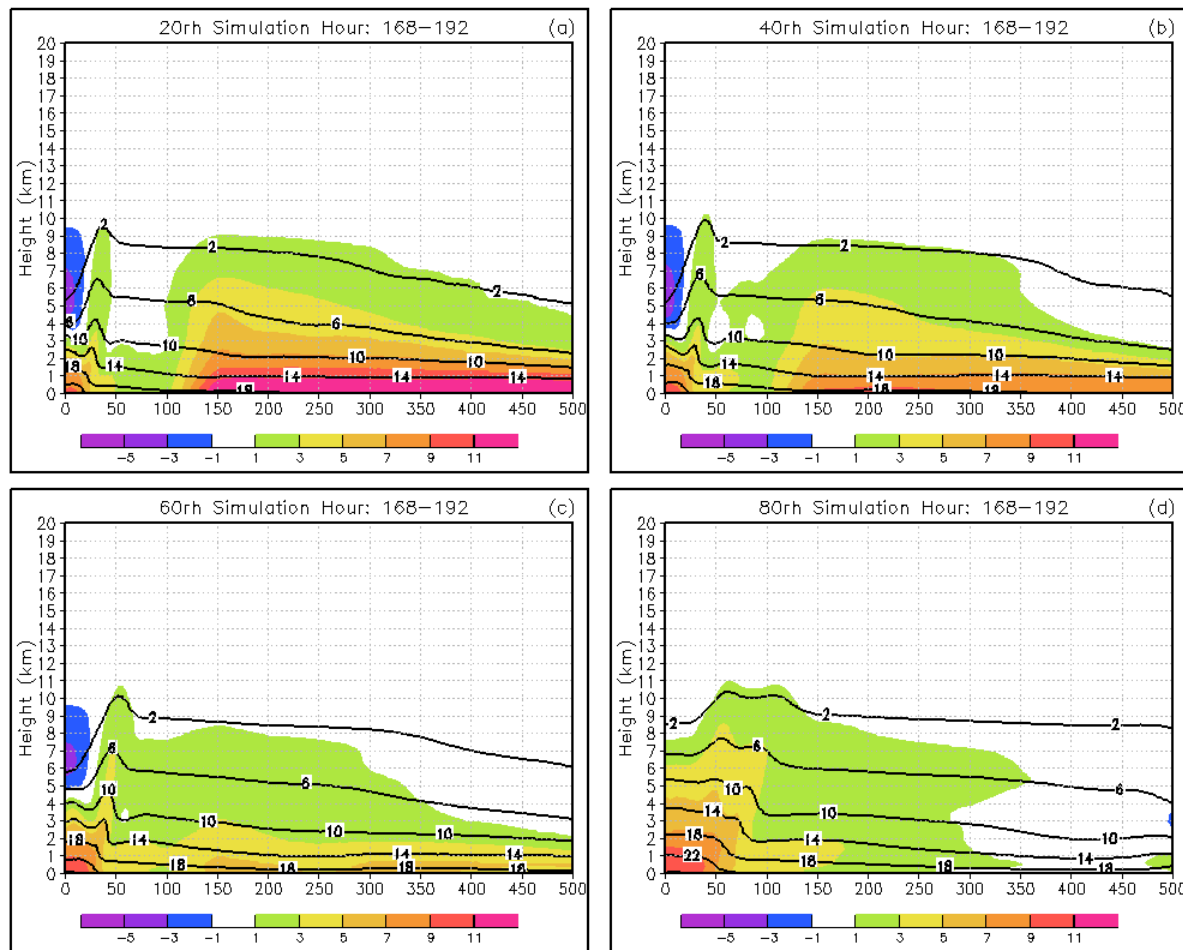


Figure 3.14: As in Fig. 3.10 except for between simulation hours 168 and 192.

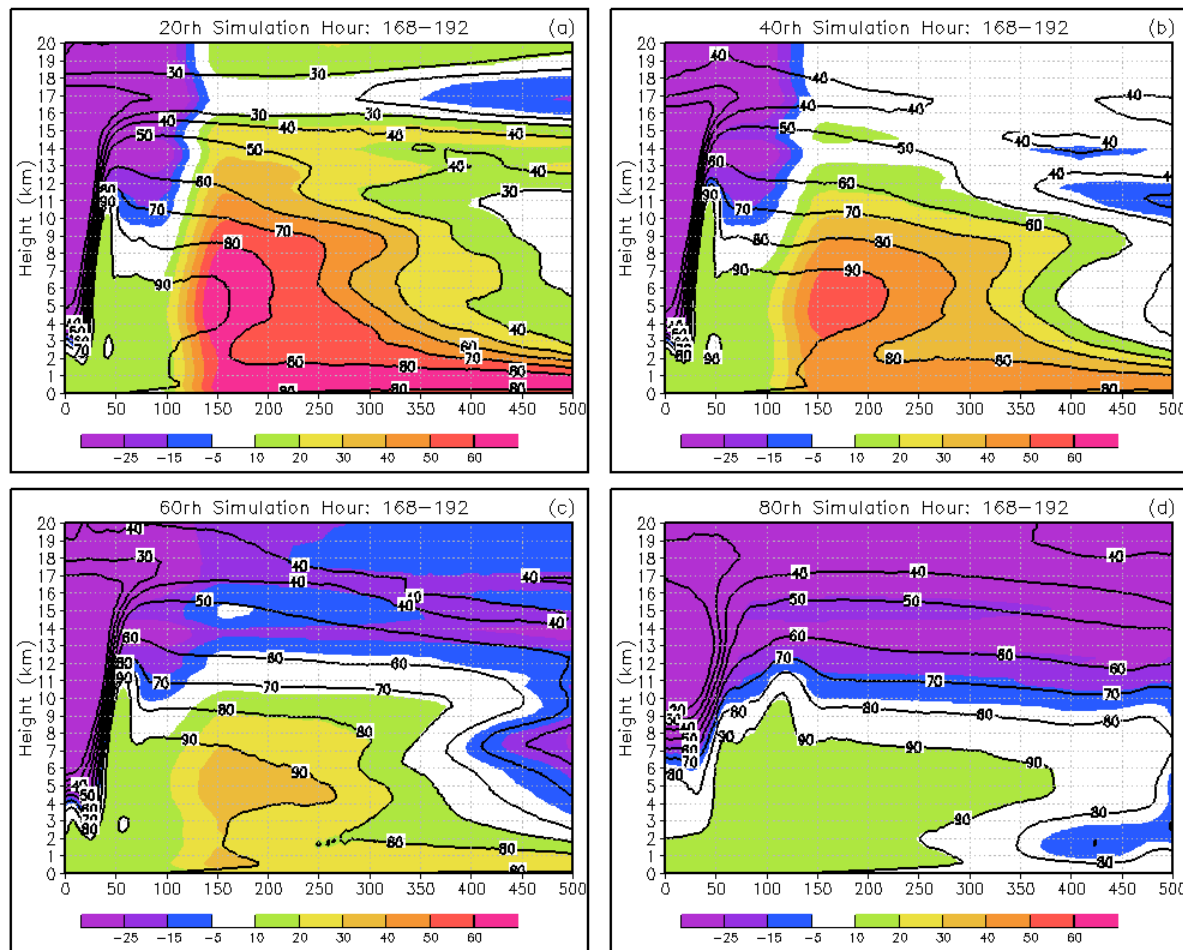


Figure 3.15: As in Fig. 3.11 except for between simulation hours 168 and 192.

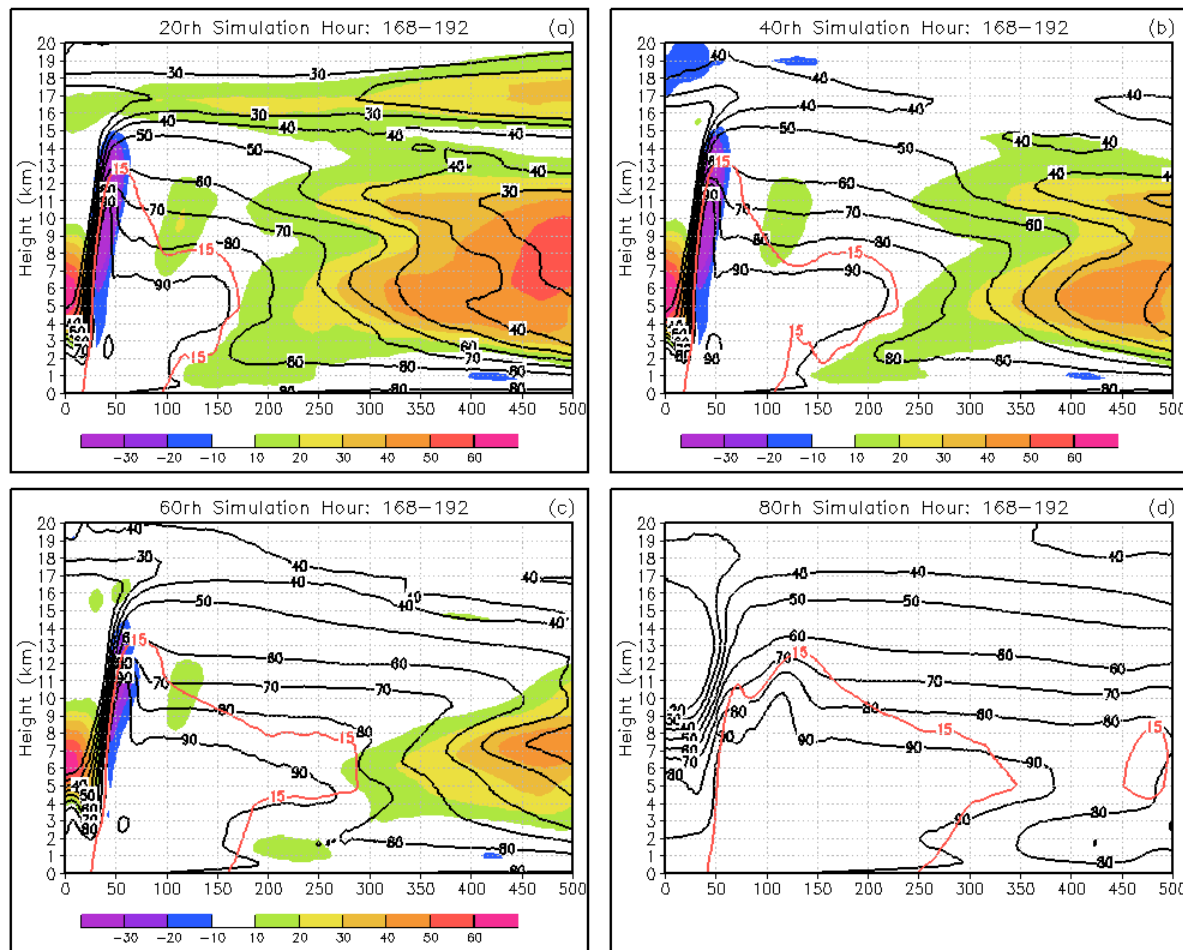


Figure 3.16: As in Fig. 3.12 except for between simulation hours 168 and 192.

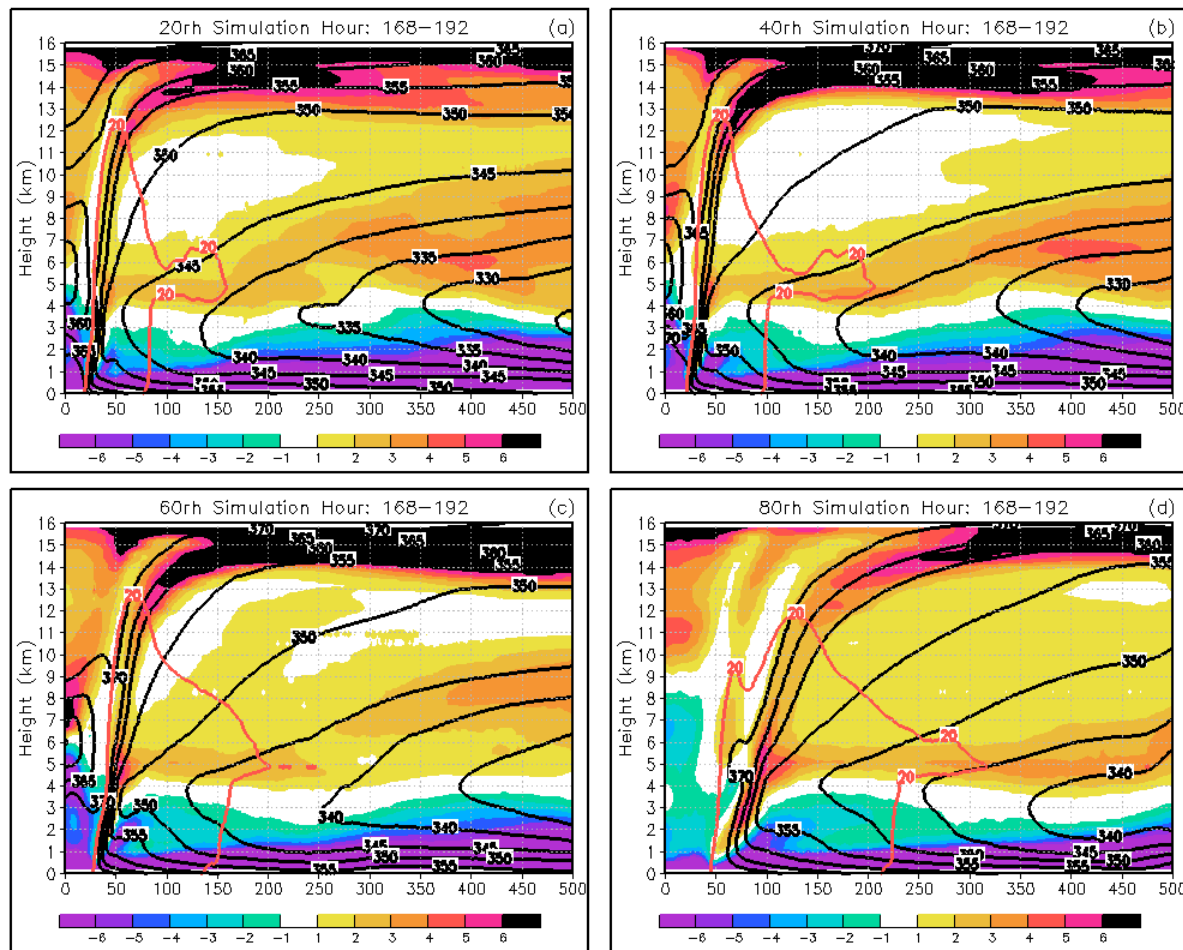


Figure 3.17: As in Fig. 3.13 except for between simulation hours 168 and 192.

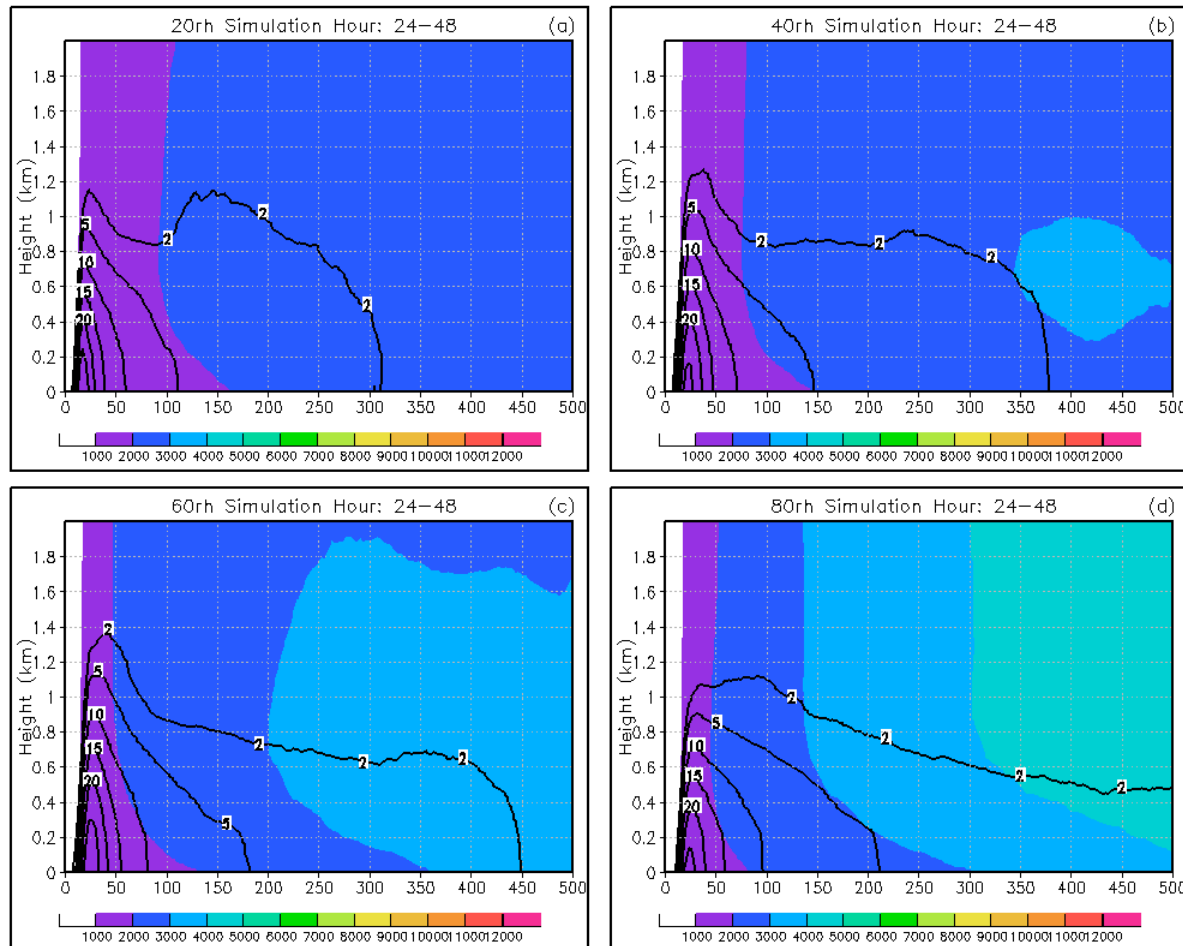


Figure 3.18: Cross-section of azimuthally averaged angular momentum (shaded; $\text{m}^2 \text{s}^{-2}$) and radial inflow (contoured; m s^{-1}) time averaged between simulation hours 24 and 48.

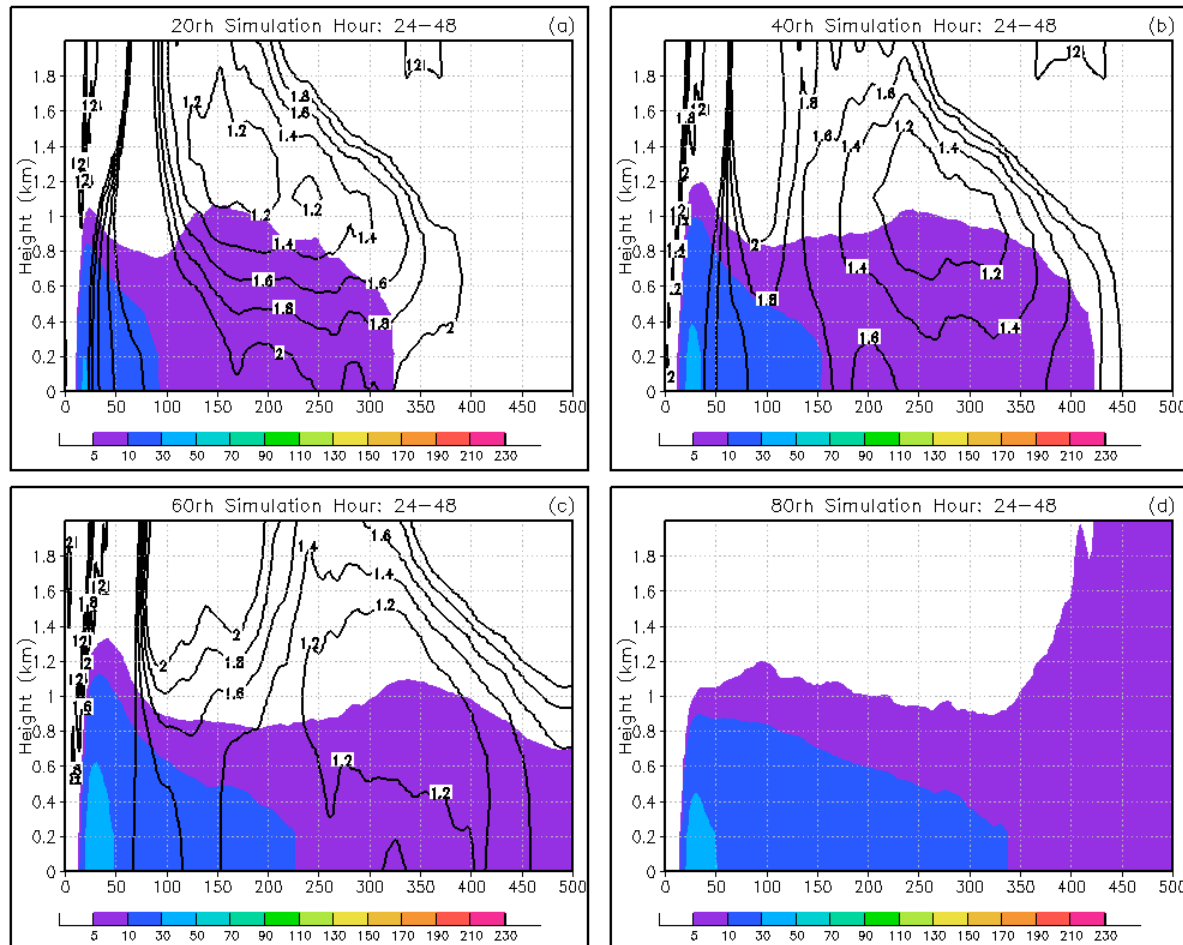


Figure 3.19: Cross-section of azimuthally averaged angular momentum multiplied by radial inflow (shaded; $\text{m}^3 \text{s}^{-3}$) and the value in the 80RH simulation divided by the value in that simulation (contoured), time averaged between simulation hours 24 and 48.

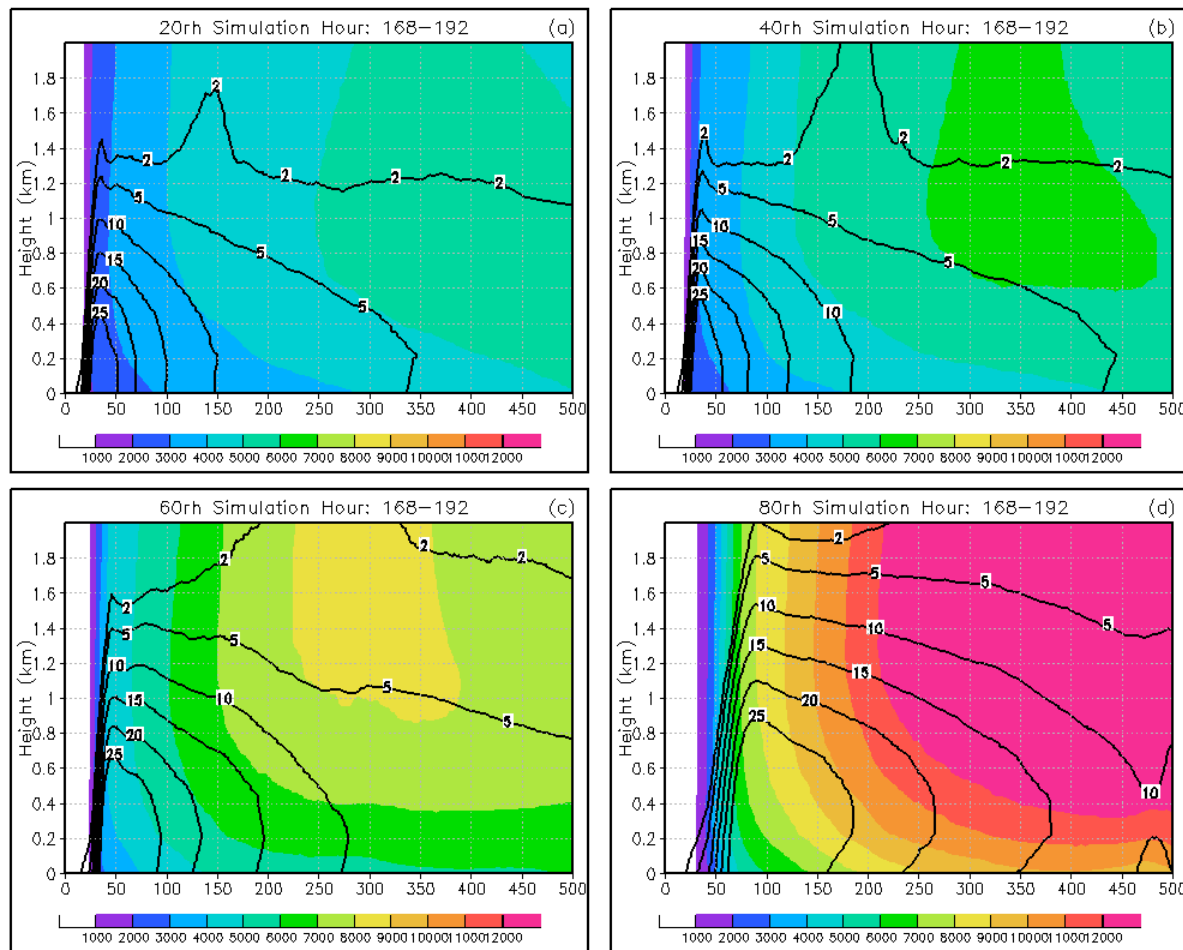


Figure 3.20: As in Fig. 3.18 except for between simulation hours 168 and 192.

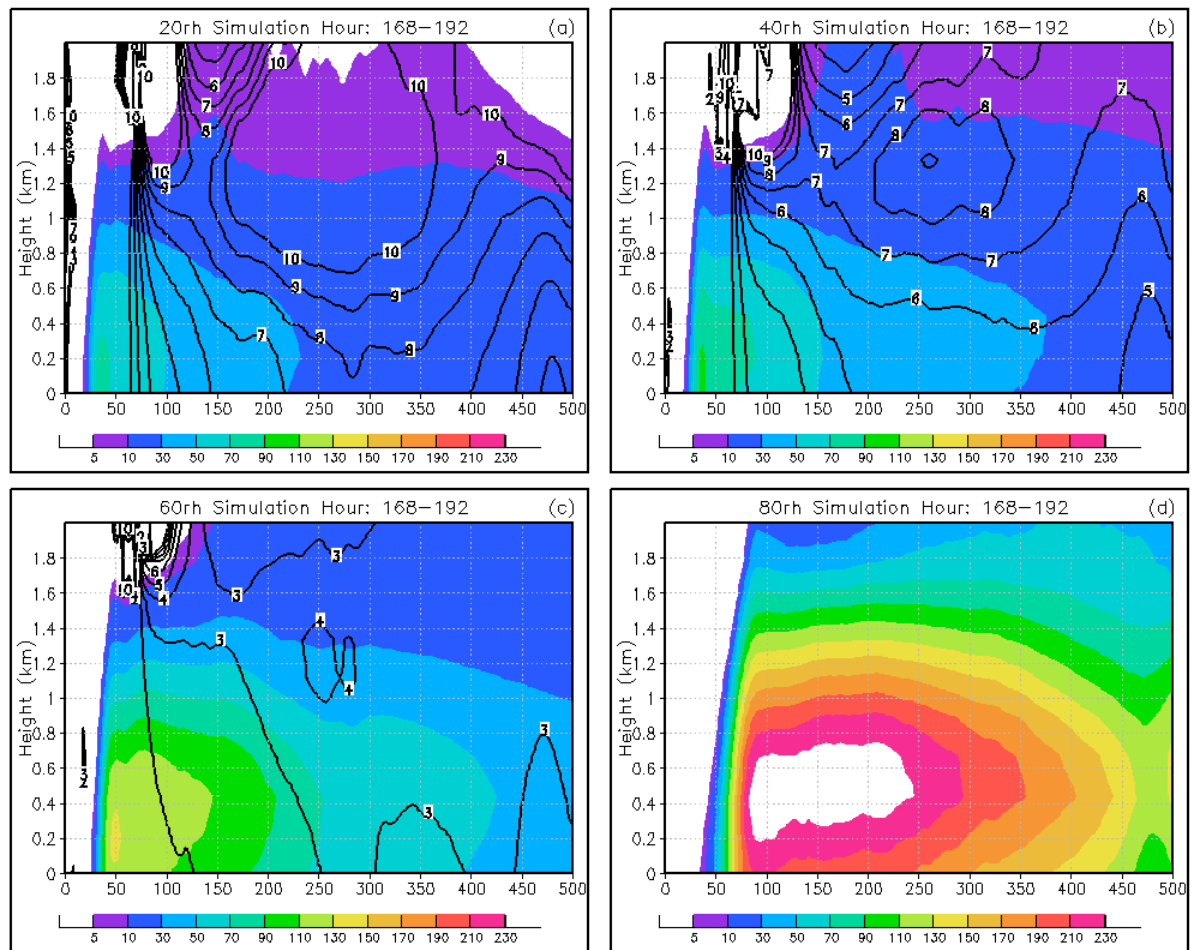


Figure 3.21: As in Fig. 3.19 except for between simulation hours 168 and 192.

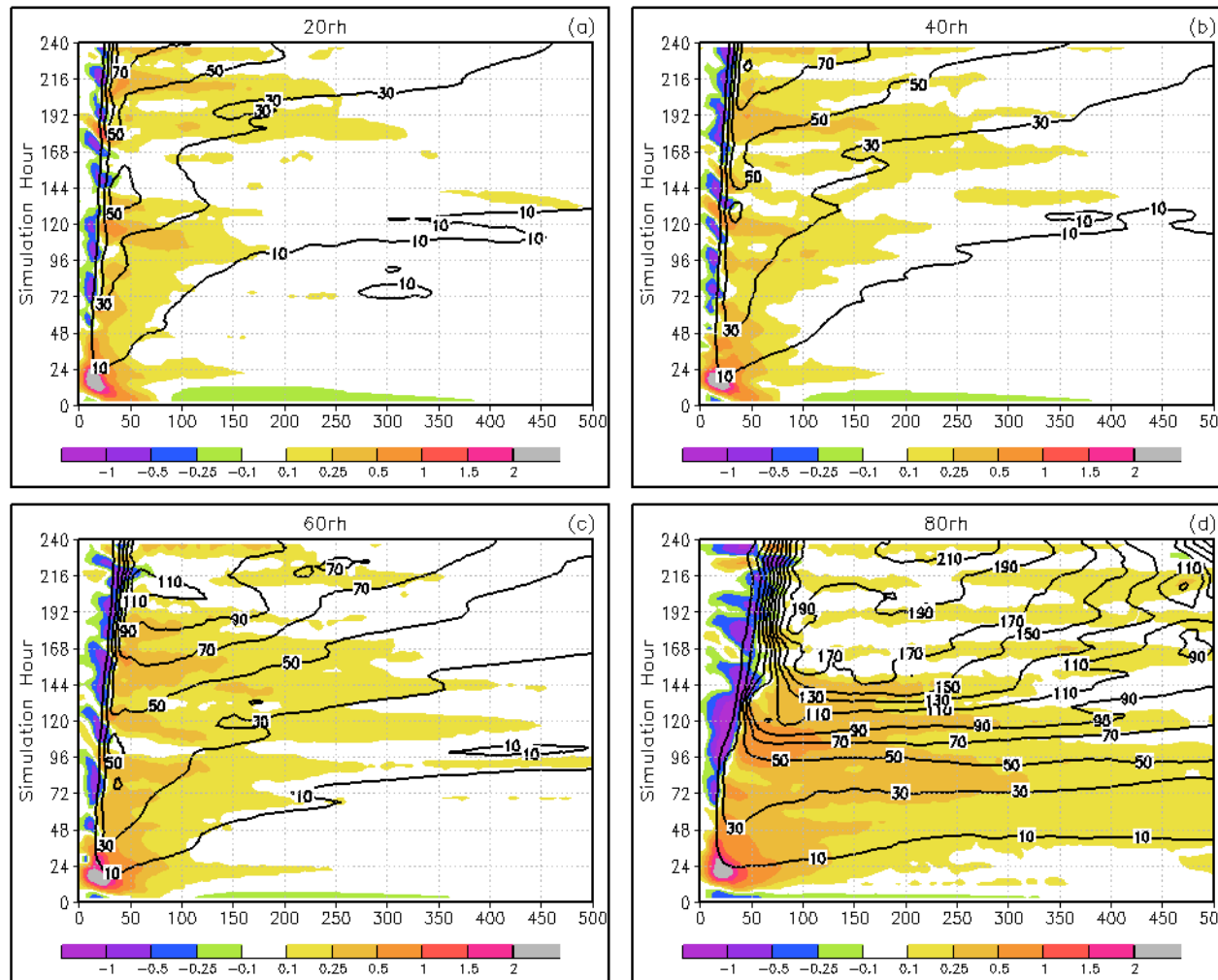


Figure 3.22: Tangential wind tendency (shaded; $\text{m s}^{-1} \text{hr}^{-1}$) and angular momentum import (contoured). Data averaged over the lowest 2-km of the troposphere.

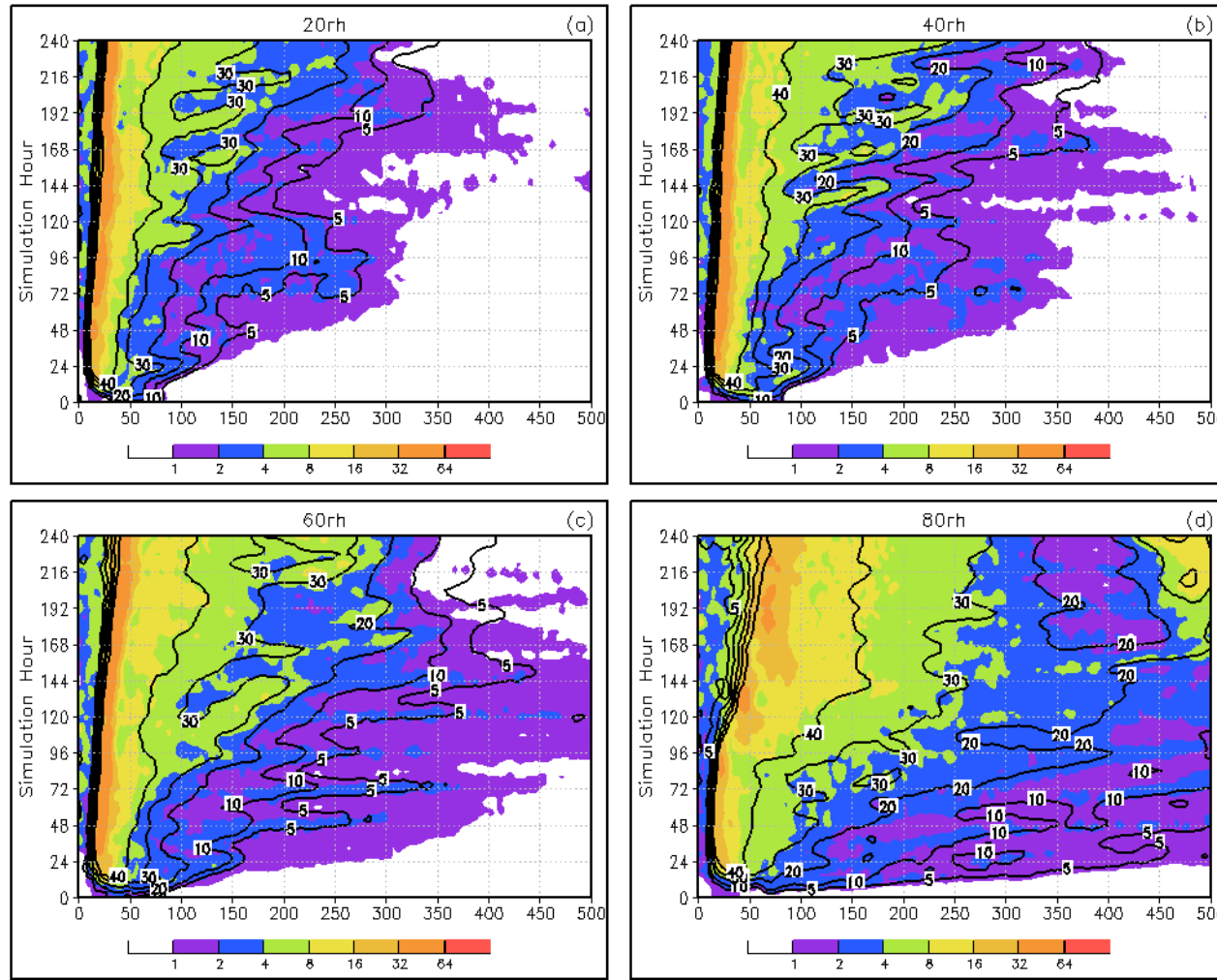


Figure 3.23: 850 – 700 hPa layer average latent heating (shaded; K hr⁻¹) and composite simulated reflectivity (contoured).

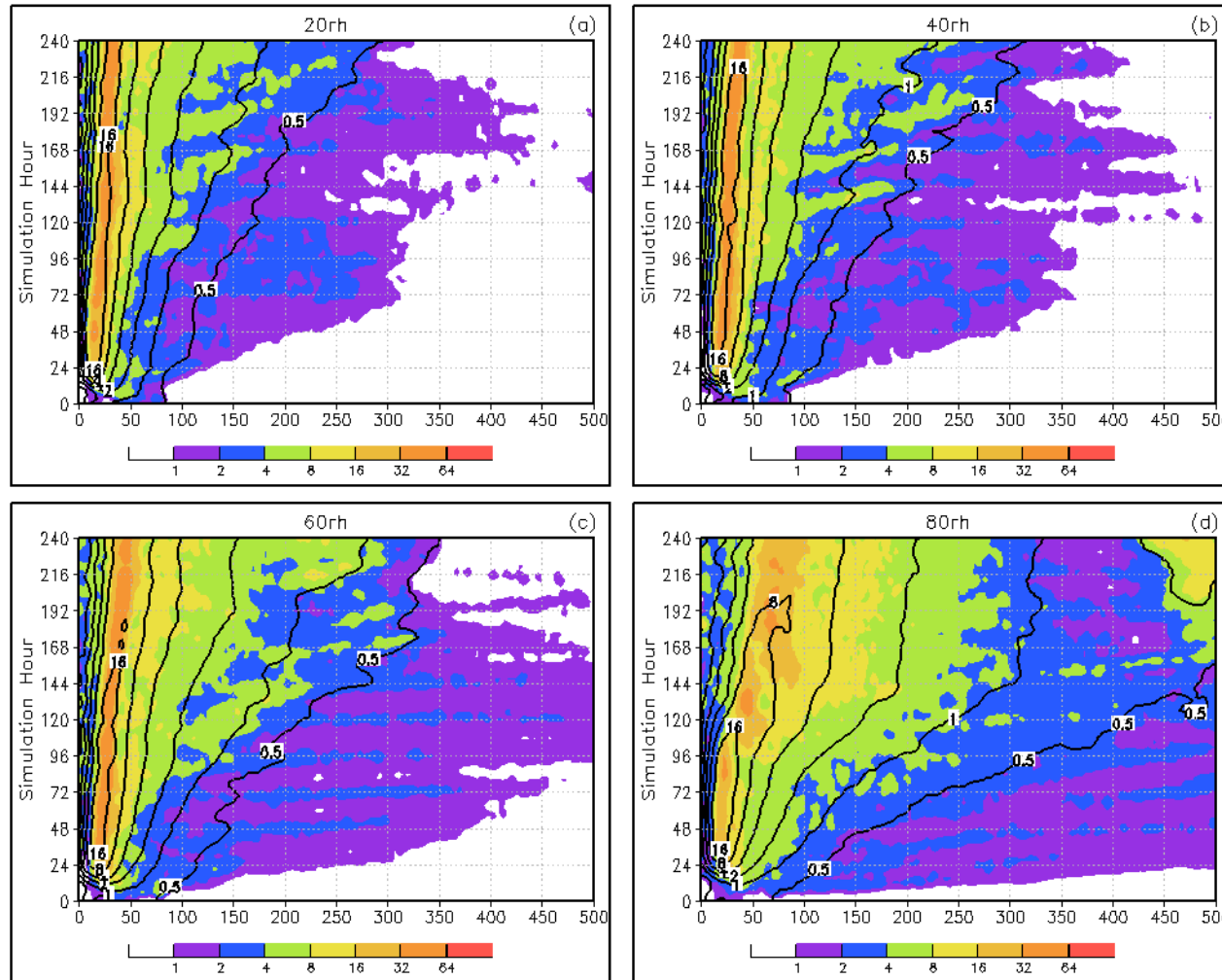


Figure 3.24: 850 – 700 hPa layer average latent heating (shaded; K hr^{-1}) and surface pressure gradient (contoured).

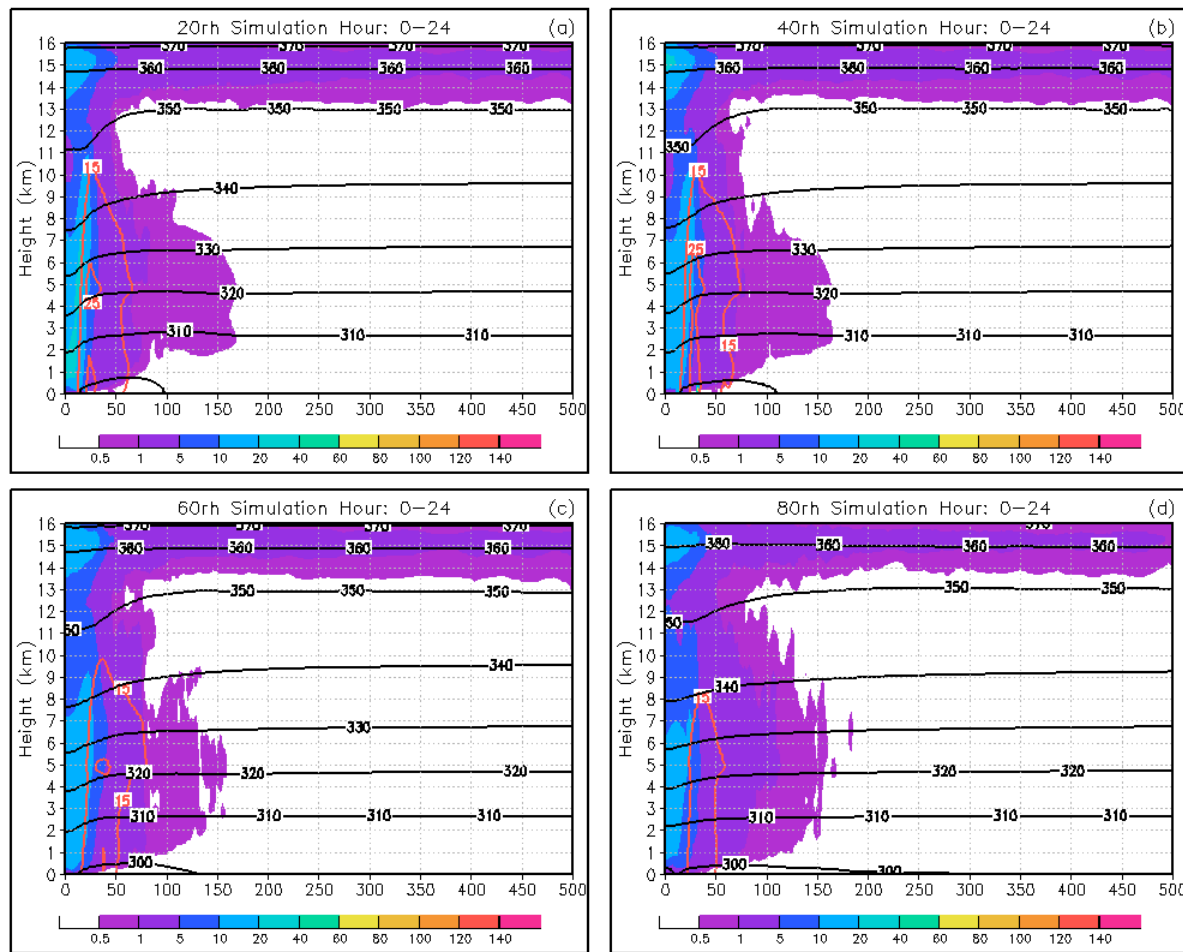


Figure 3.25: Cross-section of azimuthally averaged potential vorticity (shaded; PVU), simulated radar reflectivity (red contour; dBZ) and potential temperature (black contours; K) time averaged between simulation hours 0 and 24.

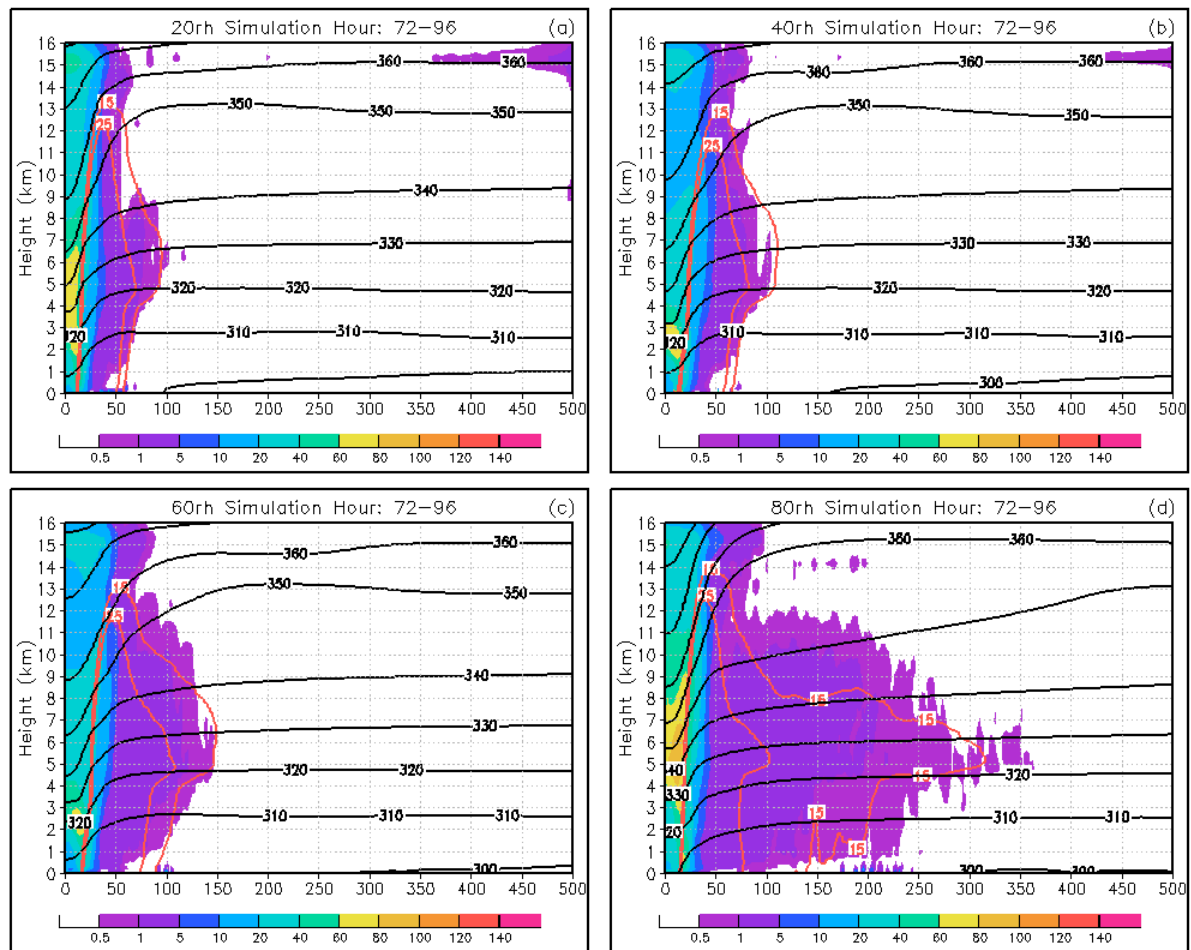


Figure 3.26: As in Fig. 3.25, except for time averaged between simulation hours 72 and 96.

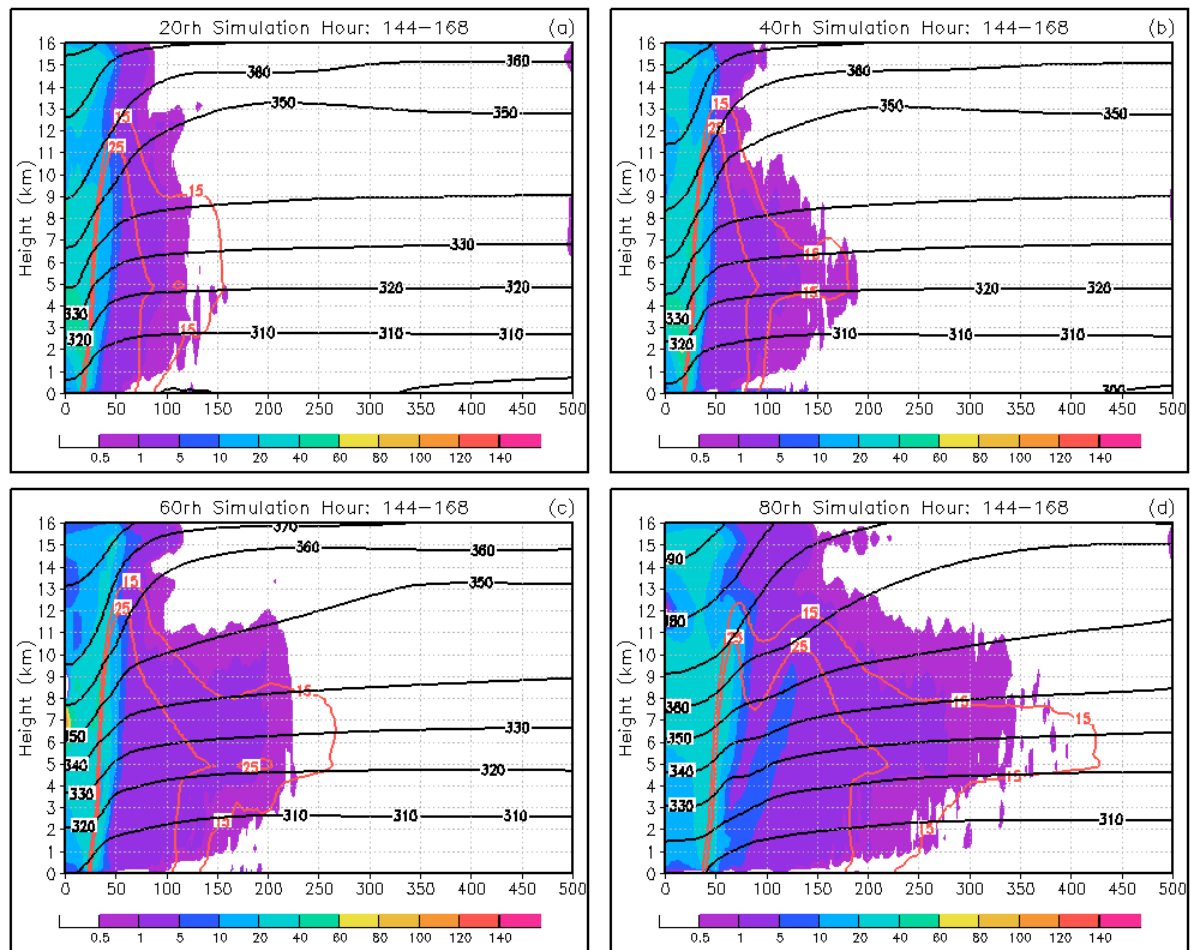


Figure 3.27: As in Fig. 3.25, except for time averaged between simulation hours 144 and 168.

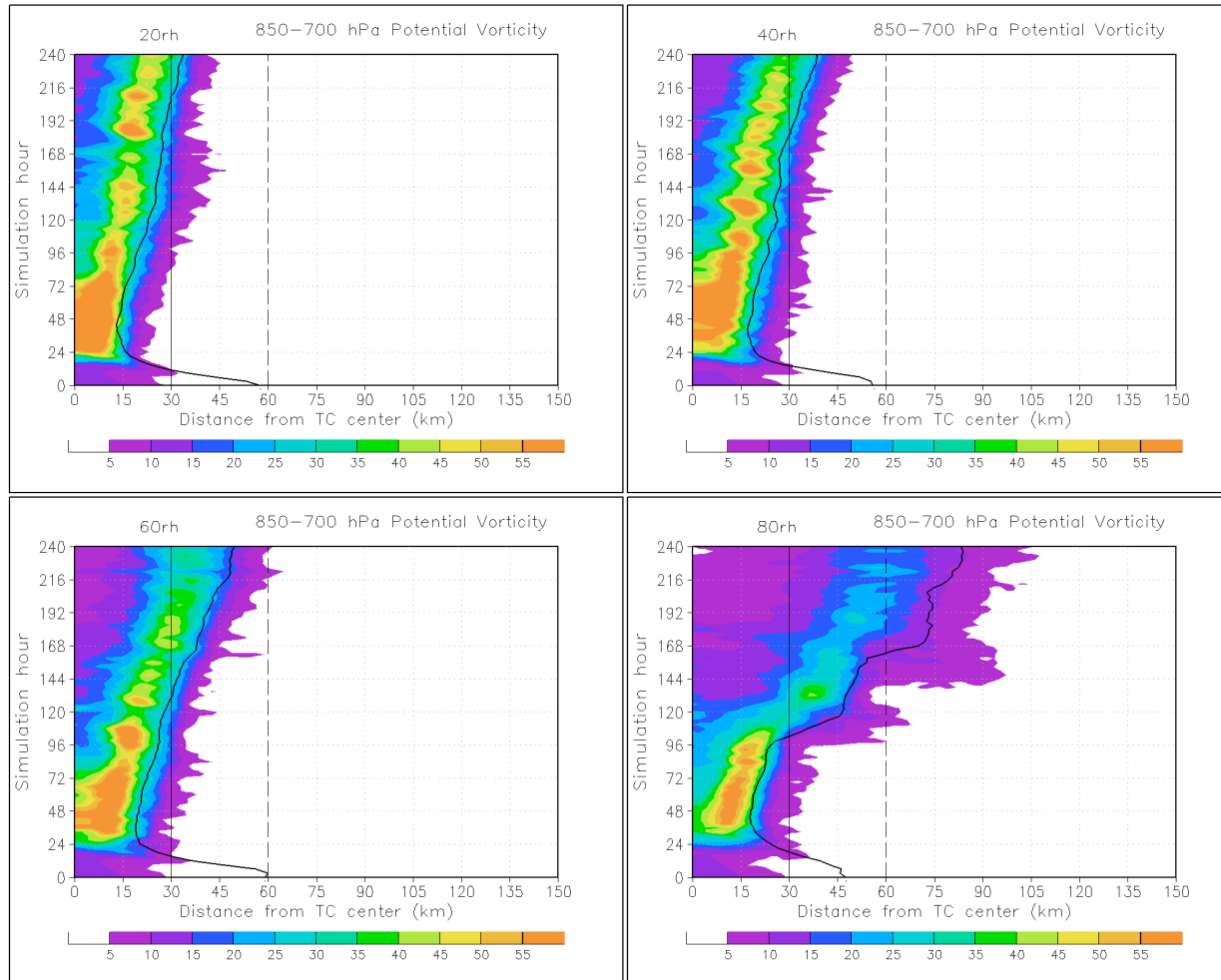


Figure 3.28: Azimuthally and layer-averaged 850–700 hPa PV (PVU, $1 \text{ PVU} = 10^{-6} \text{ m}^2 \text{ s}^{-1} \text{ K kg}^{-1}$, shaded as in legend at bottom of panels, extending to 150-km radius). The radius of maximum 10-m wind speed is shown by the thick black line and 30 and 60 km radii are highlighted for reference.

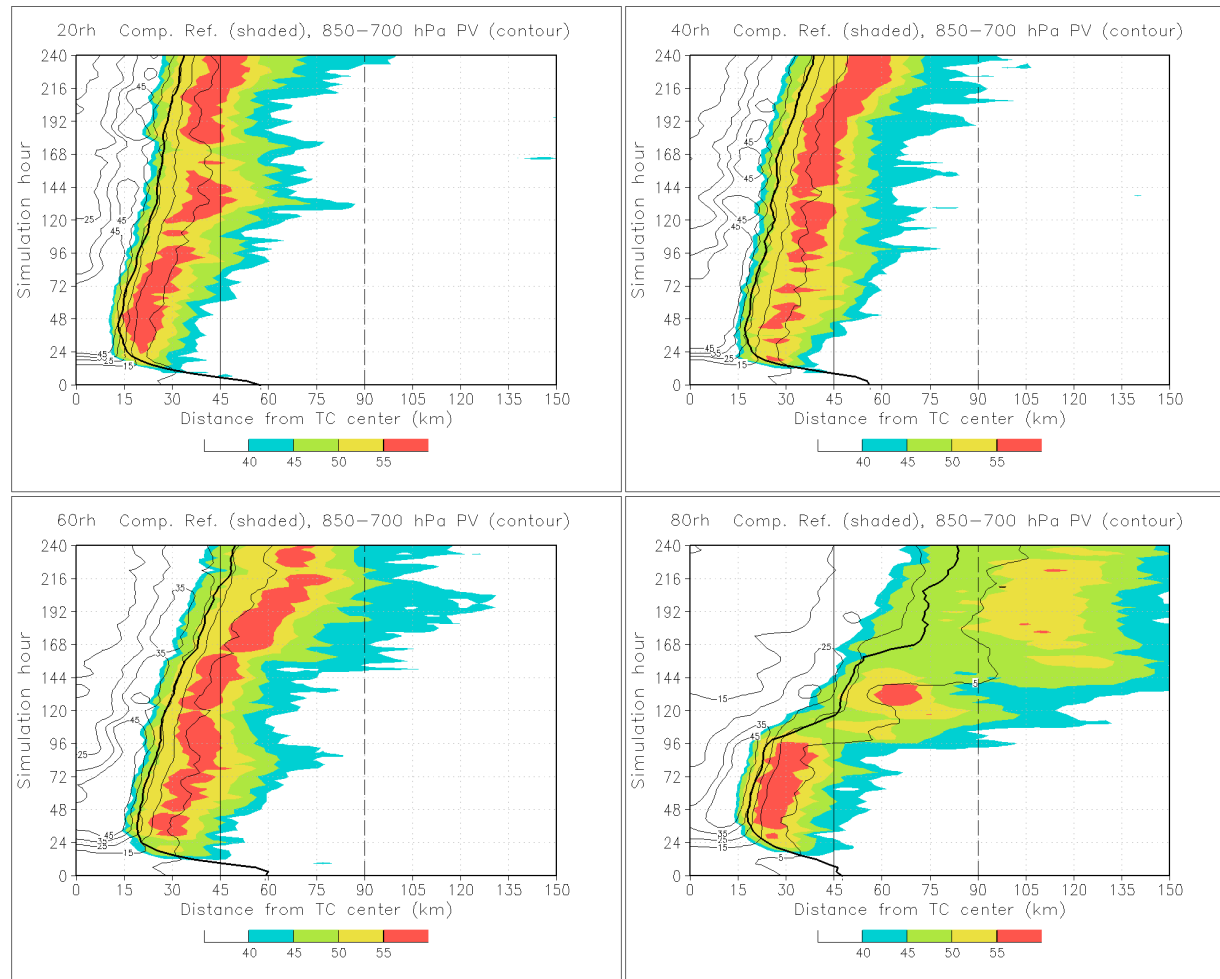


Figure 3.29: Azimuthally averaged composite reflectivity (shaded greater than 40 dBZ, as in legends) and average 850-700 hPa PV (contoured, PVU) after 1 pass with a 9-pt smoother. The radius of maximum 10-m wind speed is shown by the thick black line and radii of 45 and 90 km are highlighted.

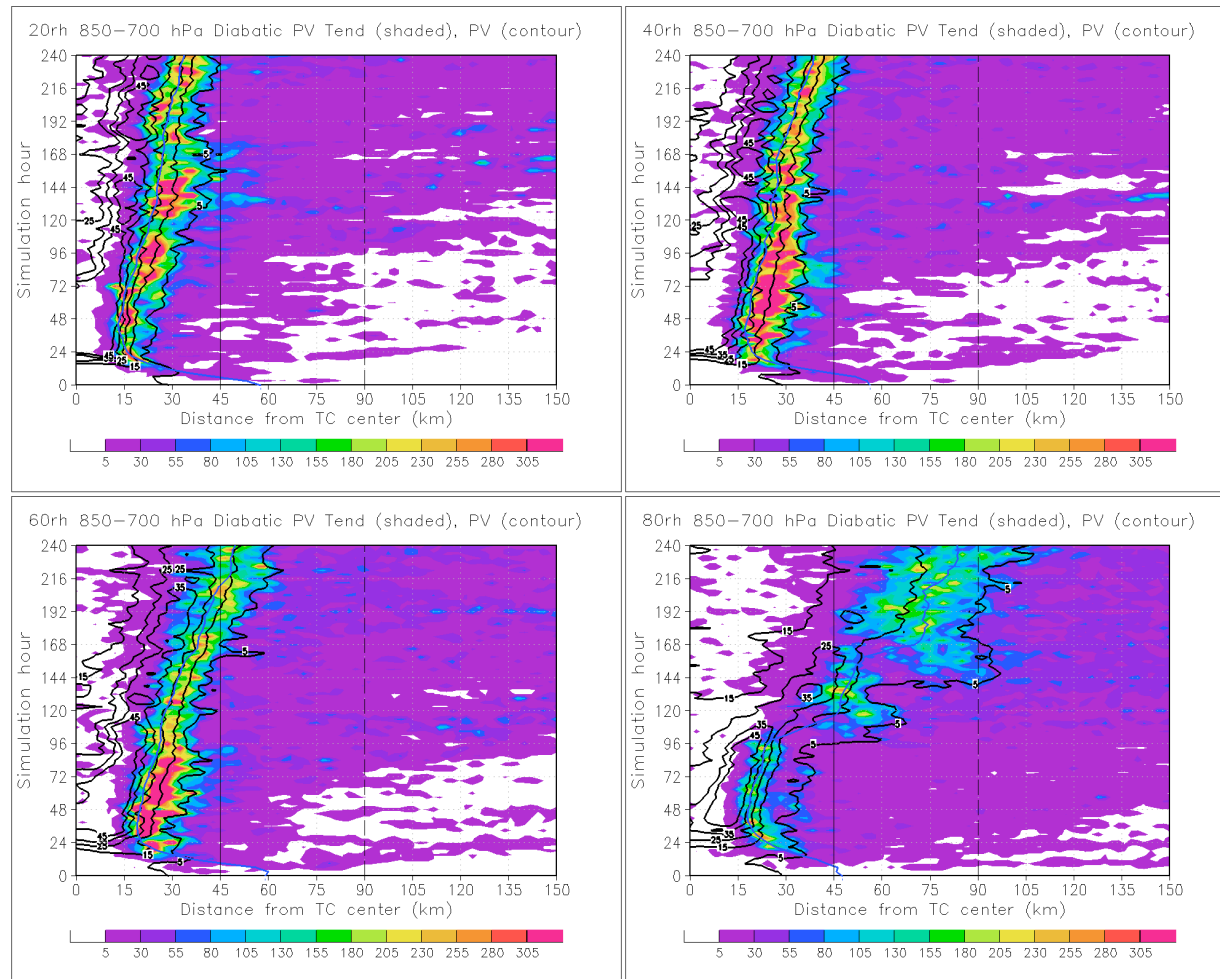


Figure 3.30: Azimuthally and layer averaged 850-700 hPa diabatic PV tendency (shaded, PVU hr^{-1}) and PV (PVU, solid black contours). The radius of maximum 10-m wind speed is shown by the thick blue line and radii of 45 and 90 km are highlighted.

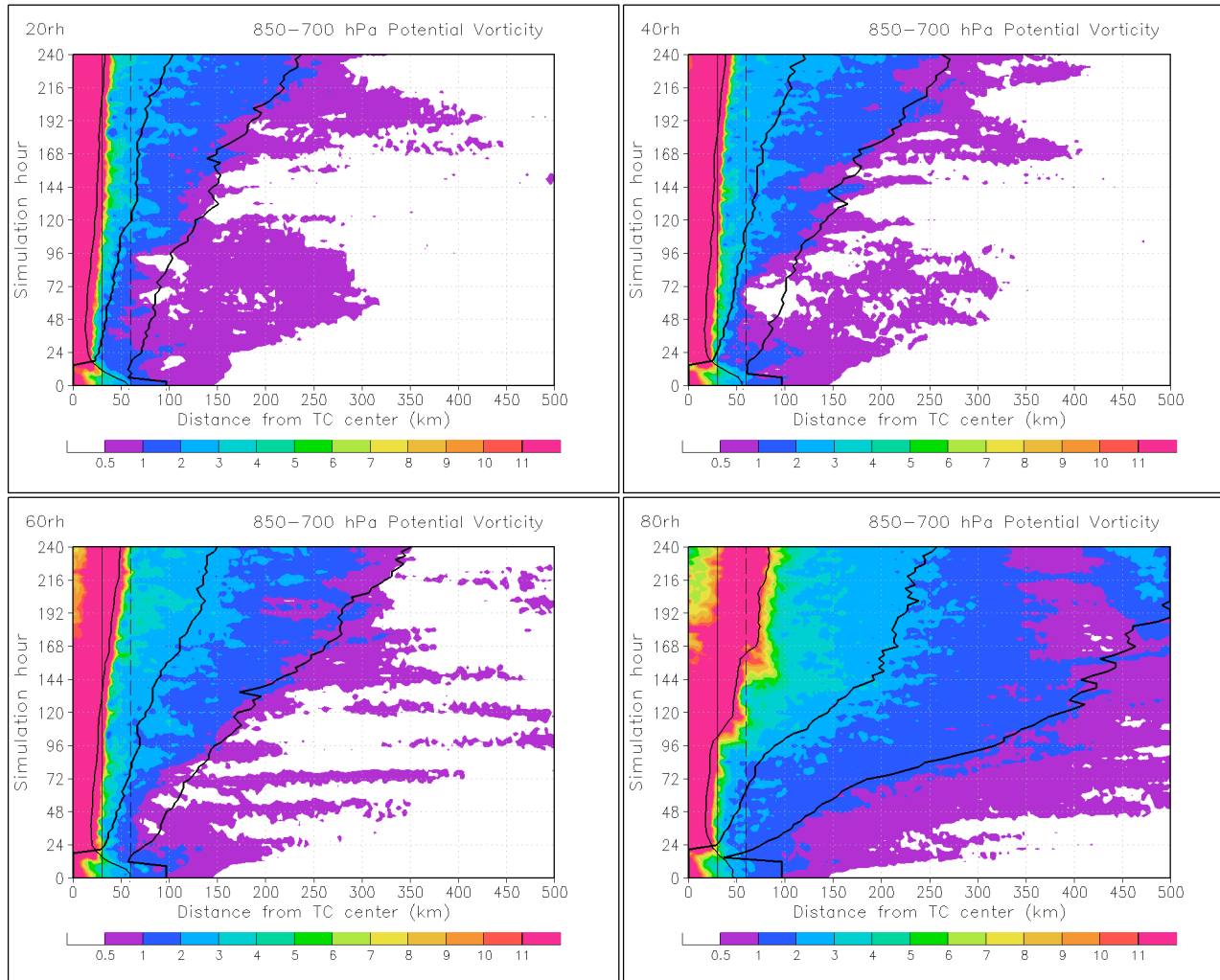


Figure 3.31: As in Fig. 3.28, except extending to 500-km radius and highlighting smaller PV values. Also, the radius of hurricane and tropical storm force wind are indicated by the thick black lines.

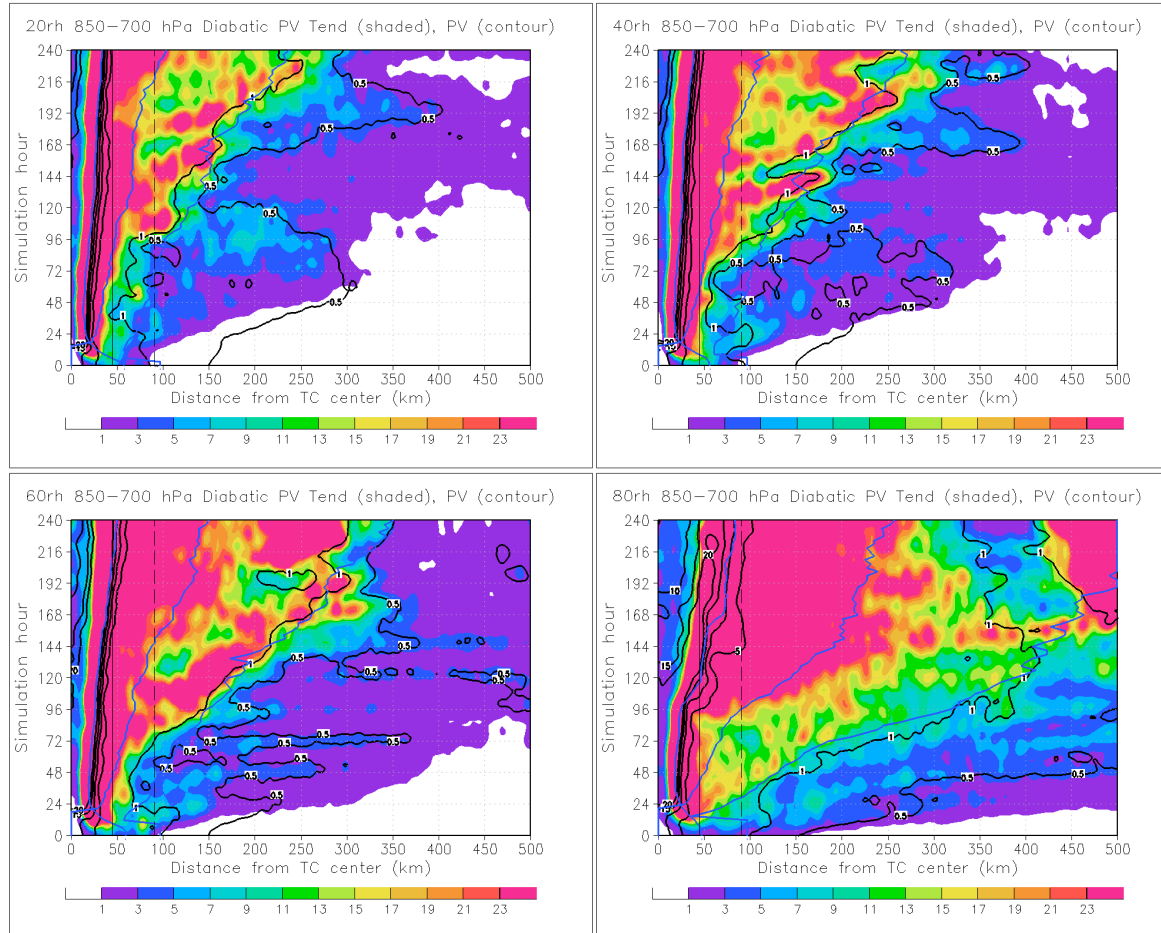


Figure 3.32: As in Fig. 3.30, except extending to 500-km radius and highlighting smaller PV values. Also, the radius of hurricane and tropical storm force wind are indicated by the thick blue lines.

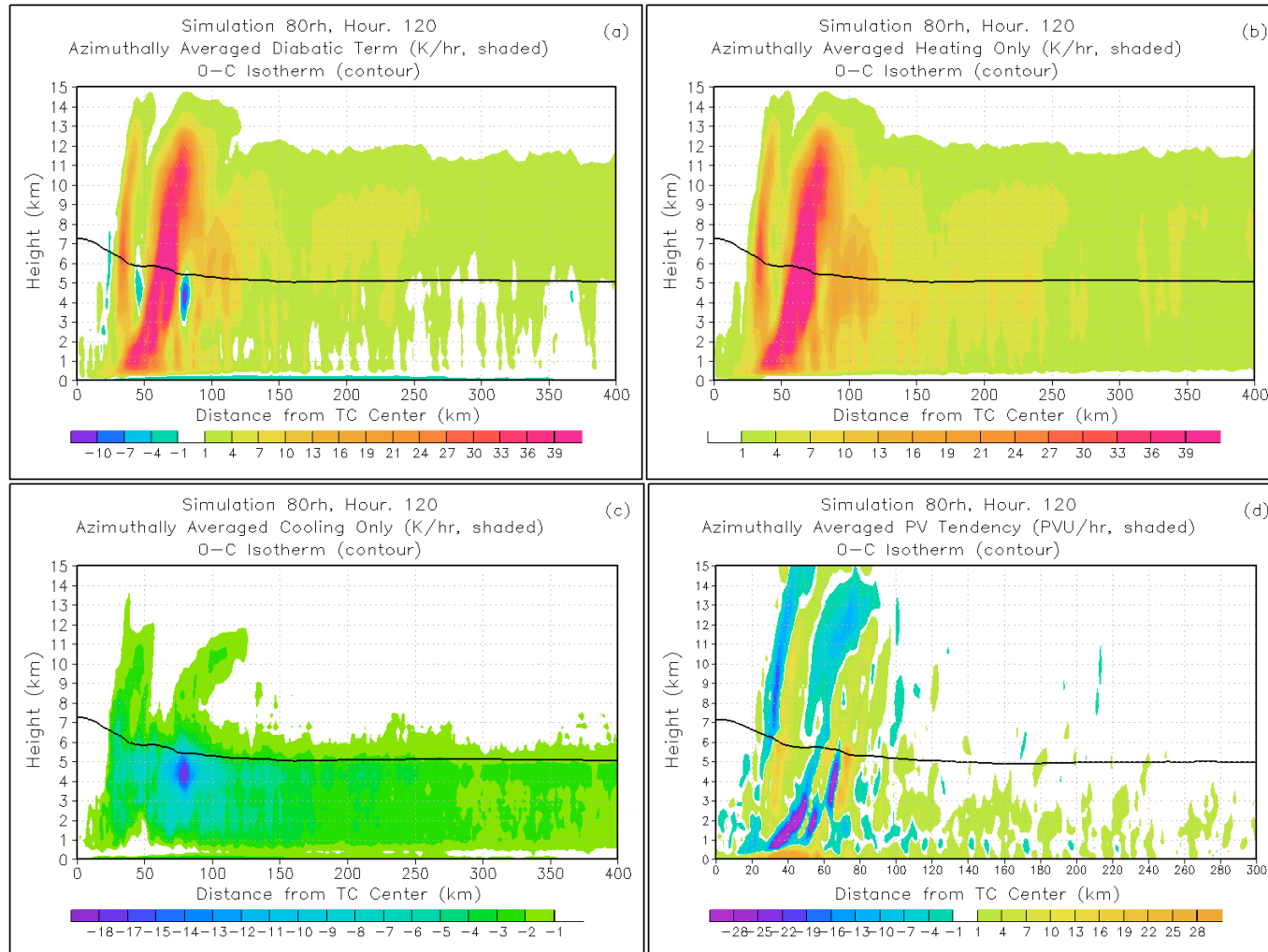


Figure 3.33: (a) Azimuthally averaged, model-output net moist diabatic tendency from 80RH_Fix simulation at 120 h (K hour^{-1}), (b) as in (a) except for positive diabatic tendency; (c) as in (a) except for negative diabatic tendency; (d) non-advective PV tendency due to moist diabatic processes.

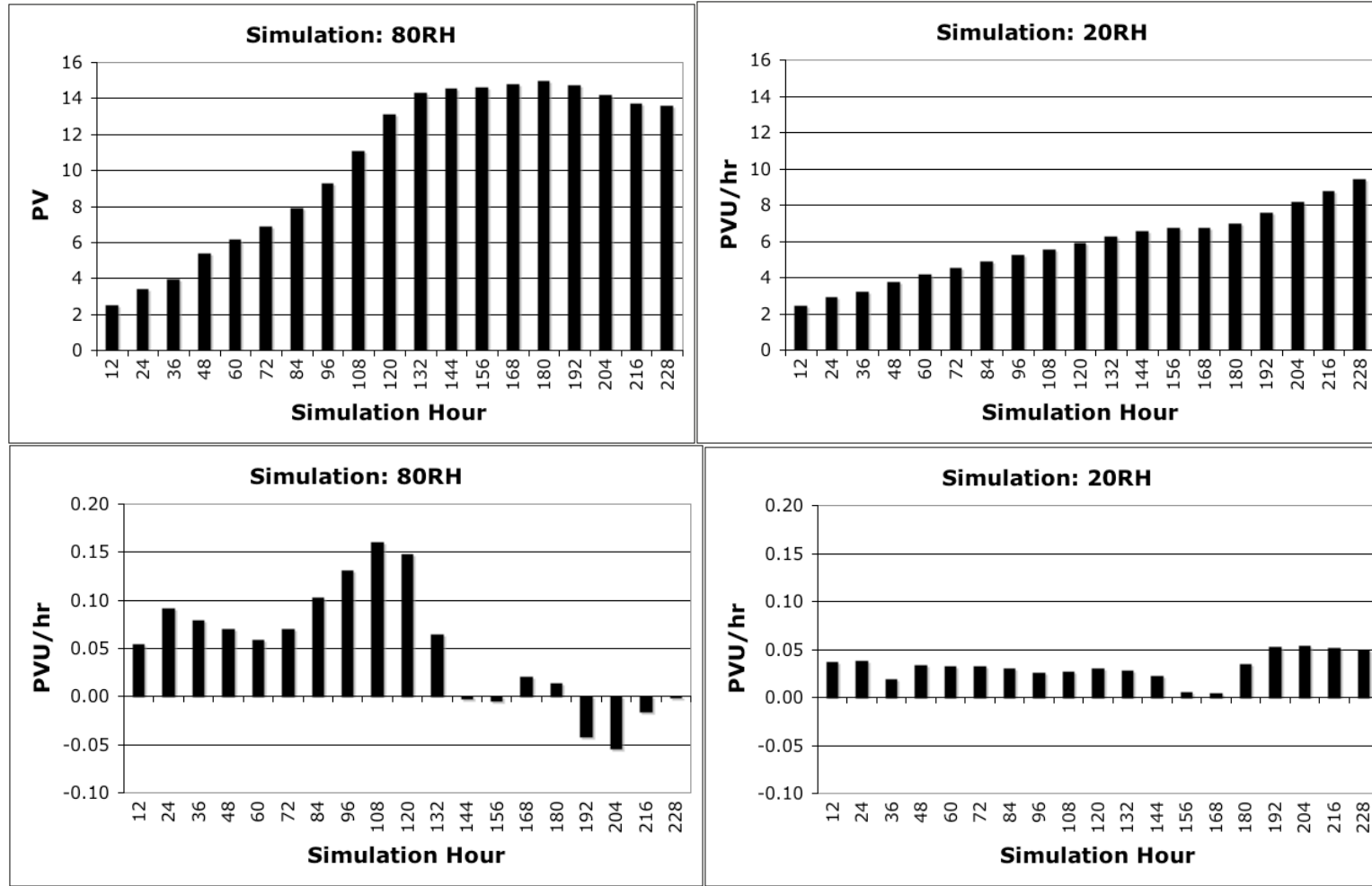


Figure 3.34: 24-hour mean volume-average (0-80km, surface-250 hPa) mass-weighted PV for the 80RH simulation (a) and 20RH simulation (b), and the corresponding hourly rate of change of average PV for the 80RH simulation (c) and 20RH simulation (d).

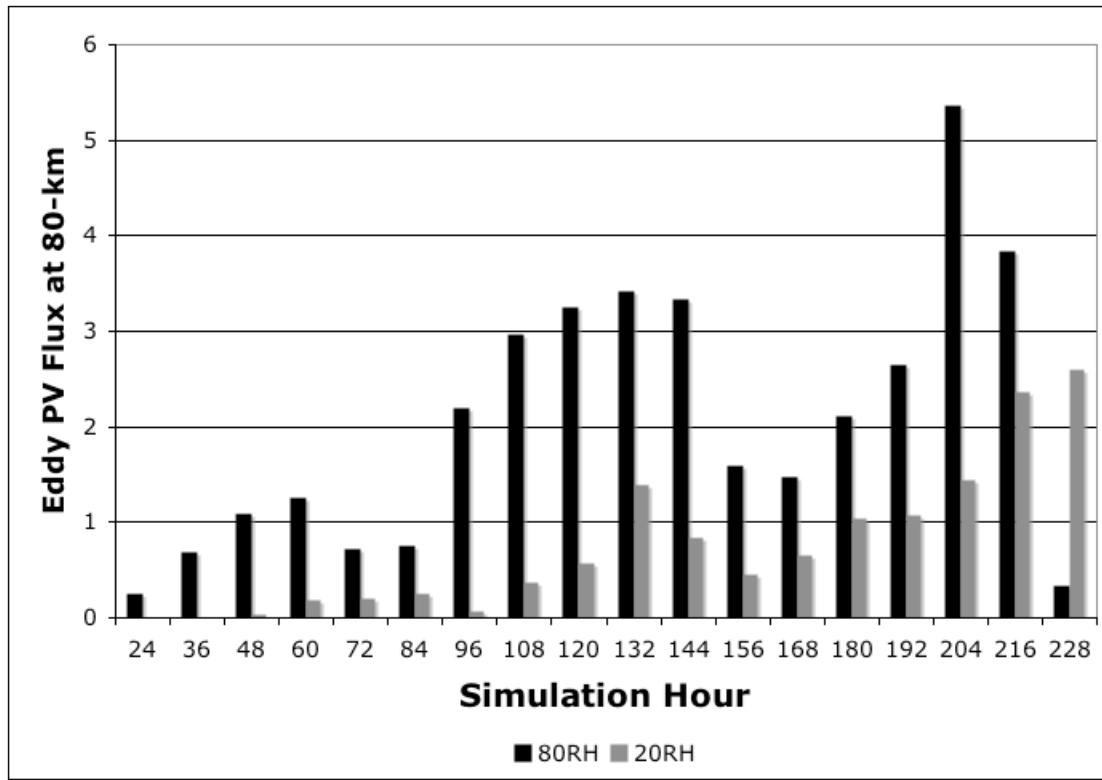


Figure 3.35: 24-hour averages of eddy PV flux (m PVU s^{-1}) in the 80-km radius ring for the 80RH simulation (black) and 20RH simulation (gray).

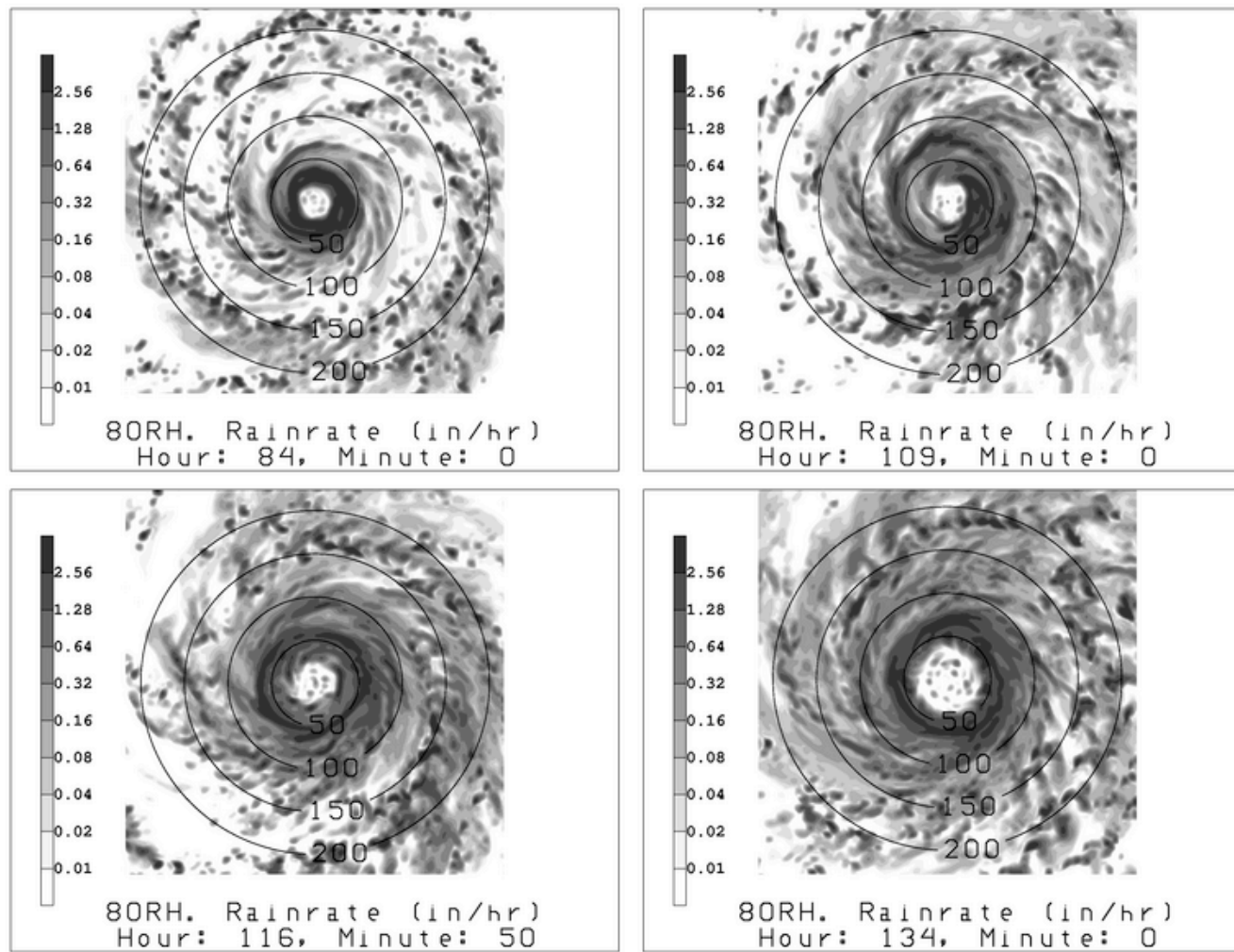


Figure 3.36: Horizontal plots of model instantaneous rainfall rate (shaded, in hr^{-1}) and distance from TC center (contoured) for the 80RH simulation valid at simulation time: a) hour 84, b) hour 109, c) hour 116 minute 50, d) hour 134.

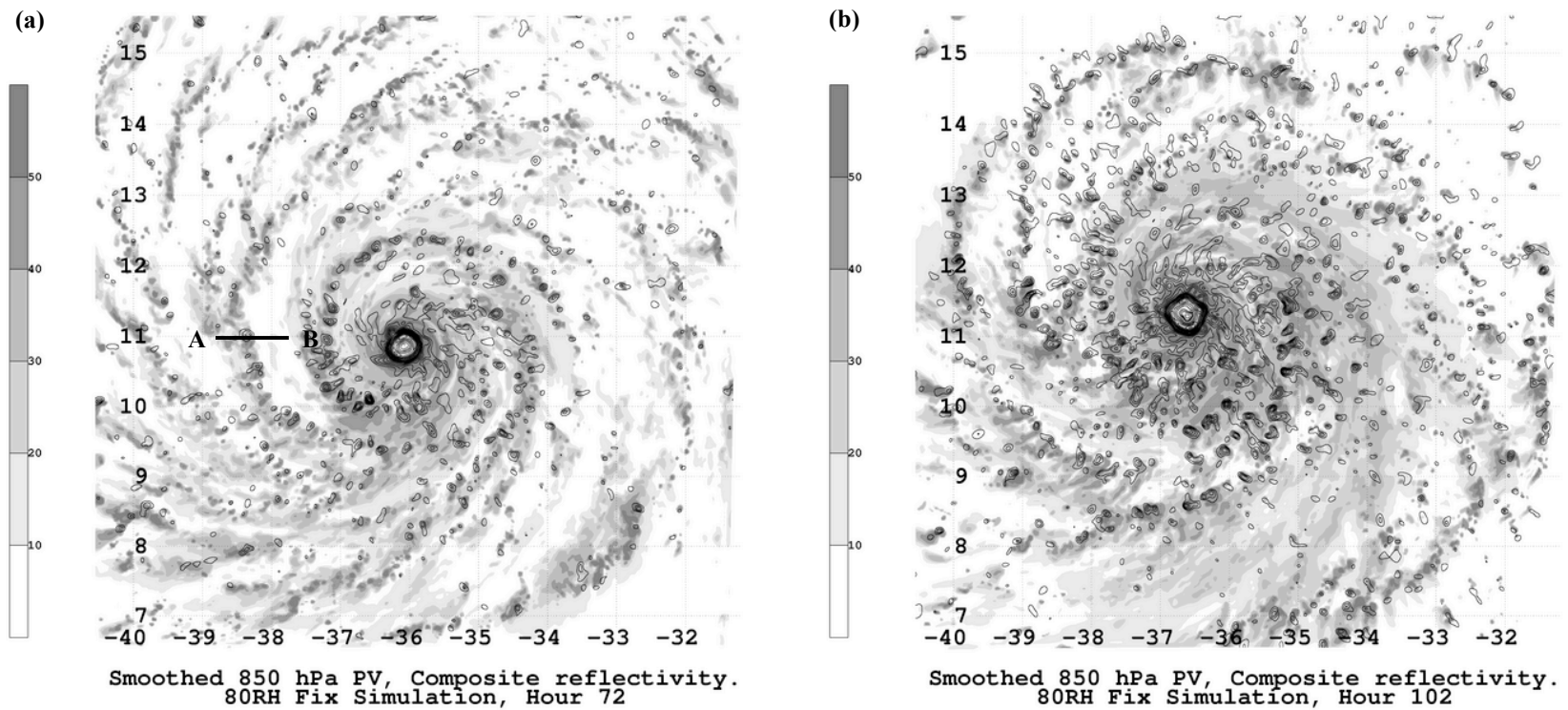


Figure 3.37: 850 hPa PV (solid contours every 2 PVU) and model simulated composite reflectivity (shaded as in legend at left of figure) at hours 72 (a), and 102 (b) 80RH_Fix simulation.

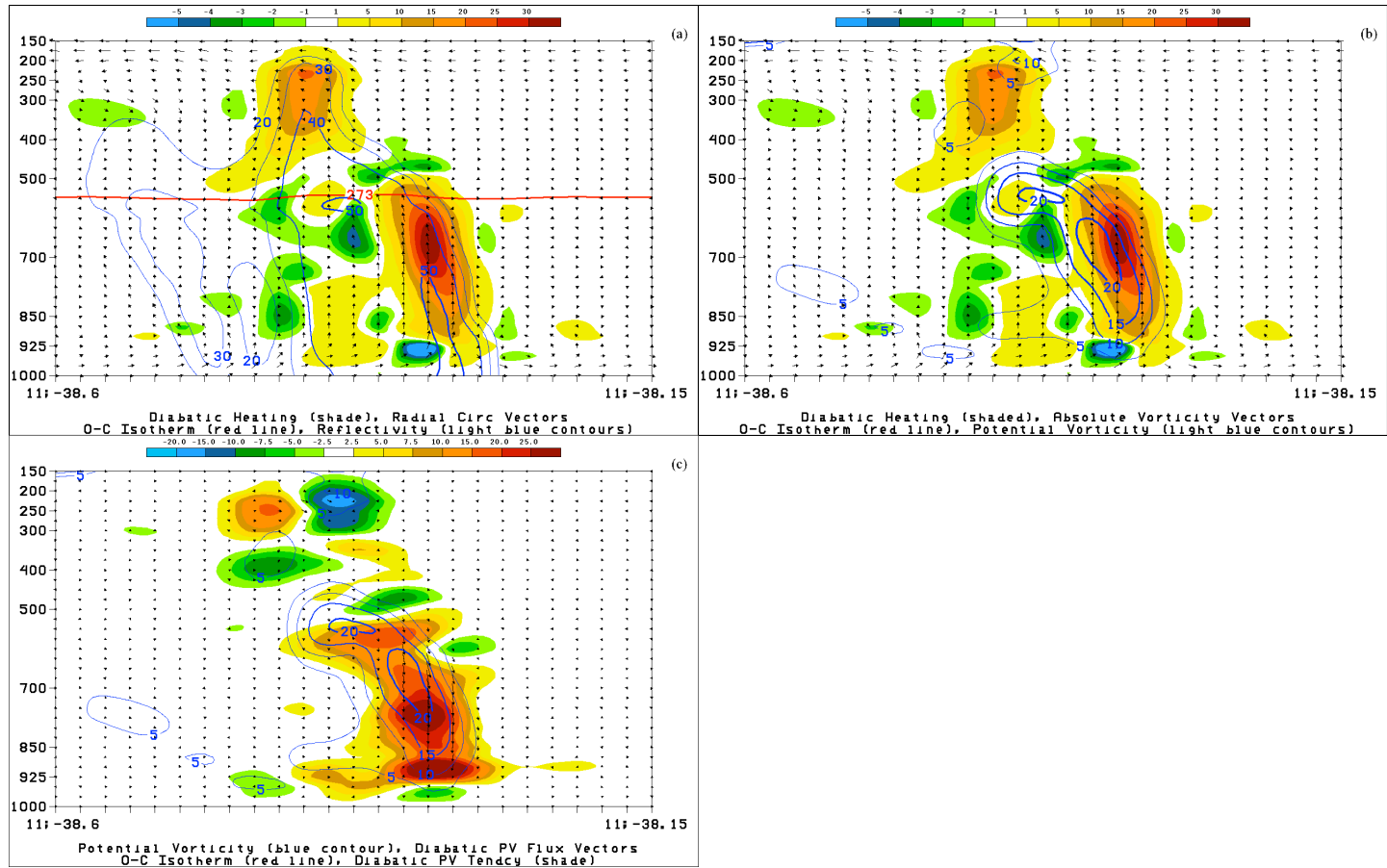


Figure 3.38: Zonal cross-section plots through band indicated in Fig. 3.37a: (a): model-output diabatic tendency ($\times 10^3 \text{ K s}^{-1}$, shaded as in legend), radial circulation (vector, vertical component scaled by 25 ub s^{-1}), 0°C isotherm (red line), and simulated radar reflectivity (light blue contours); (b) as in (a) except with absolute vorticity vectors instead of circulation, and PV (PVU, blue contours) instead of reflectivity. (c) PV (PVU, blue contours), diabatic PV flux vectors, moist diabatic PV tendency (shaded as in legend), and 0°C isotherm.

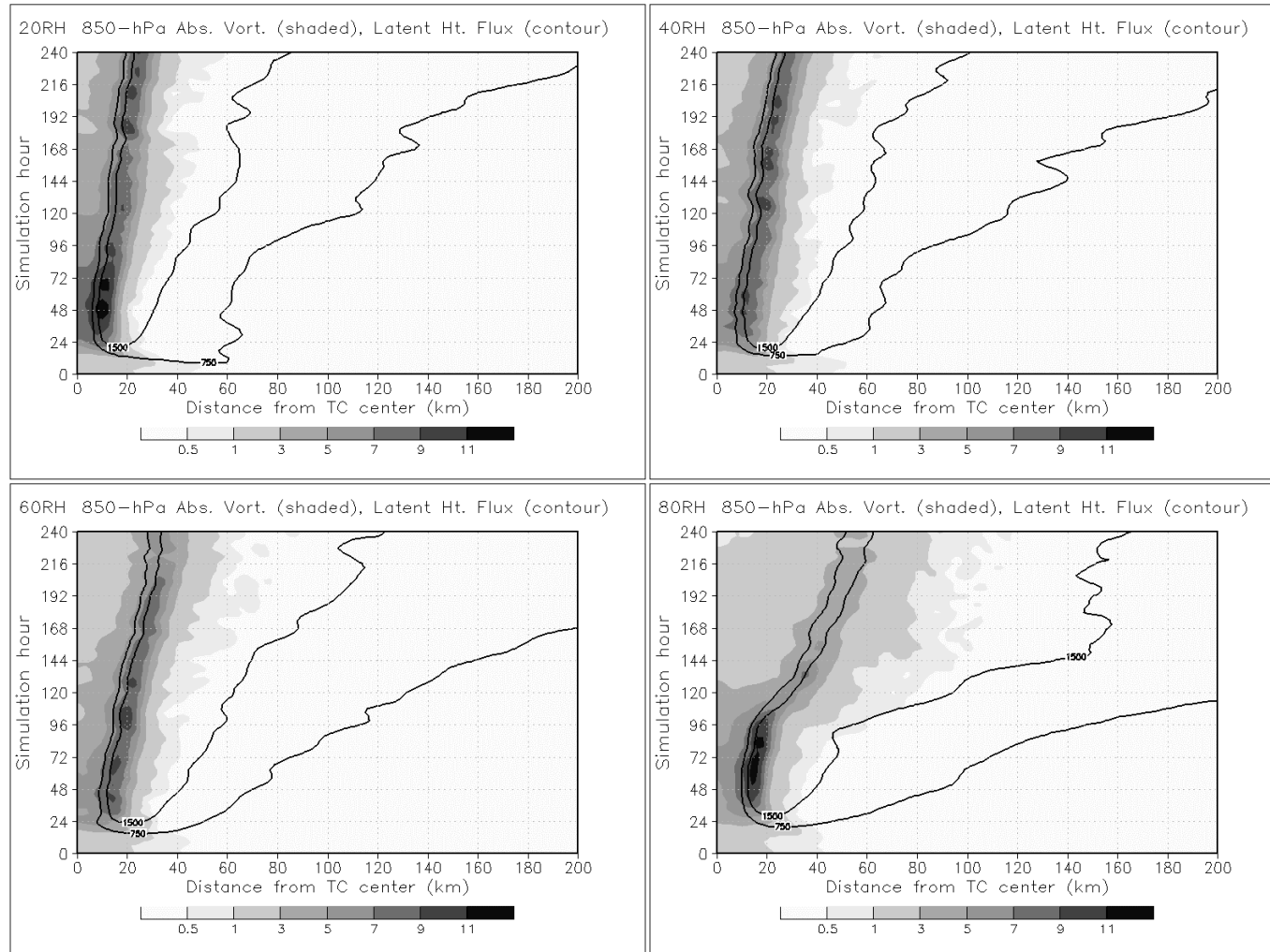


Figure 3.39: Azimuthally averaged 850-hPa absolute vorticity (shaded) and surface latent heat flux (W m^{-2} , solid black contours).

Chapter 4

Future climate change and potential changes in TC intensity, rainfall, and structure

4.1 Future projections - TC environment

In the following sections, GCM projected changes in SST, temperature, and moisture are be discussed. For each of these parameters, ensemble mean changes for each emissions scenario are presented, along with ensemble statistics in order to assess the uncertainty.

4.1.1 Environmental temperature

As anticipated based on the physical processes connecting increased greenhouse gases and changes in surface temperature, SST warming is proportional to the projected increase in greenhouse gas concentrations (Table 4.1); recall that SRESB1 features the lowest increase in greenhouse gas concentrations, SRESA1B the middle, and SRESA2 the largest. The projected warming values computed here are in general similar to previous studies that focused on changes in the tropics, and vary as one would expect with the different emissions scenarios. Within each emissions scenario there is considerable spread among the 13 GCMs considered, indicating that individual model characteristics play a role in determining model projected surface temperature changes.

The vertical profile of ensemble mean projected temperature changes derived from GCMs forced with the different emissions scenarios are of similar shape, but vary in magnitude (Fig. 4.1). Each curve indicates projected warming throughout the troposphere, which is smallest near the surface (1000-hPa pressure level) and increases to just below the height of the tropopause. The projected warming at the 1000-hPa is slightly larger than that of the SST (Table 4.1). The level of maximum warming varies in the different emissions scenarios, and is progressively higher in the emissions scenarios with higher concentrations

of greenhouse gases (i.e. maximum warming is found at 300 hPa in SRESB1, 250 hPa in SRESA1B, and 200 hPa in SRESA2). These curves are consistent with the “moist adiabatic adjustment” described in chapter 1, whereby warmer surface temperatures coupled with convection in the tropics lead to an increasingly stable temperature profile in the troposphere due to convective heating profiles. The amount of stabilization, computed as the difference between the maximum tropospheric warming and the warming at 1000-hPa is indicated in Fig. 4.1; stabilization is proportional to the assumed increase in greenhouse gases and subsequently the increase in SST, as would be anticipated.

In the stratosphere the GCMs project cooling, with the cooling again progressively increasing with higher concentrations of greenhouse gases. This relationship is consistent with the physical mechanisms described in chapter 2, whereby increased greenhouse gas concentrations lead to stratospheric cooling due to increased infrared emissivity in the stratosphere and also increased blockage of outgoing infrared energy in the troposphere. The combination of tropospheric warming and stratospheric cooling leads to an increase in the height of the tropopause. The potential impact of temperature changes in the stratosphere on TC structure and intensity will be investigated by conducting a simulation where projected stratospheric temperature changes are neglected, as was previously described.

Now focusing on the ensemble of GCMs, it is evident that within each emissions scenario considerable spread in projected temperature change exists among members (e.g., Figs. 4.2 - 4.4), with the uncertainty increasing with height in the troposphere and being maximized near the altitude of maximum warming (as indicated by both the curves and the standard deviation). As previously described, these uncertainties are largest in the upper troposphere due to GCM differences in CP, vertical resolution, and possibly ozone specification. The maximum standard deviation also is larger in emissions scenarios with larger greenhouse gas increases, reaching 1.03 K in SRESB1, 1.35 K in SRESA1B, 1.72 K in SRESA2. This increased spread with increasing greenhouse gas concentrations is likely due to the fact that each GCM has a somewhat different response to increased greenhouse gases, depending on individual physical parameterization schemes, horizontal and vertical

resolution, and other model characteristics. Therefore, larger spread would be anticipated with increasing greenhouse gas perturbations.

Although considerable spread exists among ensemble members, when simply considering the relationship between increases in SST and maximum tropospheric warming a strong relationship emerges (Fig. 4.5). Slightly over 90% of the variance in maximum tropospheric warming is explained by the projected SST increase, verifying the previously described physical linkage (at least in the GCMs) between surface temperature and tropospheric lapse rate changes in the tropics, which is likely caused by convection. Despite the generally good agreement, there are indeed GCMs which have a relationship between projected SST increase and maximum tropospheric warming that deviate from the mean relationship, as indicated by the individual data points that are farthest away from the linear trend line in Fig. 4.5.

4.1.2 Environmental moisture

Ensemble mean projected relative humidity changes are generally small (< 3%) in the lower troposphere (consistent with previous studies, e.g., Held and Soden 2006), where most tropospheric water vapor is located (Fig. 4.7). There is little difference in the projected relative humidity change among the emissions scenarios, although generally the projected increase is largest in SRESB1 and smallest in SRESA2. In the stratosphere large increases in relative humidity are projected (up to ~20%), due in large part to projected cooling as opposed to an absolute change in water vapor content (shown subsequently). These small changes in tropospheric relative humidity, combined with the previously shown temperature increases lead to tropospheric moistening (in an absolute sense) that is maximized near the surface and decreases with height (Fig. 4.8). Maximum moistening in the SRESA2 scenario ($\sim 3.7 \text{ g kg}^{-1}$) is more than double that in the SRESB1 scenario ($\sim 1.8 \text{ g kg}^{-1}$) owing to the larger temperature increase and the nonlinear relationship between temperature and saturation mixing ratio. Maximum moistening in SRESA1B falls in-between these two

extremes, reaching a maximum of $\sim 2.8 \text{ g kg}^{-1}$. Again, considerable spread within each scenario is evident (e.g., Figures 4.9 – 4.10), although in this case the largest uncertainty is near the surface where the largest increases in water vapor are located. The GCM variability increases with increasing greenhouse gas concentrations, consistent with the larger spread in temperature projections as previously shown. Considering all 39 different GCM runs, it is evident that there is a strong relationship between the projected SST increase and the maximum tropospheric moistening (Fig. 4.11). Specifically, the projected SST increase explains more than 90% of the variance in maximum tropospheric moistening. Physically, this is due to the fact that with quasi-constant future relative humidity larger increases in near-surface temperature lead to larger increases in moisture. The projected changes in moisture play a critical role in determining increases in future TC rainfall, as even with similar surface convergence and upward velocity an increase in atmospheric moisture will lead to increased vertical moisture transport and subsequently increased precipitation. The role of tropospheric moistening in future TC rainfall increases will be described in subsequent sections.

4.1.3 Large-scale conditions in sensitivity experiments

As previously described, sensitivity experiments were performed with the goal of isolating the impact of tropospheric stabilization and stratospheric cooling on future TC intensity and structure. Briefly, the large-scale conditions specified for these experiments will be summarized next, along with hypotheses regarding the impact of the large-scale changes on simulated TC intensity.

Projected temperature and moisture changes for the sensitivity experiments were described in chapter 2, and are presented visually here (Figs. 4.12, and 4.13). As a reminder, the least- and most-stable experiments are GCM based, utilizing projected changes from the GCMs with the SRESA1B scenario that estimate the smallest and largest change in tropospheric stabilization, while the no-stable and no-strat simulations utilize projected

changes that are more idealized in design. Pronounced differences in the tropospheric temperature changes are evident (Fig. 4.12), with the least-stable and most-stable projected changes bracketing the SRESA1B ensemble mean, with the no-stable projection (by design) having no tropospheric stabilization. Large differences exist in the value of maximum tropospheric warming, ranging from 2.26 K in no-stable, 3.67 in least-stable, 5.49 in SRESA1B, and 7.38 in most-stable. The no-stable and least-stable profiles are nearly identical below 500 hPa, although the upper-tropospheric warming is ~1.4 K larger in least-stable. There is also a notable difference in the pressure level of maximum tropospheric warming, with this level occurring at 300 hPa in least-stable, 200-hPa in SRESA1B, and 150-hPa in most-stable. Focusing on SSTs, projected SST increase in the least-stable run is ~1.4 K, which is consistent with the reduced tropospheric stabilization. The SST increase in the most-stable experiment the increase is ~2.2 K, which is nearly identical to that found in the other sensitivity experiments (~2.26 K). Based upon the physical linkage between SST and tropospheric stability it would have been anticipated that the SST increase in this projection would have been larger than from the ensemble mean. The SRESA1B ensemble mean SST increase is used in the no-stable and no-strat-cool experiments. Tropospheric moistening follows the expected pattern based on the near-constant relative humidity, with the least- and most-stable projections again bracketing the SRESA1B ensemble mean. Maximum moistening ranges from 1.59 g kg⁻¹ in no-stable to 2.96 g kg⁻¹ in most-stable. The no-stable and no-strat-cool experiments utilized projected moisture changes from the SRESA1B ensemble mean. Therefore, the no-stable experiment does have increased tropospheric relative humidity relative to SRESA1B (above 1000-hPa) as it combines the same mixing ratio increase but with reduced increases in saturation mixing ratio values above 1000-hPa due to the reduced tropospheric warming.

Overall, based on the results of Shen et al. (2000) and other physical principles, simulated TC intensity may be altered by changes in the inflow and outflow temperatures due to tropospheric warming, and also due to differences in moisture content and rainfall. It is anticipated that the no-stable simulation likely will be the most intense, by virtue of the fact that there is no tropospheric stabilization present to offset the intensity increase due to the

SST warming (i.e. inflow will be warmer while outflow temperature may not be altered). Relative to the SRESA1B ensemble, maximum intensity in the least- and most-stable experiments will be altered by changes in both the inflow and outflow temperature. The least-stable simulation should feature cooler inflow (owing to reduced SST increase) and cooler outflow (owing to reduced tropospheric stabilization) than the SRESA1B simulation, which will offset one another and potentially lead to a comparable intensity. The most-stable simulation should feature a similar inflow temperature (owing to the similar increase in SST) and much warmer outflow (owing to the large tropospheric stabilization) than the SRESA1B simulation, leading to reduced maximum intensity. It is unclear, physically, if changes in stratospheric temperature will have any impact on TC intensity. It is possible that the most intense TCs may have outflow that penetrates to the lower regions of the stratosphere; therefore, a projected cooling of the stratosphere may lead to more intense TCs since the outflow would thus be able to extend higher. This possibility will be tested in these model simulations, with no obvious hypothesis in mind.

4.1.4 Freezing level and tropopause height

Changes in the thermal structure of the tropospheric environment may impact the TC secondary circulation, although to our knowledge previous work has not investigated this possibility in detail. Dynamically, two aspects of the thermal structure that impacts TC structure are the height of the freezing level and the tropopause (Fig. 4.14). These graphics are computed at the initialization time, and include the idealized warm core vortex, responsible for the increased height of the freezing level and tropopause (to a lesser extent) near the TC center. Relative to the control, the outer core freezing level increases by ~500 m in the least-stable, no-stable, and SRESB1 simulations, ~750 m in SRESA1B, and ~1000 m in most-stable and SRESA2. Increases in the height of the tropopause (identified utilizing the lapse-rate specification of Hoerling et al. 1991) are slightly less than that of the freezing level, reaching ~250-m in least-stable, no-stable, and SRESB1, 500-m in SRESA1B, 750-m in SRESA2, and 800-m in most-stable. Overall, the increase in height of both of these levels

should serve to increase the height of the TC secondary circulation, and allow outflow to reach to a higher altitude in the future climate simulations. Although not analyzed here, increases in the height of the freezing level and subsequently the mid-level vortex have been shown to increase TC vulnerability to wind shear (e.g., Nolan and Rappin 2008).

4.2 TC Intensity; thermodynamic efficiency and dynamical changes

In the following sections, simulated changes in TC intensity will be discussed. Maximum intensity was determined by computing the minimum central pressure (hereafter MCP) found in model output fields for each simulation. Hereafter, an “increase in intensity” means that the future simulation is more intense than the respective control simulation. Further analysis indicated that the results were not sensitive to any sort of time-averaging, as in general the simulated TCs reach a quasi-steady maximum intensity towards the end of the integration periods. These intensity changes will be analyzed in the context of changes in the thermodynamic efficiency (inflow and outflow temperature) and also dynamical influences (increased rainfall, latent heating and PV production).

4.2.1 Simulations with 2-km grid spacing

4.2.1.1 TC intensity

Future TC simulations employing the ensemble mean projected changes from each emissions scenario surpassed the control simulation intensity (Table 4.2, Fig. 4.15). The MCP timeseries (Fig. 4.14) demonstrates that during the first ~48 hours of the simulations MCP values are fairly close. Between hours 48 and 96 the intensification rate in the control simulation is slower than in the future simulations, which all generally intensify at a similar rate. Differences in the MCP in the future simulations are not distinctly evident until after simulation hour 168. The simulation-length MCP values (Table 4.2) demonstrate that the intensity increase in the SRESA1B and SRESB1 future simulations is similar (~10 – 11 hPa),

while the increase is somewhat larger in SRESA2 (17 hPa). These intensity increases are comparable to previous studies, including Knutson and Tuleya (2004), who found an average percentage increase in MCP deficit of 14% in future climate simulations. The MPI estimates, as determined using the previously described subroutine written by Prof. K. Emanuel, are also shown in Table 4.2. Overall, the MPI estimates are weaker than the simulations, and the percentage increases in intensity in the future simulations are also underestimated.

Simulations with the MYJ parameterization scheme tend to exceed the MPI, while those with YSU are weaker, consistent with the findings of Hill and Lackmann (2009). The inconsistency between the MPI estimates and the simulations could be due to a number of factors, including several tunable parameters in the MPI subroutine. Interestingly, the MPI subroutine produces estimates of future TC intensity that are nearly identical for the different emissions scenarios. Evidently, the subroutine calculates a cancellation between the differences in SST warming and increased tropospheric stabilization, leading to the similarity in the future estimates. Increases in future TC rainfall could account for the inconsistency between MPI estimates and simulated intensity increases.

Simulation results from the sensitivity experiments are provided in a timeseries plot (Fig. 4.16) and are summarized in a table (Table 4.3). Focusing on the timeseries plot, the most-stable experiment is generally weakest throughout the simulation period. The least-stable, no-strat-cool, and SRESA1B ensemble simulations generally have similar intensity through the simulation period, although the least-stable simulation is slightly weaker than the other two. The no-stable experiment is the most intense throughout the simulation period, and features an initial intensification that is more rapid than in the other simulations.

Focusing on the specific maximum intensity values, it is evident that the least- and most-stable experiments are both slightly weaker than the SRESA1B ensemble (Table 4.3). The no-stable experiment is considerably more intense; the intensity increase (relative to the control) is more than double that in the SRESA1B ensemble. This result is consistent with Shen et al. (2000), who found that realistic values of tropospheric stabilization offset the increase in intensity due to SST warming alone by roughly half. The simulation results indicate that stratospheric cooling had little impact on simulated TC intensity.

4.2.1.2 Thermodynamic efficiency

Next, in order to understand what role the large-scale environmental changes played in altering TC intensity, the inflow and outflow temperatures in the future simulations will be examined. A qualitative depiction of the changes in temperature and the TC secondary circulation is provided (Figs. 4.17 – 4.19), which features temperature changes (relative to the control) which are shaded, future TC radial flow (black contours), and the control simulation radial flow (red contour). Focusing first on the general patterns, it is evident that the simulations feature low-level radial inflow and upper-level radial outflow, a characteristic of the TC secondary circulation (Fig. 4.17). The tropospheric warming (relative to the control) that was initialized in general remains, although it is no longer horizontally uniform as differences in the TC structure also play a role in influencing the overall temperature pattern. Interestingly, the no-stable simulation which was initialized with constant tropospheric warming features warming that increases with height by the end of the simulation period; this is likely due to the fact that the convection and vertical transport of heat has reestablished to some extent the most adiabatic adjustment pattern. Near the TC center, much of the temperature difference is due to differences in the TC intensity and eye temperature structure. Overall, it is immediately evident that in the future simulations both the radial inflow and outflow are occurring at warmer temperatures than in the control simulation, and as previously described, the warmer inflow and warmer outflow have opposite impacts on the TC intensity. In a general sense, the changes in future TC intensity are consistent with the temperature change patterns. The no-stable simulation was the most intense, and this can be explained by the fact that the SST increase in this simulation was the same as in SRESA1B, but it is evident that there is less upper tropospheric warming. The least-stable simulation has tropospheric temperature increases that appear comparable with those found in SRESB1, leading to comparable maximum intensity. The most-stable simulation features upper tropospheric warming that is similar to that in SRESA2 but lower tropospheric warming that is less, leading to the reduced intensity.

A quantitative analysis is provided in Table 4.4, which features the changes in SST, mass weighted inflow and outflow temperature, and thermodynamic efficiency in the different simulations. Methods for computation of the mass weighted values were previously described in chapter 2. First focusing on changes in the inflow, it is evident that increases in mass weighted inflow temperature are $\sim 5 - 25\%$ larger than the projected increase in SST (Table 4.4), with this percentage difference increasing with increasing SST. This increased inflow temperature is visually depicted in Fig. 4.18, as the inward flow occurs at warmer temperatures in the future simulations. Also evident in Fig. 4.17 is that the depth of the inflow layer is relatively constant in the future simulations with the exception of the no-stable experiment, which features inflow that is up to 600-m deeper than in the control (based upon the vertical extent of the 5 m s^{-1} contour). This increased depth actually leads to an increase in the mass-weighted inflow temperature that is somewhat smaller than it otherwise would be if the depth had not increased.

Next, changes in outflow temperature will be considered. Future simulations feature an increase in the altitude of the outflow layer, as indicated by a comparison of the 5 m s^{-1} contours in the control and future simulations (Fig. 4.19). In future ensemble mean simulations, increases in the maximum altitude of the 5 m s^{-1} contour range between ~ 500 m in SRESB1 to ~ 1 km in SRESA1B and SRESA2. In the sensitivity experiments, increases range between ~ 500 m in most-stable, ~ 1 km in least-stable, and ~ 1.5 km in no-stable. Despite the fact that the inflow increases in height, it generally occurs at warmer temperatures than in the control. The height increases are roughly comparable to the increase in the height of the freezing level and the tropopause, which will be discussed in subsequent sections.

Quantitatively, focusing first on the future simulations with ensemble mean projected climate change, outflow warming is 0.4 K in SRESB1, 1.2 K in SRESA1B, and 1.8 in SRESA2. These increases are much less than the temperature change at the future outflow level indicated in Figs. 4.17 – 4.19 as the increase in height of the outflow does offset somewhat the increase in temperature that would occur if the outflow remained at the same

level. As anticipated, the outflow warms more in GCM projections forced with higher greenhouse gas concentrations, due to the higher amount of tropospheric stabilization. Despite the warmer outflow, the thermodynamic efficiency multiplied by the SST (a measure of how much energy the TC can extract from the ocean) still increases in the future runs based on the ensemble data, leading to increased intensity.

Focusing specifically on the sensitivity experiments, it is again evident that tropospheric stabilization leads to warmer outflow. The least-stable simulation features colder outflow than the control, and this, combined with a modest increase in the inflow temperature, leads to maximum intensity that is comparable to SRESA1B, despite having a SST increase that is \sim 0.75 K less than SRESA1B. The most-stable simulation features inflow that is much warmer than SRESA1B (2.73 K warmer) and a similar inflow temperature, due to a comparable increase in SST. These changes combined lead to the lowest thermodynamic efficiency of all the future simulations, and subsequently the lowest intensity. The no-stable experiment was attained the highest intensity, by a large margin. It is evident that this simulation featured inflow that warmed by an amount similar to that in the SRESA1B ensemble, but in conjunction with this the lack of tropospheric stabilization allowed for the outflow temperature to remain nearly as cold as in the control (only 0.10 C warmer). This combination of warmer inflow and almost identical outflow leads to an increase in efficiency that is larger than in the other simulations, consistent with the greater intensity. The difference in efficiency between the no-stable experiment and the SRESA2 ensemble is not terribly large, which does beg the question of why the no-stable experiment was able to get so much more intense.

Finally, the impact of stratospheric cooling on simulated TC intensity was quite minor, and based upon the inflow and outflow temperatures it is evident that the thermodynamic efficiency multiplied by SST is comparable in these simulations. The outflow is not colder in the no-strat-cool simulation (in fact it is \sim 0.34 C warmer), so evidently the TC outflow does not appear to respond to changes in stratospheric temperature.

Although it is useful to analyze single mass-flux weighted numbers for inflow and outflow, further perspective can be gained by analyzing the outward mass flux as a function of temperature (Figs. 4.20, 4.21). In these analyses, the outward mass flux has been binned by temperature, with a bin width of 5°C . Values displayed are the fraction of the total outward mass flux between simulation hours 216 and 240 that occurred within that specific temperature bin. In these graphics, bin midpoints varied between -72.5 and -22.5°C in order to display the full distribution, although the main focus will be on the colder outflow temperatures (midpoint temperatures of -52.5°C or colder). Focusing on the control simulation and the future simulations with ensemble mean projected changes, it is evident that the coldest outflow (bin midpoints of -67.5 and -62.5°C) constitutes a smaller fraction of the total outflow in the future runs than in the control, and is less in future runs with more tropospheric stabilization (Fig. 4.20). This is consistent with the mass flux weighted outflow temperature and also the cross sections of temperature change and radial flow that were previously shown.

The sensitivity experiments (Fig. 4.21) further elucidate the impact of tropospheric stabilization on the outflow temperature distribution. The most-stable simulation has an outflow pattern that is significantly different than in the others, with little outflow occurring in the cold bins, and the largest outflow occurring in the -47.5 and -42.5°C bins. The least-stable and no-stable simulations, by contrast, have the largest outflow occurring in the -57.5°C bin, and a large fraction of the total outward mass flux at temperatures colder than -57.5°C . Overall, the simulations indicate that the effect of tropospheric stabilization is to increase the mass-weighted outflow temperature, shifting the outflow temperature distribution towards warmer temperatures. It is this shift towards warmer outflow in the future simulations that partially offsets the intensity increase that would occur to the SST warming alone.

4.2.1.3 Dynamical influences: rainfall and PV

As previously shown, future projections indicate an increase in tropospheric water vapor, due to increasing temperature combined with quasi-constant relative humidity. Due to this increase in water vapor, it is possible that future TCs will feature heavier rainfall, which could lead to an increased freshwater flooding threat. This increase in rainfall could also potentially impact TC intensity, through increased latent heat release and potential vorticity production. Fig. 4.22 displays the rainfall rate, averaged between simulation hours 216 and 240, in the control and in future simulations with ensemble mean projected changes. Although difficult to analyze quantitatively, this figure is included in order to provide a better spatial sense of rain rate differences. In each simulation, there is a well-defined symmetric eyewall maximum in rainfall, surrounded by a region of enhanced outer-core rainfall, and then the rainband region with generally lower precipitation rates. In general, maximum eyewall rain rates are higher in the future simulations with the exception of the SRESA2 simulation, which features a double maximum in precipitation that is likely due to changes in structure during the time averaging period. Time averaging tends to smear the heaviest rainfall rates, and as such these time-averages are not designed to investigate changes in maximum precipitation rate. The no-stable simulation (Fig. 4.23) features a wider region of heavy eyewall rain rates, perhaps due to small changes in size during the time averaging period, and also a broader region of heavier rainfall just outside of the eyewall. A comparison of the least-stable and most-stable simulations indicates a clear reduction in both the areal-coverage of heavy rainfall and also in the maximum eyewall rain rate in most-stable.

Previous studies (e.g., Knutson and Tuleya 2004) have typically analyzed area-averages near the TC center in order to assess future changes in TC rainfall. Increases in TC rainfall averaged within 250-km of the center during the last 24-h of the simulations are shown in Fig. 4.24. Immediately evident is the large increase in the no-stable experiment, but first let's consider the increase in the future runs with ensemble mean projected changes. The increase in these runs varies between $\sim 7 - 26\%$, with the increases being proportional to

the previously described increases in tropospheric water vapor. In order to further elucidate the role of the moisture increase in the rainfall increase, 250-km area averages of vertical velocity, mixing ratio, and the product of vertical velocity and mixing ratio (hereafter referred to as vertical moisture transport) were computed at the 700-hPa level (Fig. 4.25). For each simulation, the percentage increase in vertical moisture transport closely matches the percentage increase in precipitation, as would be expected. For the SRESA1B and SRESA2 simulations it is evident that the increase in mixing ratio is responsible for the calculated increase in vertical moisture transport, and subsequently the increase in precipitation. In other words, with the same amount of vertical motion the TC is able to produce more precipitation, since the troposphere is more moist. For the SRESB1 simulation the percentage increase in precipitation is less than the percentage increase in moisture, because the average vertical velocity is slightly weaker than in the control. Overall, however, it is evident that the increase in precipitation in the future simulations is closely related to the increase in tropospheric water vapor.

Focusing next on the sensitivity experiments, the increase in precipitation in the no-stable simulation is an astounding 95%. The increase in vertical moisture transport closely matches this value (Fig. 4.25), and the analysis reveals an increase in upward motion is largely responsible for this, accounting for ~75% of the increase. In the absence of the tropospheric stabilization and with a much more intense TC, the secondary circulation increases in strength considerably, leading to the large increase in precipitation. The impact of stabilization can further be seen by focusing on the least- and moist-stable experiments. The least-stable simulation features an increase in precipitation of ~20%, which can be tied to an increase in both atmospheric moisture and vertical velocity. The most-stable simulation features the least increase in precipitation (~2%), and this is due to reduced vertical velocity that leads to less vertical moisture transport despite the larger tropospheric water vapor content. Overall, changes in vertical velocity and tropospheric water vapor both impact future precipitation changes. In the future simulations with ensemble mean projected climate change, the change in tropospheric water vapor tends to be the dominant factor. When considering future climate changes from individual GCMs that depart considerably from the

ensemble mean, however, the impact of changes in vertical velocity play a large role, illustrating the impact of tropospheric stabilization on future rainfall changes.

Although analysis of the time or area averaged rainfall totals are useful, the averaging tends to smear the highest rates. In order to further investigate the change in future TC rainfall, Fig. 4.26 provides a depiction of the number of grid cells with certain rain rates throughout the simulation period. In the future simulation graphics, values from the control simulation are shown for reference. The heaviest rainfall rates are larger in the future simulations, reaching ~ 3 in hr^{-1} in the control simulation, ~ 4 in hr^{-1} in SRESA1B and SRESB1 (albeit for a brief time), and up to 4.5 in hr^{-1} in the SRESA2 simulation. These highest rain rates are found in the eyewall, where moisture convergence is maximized. In order to compare the rainfall rate distributions in the future simulations to the control, compare the shading with the contoured value; e.g., a comparison between the extent of the 0.01 contour from the control simulation and the blue shading in the future simulations demonstrates an increase in the frequency of rainfall rates exceeding 3 in hr^{-1} in the future simulations. The increased frequency of these heavy rain rates is largest (smallest) in the future simulation with the largest (smallest) increase in water vapor content, SRESA2 (SRESB1). Focusing on lower rain rates ($1 - 2$ in hr^{-1}) it is evident that there is a small increase in frequency in the future simulations, although in general the distribution of lower rainfall rates appears to be similar.

Analysis of rainfall rates in the sensitivity experiments is provided in Fig. 4.27, which also shows the SRESA1B simulation for comparison. The no-stable experiment, which had the largest increase in future rainfall (95%) features an increased frequency of rainfall rates > 3 in hr^{-1} , consistent with the other future simulations. The bulk of the increase in area-averaged rainfall, however, appears tied to a large increase in the frequency of less extreme rainfall rates. For rainfall rates between 1 and 2 in hr^{-1} , there is a large increased frequency in this run; this increase in the “moderate” rainfall rates is consistent with the time-averaged rainfall distribution (Fig. 4.23), which featured much heavier rainfall just outside the eyewall maximum than in the other simulations. Evidently, the large increase in precipitation in this

run is more due to an increase in the spatial coverage of heavy rainfall rates than an increase in the heaviest rain rates. Focusing next on the least- and most-stable experiments, it is again evident that these runs feature an increase in the frequency of rainfall rates exceeding 3 in hr^{-1} . In the least-stable simulation there is less of an increase in the rainfall rates exceeding 3 in hr^{-1} than in SRESA1B, likely due to the fact that the temperatures throughout much of the troposphere are cooler, thus reducing the saturation mixing ratio. In the least-stable simulation there is little change in the frequency of “moderate” rainfall, and this, combined the moderate increase in heavy rain-rates leads to an increase in area-averaged precipitation that is less than from SRESA1B. The most-stable simulation featured the smallest increase in area averaged rainfall rate. Despite possessing an increase in the rain rates exceeding 3 in hr^{-1} that is comparable to in SRESA1B, it is evident that there is a decrease in the “moderate” rain rates; this can be seen in Fig. 4.27, and is also demonstrated in Fig. 4.23 by the reduced spatial area covered by moderate rain rates. Overall, the reduced coverage of “moderate” rainfall in the most-stable simulation leads to only a modest (2%) increase in area-averaged rainfall despite the increase in the heaviest precipitation rates.

Increased precipitation in the future simulations should lead to an increase in diabatic PV production and subsequently a stronger interior diabatic PV maximum; the PV structure of the simulated TCs is now examined for this potential change (Figs. 4.28 – 4.29). Relative to the control simulation, there is an increase in the strength of the average PV structure; maximum lower tropospheric (below 2-km) average PV values are $\sim 20 - 25$ PVU in the control and $\sim 30 - 35$ PVU in the future ensemble simulations. Overall, the previously described changes in future rainfall appear consistent with the change in PV structure, with the largest PV values being found in SRESA2, the lowest in SRESB1, and SRESA1B being in the middle. Focusing on the sensitivity experiments (Fig. 4.29), maximum lower tropospheric PV reaches values of $\sim 25 - 30$ PVU, which is larger than in the control but not larger than in SRESA1B. The averaging and also changes in TC structure during the averaging period tends to smear the maximum values. The no-stable simulation featured a very large increase in area-averaged rainfall within 250-km of the TC center; although the lower tropospheric maximum PV has not increased substantially relative the control, it is

evident that these simulations feature a wider PV tower (Fig. 4.29, upper right panel). The most-stable simulation, which featured little change in area-averaged rainfall, features a narrower PV structure than was found in the control, consistent with the reduction in rainfall and the spatial coverage of rainfall as previously described. Focusing on the potential vorticity in a more quantitative manner, it is evident that the future increases in volume-averaged PV and rainfall are highly correlated with one another (Fig. 4.30 top left, top right panels). The no-stable simulations are quite different from the others, but even when they are not considered the strong correlation remains. The volume-averaged PV correlates strongly with area-averaged MCP (4.30 bottom left, bottom right panels), verifying that the increase in rainfall, diabatic PV production and PV in future TCs plays a role in increasing intensity, along with the previously described increase in thermodynamic efficiency.

4.2.2 Simulations with 6-km grid spacing

4.2.2.1 TC intensity

As described in chapter 2, a larger number of simulations with 6-km grid spacing were performed, which utilized projected changes from individual GCMs. In order to examine the future intensity change from the large number of simulations, frequency diagrams with the increase in central pressure deficit (%; relative to the ambient environment) placed into bins will next be discussed. To facilitate analysis, frequency diagrams for simulations run with projected changes from each emissions scenario (Figs. 4.31 – 4.33) along with a diagram for all future simulations (Fig. 4.34) are provided. The SRESA1B and SRESA2 frequency diagrams illustrate that the largest number of simulations indicate increases in central pressure deficit of 9-12%, consistent with the average of 11% for each of these scenarios. There is considerable spread around this mean value, however, ranging from 2 simulations that indicate weakening (SRESA2) to several simulations which indicate increases in central pressure deficit of greater than 18%. The SRESB1 emissions scenario has a smaller average increase in central pressure deficit (8%), with frequency

maximized in the 3 – 6% frequency bin. In total, 3 future simulations indicated a reduction in future TC intensity. Two of the three simulations featured climate change values projected using the same GCM, the IPSL model. This GCM had a tendency to project large values of upper tropospheric warming (relative to its SST increase), and evidently the increase in inflow temperature was not able to compensate for the increase in outflow temperature in these simulations, leading to the reduced intensity.

The increase in MCP deficit in the 6-km simulations tends to be slightly less than that found with the 2-km simulations; e.g., increases of 12, 19, and 11% were found with 2-km grid spacing, while average increases of 11, 11, and 8% were found with 6-km grid spacing, for the SRESA1B, SRESA2, and SRESB1 emissions scenarios, respectively. Simulations with 6-km grid spacing were overall less intense than with 2-km, consistent with previous studies that analyzed the impact of model resolution on simulated TC intensity (e.g., Hill and Lackmann 2009; Fierro et al. 2009; Gentry and Lackmann 2010). Given the trends found here, it is possible that further increases in model resolution may lead to larger estimates of future intensity increase. The relatively small number of simulations with 2-km grid spacing, however, leads to some uncertainty in the projection from these high-resolution simulations. Utilizing the large-scale environments created from individual GCM projections of climate change, the MPI subroutine produced increases in central pressure deficit of 6, 7, and 5%, when averaged over the SRESA1B, SRESA2, and SRESB1 emissions scenarios, respectively. These percentage increases are again smaller than those that were found in the model simulations, and again suggest that increases in future rainfall and associated dynamical changes play a role in the increased future TC intensity.

4.2.2.2 Thermodynamic efficiency

There is some discrepancy between the MPI subroutine estimates of maximum intensity and those found in the TC simulations (Fig. 4.35). In this figure, the simulations with MYJ and YSU parameterization schemes are considered separately, as systematic

differences in simulated intensity were found. Most notably, it is immediately evident that the MYJ simulations tend to exceed the MPI, while the YSU simulations tend to not reach it. This behavior has been noted previously, and was described in Hill and Lackmann (2009) and attributed to differences in the moisture exchange coefficient. Considering simulations performed with each parameterization scheme separately, the data indicates that ~70% of the variance in the MCP values of the MYJ simulations is explained by the differences in MPI, while only ~50% is explained in YSU. It is possible that tunable parameters in the MPI subroutine have been adjusted to closely match observed data, and the use of future environments leads to environmental values which are outside of the range that the tuning has been customized within. Regardless, the discontinuity between the MPI estimates and the simulation results suggests that simple examination of MPI changes from GCM future projections may not provide accurate estimates of the impact of climate change on maximum TC intensity.

Next, linkages between the future simulated TC intensity changes and the projected changes in the large-scale environments will be discussed. Mass-weighted inflow and outflow temperatures were calculated for each simulation with 6-km grid spacing, with averaging taking place during the last 24-h of each simulation. These inflow and outflow temperatures were then used to calculate the average thermodynamic efficiency; the simulated MCP versus the thermodynamic efficiency is shown in Fig. 4.36. There is a high degree of correlation between these two quantities, as would be anticipated based upon MPI theory. There is distinct clustering that exists; this is due to the fact that the TCs simulated with the YSU parameterization scheme were weaker, and tended to have a lower thermodynamic efficiency than those simulated with MYJ. Specifically, TCs simulated with the YSU parameterization scheme consistently had a warmer outflow temperature than those simulated with MYJ. The total energy that a TC can extract from the ocean is proportional to the product of the thermodynamic efficiency and the SST; this quantity is again highly correlated with the simulated MCP (Fig. 4.36, right panel).

As previously described, the future simulations had a tendency to exhibit warmer inflow, consistent with the increased SST, along with warmer outflow, with the change in outflow temperature being related to the projected tropospheric stabilization. Figure 4.37 demonstrates the relationship between the SST and the inflow temperature; ~90% of the variability in the increase in inflow temperature can be explained by the increase in SST. In other words, the larger the projected increase in SST, the larger the increase in simulated inflow temperature. This close correlation was anticipated based upon both physical arguments and also the 2-km simulations.

Next focusing on the outflow temperature, it is evident that there is little correlation between the change in outflow temperature and the projected SST increase (Fig. 4.38, left panel). Specifically, the SST increase explains ~40% of the variability in the outflow temperature. Although the relationship is weak, there is a tendency for increased outflow temperature with increasing SST, consistent with the argument that warming of the TC outflow reduces the intensification that would occur due to SST increase alone. The correlation between the tropospheric stabilization and the change in outflow temperature is somewhat higher, explaining ~50% of the variability associated with the change in outflow temperature (Fig. 4.38, right panel). As expected and previously discussed, tropospheric stabilization leads to warmer outflow. There are several outliers, where the increase in tropospheric stabilization in the large-scale environment does not appear to explain the change in outflow temperature. Therefore, it is evident that other factors impact the outflow temperature as well, including the actual TC intensity, which is not entirely regulated by the change in tropospheric stabilization.

4.2.2.3 Dynamical influences: rainfall

Detailed analysis of simulations with 6-km grid spacing revealed that TC structure is not as accurately simulated as with the 2-km grid spacing; specifically, these simulations are not able to produce realistic spiral bands, and the inner-core is also not as well represented.

6-km likely represents the lower-end of the resolution required in order to omit cumulus parameterization for simulating TCs (e.g., Gentry and Lackmann 2010). With these caveats in mind, next changes in future TC rainfall in the 6-km simulations will be analyzed, although deficiencies in the representation of the TC inner-core and rainband structure suggest that these results are not as robust as those found with 2-km grid spacing.

Similar to Fig. 4.31, Fig. 4.39 is a frequency diagram displaying increases in the 0–250 km area-averaged rain rate in the 6-km simulations. Overall, there is a considerable amount of spread in the simulations, with more than 25% of the simulations indicating a future reduction in rainfall, and ~6% indicating future increases of 25 – 30%. The overall average projected increase is 7%, which is less than was found with the 2-km simulations. There is, however, substantial variability associated with the averaging distance chosen. Within 100-km of the TC center, the average increase in future rainfall is 21%, (Fig. 4.40), which is similar to that found in simulations with 2-km grid spacing. Further analysis revealed that the majority of simulations with 6-km grid spacing feature an increase in eyewall rainfall, but a decrease in rainfall outside of the inner-core. The increases in eyewall rainfall and diabatic PV production may play a role in increasing future TC intensity, as previously described.

This reduction in rainfall outside of the eyewall may be due to the increase in environmental static stability, owing to tropospheric lapse rate stabilization. This change in rainfall distribution also has important implications for TC size; as previously described, it is hypothesized that outer-core rainfall plays a role in determining TC size. The future TCs in general are smaller than in the control experiments; this result will be discussed in a subsequent section.

4.3 Structural analysis (2-km simulations)

Next, additional changes in TC structure in the 2-km simulations that have not yet been considered will be investigated. Time-averaged quantities will be presented in order to

dampen temporal variability; these averages were computed using hourly output during the last 24 hours of each simulation. Contoured frequency by altitude (CFAD) diagrams will also be utilized in order to assess the distribution of a variable as a function of height. These CFAD diagrams were calculated using all grid cells within 500-km of the TC center, and again were averaged over the last 24 hours of each simulation. The advantage of CFAD diagrams over time-averages is changes in TC size do not impact the results, and the maximum and minimum values are not smeared as occurs in the time averaging. Finally, some time-averaged cross sections will also be analyzed.

4.3.1 Vertical velocity

Fig. 4.41 is a CFAD diagram of vertical velocity for the control simulation and future ensemble simulations. The shaded quantity in these graphics represents the percentage of grid points at that height that possesses the vertical velocity specified on the x-axis. In the future graphics, the 0.01% contour from the control simulation is also indicated, to facilitate comparison. Qualitatively, the results agree fairly well with the previous observational study of Black et al. (1996), and recent high-resolution modeling studies of observed TCs (e.g., Rogers et al. 2007; Fierro et al. 2009; Gentry and Lackmann 2010). The vast majority of grid cells possess vertical velocity values that are less than 1 m s^{-1} (in an absolute sense), as these grid cells are located outside of the eyewall and high precipitation areas. The lower frequency contours represent more interesting regions of the TC, which feature large vertical motions. Each simulation features a qualitatively similar distribution of vertical motion, with updrafts that peak at $\sim 4 \text{ km}$ and downdrafts that peak at $\sim 3\text{-km}$. Focusing on upward motion, it is evident that there are some systematic differences in the future simulations than in the control. While maximum updraft speeds appear similar, the altitude of maximum updrafts is $\sim 1\text{-km}$ higher in the future simulations. The increase in height of maximum updrafts in future simulations is roughly equivalent to the increase in height of the freezing level in the eyewall. Updraft velocities are generally larger in the future simulations than in the control

from just above the altitude of maximum updrafts through \sim 15-km, consistent with the increased outflow altitude, previously described.

The impact of tropospheric stabilization on the vertical velocity profile is evident in Fig. 4.42, a CFAD diagram of vertical velocity in the SRESA1B run and in the sensitivity experiments. The no-stable experiment features much stronger updrafts and downdrafts than any of the other simulations, consistent with its higher intensity and the area-averaged vertical velocity previously described. Specifically, updrafts reach up to \sim 12.5 m s $^{-1}$, or \sim 2 m s $^{-1}$ higher than in the other simulations. The least-stable simulation features a vertical velocity profile that is quite similar to the control, although the altitude of maximum updrafts is still displaced upward slightly. The most-stable simulation features vertical velocity that is weaker than in the control, consistent with its weaker intensity. The altitude of maximum updrafts, however, is still higher than in the control simulation, consistent with the increased height of the freezing level. Overall, future simulations tend to feature a profile of vertical velocity values that is displaced upward, consistent with the increase in the height of the freezing level and the tropopause, and leading to an increased depth of the secondary circulation.

4.3.2 Inflow

Changes in the inflow in the future ensemble experiments are demonstrated in Fig. 4.43, a CFAD diagram of radial velocity below 2-km altitude. Qualitatively the simulations feature similar inflow velocity patterns, with a peak in the lowest several hundred meters and decreasing above. The future runs feature stronger maximum inflow than the control, \sim 6 m s $^{-1}$ stronger in SRESA1B and SRESB1, and \sim 2 m s $^{-1}$ stronger in SRESA2. A large increase in inflow velocities is found in the no-stable experiment (Fig. 4.44), consistent with its greater intensity and stronger vertical velocities. Maximum inflow reaches \sim 50 m s $^{-1}$, or \sim 13 m s $^{-1}$ stronger than in the control. The least- and most-stable simulations generally feature

similar maximum inflow velocities to the control, although peak velocity tends to extend slightly higher in the lower troposphere.

4.3.3 Outflow

Previously, time and azimuthally averaged outflow values were analyzed in order to ascertain differences in outflow temperature among the simulations. The averaging obscured any possible differences in maximum outflow strength, which now can be analyzed in further detail with the aid of a CFAD diagram (Fig. 4.45). In general, the future simulations have stronger maximum outflow velocity, with increases of $\sim 4 \text{ m s}^{-1}$ in SRESA1B and SRESA2, and $\sim 3 \text{ m s}^{-1}$ in SRESB1. There is also a distinct shift upward in the outflow pattern, as previously described; increases in the altitude of the maximum outflow of $\sim 1 \text{ km}$ is evident in the future simulations. Focusing on the sensitivity experiments, it is again evident that the secondary circulation is much stronger in the no-stable simulation than in the others; maximum outflow exceeds 40 m s^{-1} , which is $\sim 10 \text{ m s}^{-1}$ stronger than in the control simulation (Fig. 4.46). The least-stable simulation features similar maximum outflow velocity to the control, with the upward shift again evident. The most-stable simulation features weaker outflow than in the control, and also is characterized by a decrease in the altitude of maximum outflow of $\sim 1 - \text{km}$. This is the only future simulation that exhibits a reduction in the altitude of maximum outflow, and this can be attributed to the enhanced upper tropospheric warming and also the reduced intensity.

4.3.4 Eye structure

Hydrostatic pressure in the TC center is related to the layer-average temperature in the overlying air column; thus we now examine time-height diagrams of the eye-temperature anomaly, where the anomaly is computed as the difference in temperature between the TC eye and the original large-scale environment (Figs. 4.47 – 4.48). The TC “eye” here is

defined as those grid cells that are centered within 2 km of the grid point with the lowest smoothed sea level pressure (5 grid points total). This small area does not necessarily encompass the entire TC eye, although results are not highly sensitive to the specified area. In each simulation the eye does not begin warming significantly until after simulation hour 24, consistent with the initial delay in intensification. After 24-h, mid-level warming begins to occur, and as the simulation progresses and the TCs become more intense the upper levels of the troposphere warm significantly as well. Focusing first on the control simulation and the future ensemble runs, it is evident that the maximum eye temperature anomaly is larger in the future simulations, consistent with their higher intensity (Fig. 4.47). The altitude of maximum warming and the maximum altitude of any warming is also slightly higher in the future simulations, consistent with the increased height of the freezing level, the vertical velocity profile, and outflow, as previously described. Focusing on the sensitivity experiments (Fig. 4.48) it is evident that the no-stable simulation features the largest eye temperature anomaly, consistent with it being the most intense simulation. The least-stable simulation has eye temperature anomalies that are generally similar to SRESA1B, and the height of the warm core is clearly reduced in the most-stable simulation. In the most-stable simulation, maximum warming is at \sim 11 km, which is well below that found in the control or SRESA1B simulations. This reduction in the height of the warm core is consistent with the reduced depth of the TC circulation and outflow. In general, the future simulations feature stronger eye subsidence than in the control. The tropopause, identified as the altitude where the temperature decrease becomes less than 2 K km^{-1} , is higher in the future simulations and tends to increase in height during the integration period.

In order to further isolate differences in the TC warm core structure, Fig. 4.49 displays a difference plot of the eye temperature anomaly field; in these graphics, the temperature anomalies from the control simulation are subtracted from that found in the future runs. Above 6-km, the future TC eyes are generally warmer than in the control, with the exception of the most-stable simulation, which will be described in more detail later. The SREA1B and SRESA2 values indicate an increased eye temperature of \sim 5 – 6 K at \sim 14 – 18 km; the warmth is likely due to both an increase in the height of the warm core and an increase in the

strength of the warm core. The SRESB1 simulation features less of an increase in eye temperature, consistent with the reduced depth of the warm core (relative to SRESA1B and SRESA2). The no-stable simulation features eye temperatures that are much warmer than the control, with differences of > 6 K. The least-stable simulation has a pattern than is quite similar to that in SRESB1, consistent with a modest increase in the depth of the warm core. Finally, the most-stable simulation features a warmer eye at $\sim 8 - 12$ km, relative coolness at $\sim 13 - 15$ km, and warmth above 17-km. This structure is consistent with the reduced depth of the warm core in this simulation, which leads to the enhanced warmth near where the warm core is maximized, but reduced warmth farther up as the warm core does not extend as deep. The warmth above 17-km is mainly due to differences in the height of the tropopause, as the eye temperature anomalies relative to the ambient environment are nearly 0 above 17-km in the control and most-stable simulations.

4.4 TC Size

As previously described, we hypothesize that the size of a TC is related to the amount and extent of precipitation occurring outside of the TC core; this hypothesis was tested by using idealized simulations with different relative humidity values, which will be described in chapter 4. There are, however, other environmental factors that may influence the amount of outer-core precipitation. One such factor is environmental stability; we hypothesize that tropospheric stabilization, present in the climate change projections, could potentially lead to a reduction in outer core precipitation, and subsequently a reduction in size. Size differences have been touched upon previously by looking at the precipitation structure; in the following sections, changes in outer-core precipitation and TC size in the future simulations will be further analyzed.

4.4.1 6-km Simulations

Averaged over the last 24-h of each simulation, a reduction the maximum radius of tropical storm force wind is noted in the future simulations with 6-km grid spacing (Fig. 4.50). The reduction in size is larger in the runs with larger tropospheric stabilization, as would be anticipated based upon the hypothesized link between tropospheric stabilization, precipitation, and size. Although the maximum reduction of ~9 km (in the SRESA2 future simulations) may seem small, this corresponds to a reduction in the area covered by tropical storm force wind of ~5%, which could lead to differences in damage potential near the periphery of a TC.

Examination of rainfall, the size of the wind field, and also the surface pressure gradient reveals that at least qualitatively the future simulations feature reduced outer-core precipitation and pressure gradient, and a reduction in the radius of tropical storm force and to a lesser extent hurricane force wind, consistent again with the hypothesized mechanisms (Figs. 4.51 – 4.54). In each future simulation, there is more precipitation near the TC center, but a general reduction in the rainfall outside of the eyewall. The reduction in rainfall is largest in SRESA2 (Fig. 4.52) and smallest in SRESB1 (Fig. 4.54), consistent with the hypothesis that tropospheric stabilization could lead to a reduction in outer-core precipitation and reduced TC size. Consistent with the reduction in precipitation, the reduction in outer-core pressure gradient also appears to scale with the tropospheric stabilization.

4.4.2 2-km simulations

Little difference is noted in the maximum radius of tropical storm force wind in the control and ensemble mean simulations (Fig. 4.54, left panel), although large differences exist among the sensitivity experiments (Fig. 4.54, right panel). Specifically, the maximum radius of tropical storm force wind reaches ~390 – km in the control and future ensemble simulations, and is much larger (~445 km) in the no-stable simulation and much smaller (~320 km) in the most-stable simulation. These differences can partially be attributed to the

large contrast in tropospheric stabilization, which ranges between 0 in the no-stable simulation to \sim 7 K in most-stable, although the large differences in intensity likely also play a role. Again focusing on the physical mechanisms behind the size changes, Figs. 4.55 – 4.60 demonstrate differences in precipitation, pressure gradient, and wind radii between the control and future simulations. The future ensemble simulations (Figs. 4.55 – 4.57) generally feature no clear signal in outer-core rainfall changes, with alternating regions of increased or decreased precipitation. There is also generally little change in the outer-core pressure gradient, and subsequently little difference in the outer wind radii. The no-stable simulations (Fig. 4.58) feature a large increase in outer-core precipitation and pressure gradient, as anticipated based on previous analysis and consistent with specification of no-stabilization and the high-simulated intensity. The least and most-stable simulations further illustrate the role of stabilization; a small reduction in outer-core precipitation is noted in the least-stable simulation, while a large decrease is present in the most-stable simulation. Subsequently, little change in outer-core pressure gradient is found in least-stable, which features a modest reduction in the size of the TC wind field. The wind field is dramatically reduced in size in the most-stable simulation.

4.5 Summary

TC simulations with the WRF model were performed in order to examine the impact of projected climate change on TC intensity and structure. The first set of experiments utilized 2-km grid spacing, and featured a control simulation along with simulations of TCs in large-scale environments consistent with projected climate changes from a 13 GCM ensemble forced with either the SRESA1B, SRESA2, or SRESB1 emissions scenario. A second set of experiments with 2-km grid spacing was also performed to isolate the impact of tropospheric stabilization and stratospheric cooling on TC intensity. These idealized experiments included simulations with the projected changes from the SRESA1B GCM with the least or most tropospheric stabilization, and more highly-idealized experiments featuring no tropospheric stabilization or no stratospheric cooling. Finally, a third set of simulations

with 6-km grid spacing was performed using GCM projected changes from individual GCMs; in this case, a large number (78) of future simulations were performed, with the goal of assessing the uncertainty associated with GCM choice.

Overall, the results indicate a likely increase in future TC intensity. With projected changes from the SRESA1B, SRESA2, and SRESB1 emissions scenarios, simulations with 2-km grid spacing indicated an increase in the central pressure deficit of 12, 19, and 11%, respectively. Averaged over the 13 individual simulations for each scenario, the 6-km grid spacing simulations indicated an increase in central pressure deficit of 11, 11, and 8%, respectively. In general, these results are comparable to similar previous studies (e.g., Knutson et al. 2004; Knutson et al. 2010), who found an average increase in future TC pressure deficit of 14%. Projected future intensity increase was found to be less using a subroutine designed to provide estimates of MPI than was found in the model simulations, indicating that increases in thermodynamic efficiency alone may not fully account for simulated future intensity increases.

The increase in future inflow temperature was shown to be highly correlated with SST warming, in all experiments, as was anticipated. The relationship between outflow temperature and SST warming is less robust but still present, with a tendency for progressively warmer outflow as the SST (and subsequently tropospheric stabilization) increases. An emphasis was placed on analyzing the impact of tropospheric stabilization on projected intensity changes, as projections of upper tropospheric warming and tropospheric stabilization are less certain than that of SST changes. The no-stable experiment, designed to isolate the impact of tropospheric stabilization, indicated that tropospheric stabilization reduces the increase in future TC intensity by ~50% over what it would be based only on increased SST. Simulations with the least and most tropospheric stabilization reached a fairly similar maximum intensity, with the least-stable simulation featuring colder outflow, but also cooler inflow than in most-stable, leading to a thermodynamic efficiency that was fairly close to the control. Finally, the sensitivity experiments indicated that stratospheric cooling played little role in influencing simulated future TC intensity.

Increases in tropospheric water vapor content generally lead to increased rainfall in future simulations, which could increase the freshwater flooding threat and also plays a role in influencing TC intensity. The increased precipitation was shown to correlate highly with an increase in near-center volume averaged PV, which in turn is highly correlated with increased central pressure deficit. Thus, part of the future intensification is likely due to a dynamical influence, in addition to the aforementioned increase in thermodynamic efficiency.

Future TCs generally featured stronger secondary circulations, with increased inflow and outflow, and vertical velocities. An increase in the height of the secondary circulation was also simulated, consistent with increases in the height of the future freezing level and tropopause.

Although future TCs in general featured heavier eyewall rainfall, a reduction in the outer-core rainfall in all simulations was found. This reduction is hypothesized to be due to increased tropospheric stability in the future climate, associated with lapse rate stabilization. As previously described, a reduction in outer-core rainfall is hypothesized to influence TC size; this linkage was found in the simulations, with a reduction in the radius of tropical storm wind found in simulations with 6-km grid spacing. Little change in the radius of tropical storm force wind was found in future simulations with ensemble mean projected climate changes. A large reduction in the outer-core wind field size was found in the most-stable simulation, illustrating the link between tropospheric stability, rainfall, and TC size.

Table 4.1: Summary of projected changes in SST from the different emissions scenarios.

Emissions Scenario	Mean	Min	Max
SRESB1	1.4	1.0	2.0
SRESA1B	2.2	1.4	2.9
SRESA2	2.7	2.2	3.5

Table 4.2: Summary of simulated maximum intensity in 2-km simulations with ensemble mean projected climate changes, and MPI estimates. For the WRF simulations, the minimum values shown are the average of the minimum values in the MYJ and YSU runs.

Simulation Name	Minimum SLP (hPa)	Decrease in MSLP (hPa) relative to control	Increase in MSLP deficit (%) relative to control	MPI subroutine MSLP	MPI Subroutine increase in MSLP deficit (%) relative to control
Control	919			929	
SRESA1B Ensemble	908	11	12	924	6
SRESA2 Ensemble	902	17	19	924	6
SRESB1 Ensemble	909	10	11	924	6

Table 4.3: Summary of maximum intensity in 2-km simulations and sensitivity experiments.

Simulation Name	Minimum SLP (hPa)	Increase in SLP deficit (%) relative to:	
		Control	SRES A1B Ensemble
Control	919		
SRES A1B Ensemble	908	12	
Least-stable	912	8	-4
Most-stable	914	5	-6
No-stable	893	28	15
No-strat-cooling	908	12	0

Table 4.4: Mass weighted inflow and outflow temperature (C), and relative to control. Thermodynamic efficiency multiplied by SST, and increase relative to control (%).

Simulation Name	SST increase relative to control	Mass weighted inflow temperature (relative to control)	Mass weighted outflow temperature (relative to control)	Thermodynamic efficiency * SST (% increase relative to control)
Control		21.56	-53.48	9.68
SRES A1B Ensemble	2.21	23.99 (+2.43)	-52.29 (+1.19)	10.55 (9.0%)
SRESA2 Ensemble	2.73	24.71 (+3.16)	-51.67 (+1.82)	10.71 (10.7%)
SRESB1 Ensemble	1.44	23.08 (+1.52)	-53.09 (+0.40)	10.30 (6.5%)
Least-stable	1.45	23.42 (+1.86)	-54.15 (-0.67)	10.54 (9.0%)
Most-stable	2.11	23.89 (+2.33)	-50.76 (+2.73)	10.22 (5.6%)
No-stable	2.21	23.99 (+2.43)	-53.39 (+0.10)	10.75 (11.1%)
No-strat-cooling	2.21	23.78 (+2.22)	-51.95 (+1.53)	10.45 (8.0%)

Table 4.5: Summary of intensity statistics for 6-km simulations.

Large scale environment	MYJ Average	YSU Average	Overall Average	MPI	Overall Average Change	MPI Change	MPI/Overall (%)
Control	923	940	932	929			
SRES A1B	912	933	923	923	9	6	65
SRES A2	915	932	923	922	8	7	83
SRES B1	915	936	926	924	6	5	80

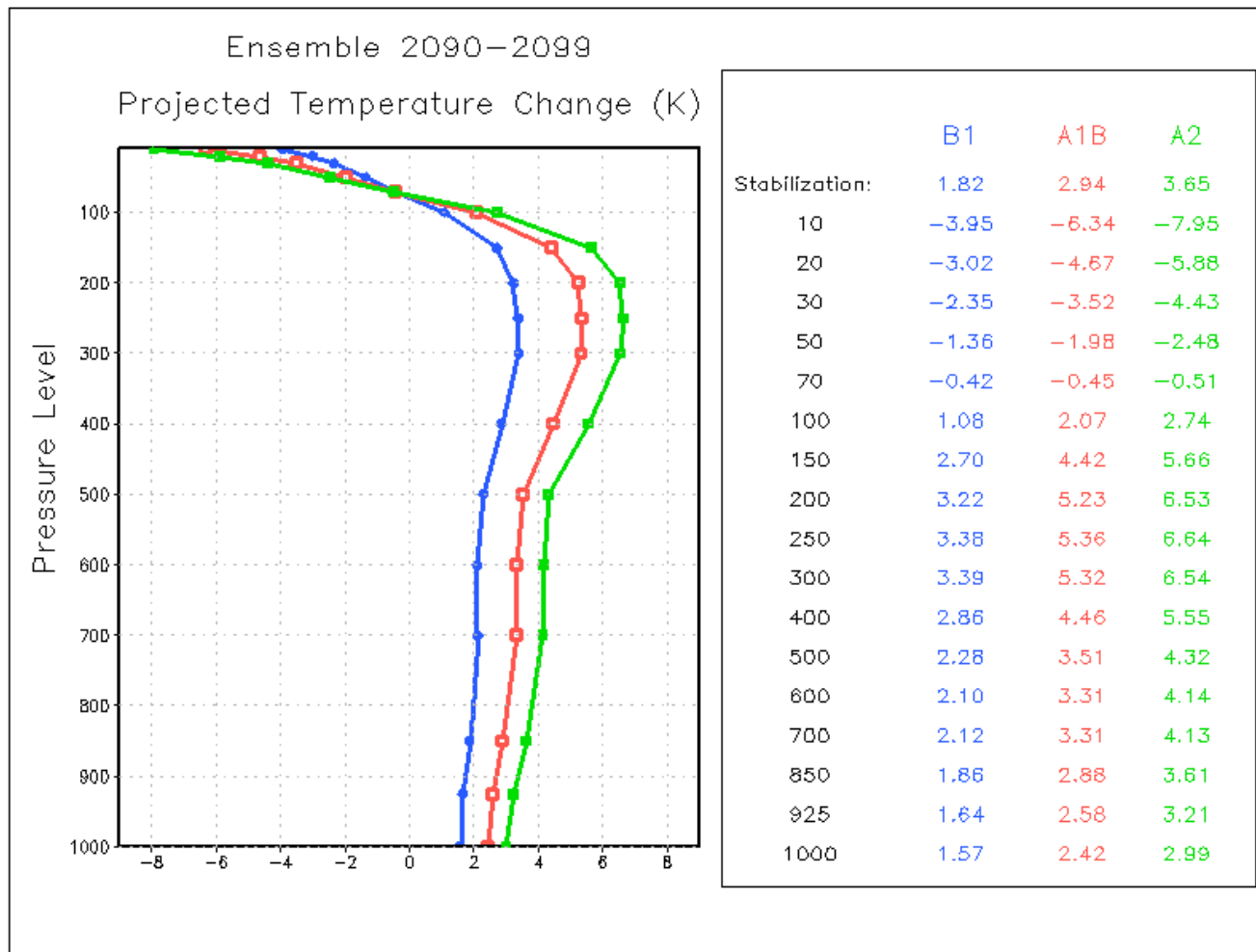


Figure 4.1: Ensemble mean projected change in temperature (K) for each emissions scenario.

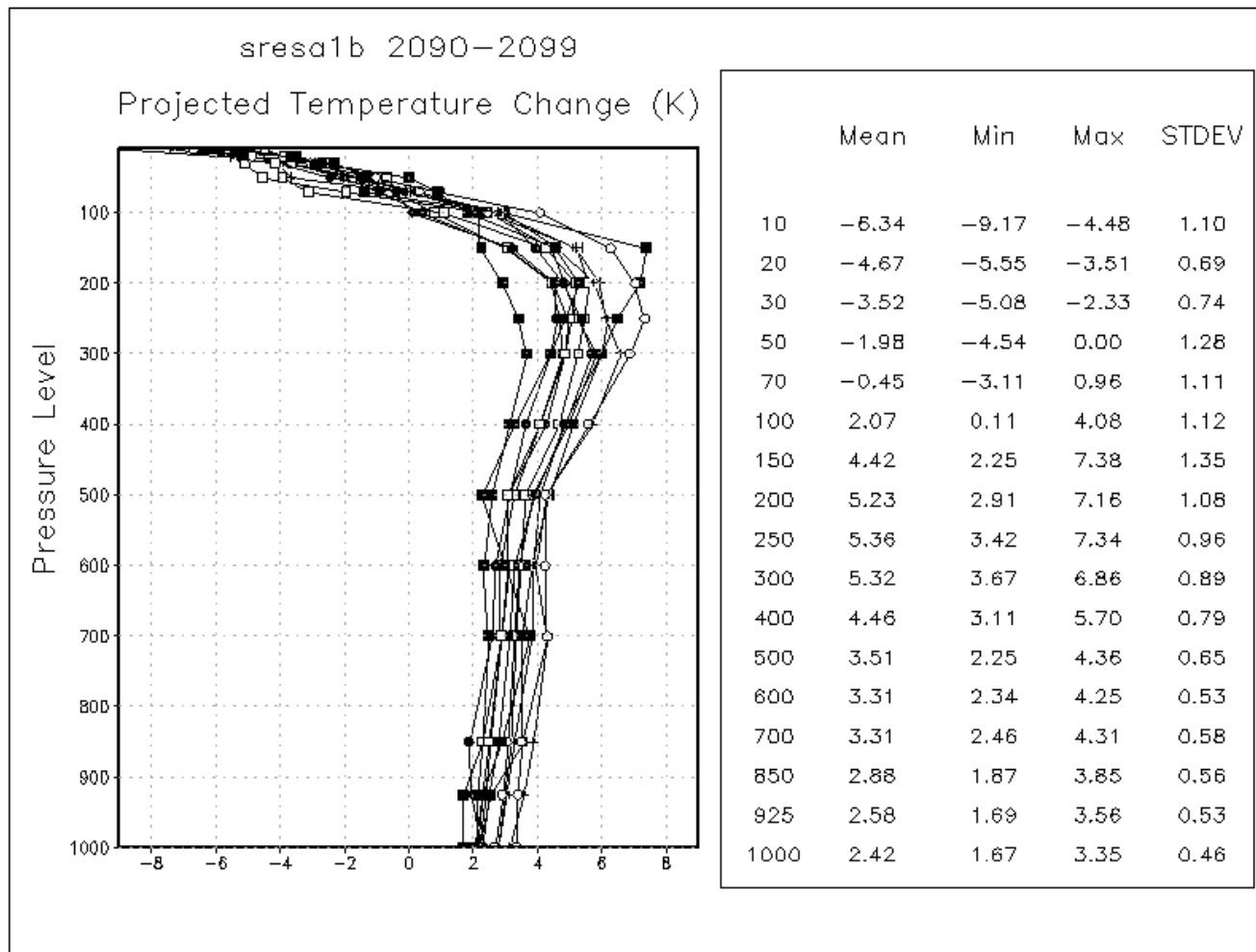


Figure 4.2: Projected change in temperature (K) for each of the 13 GCMs used from the SRES A1B emissions scenario. Data table on the right provides mean, minimum, maximum, and standard deviation values at each pressure level.

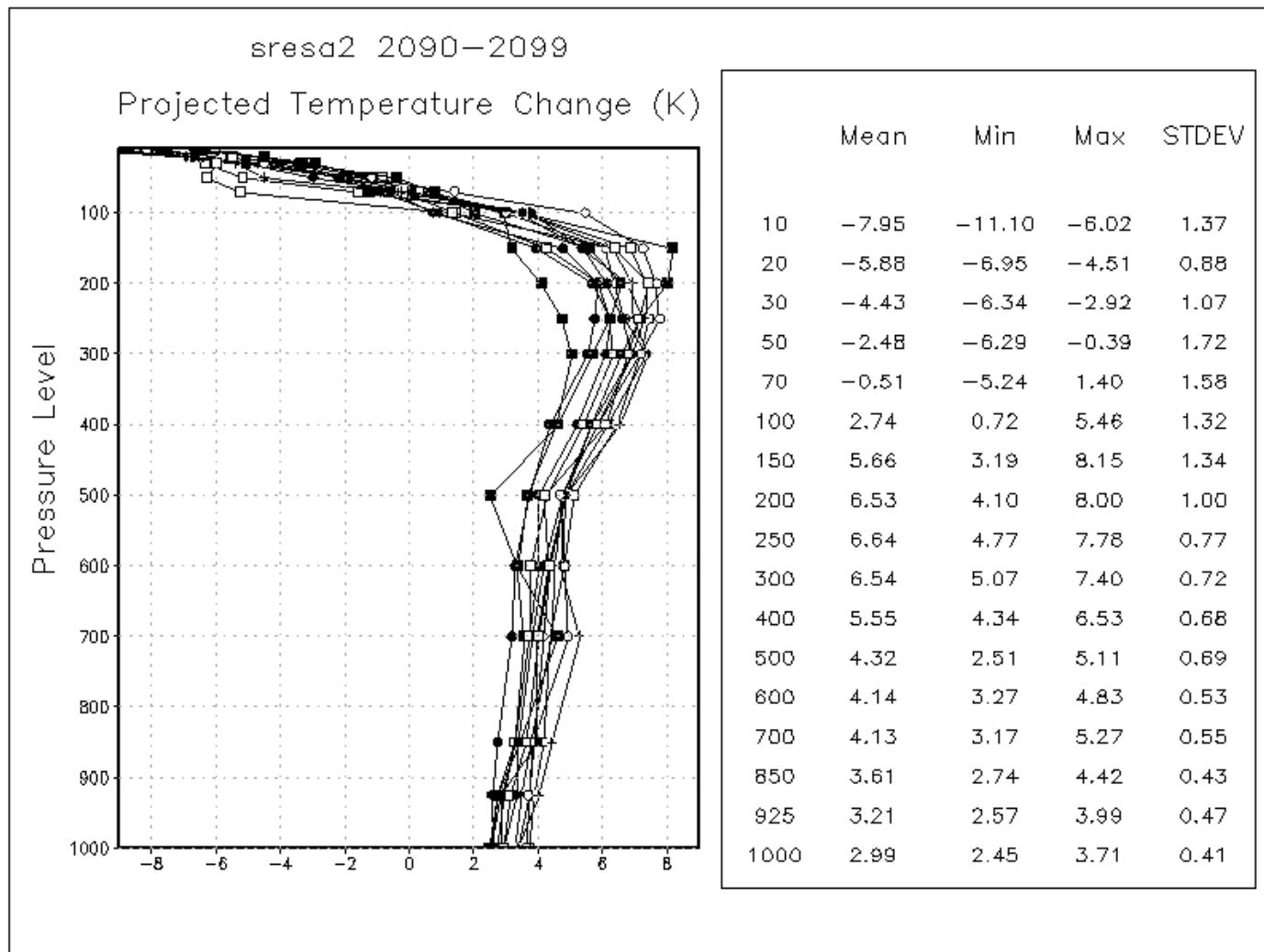


Figure 4.3: As in Fig. 4.2, except for the SRESA2 emissions scenario.

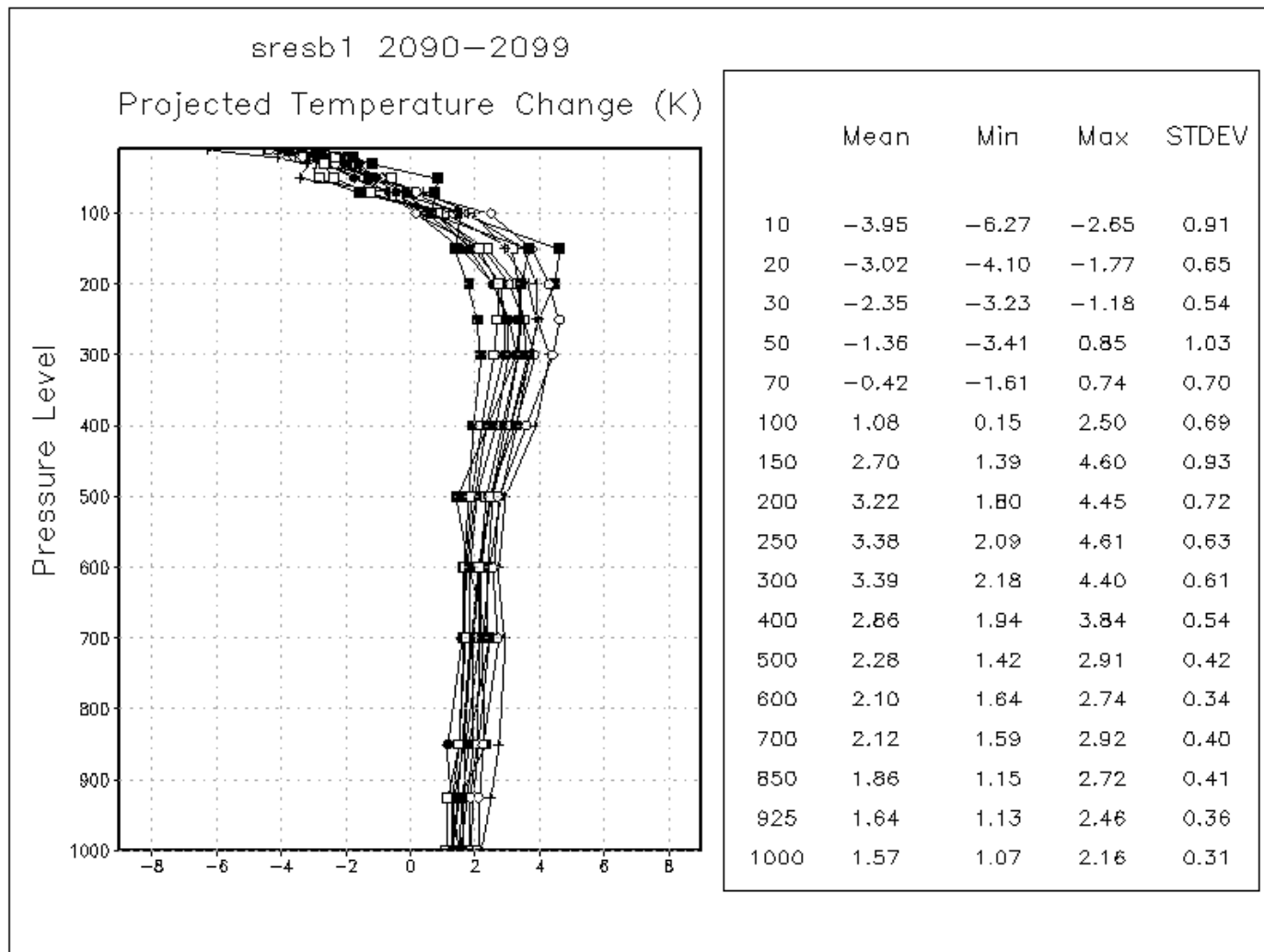


Figure 4.4: As in Fig. 4.2, except for the SRESB1 emissions scenario.

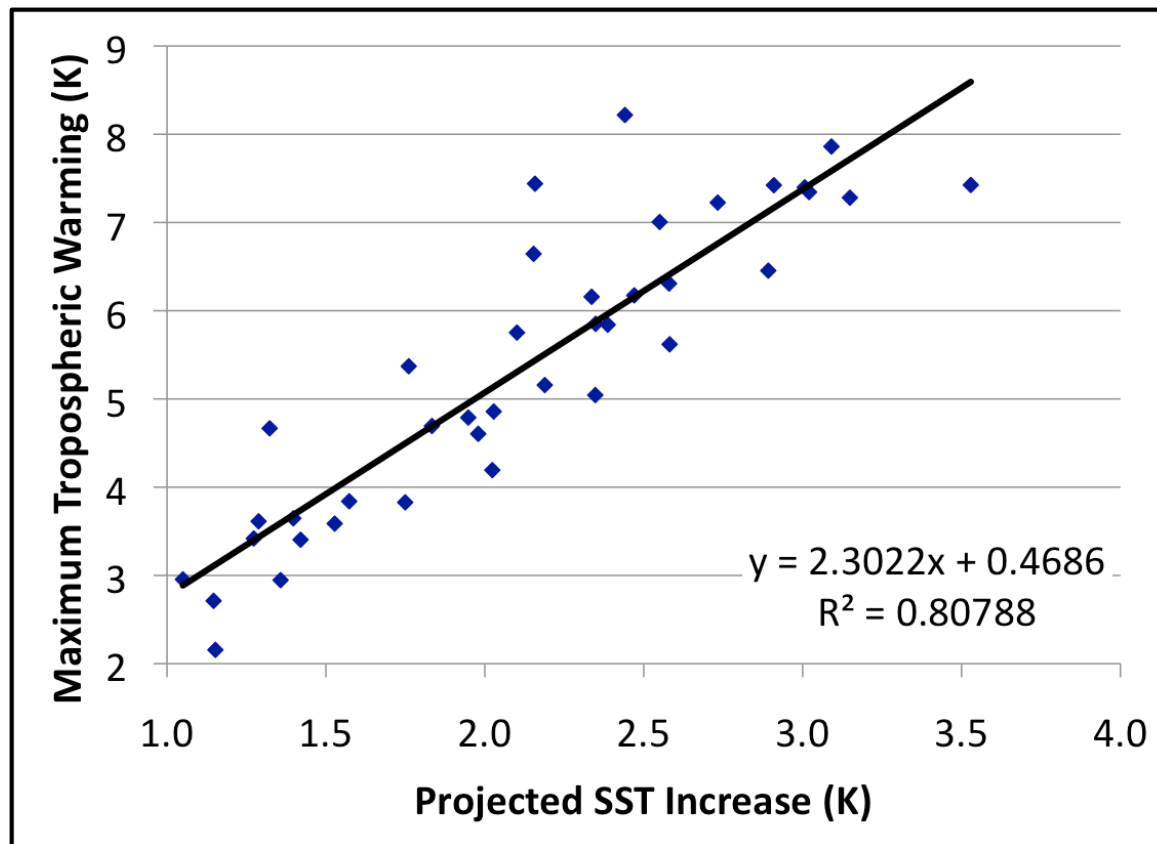


Figure 4.5: Projected SST increase (K) versus maximum tropospheric warming (K) for each of the GCMs.

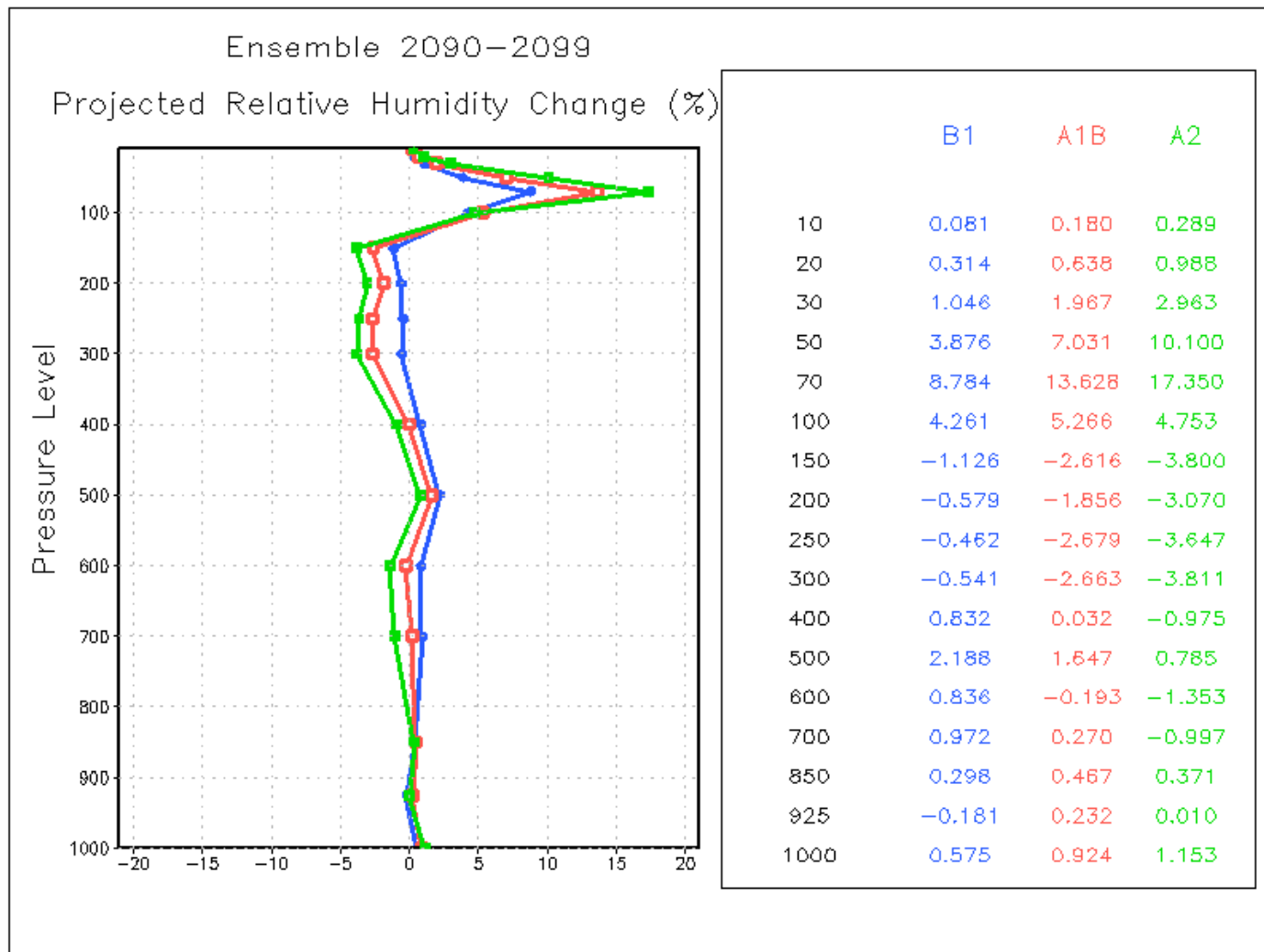


Figure 4.6: Ensemble mean projected change in relative humidity (%) for each emissions scenario.

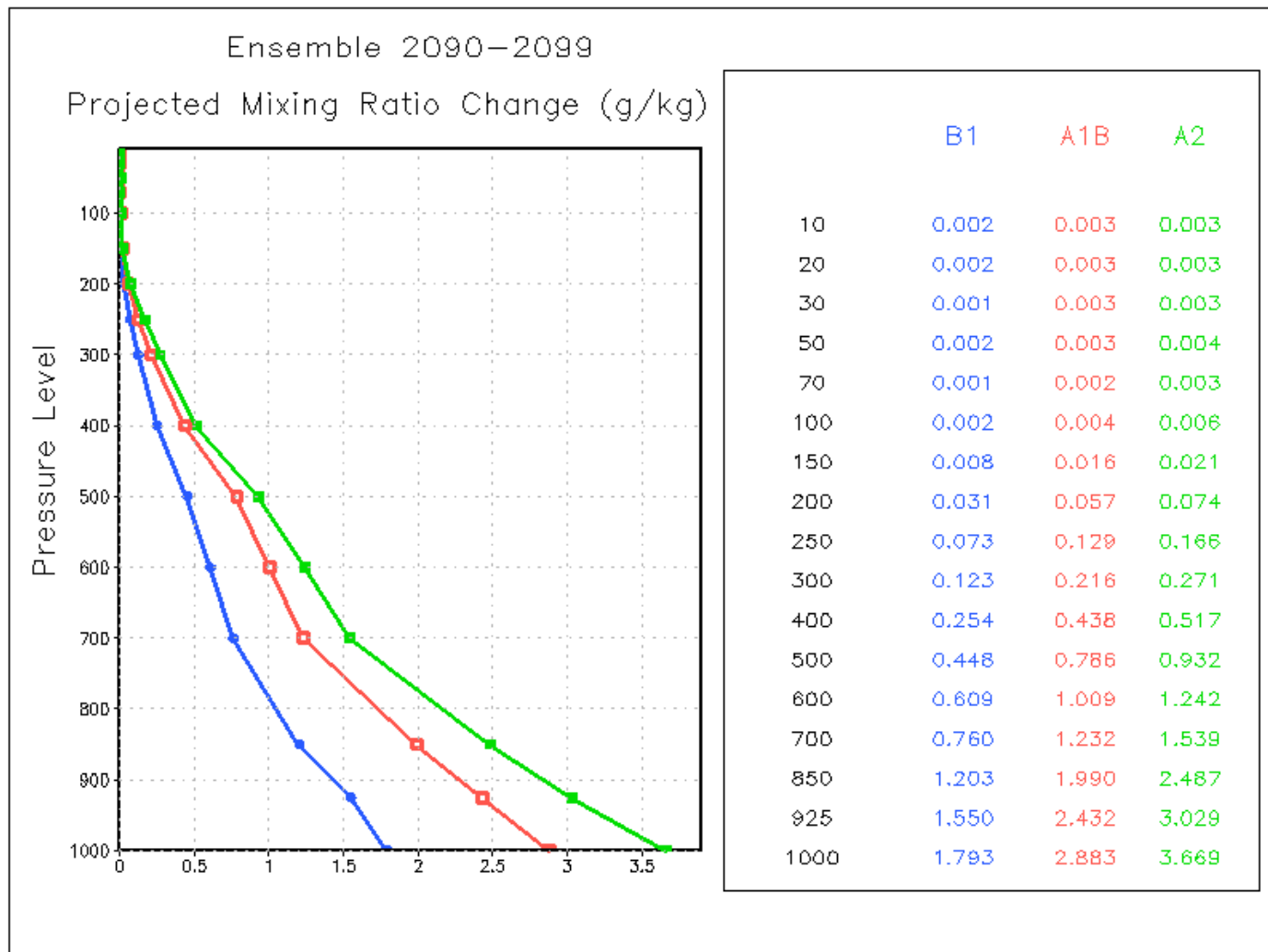


Figure 4.7: Ensemble mean projected change in mixing ratio (g kg^{-1}) for each emissions scenario.

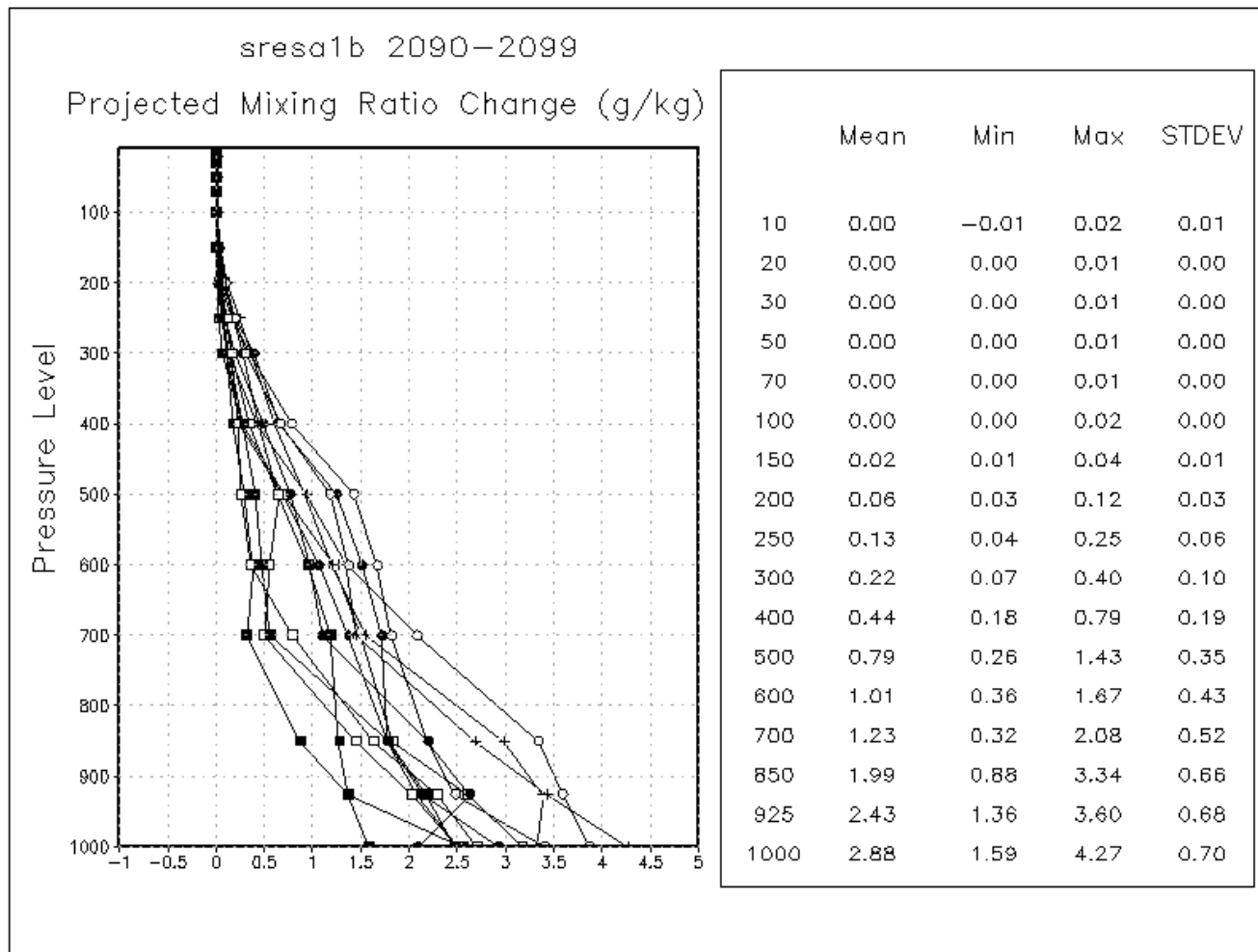


Figure 4.8: Projected change in mixing ratio (g kg^{-1}) for each of the 13 GCMs used from the SRESA1B emissions scenario. Data table on the right provides mean, minimum, maximum, and standard deviation values at each pressure level.

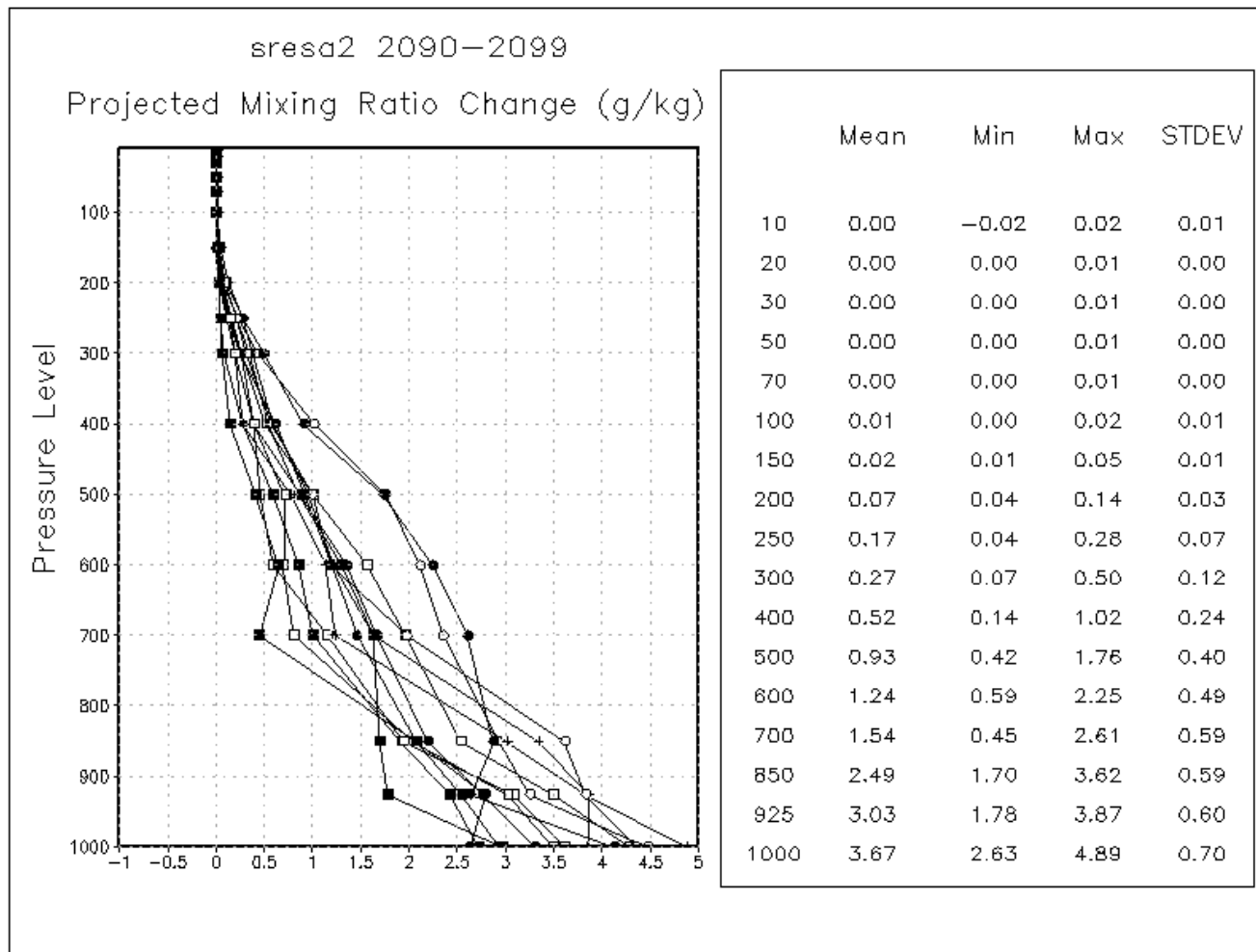


Figure 4.9: As in Fig. 4.8, except for the SRESA2 emissions scenario.

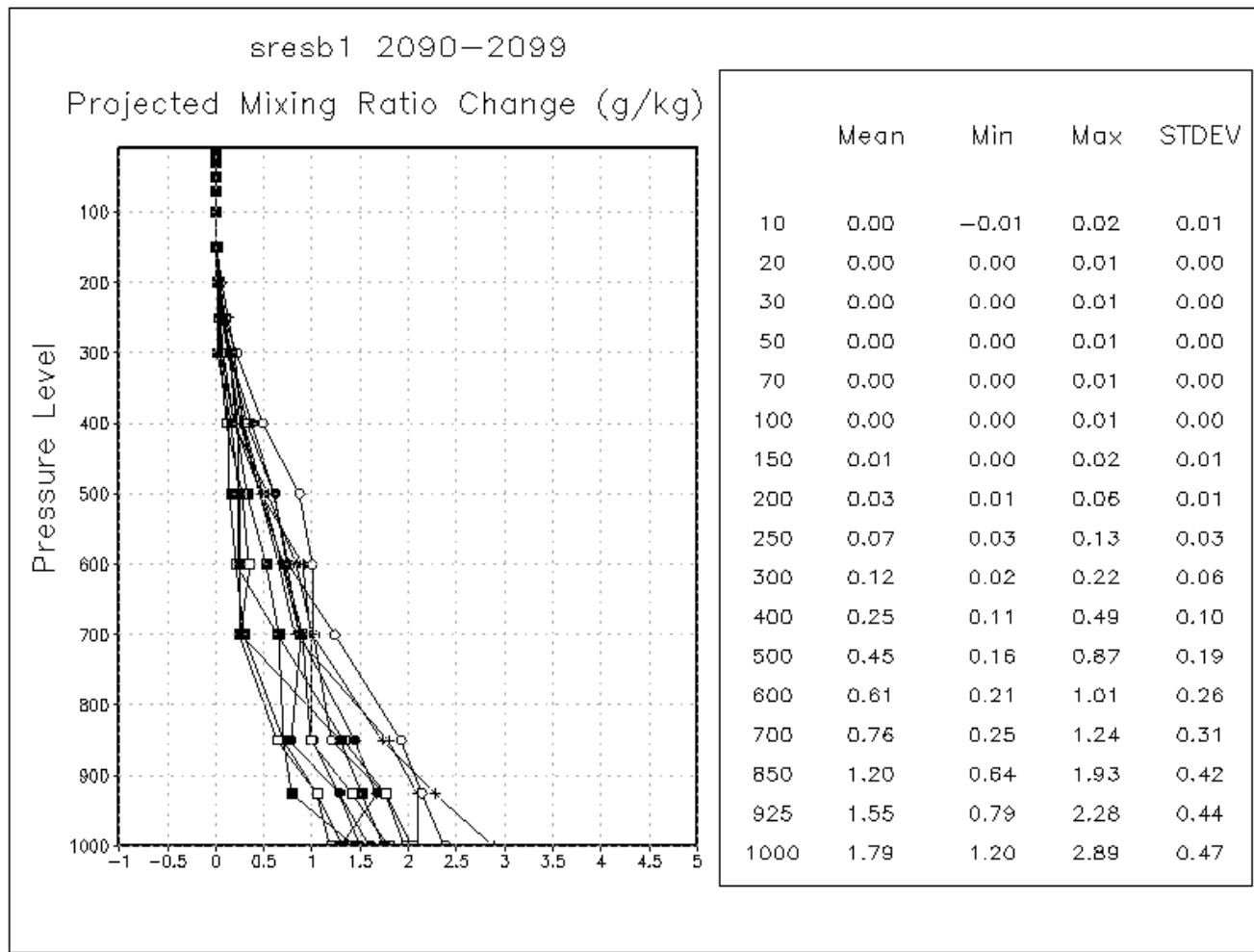


Figure 4.10: As in Fig. 4.8, except for the SRESB1 emissions scenario.

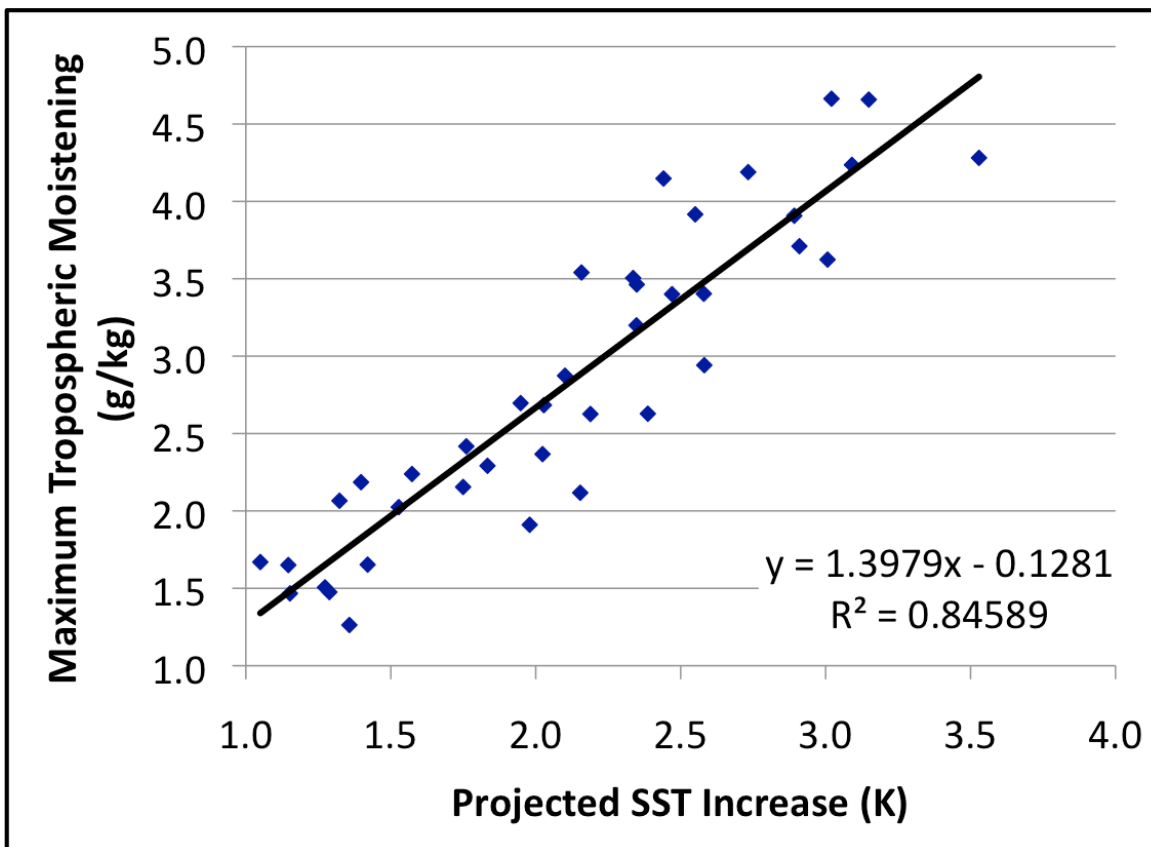


Figure 4.11: Projected SST increase (K) versus maximum tropospheric moistening (g kg^{-1}) for each of the GCMs.

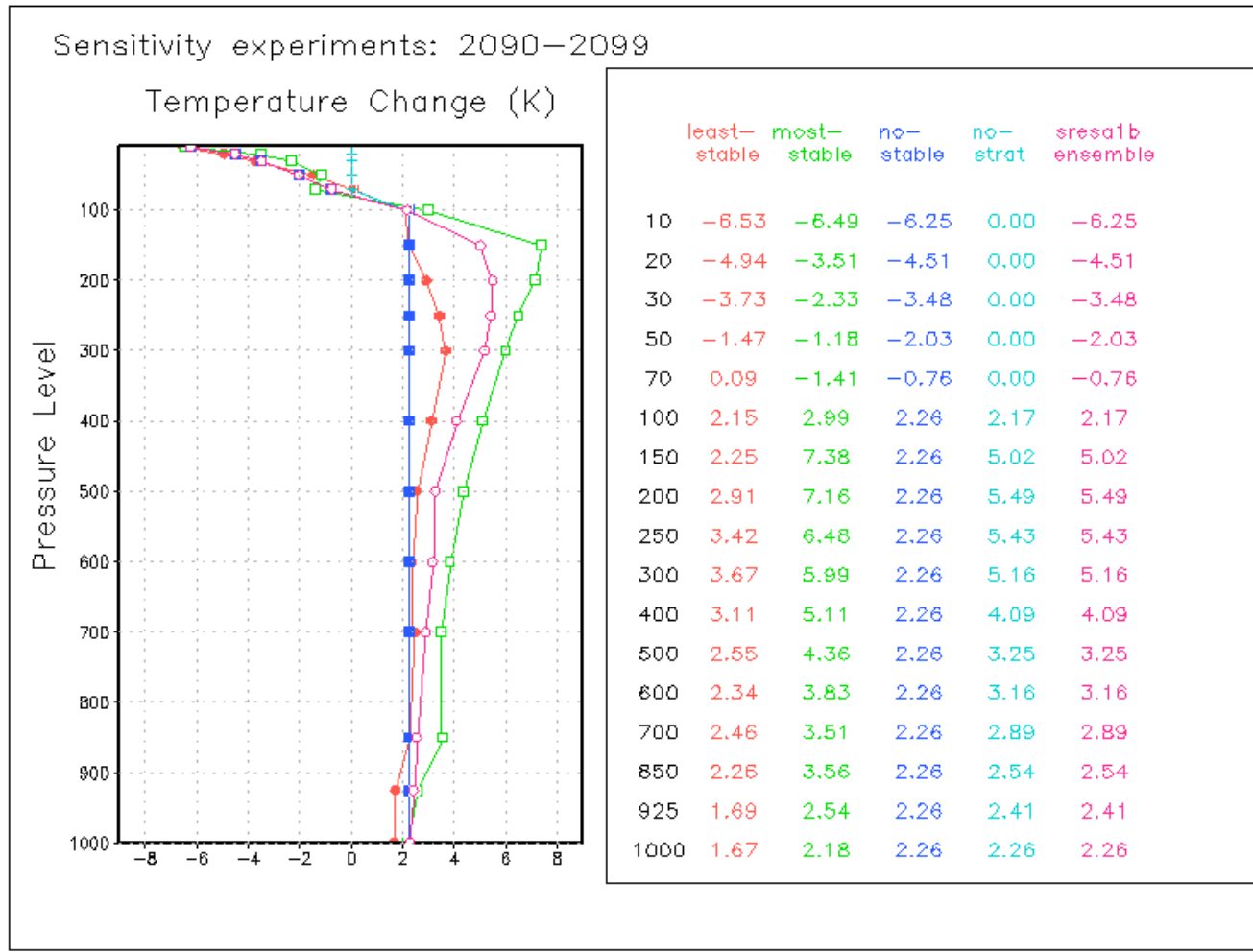
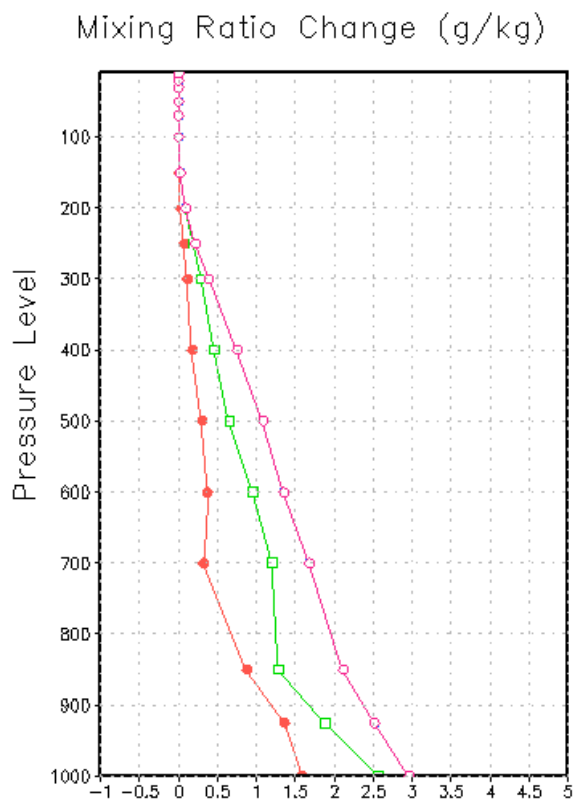


Figure 4.12: Projected temperature (K) changes in sensitivity experiments. Although SST changes are not listed, they follow closely the projected temperature change at the 1000-mb level.

Sensitivity experiments: 2090–2099



	least-stable	most-stable	no-stable	no-strat	sresai b ensemble
10	0.01	0.00	0.00	0.00	0.00
20	0.00	0.00	0.00	0.00	0.00
30	0.00	0.00	0.00	0.00	0.00
50	0.00	0.00	0.00	0.00	0.00
70	0.00	0.00	0.00	0.00	0.00
100	0.01	0.00	0.00	0.00	0.00
150	0.01	0.03	0.02	0.02	0.02
200	0.03	0.09	0.09	0.09	0.09
250	0.07	0.18	0.22	0.22	0.22
300	0.11	0.29	0.39	0.39	0.39
400	0.18	0.46	0.75	0.75	0.75
500	0.30	0.65	1.09	1.09	1.09
600	0.38	0.96	1.35	1.35	1.35
700	0.32	1.20	1.68	1.68	1.68
850	0.88	1.28	2.12	2.12	2.12
925	1.36	1.88	2.52	2.52	2.52
1000	1.59	2.56	2.96	2.96	2.96

Fig. 4.13: As in Fig. 4.12, except for mixing ratio (g kg^{-1}).

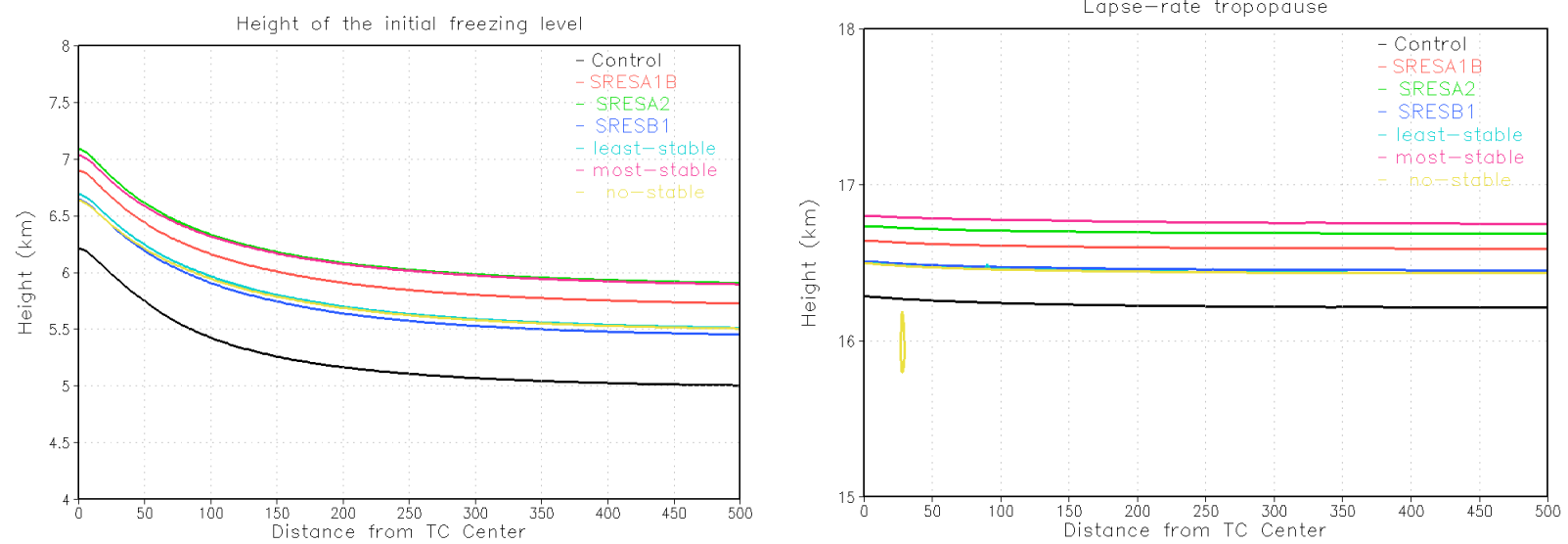


Figure 4.14: Freezing level (left) and lapse-rate tropopause (identified as the height at which the lapse rate becomes less than 2 K km^{-1}) at simulation hour 0.

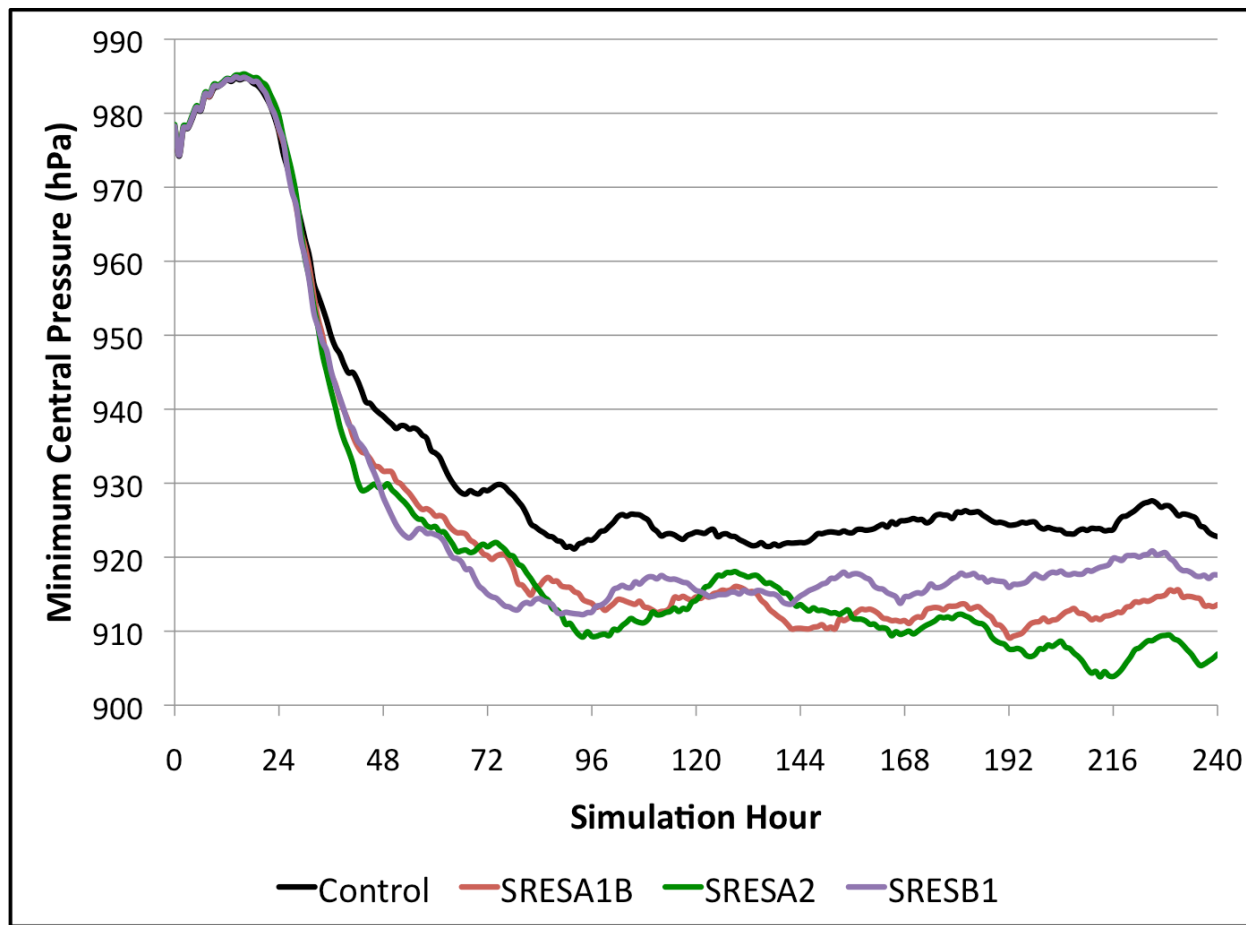


Figure 4.15: Time-series of simulated minimum central pressure (hPa) in the control (black) and with ensemble mean projected future climate changes (see legend).

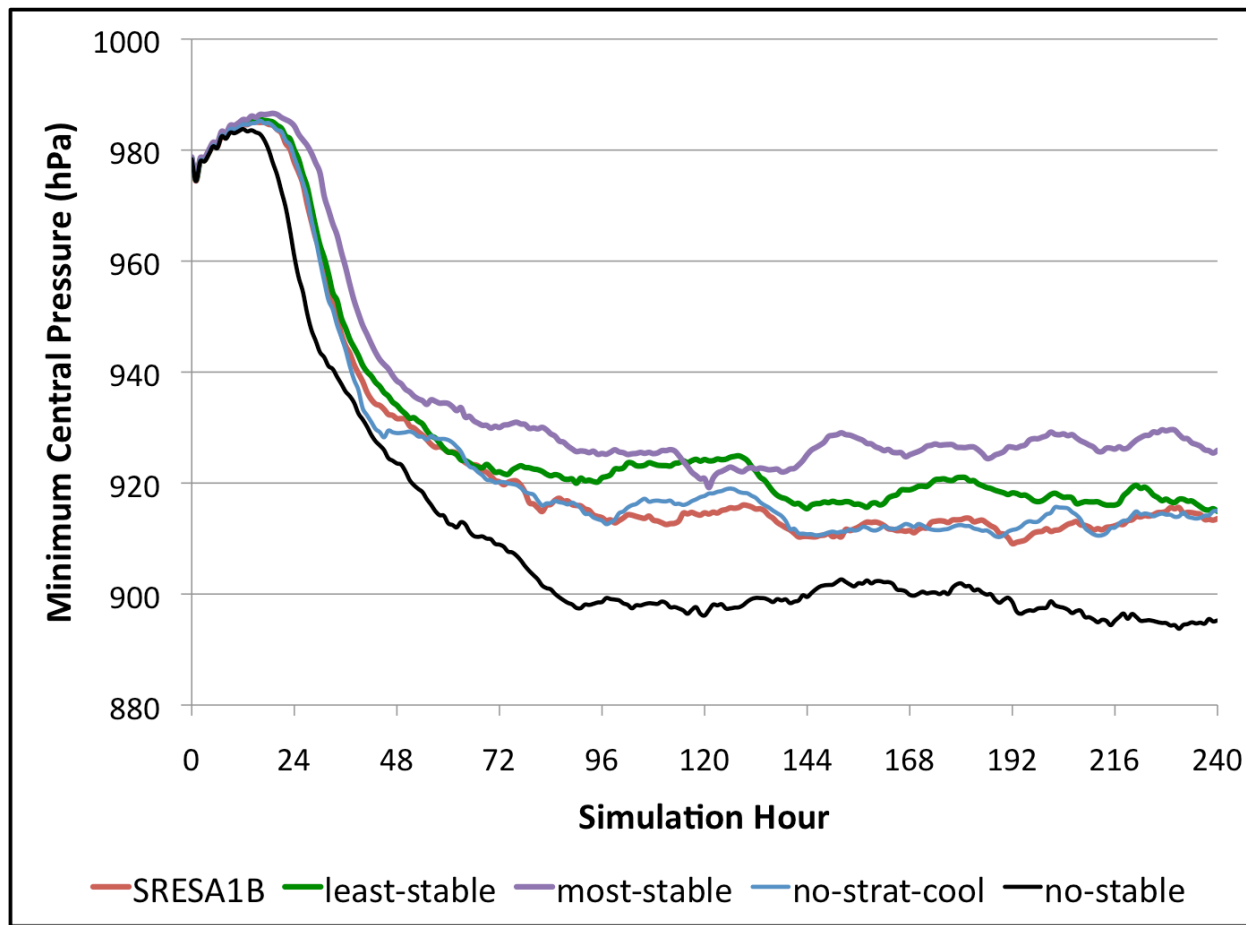


Figure 4.16: As in Fig. 4.15, except for the SRESA1B future simulation and the sensitivity experiments (see legend).

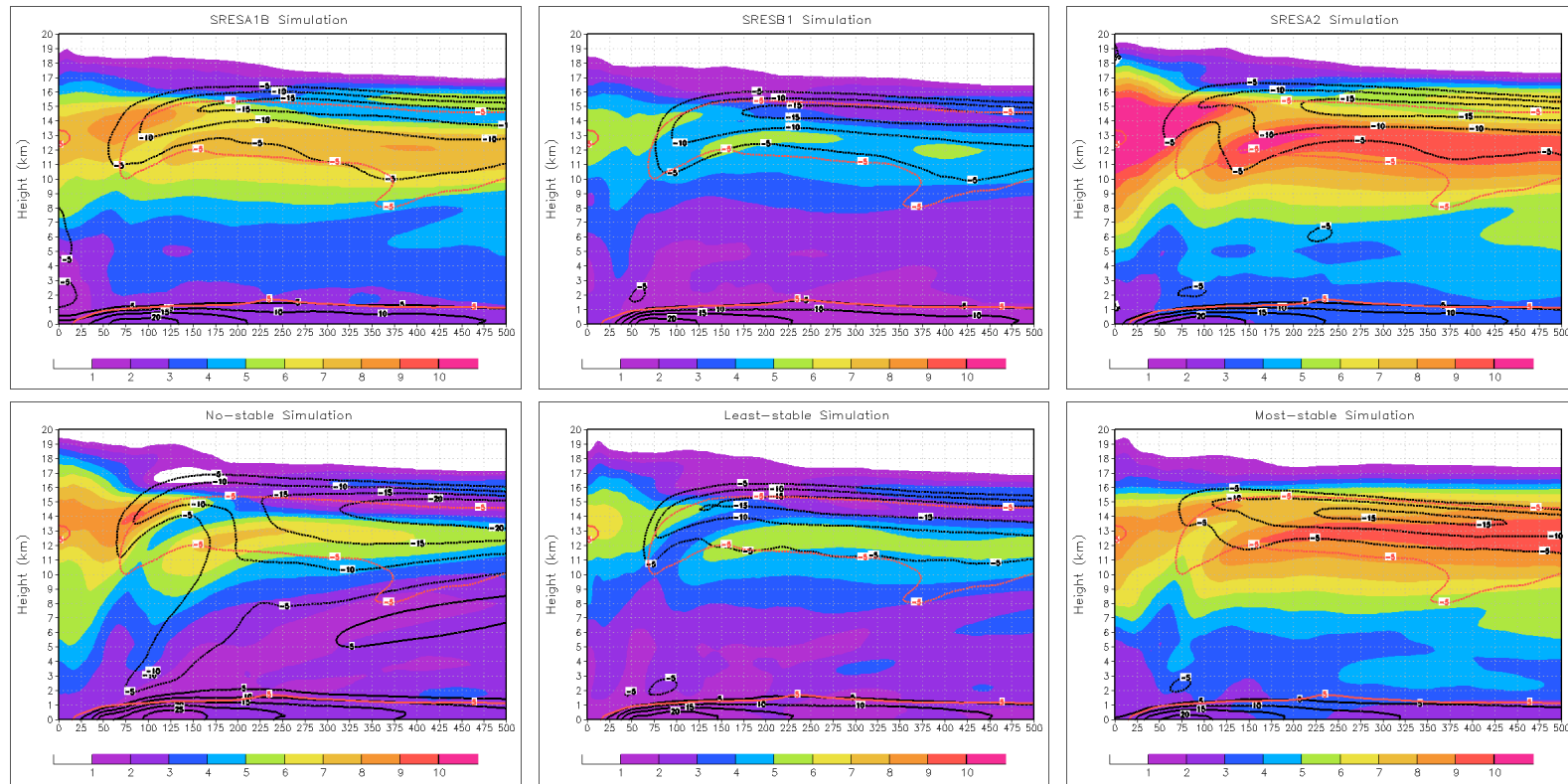


Figure 4.17: Cross sections of temperature difference between the future environment and the control (K; shaded), future radial flow (m s^{-1} ; black contours), and current radial flow (contoured at 5 m s^{-1} ; red contour). Vertical axis extends from the surface to 20-km.

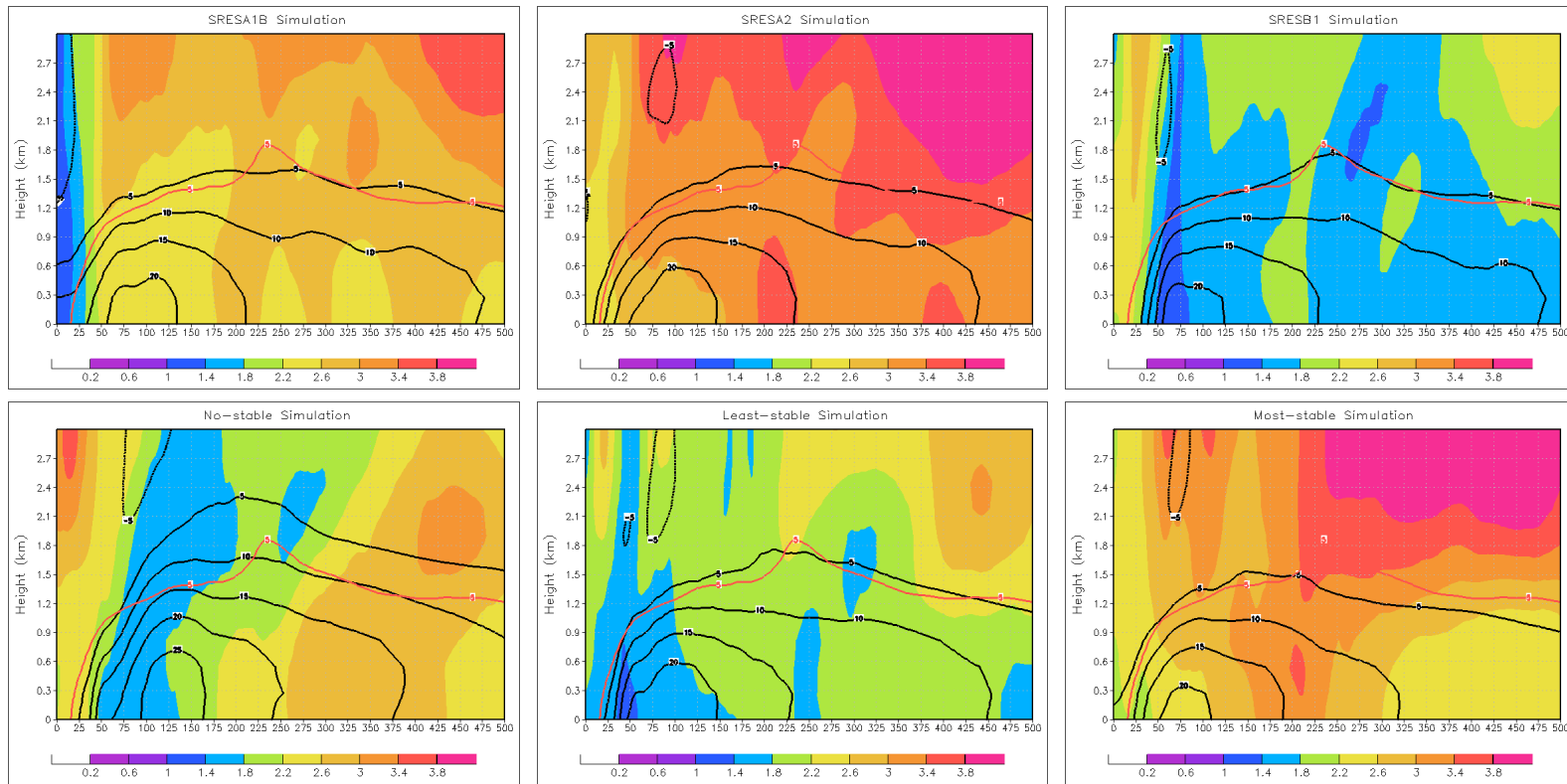


Figure 4.18: As in Fig. 4.17, except covering the lower troposphere (0 – 3 km).

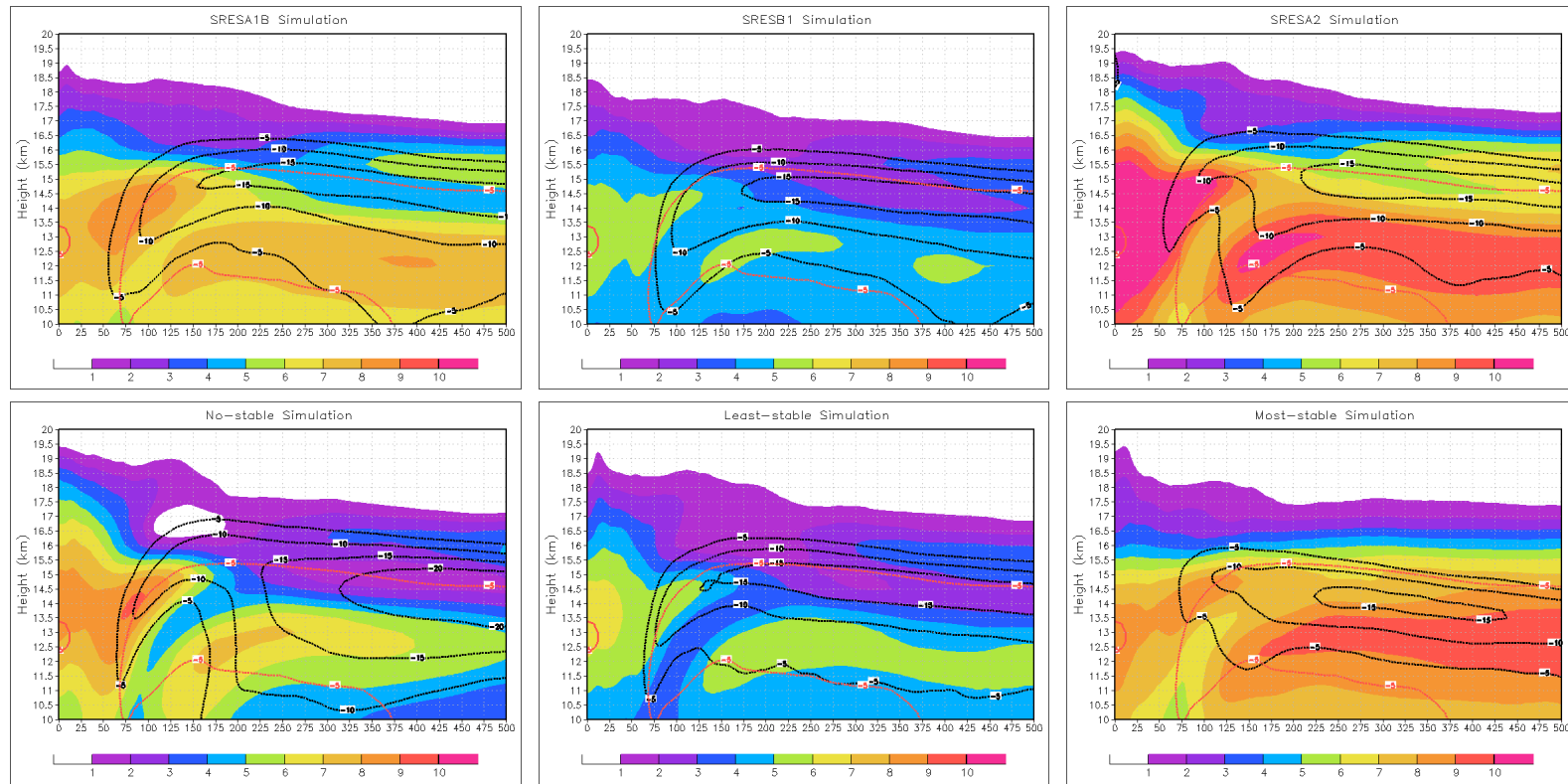


Figure 4.19: As in Fig. 4.17, except covering the upper troposphere (10 – 20 km).

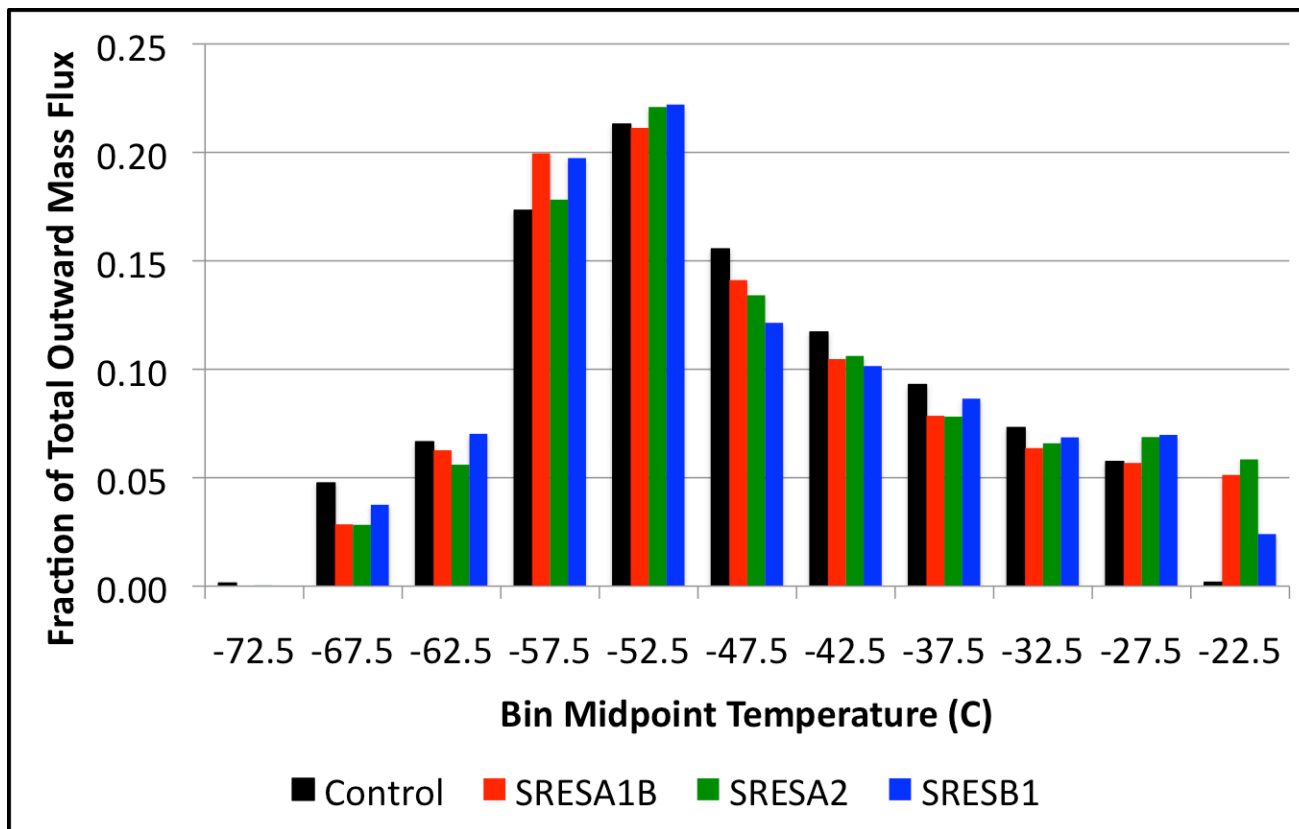


Figure 4.20: Outward mass flux as a function of temperature in the control simulation and in simulations with ensemble mean projected changes. Outward mass flux placed into temperature bins that were 5° C wide.

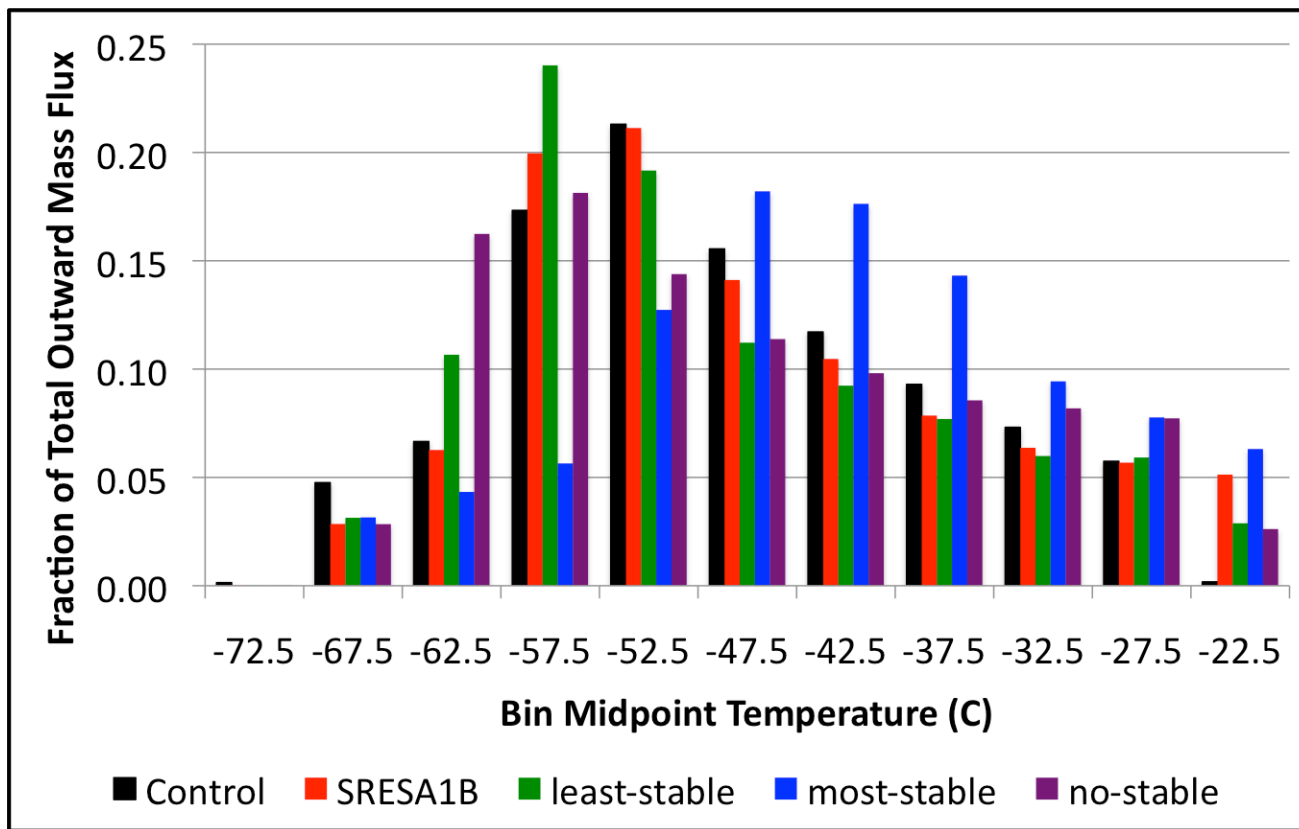


Figure 4.21: Outward mass flux as a function of temperature in the control, the SRESA1B, and the sensitivity experiments.

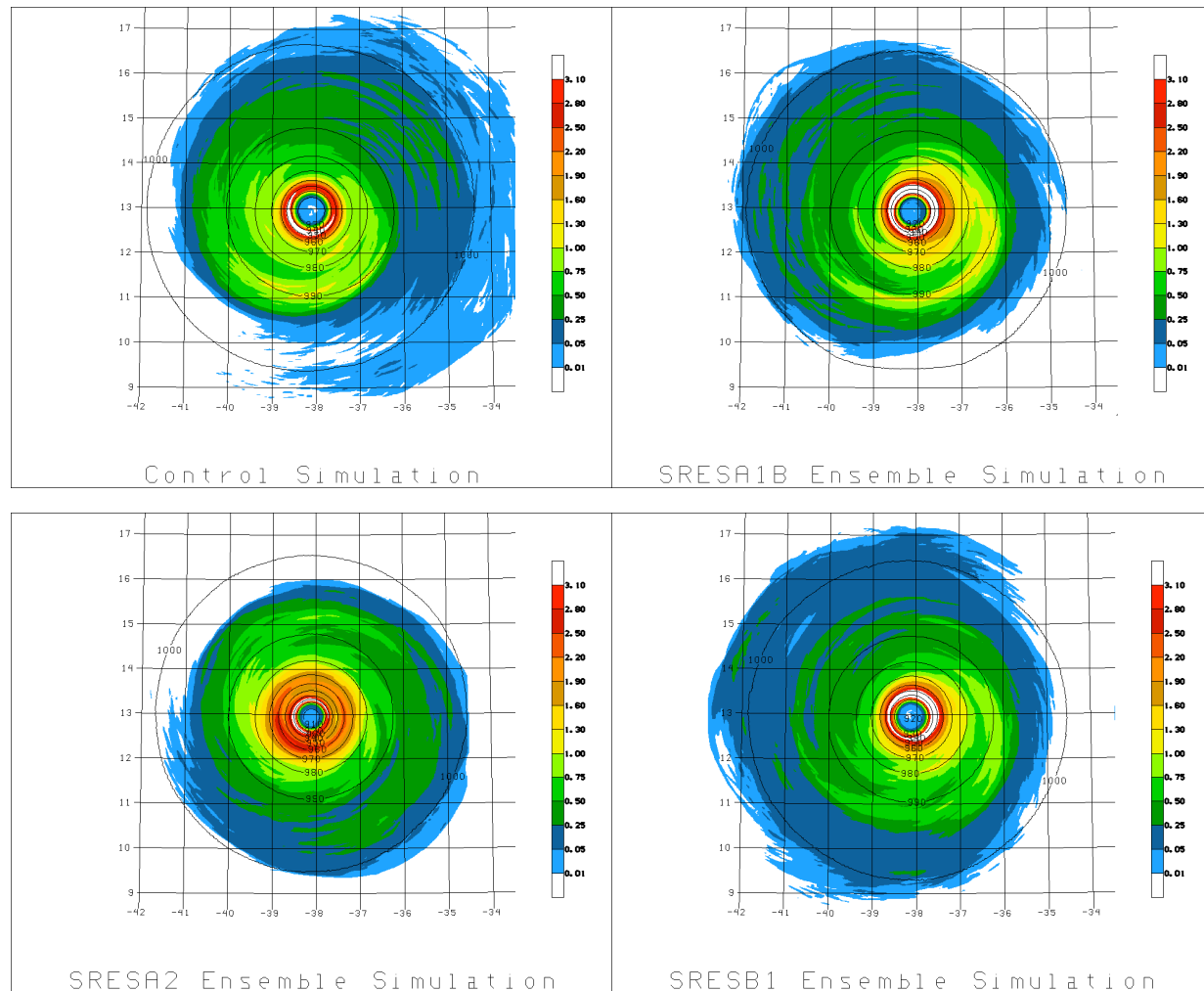


Figure 4.22: Rain-rate (in hr^{-1}) averaged between simulation hours 216 and 240, for the control and future simulations with ensemble mean projected changes (emissions scenario indicated in each image).

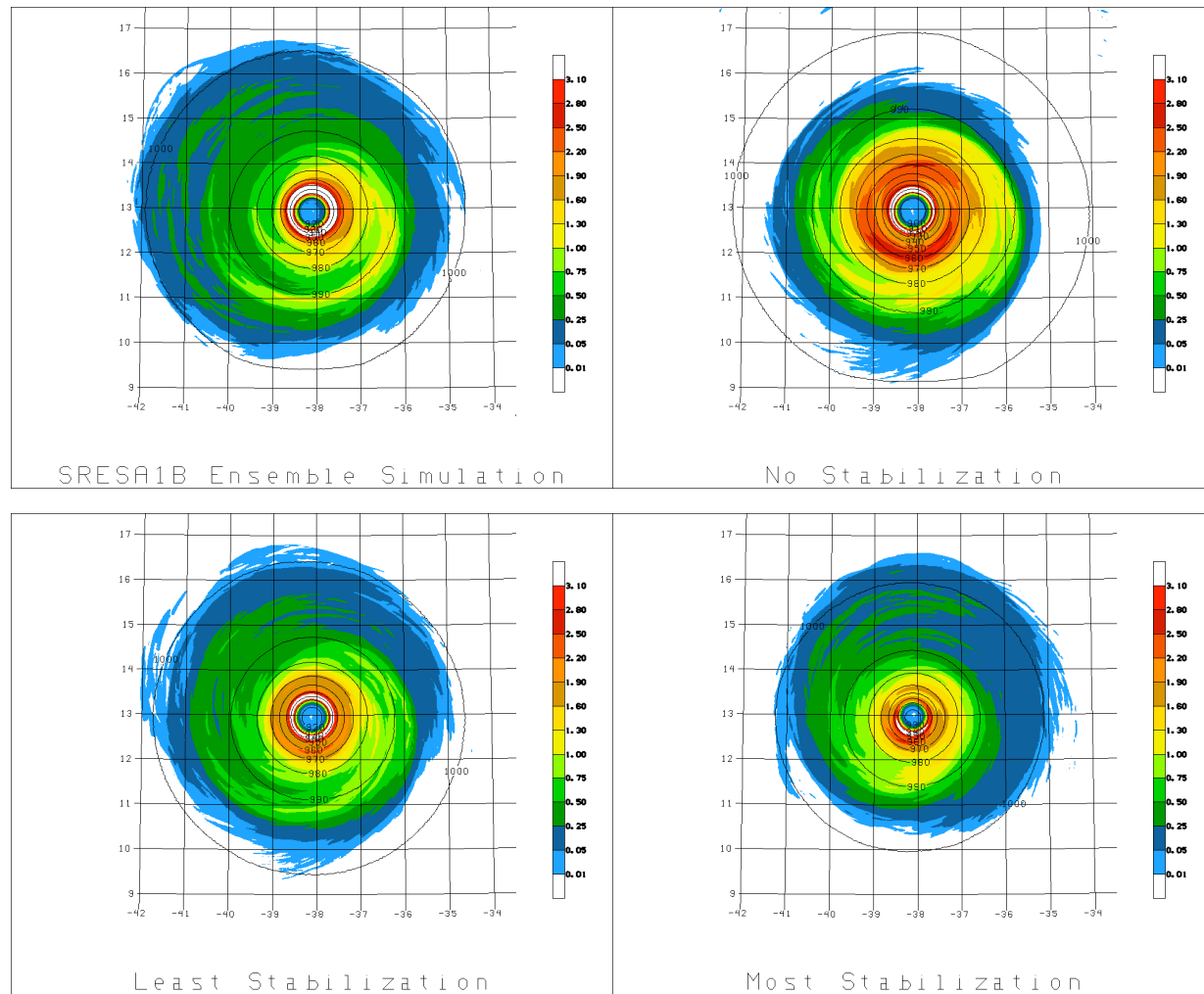


Figure 4.23: As in Fig. 4.22, except for the simulation with projected changes from the SRESA1B ensemble, and in tropospheric stabilization sensitivity experiments.

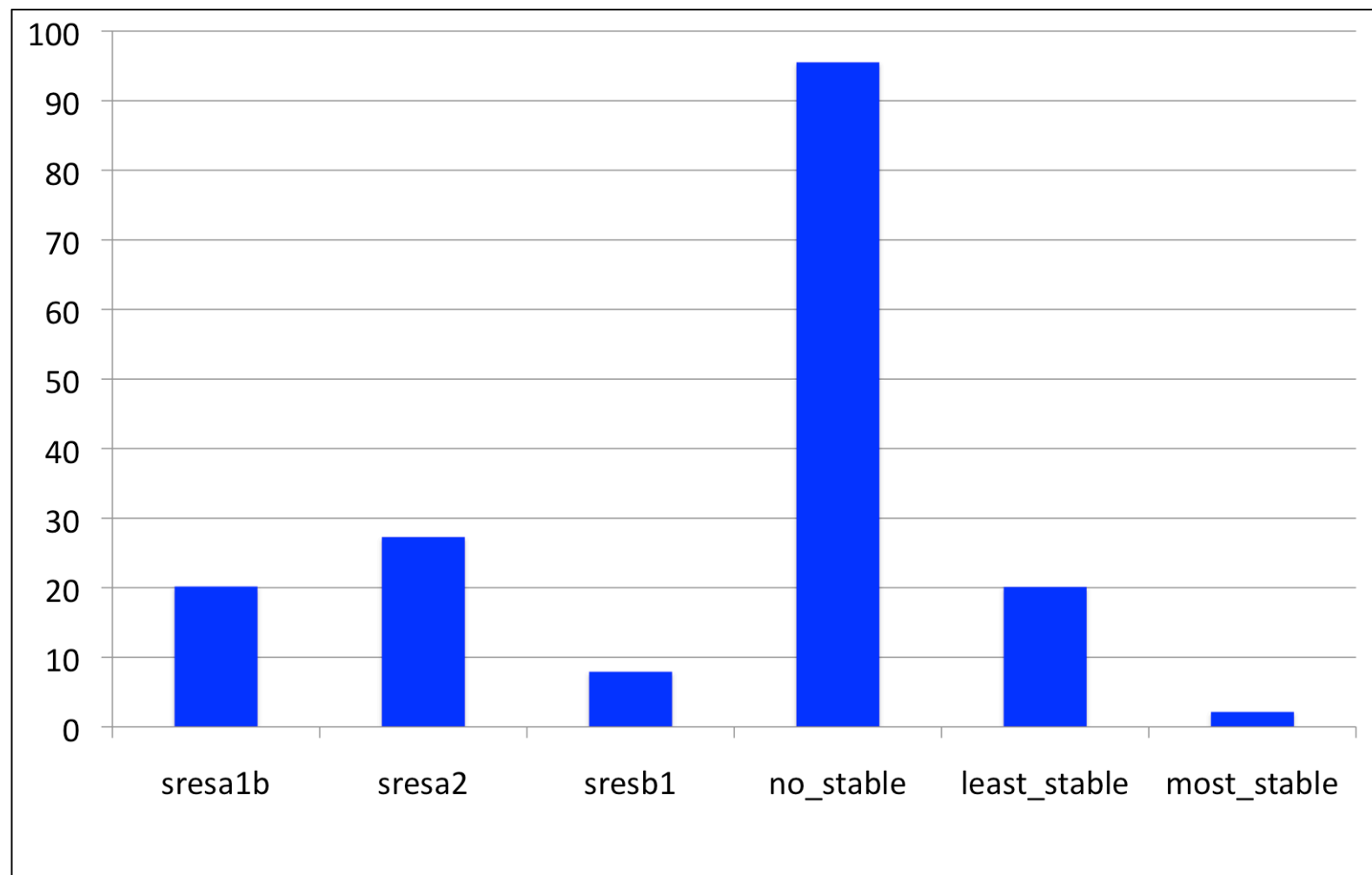


Figure 4.24: Percentage increase in average rainfall in future climate experiments relative to the control simulation within 250-km of the TC center. Values were averaged between simulation hours 216 and 240.

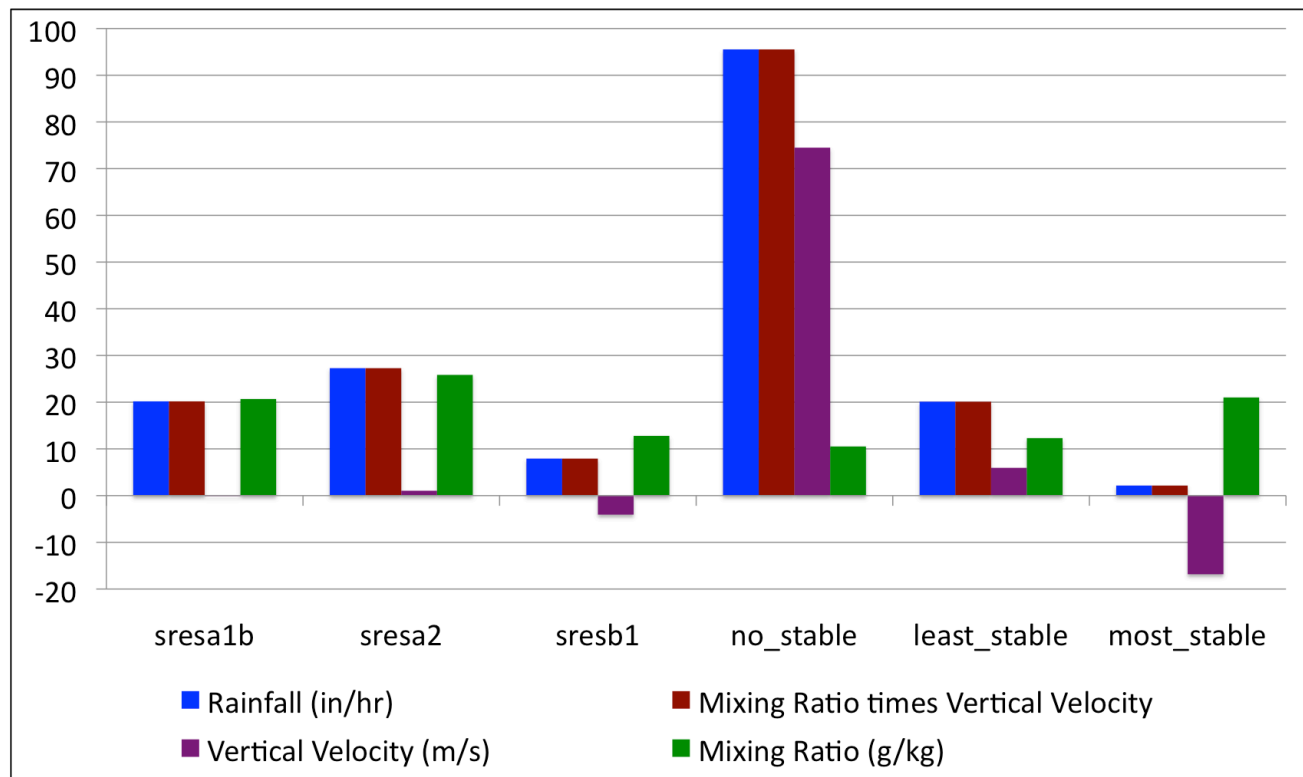


Figure 4.25: Area averaged (within 250-km of the TC center) percentage increases (relative to the control simulation) of various quantities (indicated by legend). Parameters other than rainfall were computed at the 700-hPa pressure level. Values were averaged between simulation hours 216 and 240.

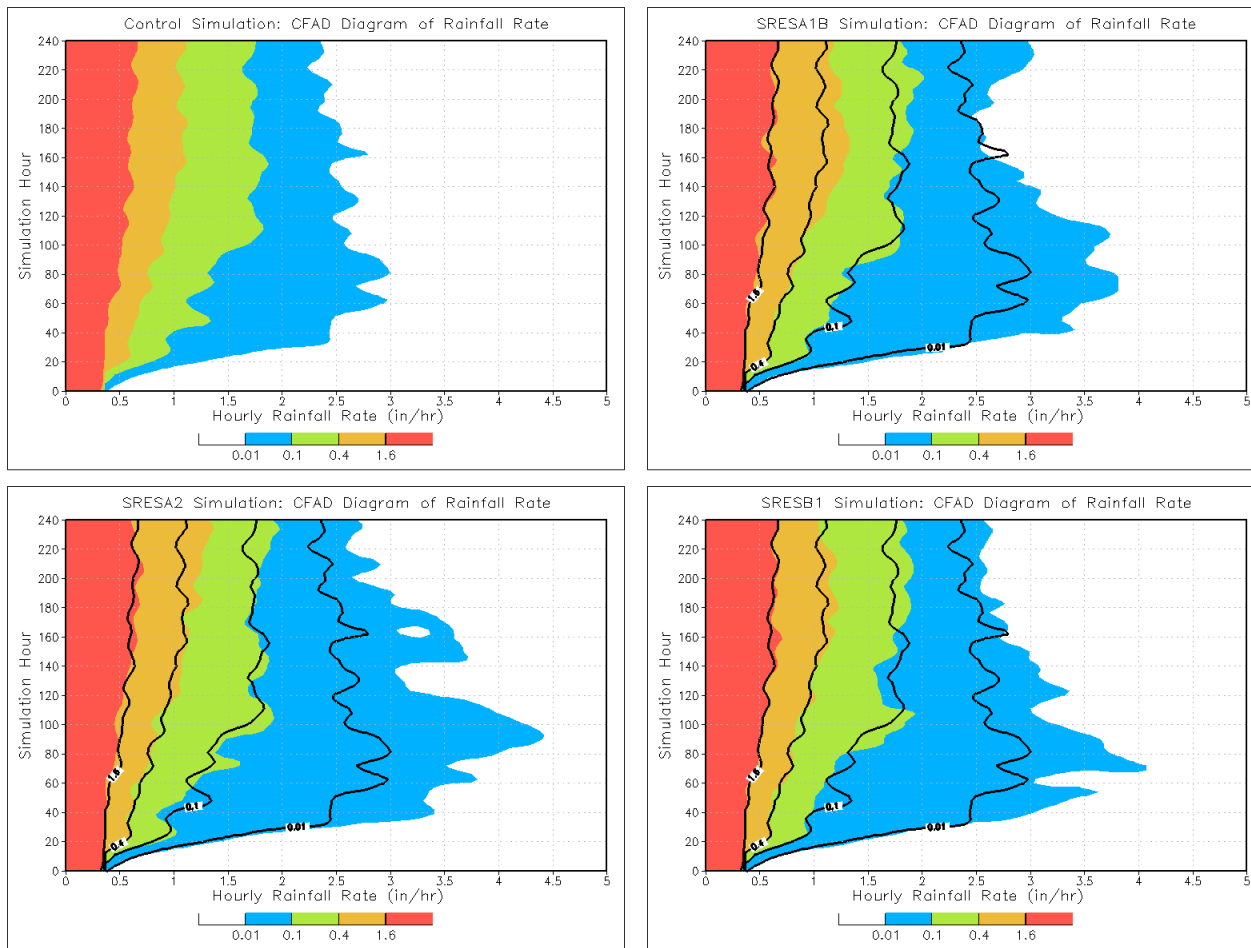


Figure 4.26: Contoured frequency diagram of hourly rainfall rate (in hr^{-1}) as a function of time in the control simulation and future simulations with ensemble mean projected changes. Grid cells within 500-km of the objectively determined TC center were used. In future simulations, contours from the control simulation are shown for reference.

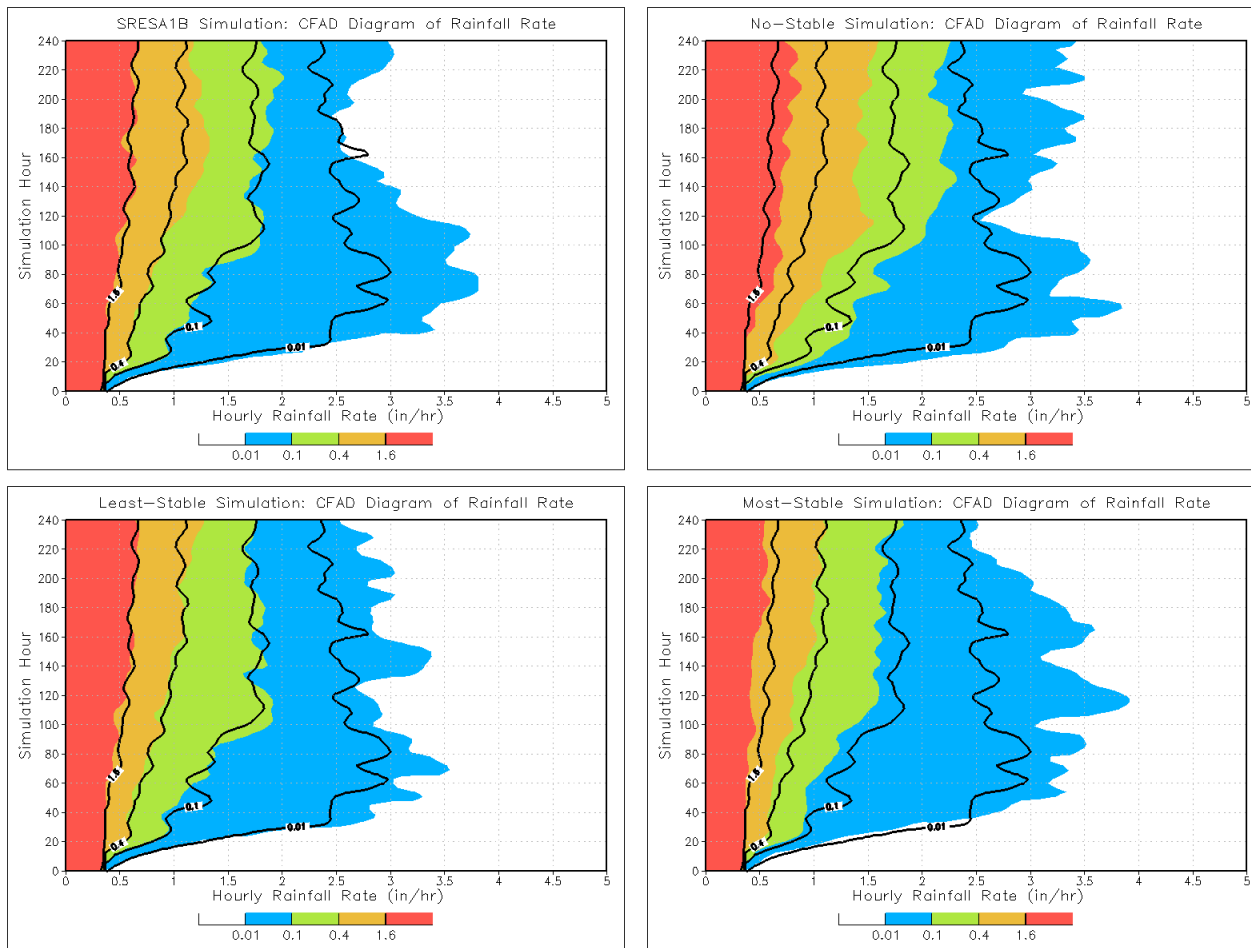


Figure 4.27: As in Fig. 4.26, except for in the SRESA1B future simulation and in the sensitivity experiments.

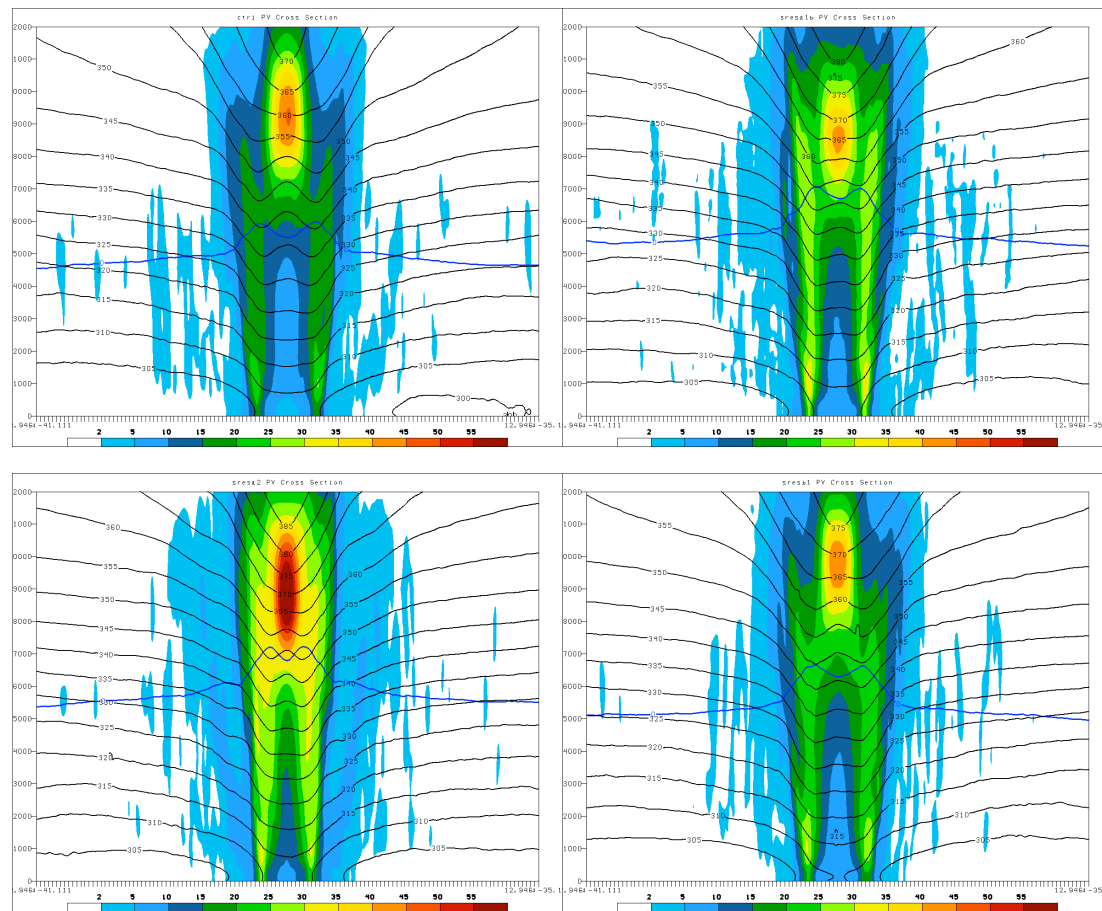


Figure 4.28: Cross sections of time-averaged (simulation hours 216 – 240) potential vorticity (PVU; shaded), potential temperature (K; black contours), and the 0-C isotherm (blue contour) for the following simulations: control (upper left), SRESA1B (upper right), SRESA2 (lower left), and SRESB1 (lower right).

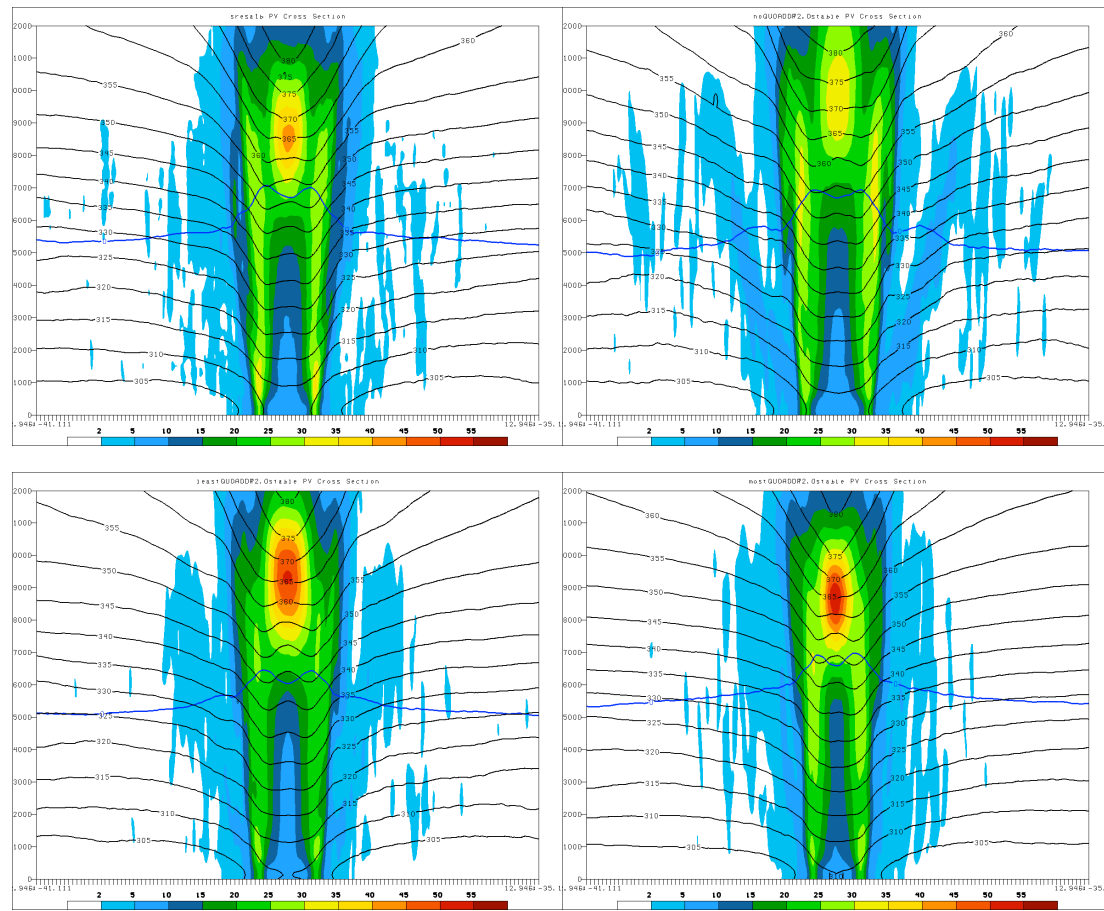


Figure 4.29: As in Fig. 4.28, except for the SRESA1B and sensitivity experiments.

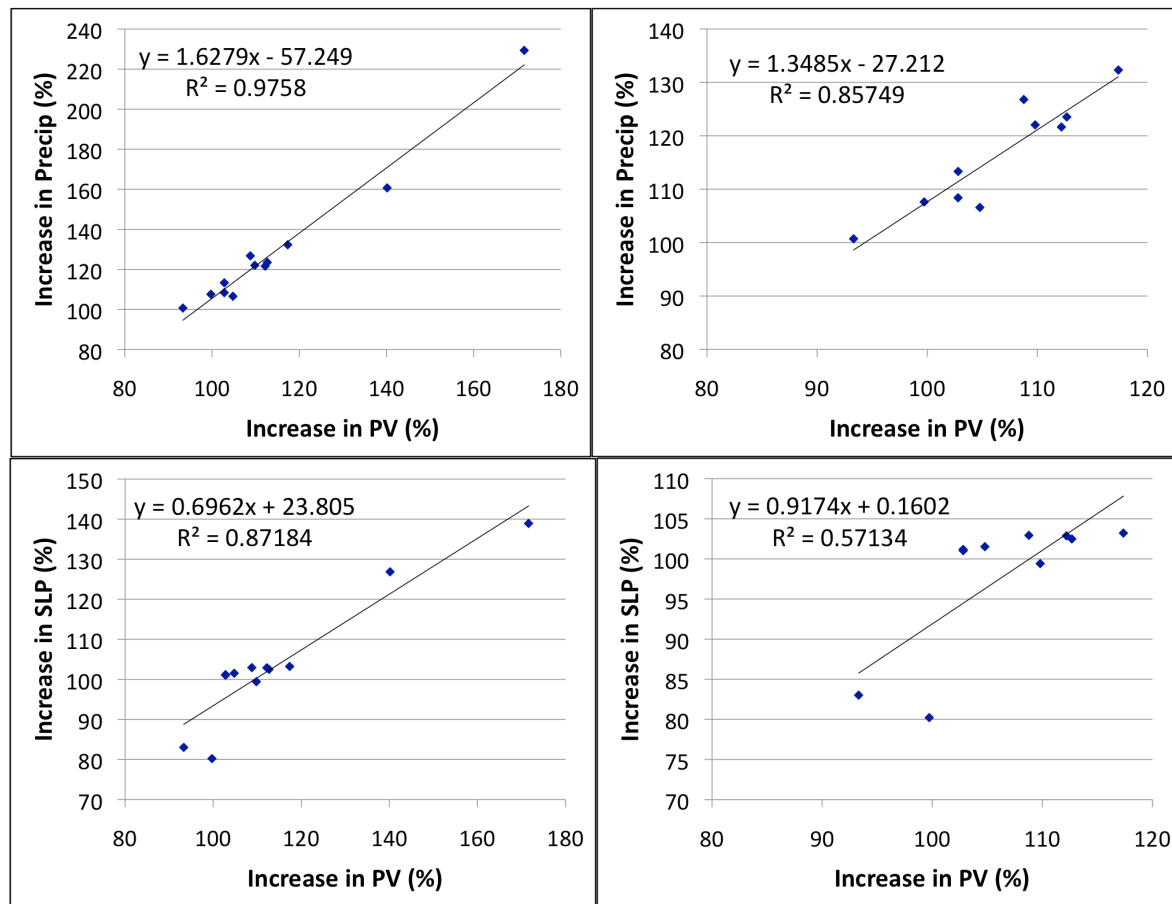


Figure 4.30: Scatter plot of (top left panel) percentage increase in area-averaged (within 200-km of center) 850 – 700 hPa PV versus increase in precipitation averaged between simulation hours 216 – 240 for all future simulations with 2-km grid spacing, (top right) as in top left but excluding no-stable future simulations, (bottom left) as in top left panel except PV versus increase in SLP deficit, and (bottom right) as in bottom left except excluding no-stable future simulations.

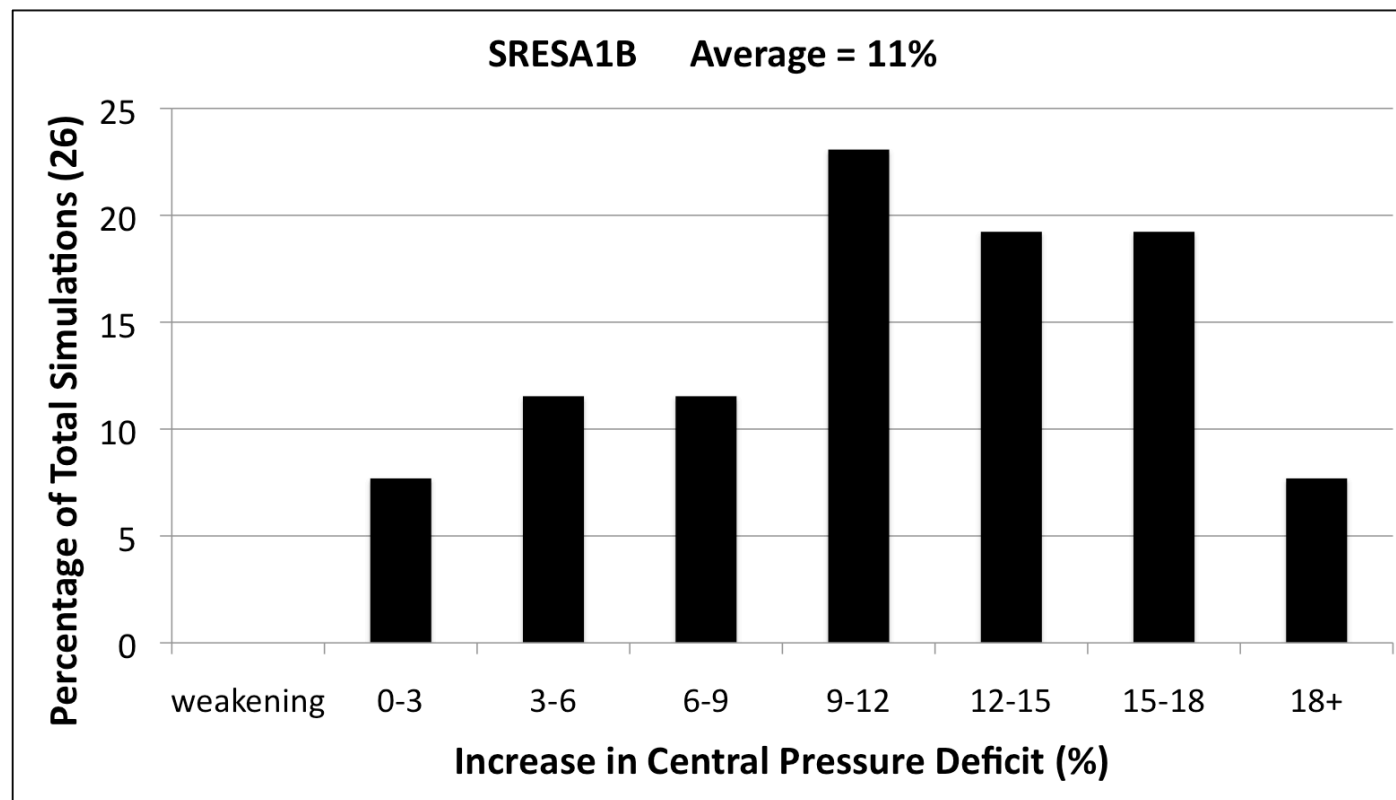


Figure 4.31: Central pressure reduction in future simulations (relative to control; central pressure deficit defined relative to the ambient environment) for future simulations with projected changes from individual GCMs driven by the SRESA1B emissions scenario.

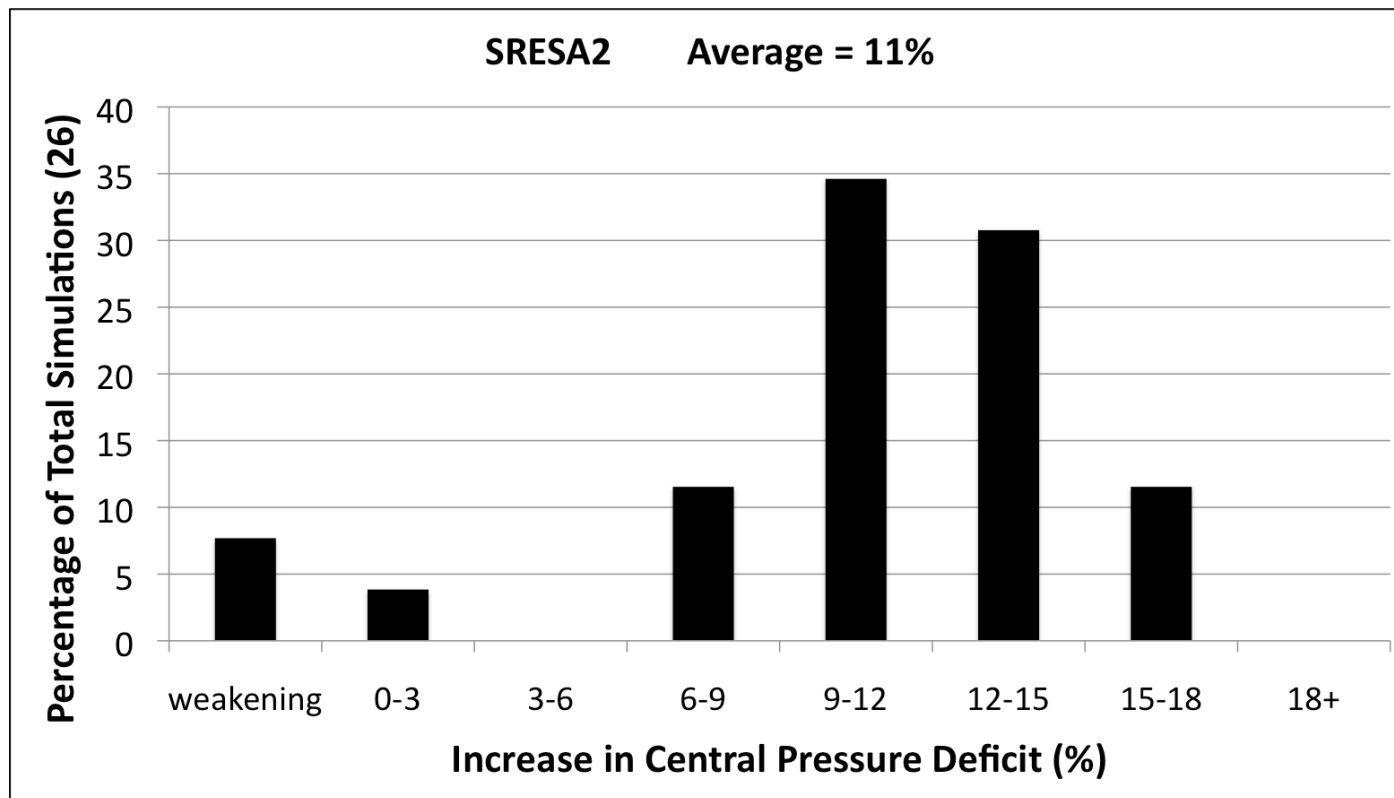


Figure 4.32: As in Fig. 4.31, except for projected changes from the SRESA2 emissions scenario.

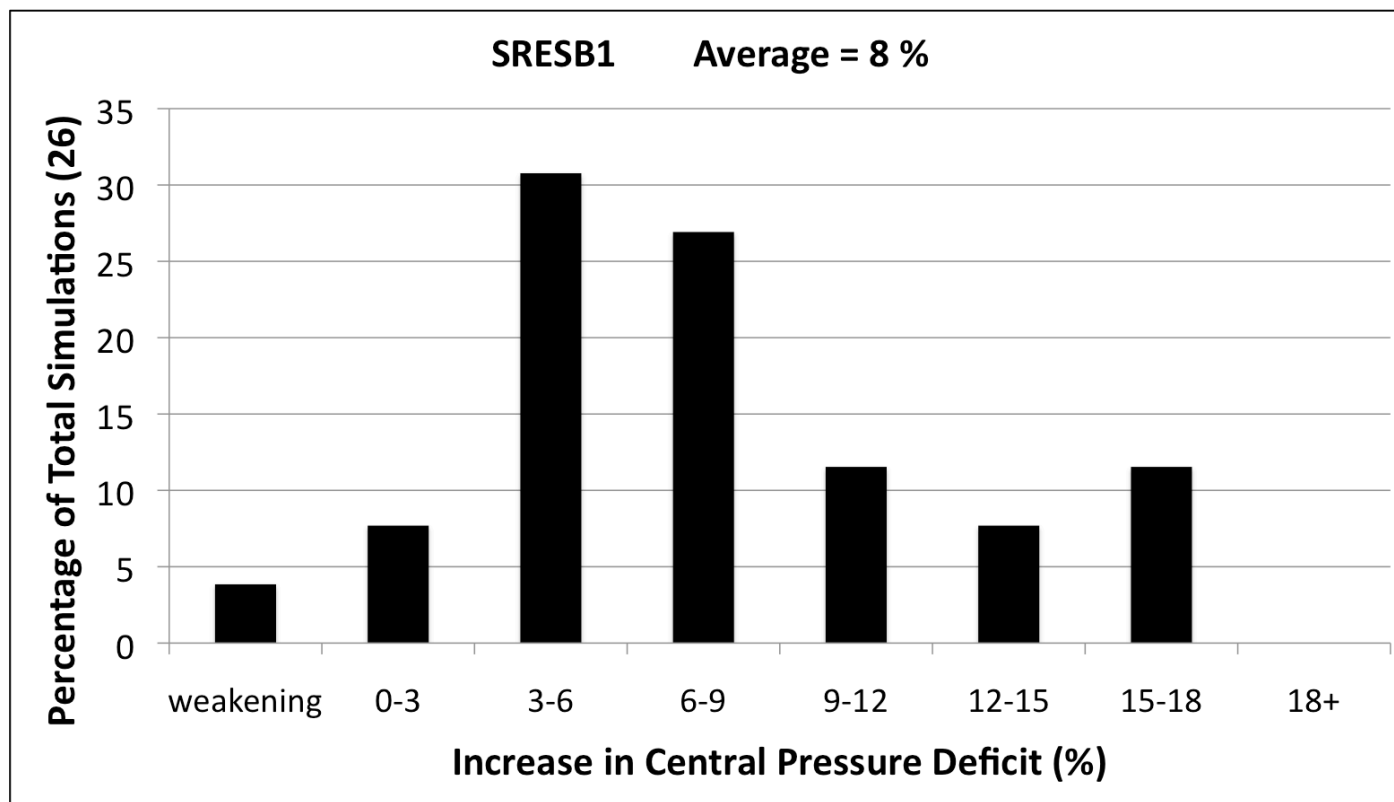


Figure 4.33: As in Fig. 4.31, except for projected changes from the SRESB1 emissions scenario.

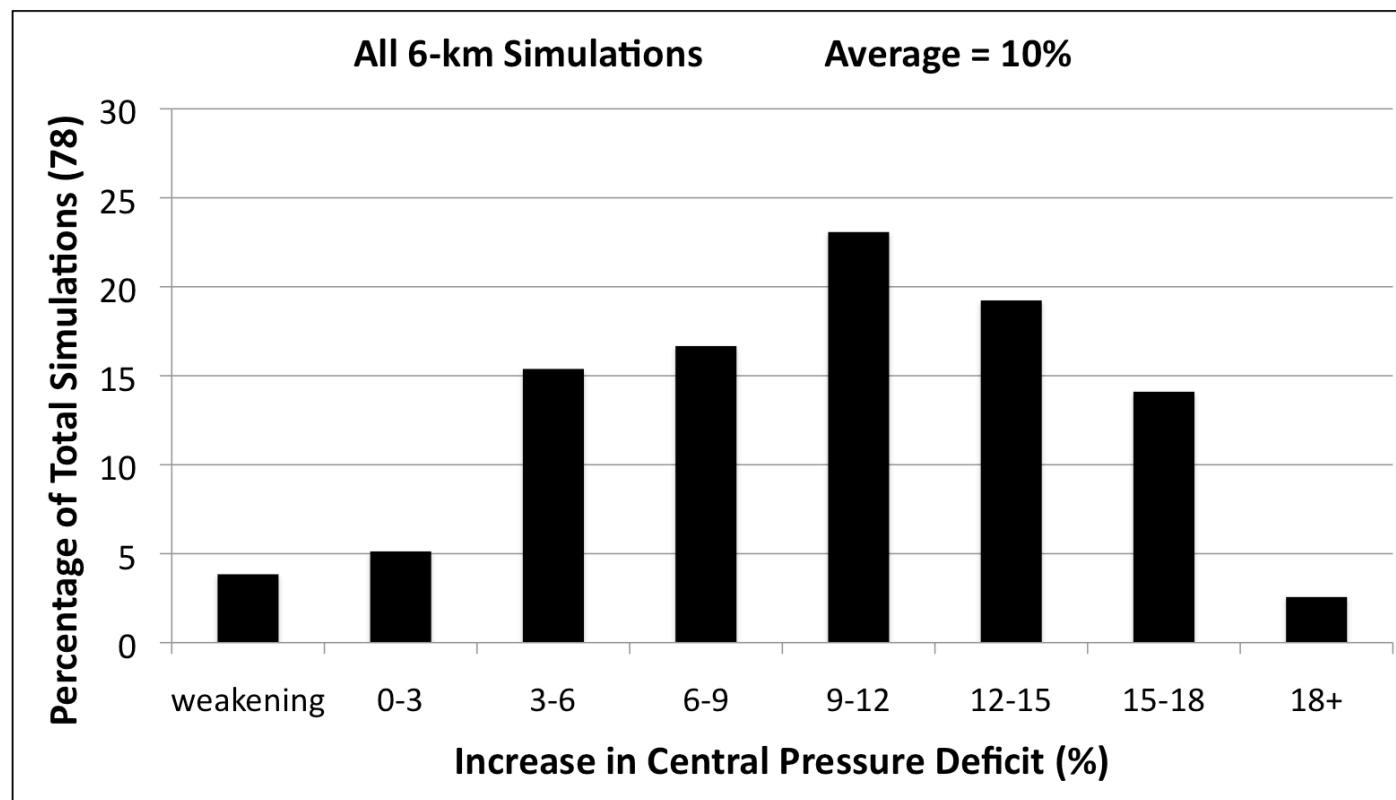


Figure 4.34: As in Fig. 4.31, except for projected changes from all emissions scenarios.

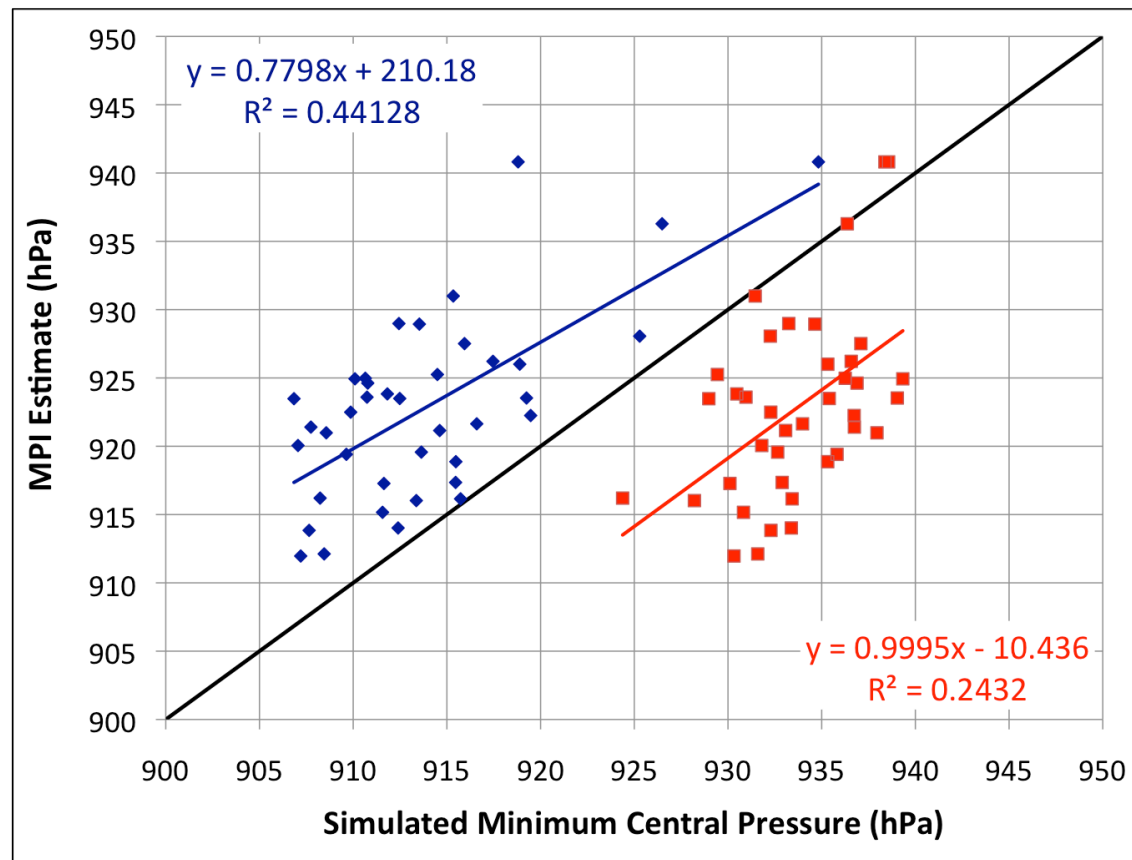


Figure 4.35: Simulated minimum central pressure versus MPI estimates (hPa). Simulations with the YSU (red) and MYJ (blue) parameterization schemes are shown separately in order to highlight the differences. Separate linear regression lines and best fit parameters are also indicated.

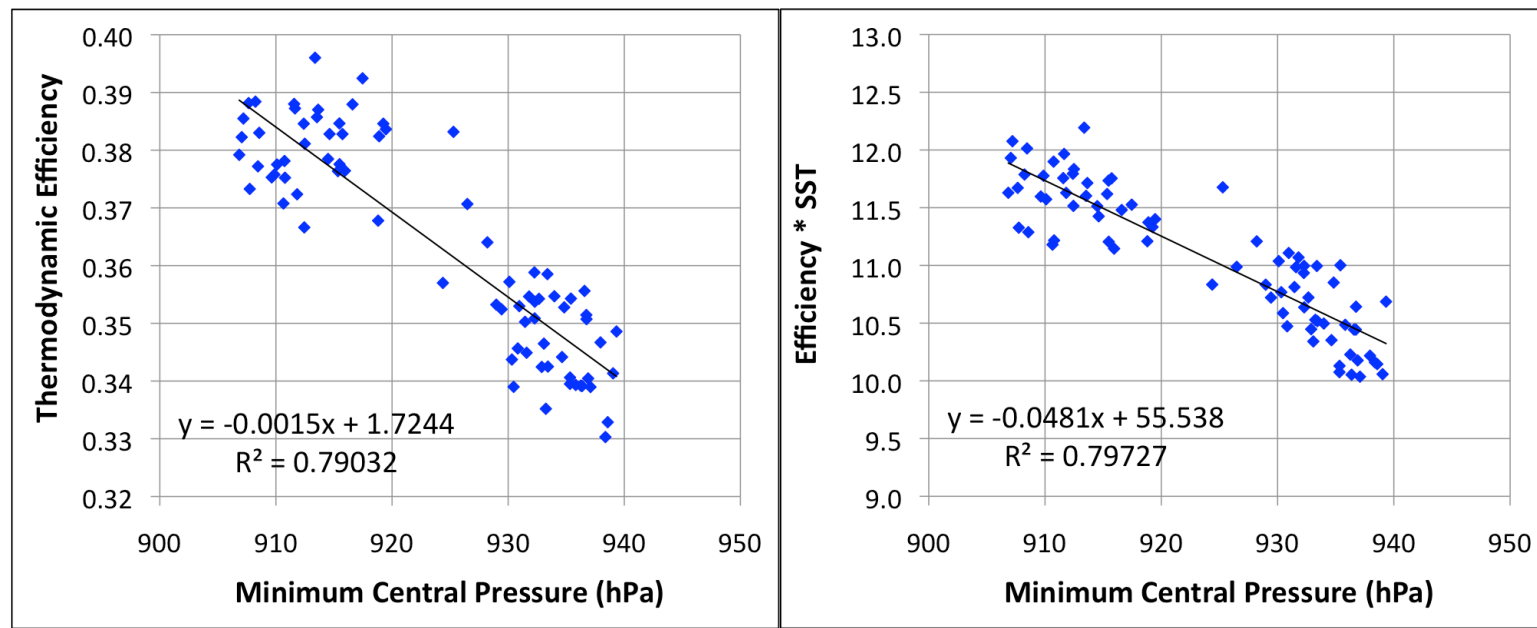


Figure 4.36: Left: minimum central pressure (hPa) versus thermodynamic efficiency in all 78 future simulations with 6-km grid spacing. Right: as in the left panel, but y-axis displays the thermodynamic efficiency multiplied by the SST.

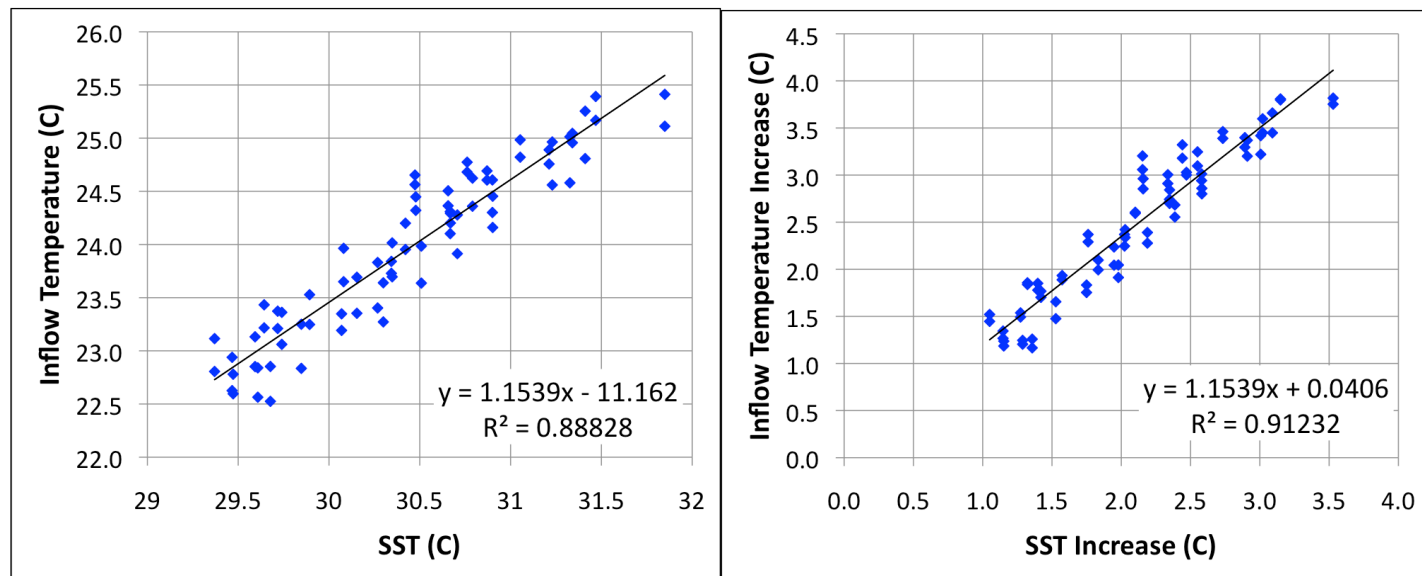


Figure 4.37: Left: relationship between SST and mass-weighted inflow temperature ($^{\circ}\text{C}$) in all 78 future simulations with 6-km grid spacing. Right: relationship between the increases (relative to control) in SST and inflow temperature ($^{\circ}\text{C}$).

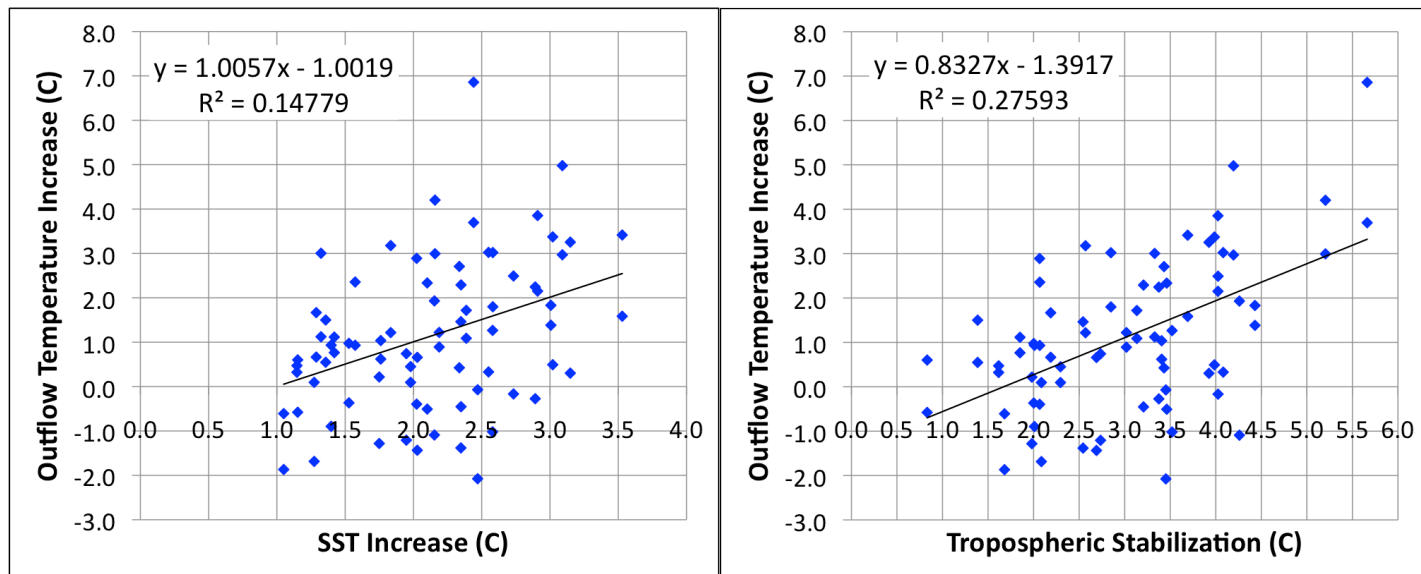


Figure 4.38: Left: relationship between SST and mass-weighted outflow temperature ($^{\circ}\text{C}$) in all 78 future simulations with 6-km grid spacing. Right: relationship between the increases (relative to control) in SST and inflow temperature ($^{\circ}\text{C}$).

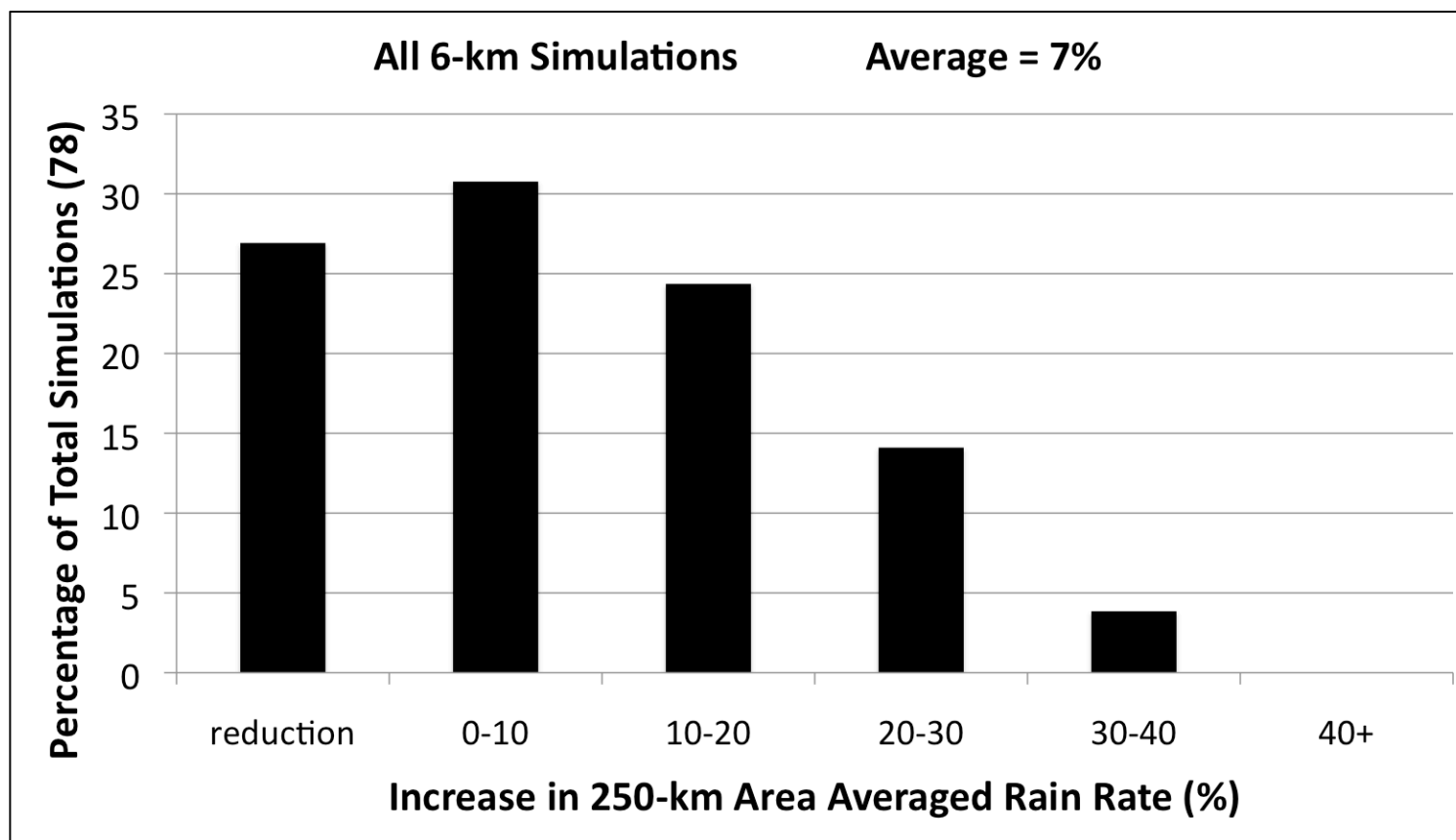


Figure 4.39: Percentage increase in area averaged rainfall in future simulations (relative to control) all 78 future simulations with 6-km grid spacing.

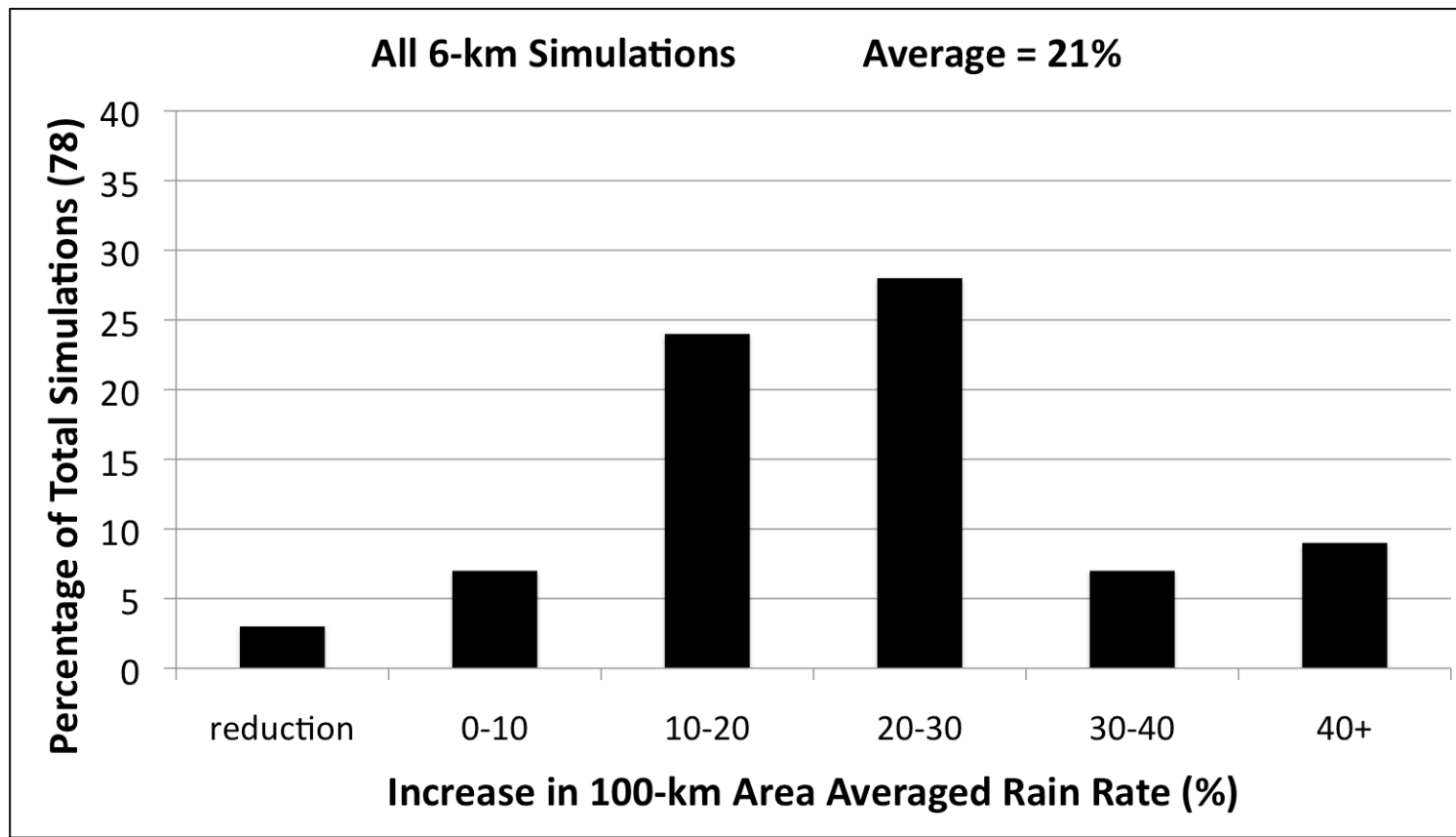


Figure 4.40: As in Fig. 4.39, except separated for each PBL scheme.

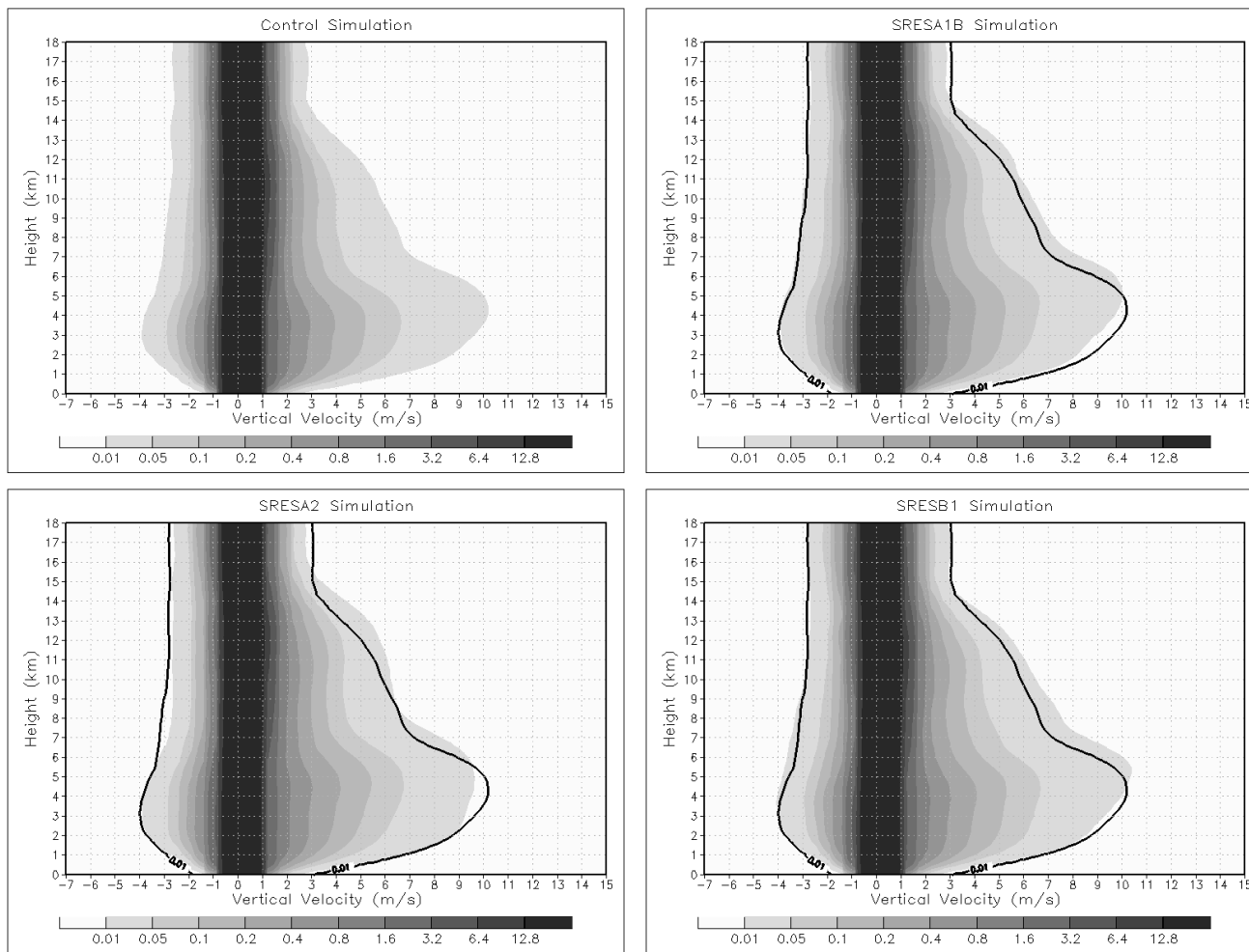


Figure 4.41: Contoured frequency by altitude diagram of vertical velocity (m s^{-1}) in the control simulation and future simulations with ensemble mean projected changes.

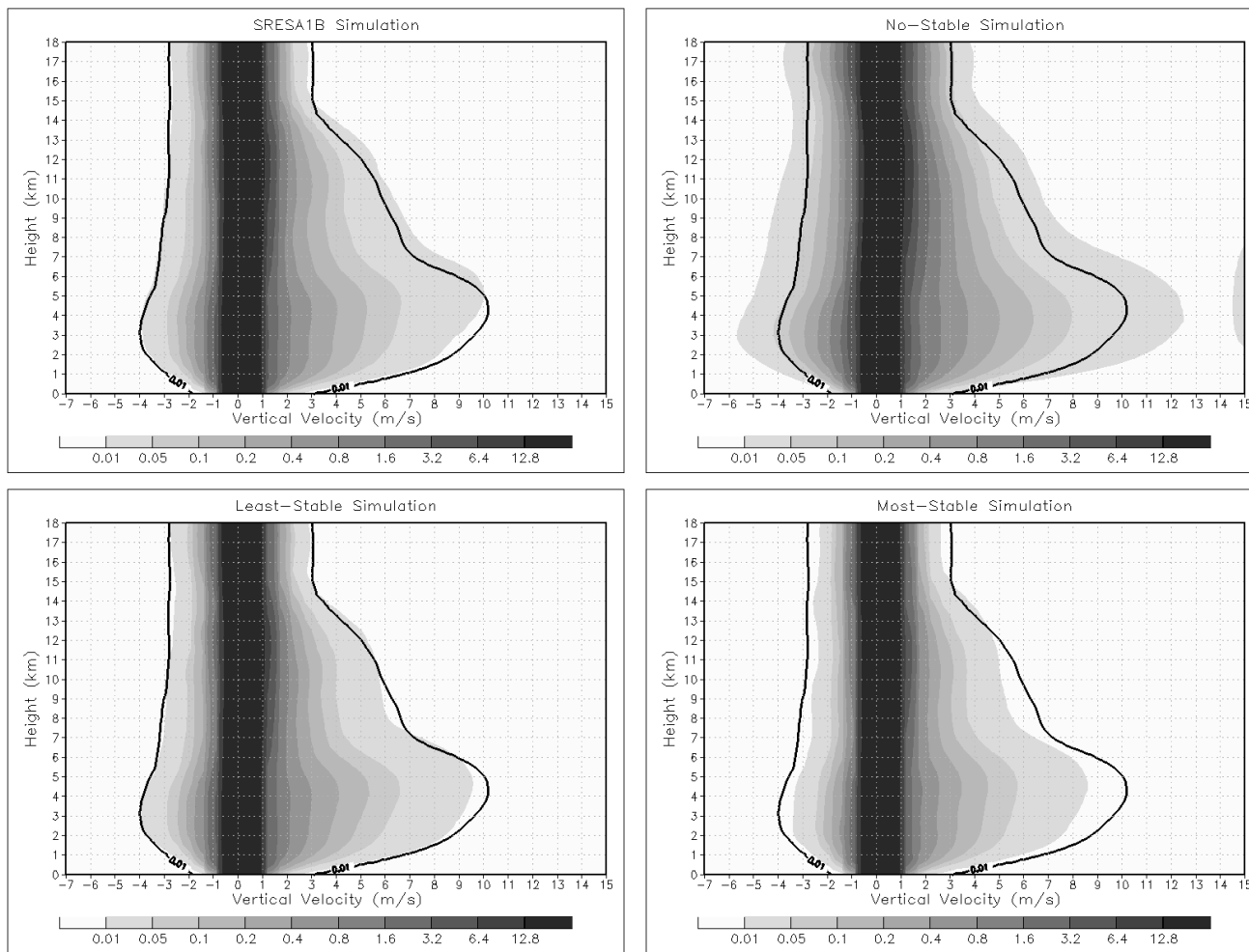


Figure 4.42: As in Fig. 4.41, except for the SRESA1B future simulation and the sensitivity experiments.

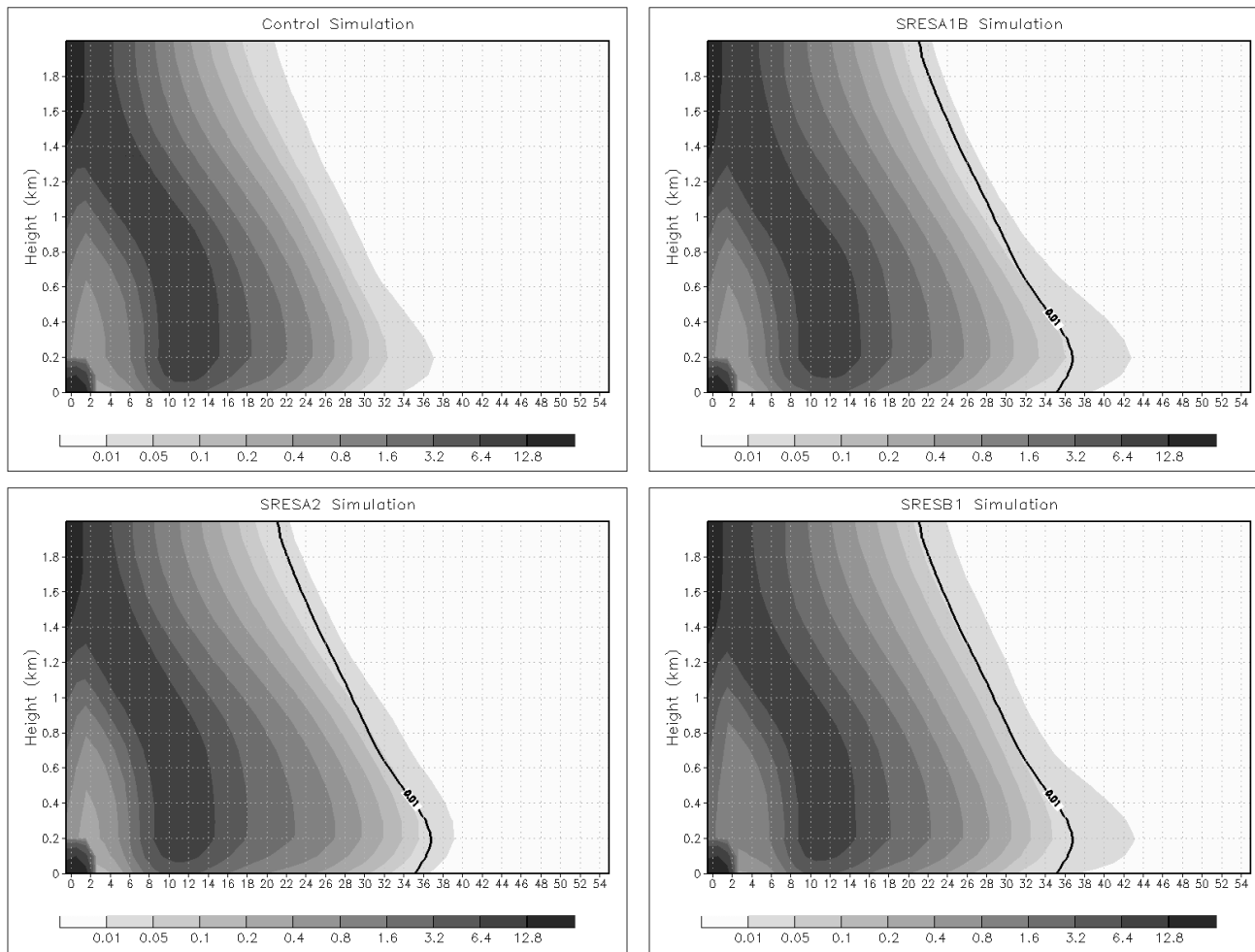


Figure 4.43: Contoured frequency by altitude diagram of inflow velocity (m s^{-1}) in the control simulation and future simulations with ensemble mean projected changes.

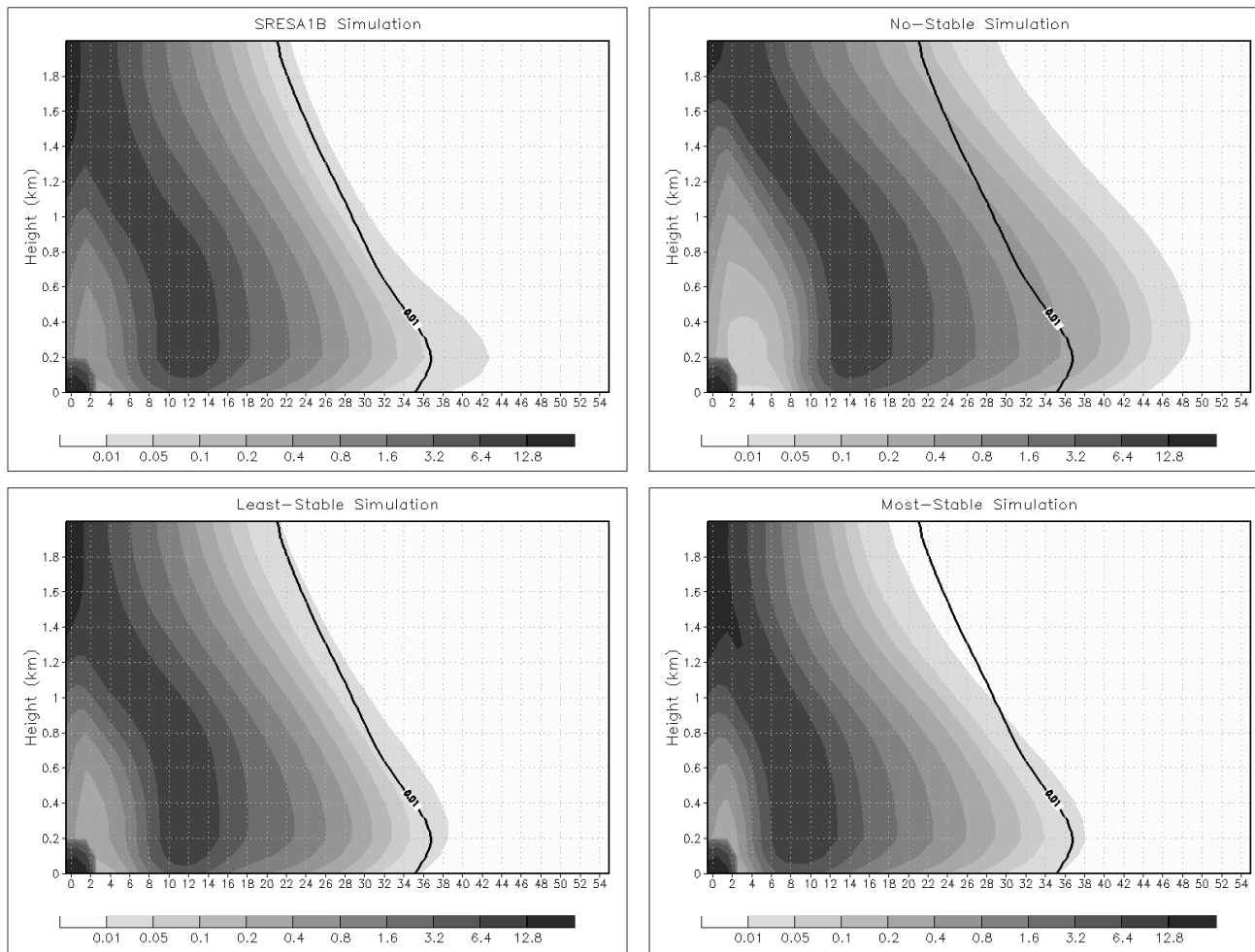


Figure 4.44: As in Fig. 4.43, except for the SRESA1B future simulation and the sensitivity experiments.

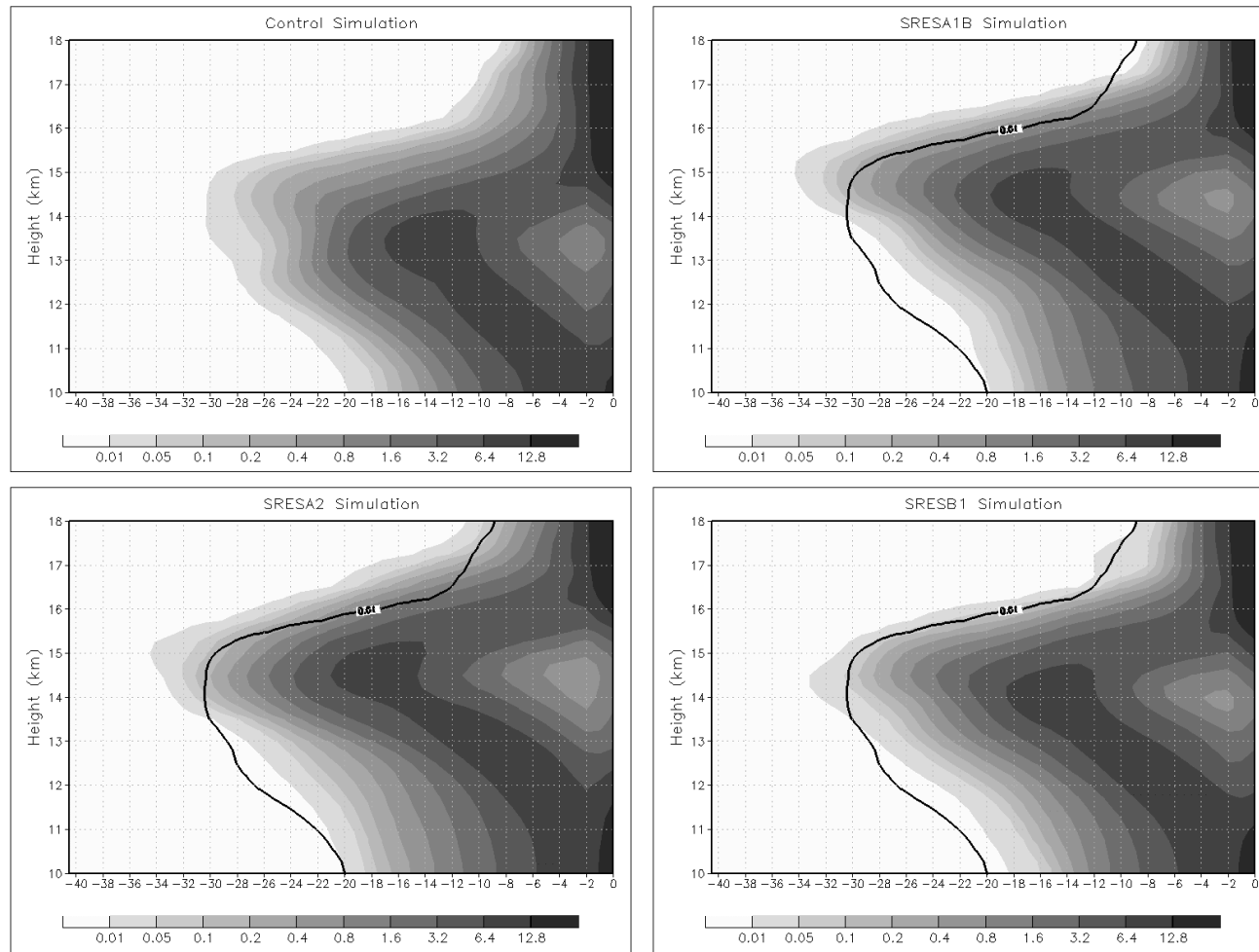


Figure 4.45: Contoured frequency by altitude diagram of outflow velocity (m s^{-1}) in the control simulation and future simulations with ensemble mean projected changes.

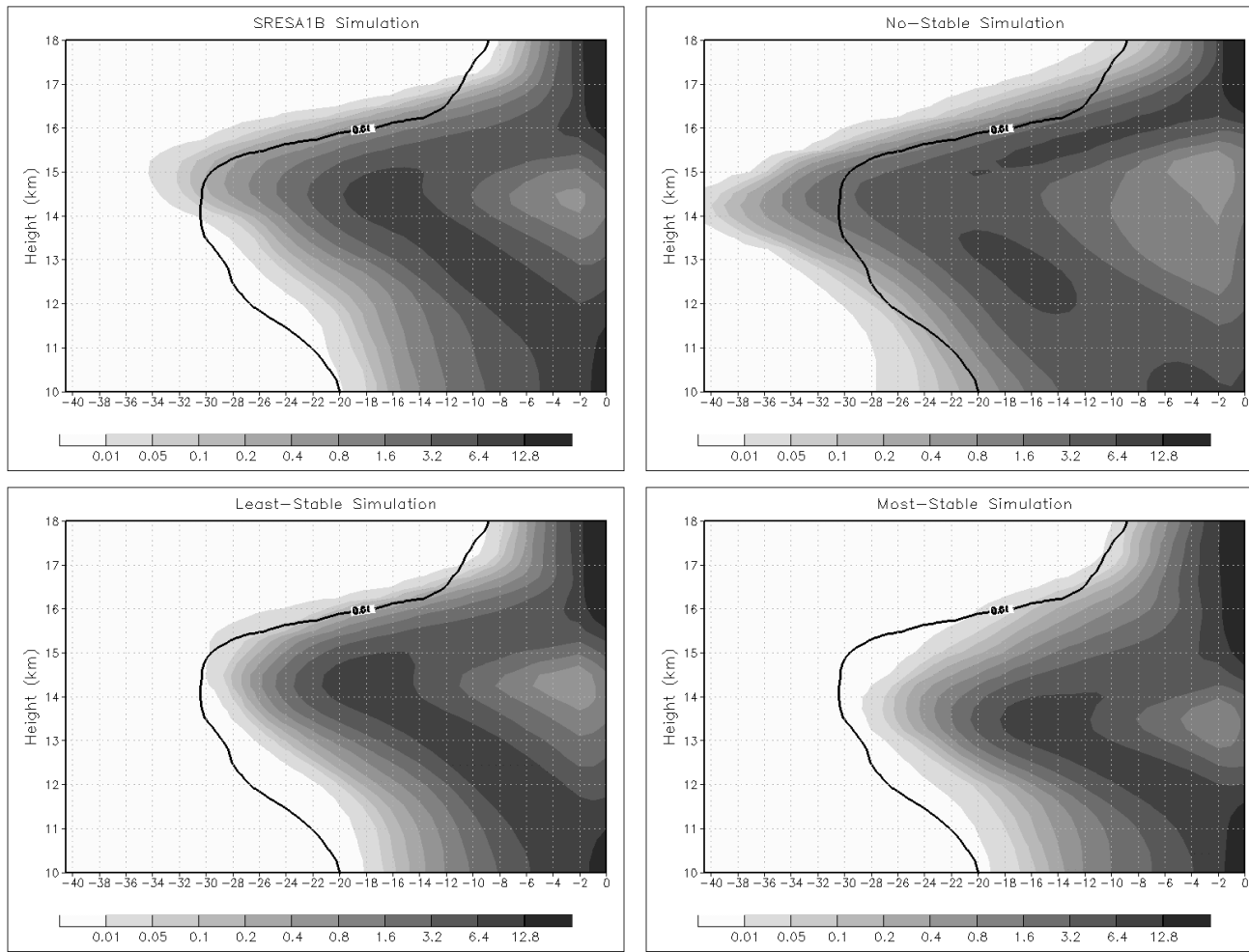


Figure 4.46: As in Fig. 4.45, except for the SRESA1B future simulation and the sensitivity experiments.

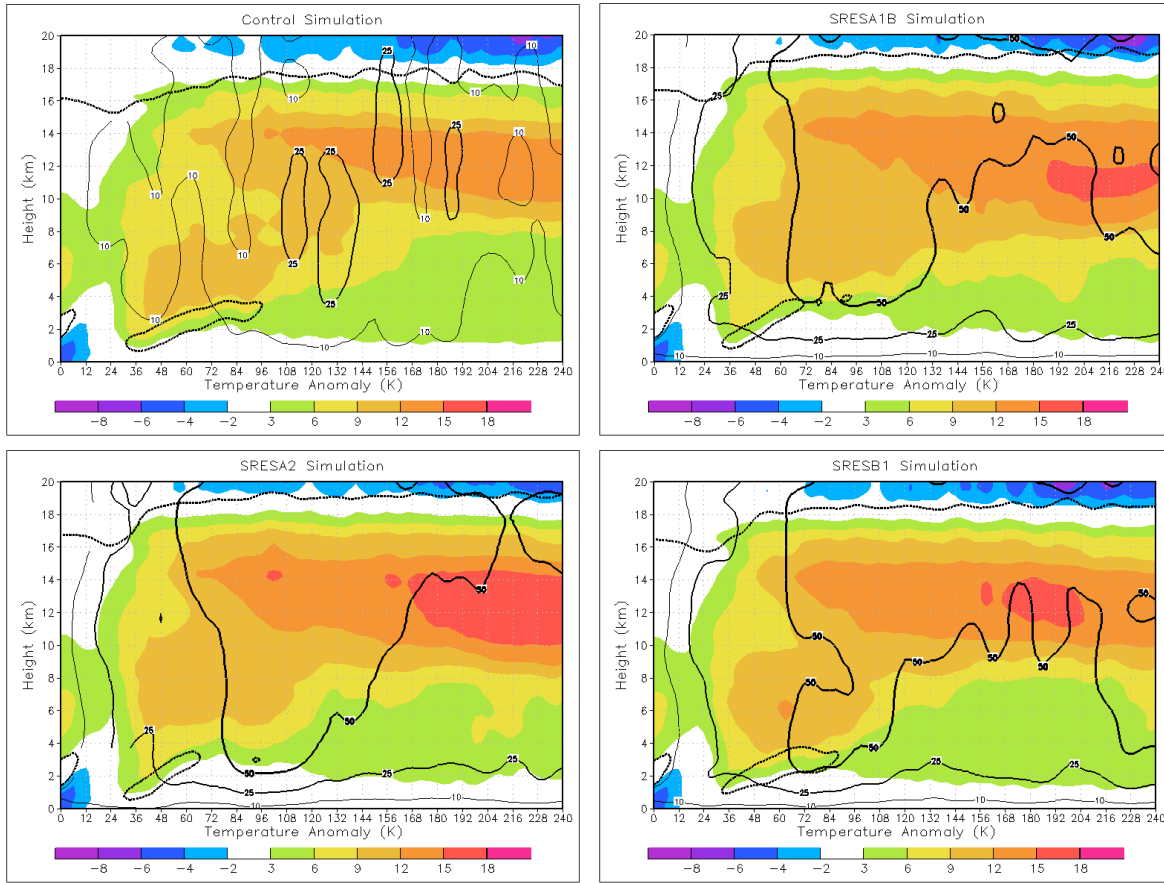


Figure 4.47: Time (ordinate) – height (abscissa) plot of eye temperature anomaly (shaded; $^{\circ}\text{C}$) and vertical velocity (black contours; cm s^{-1}). The dashed black contours indicate the eye subsidence (cm s^{-1}) and the dashed line represents the thermal tropopause, where the lapse rate becomes less than 2 K km^{-1} . The “eye” is defined as the 5 grid cells located within 2-km of the TC center, although the results are not sensitive to this choice.

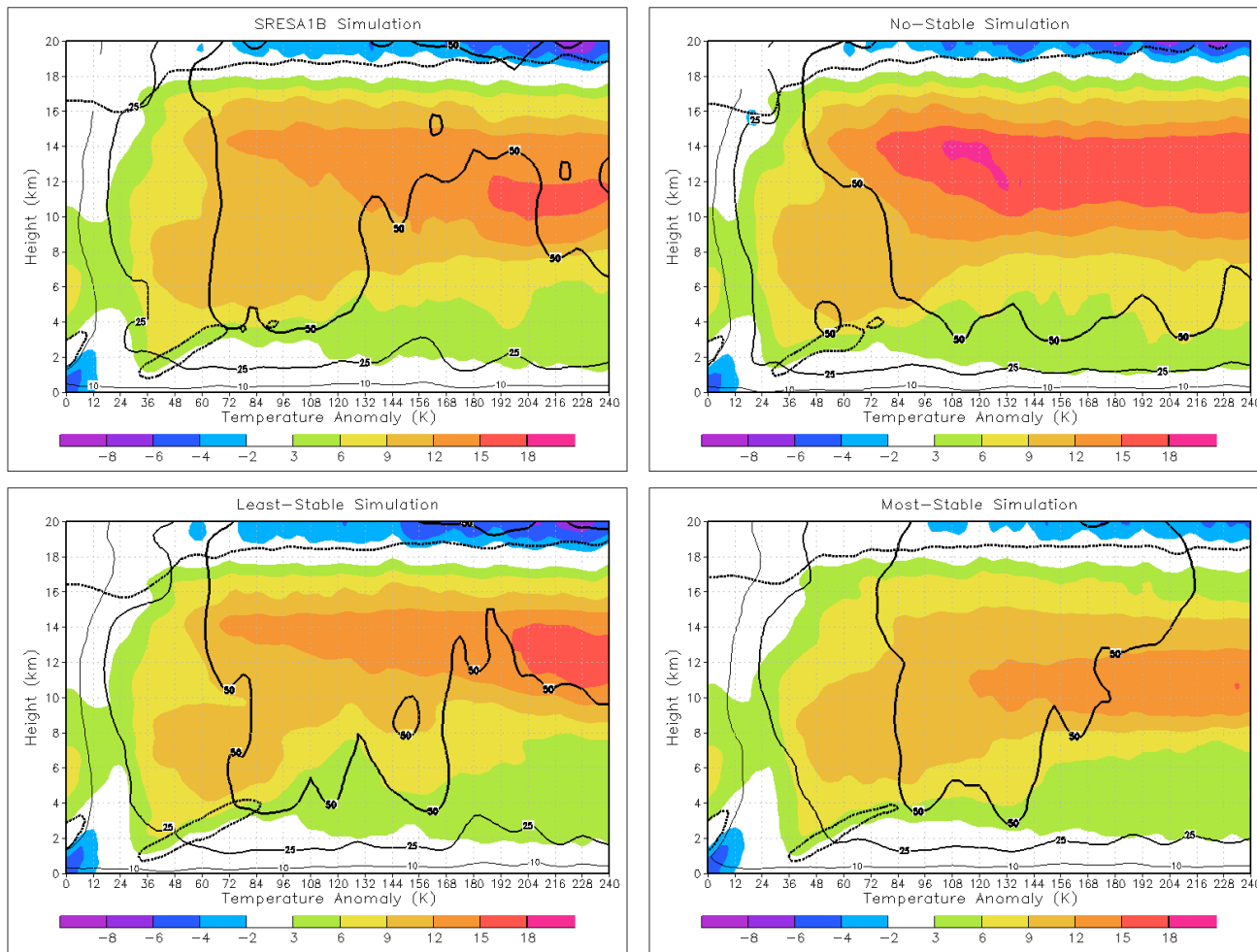


Figure 4.48: As in Fig. 4.47, except for the SRESA1B simulation and the sensitivity experiments.

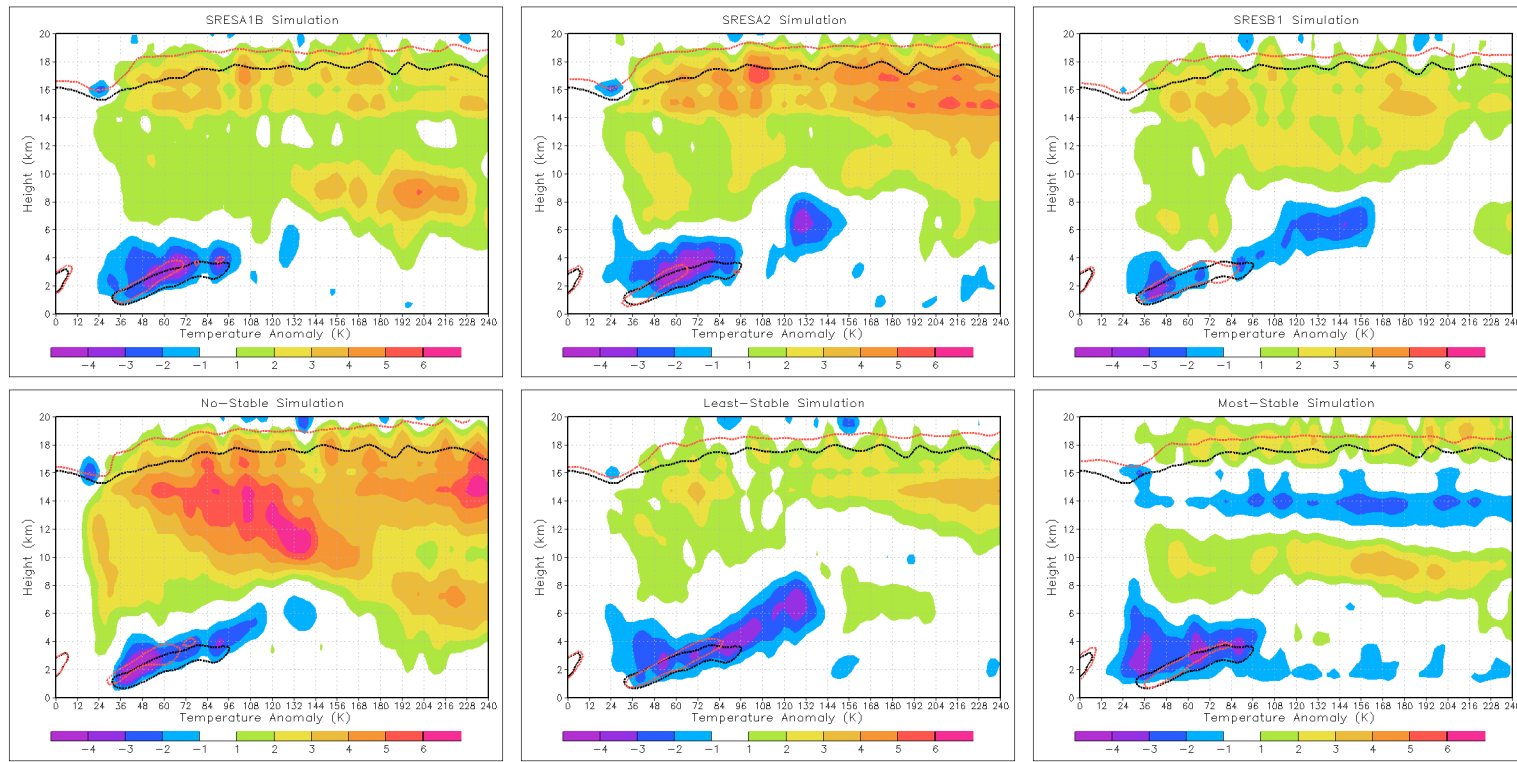


Figure 4.49: Time-height plot of eye temperature anomaly difference ($^{\circ}\text{C}$; shaded, relative to the control simulation). The thermal tropopause, where the lapse rate becomes less than 2 K km^{-1} , is dashed black in the control and red in the future simulation.

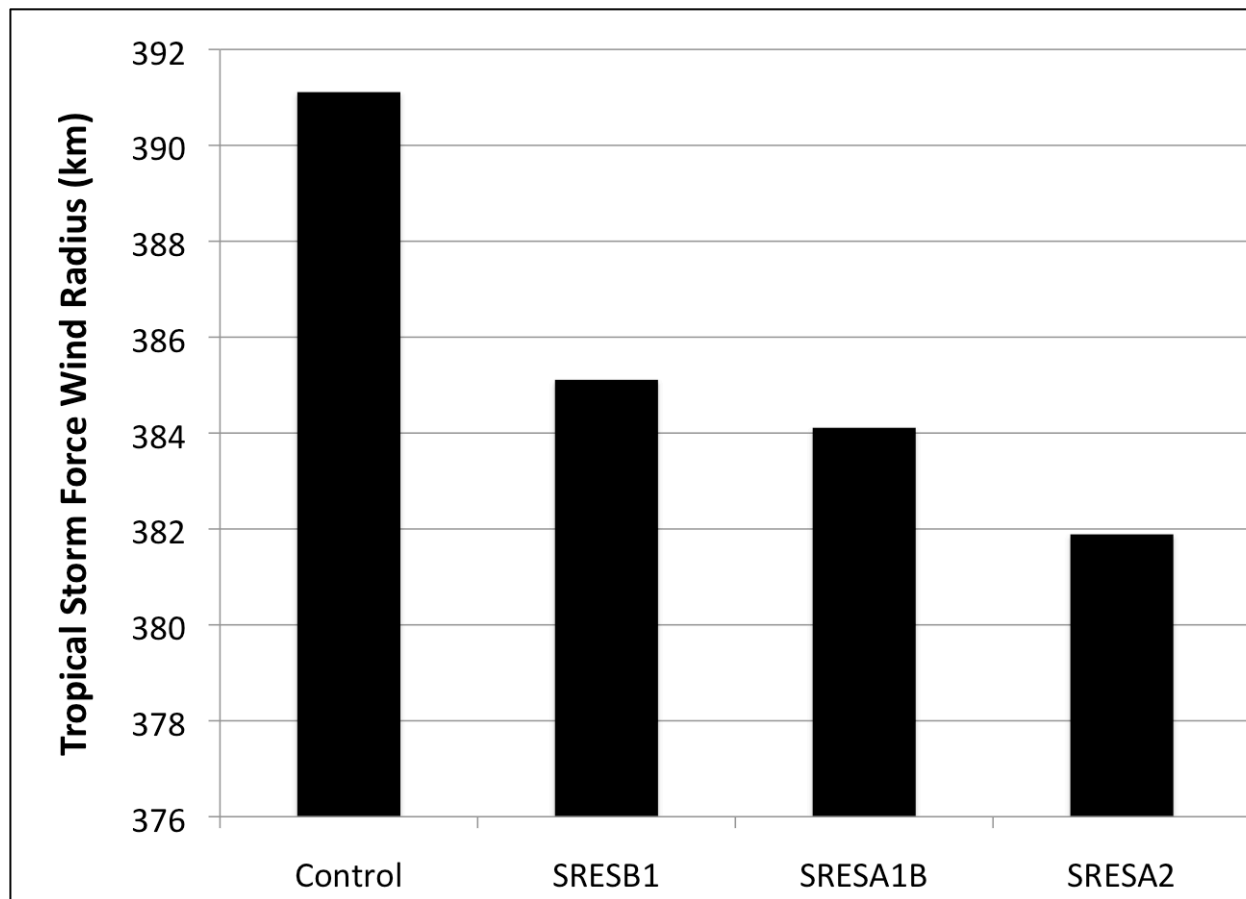


Figure 4.50: Average maximum radius of TS force wind (km). For each simulation within each large-scale environment, the maximum radius of TS force wind was averaged over simulation hours 96 – 120.

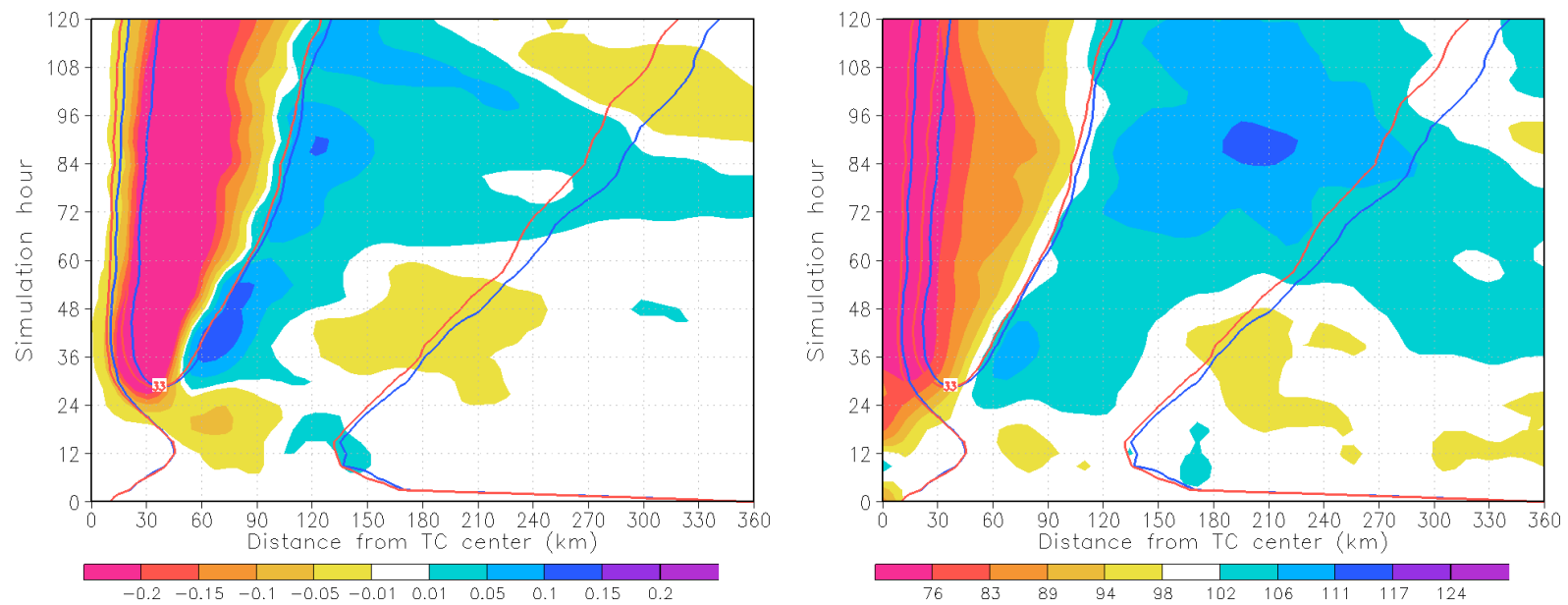


Figure 4.51: Left panel: relative to the control simulation, the change in hourly rain rate (in hr^{-1} ; shaded, positive denotes heavier rainfall in control simulation). Tropical storm and hurricane force wind contours for the control simulation (blue) and SRESA1B simulation (red). Right panel: relative to the control simulation, the percentage change in surface pressure gradient (shaded; positive denotes larger gradient in control simulation). Wind contours as in left panel. Future climate values averaged over all 26 future simulations with projected changes from SRESA1B GCMs.

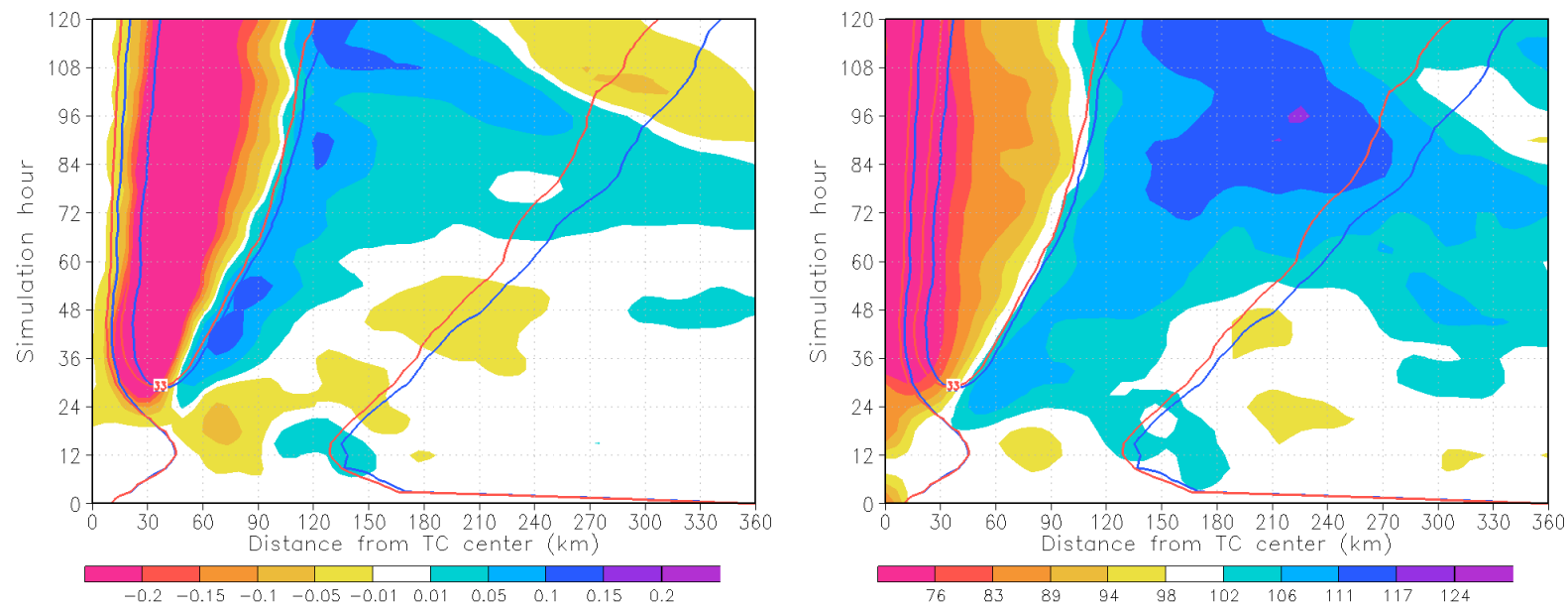


Figure 4.52: As in Fig. 4.51, except for the SRESA2 simulations.

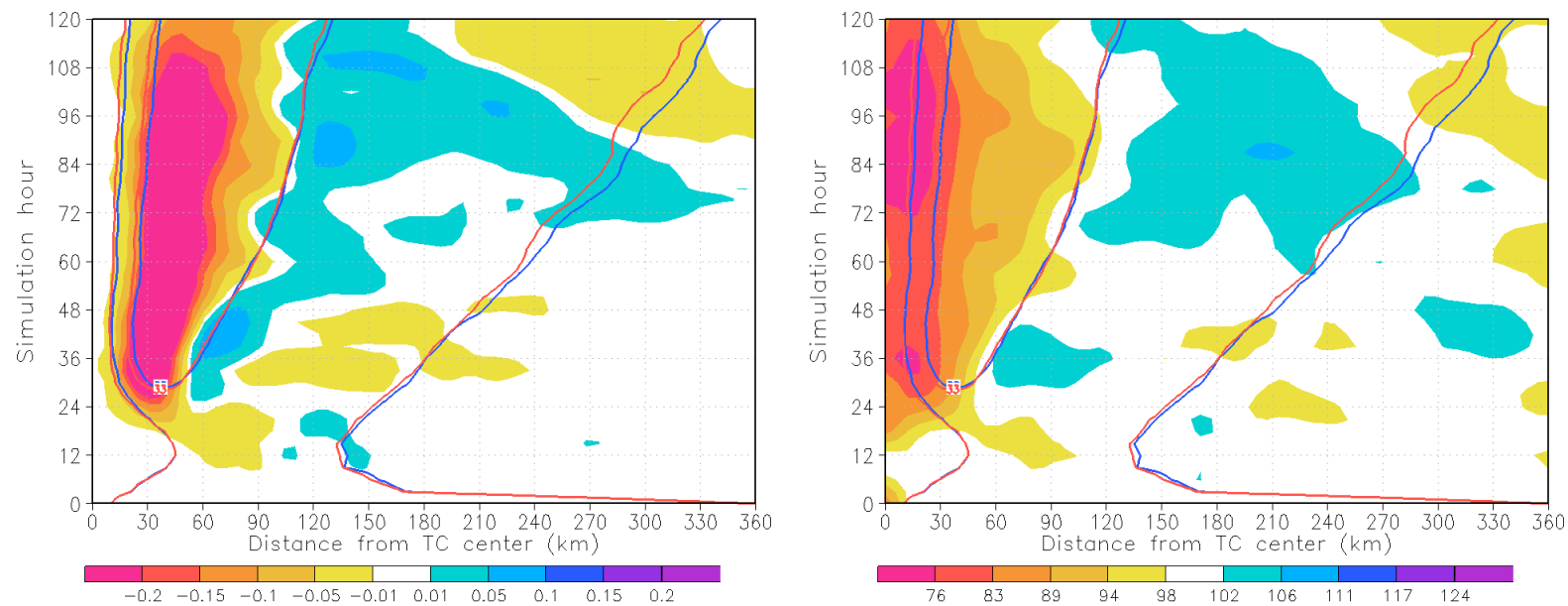


Figure 4.53: As in Fig. 4.51, except for the SRESA2 simulations.

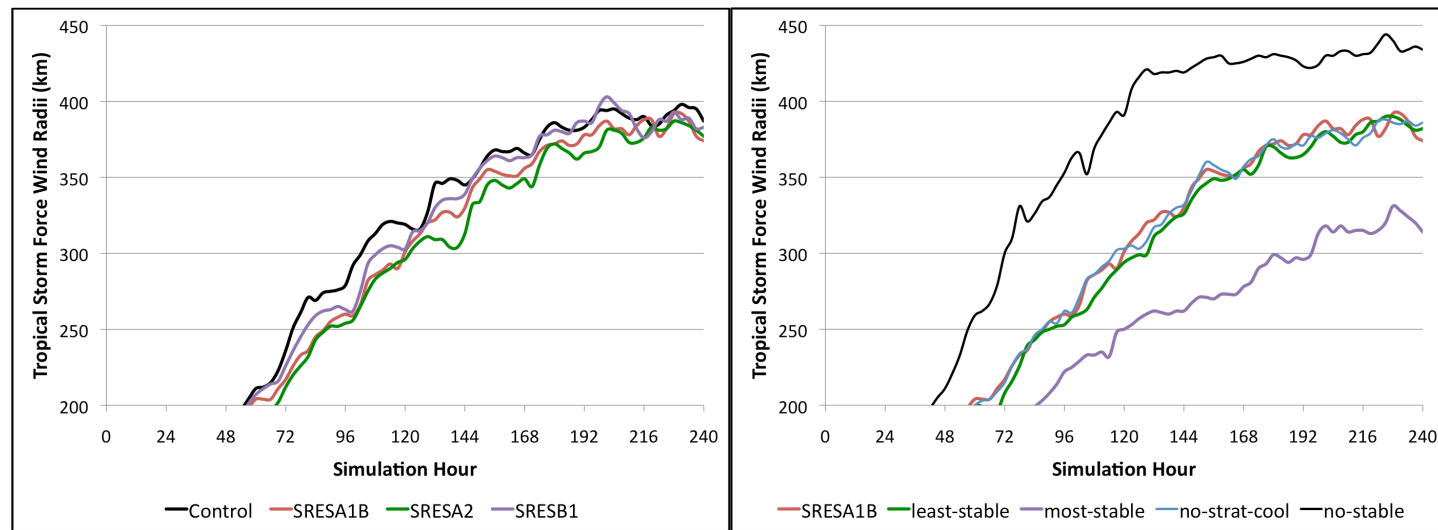


Figure 4.54: Tropical storm force wind radii (km) in simulations with 2-km grid spacing.

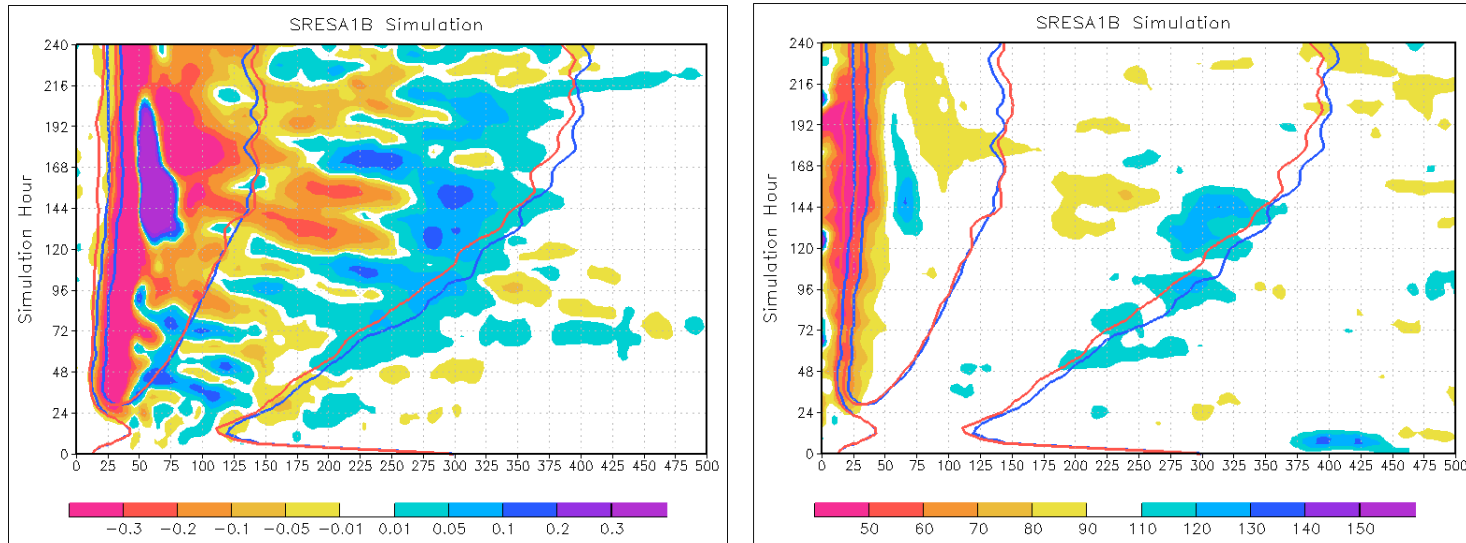


Figure 4.55: As in Fig. 4.51, except for the SRESA1B simulations with 2-km grid spacing.

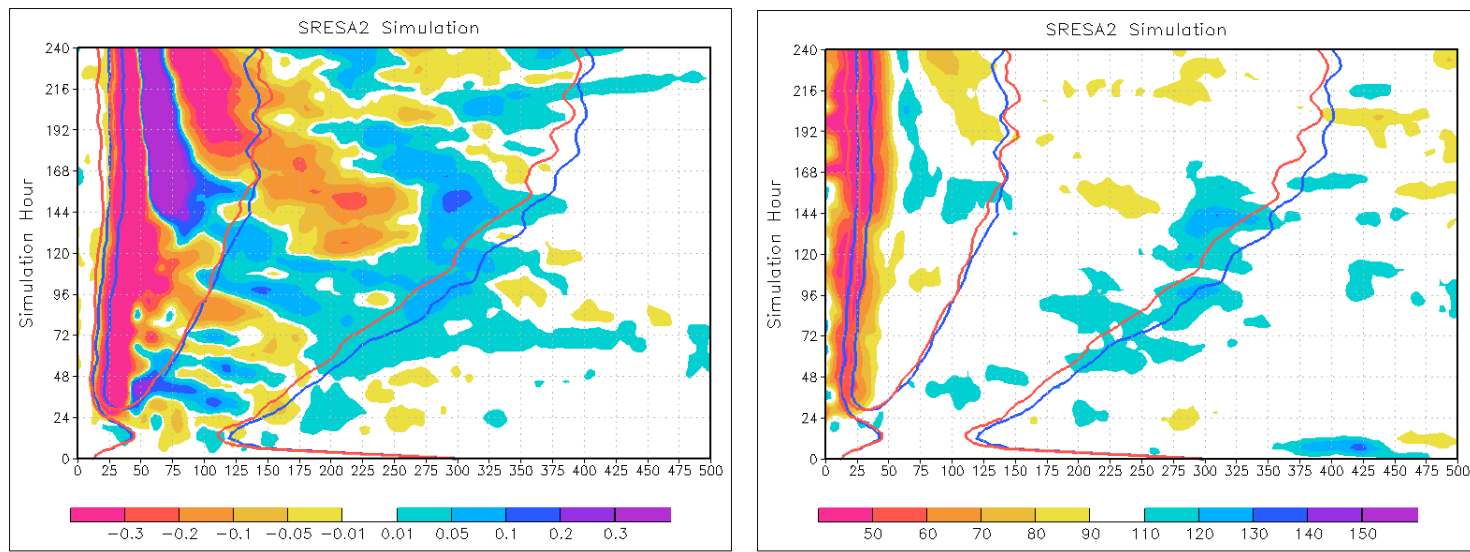


Figure 4.56: As in Fig. 4.51, except for the SRESA2 simulations with 2-km grid spacing.

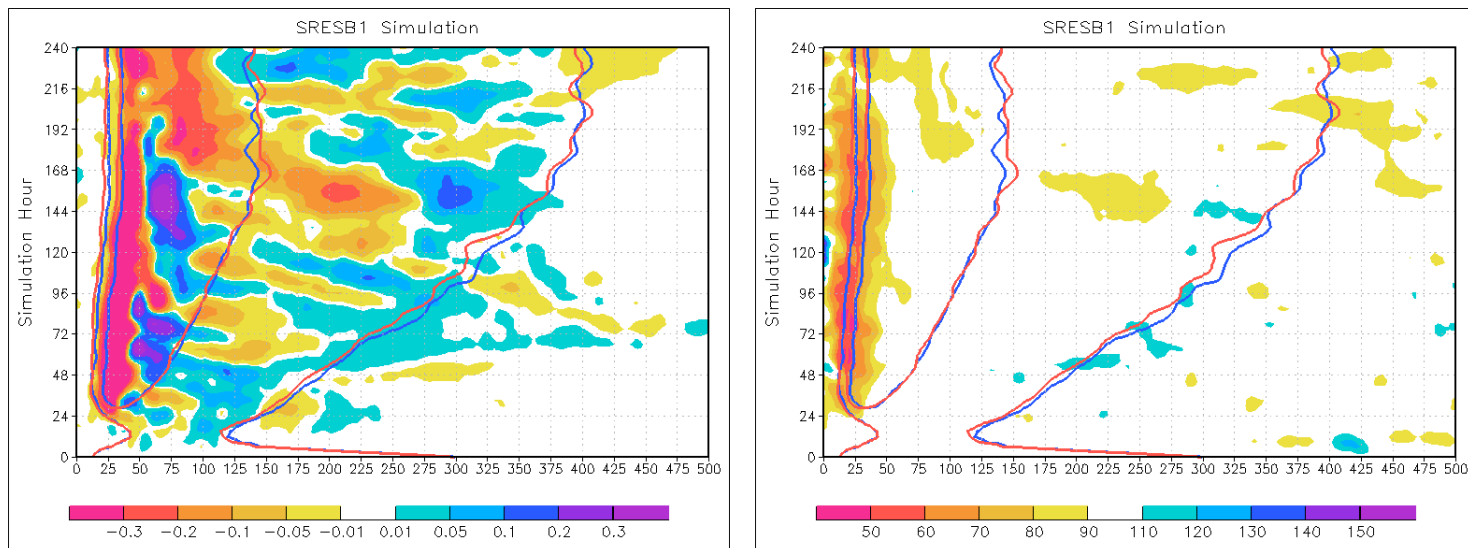


Figure 4.57: As in Fig. 4.51, except for the SRESB1 simulations with 2-km grid spacing.

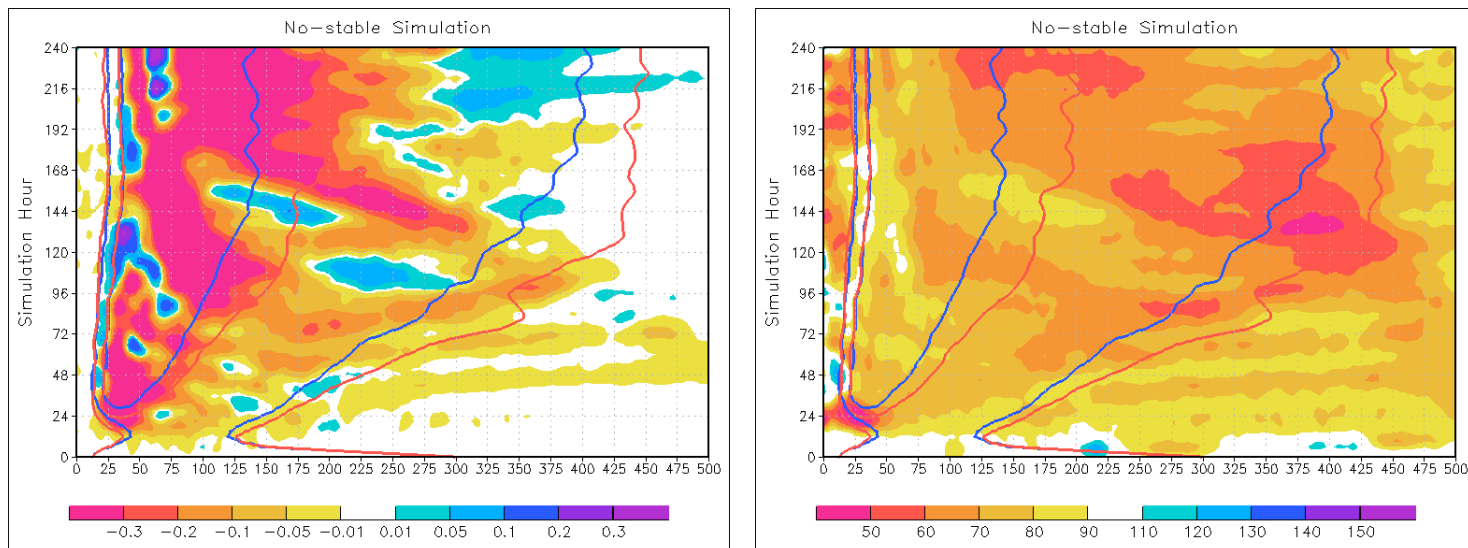


Figure 4.58: As in Fig. 4.51, except for the no-stable simulations with 2-km grid spacing.

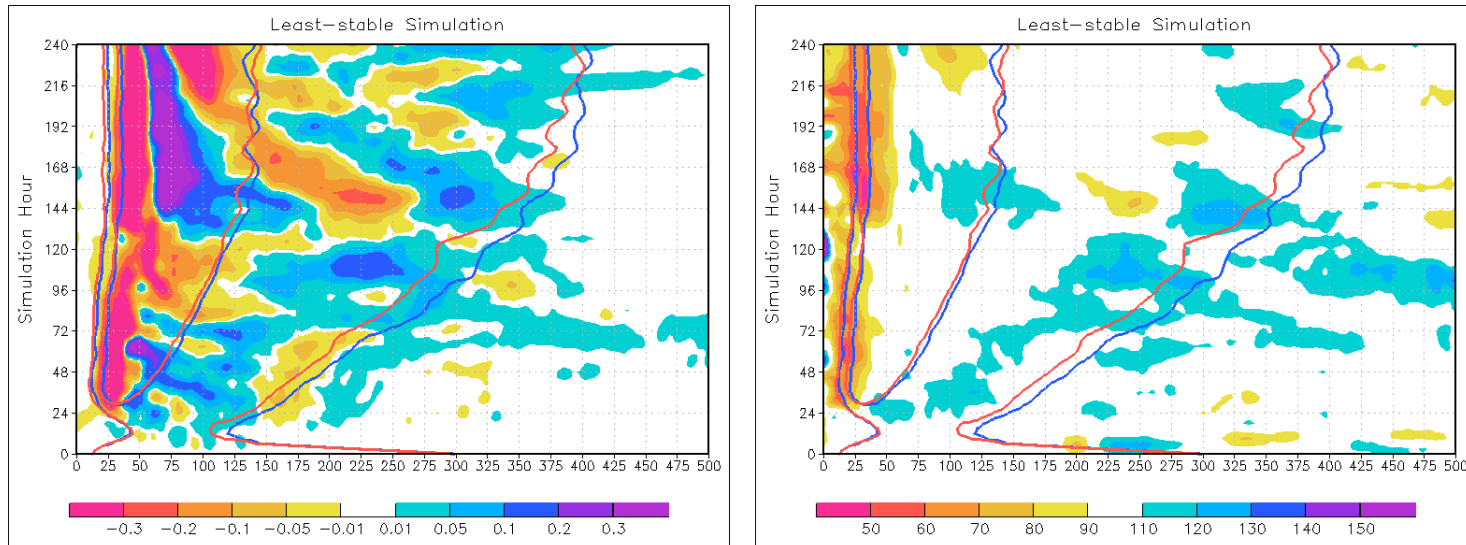


Figure 4.59: As in Fig. 4.51, except for the least-stable simulations with 2-km grid spacing.

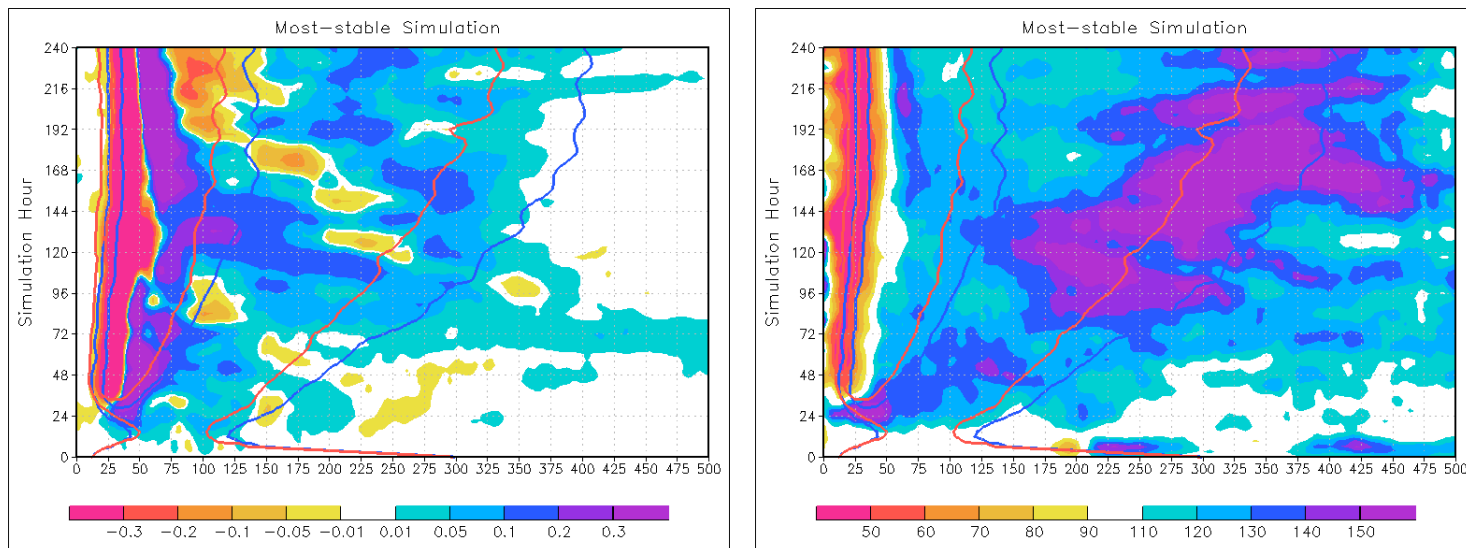


Figure 4.60: As in Fig. 4.51, except for the most-stable simulations with 2-km grid spacing.

Chapter 5

Discussion and concluding remarks

Tropical cyclones are the costliest natural disasters in the United States (Pielke and Landsea, 1998), and the cost associated damage from TCs has been enhanced in the last few decades by a significant increase in population growth in coastal and near coastal regions; as a result the United States is now more vulnerable to TCs than ever before (e.g., Sheets 1990; Marks et al. 1998; Pielke et al. 2008). This study serves to investigate two separate but somewhat related questions pertaining to TCs; what controls TC size, and how will climate change influence TCs. Carefully constructed idealized TC simulations were utilized in order to isolate the impact of specific environmental factors on TC intensity, size, and structure. For the purposes of this study, idealized simulations were superior to real-cases as they allowed for examination of specific hypotheses. In the following sections, the methods and results will be briefly highlighted, and broader implications and future research directions will be discussed.

5.1 TC Size

The size of a TC is important for a number of reasons, including its role in influencing TC impacts, environmental interaction, and also track. Specifically, the size of a TC, in addition to intensity, has a direct influence on the extent of evacuations, ship re-routing, along-track timing of the arrival of storm conditions, and the duration of high winds and storm total rainfall at a given location. Several recent landfalling TCs, such as Katrina and Ike, caused significant damage along the Gulf coast in part due to their large size. Despite the importance of TC size, the physical mechanisms determining this have received limited attention in the scientific literature (e.g., Liu and Chan 2002).

The work presented here investigates the impact of relative humidity on TC size in idealized WRF simulations. It is hypothesized that outer-core precipitation influences TC

size, and therefore environmental factors that influence the amount and extent of outer-core precipitation in turn influence TC size. Outer-core precipitation affects TC size through the diabatic generation of lower-tropospheric PV, which can amalgamate with the TC central PV tower or remain at radius. One environmental factor, relative humidity, was analyzed here, although it is speculated that other environmental factors such as static stability also likely play a role in influencing TC size. The influence of changes in static stability due to climate change on TC rainfall and size were investigated as well, and will be summarized in subsequent discussion.

Four idealized high-resolution numerical simulations with the WRF model were performed in order to test the hypothesized sensitivity of TC size to environmental humidity. Identical vortices, placed within a moist envelope, were allowed to evolve in environments with initial relative humidity varying between 20 and 80% outside of the TC core. Results are consistent with the hypothesis that moist environments favor the development of larger TCs, with progressively larger storms evident with each incremental RH increase. Differences in TC size between the runs were substantial, with the TC in the 80RH run exhibiting a RMW that was triple that in the 20RH run by hour 240 (Fig. 3.3). During the simulation period, moisture fluxes led to similar moisture content in the boundary layer in all simulations despite the differences in the initial moisture specification (Fig. 3.16). Large differences remained, however, above the boundary layer in the middle troposphere (\sim 3 – 7 km) and outside of the initial moist envelope, where relative humidity values remained up to \sim 50% less in the 20RH simulation than in 80RH. A close correspondence between the inward protrusion of the dry air and the formation of persistent precipitation was found, indicating that the presence of dry air was responsible for differences in simulated precipitation outside of the eyewall.

The more moist runs did not exhibit heavier eyewall precipitation or a more intense cyclonic PV tower; in fact, the 80RH simulation featured a broader, more diffuse eyewall precipitation PV structure (Figs. 3.28, 3.31). However, more precipitation in outer rainbands occurred in the more moist simulations, which led to diabatic production of lower

tropospheric PV (Fig. 3.32). Lower-tropospheric diabatic PV production in spiral bands led to a broadening of the cyclonic PV distribution both through the contribution to a broadening of the central PV tower as PV filaments spiraled inwards, and also through the presence of enhanced cyclonic PV near the spiral bands at larger radial distances from the core. Control-volume analysis revealed that the inward flux of PV during a period of growth in the 80RH simulation was \sim 5 times larger relative to that in the 20RH simulation during this same time period, consistent with much more vigorous rainband activity in the 80RH simulation (Fig. 3.35). The TC in the 80RH simulation also exhibited eyewall replacement cycles, unlike the TCs in drier simulations.

Growth of the TC wind field was also found in the initially dryer simulations, although to a lesser extent. After a sufficient period of moistening, spiral band activity began to increase in all of the simulations, although the delay was longer in the initially dryer simulations. Feedback mechanisms likely enhance the wind field expansion. Rainband activity leads to an increase in the outer-core wind speed and the lateral extent of radial inflow, and subsequently an increase in angular momentum import, which subsequently leads to increased winds, moisture flux, and precipitation, in a positive feedback loop. As the wind field and zone of diabatically generated lower-tropospheric PV expands, the radial annulus that exhibits a favorable PV gradient for Rossby wave propagation may also broaden, which we speculate could allow further outward radial expansion of spiral bands. As the cyclonic wind field expands, heating in spiral bands is more effective in lower tropospheric PV generation, and the local Rossby radius decreases, leading to a stronger balanced response to heating at an increasingly large radius (e.g., Bister 2001). Also, as the cyclonic PV distribution grows in size, the strengthening outer wind field leads to enhanced upward heat and moisture flux over a larger area (Fig. 18), which could serve to further enhance precipitation and diabatic PV generation in outer spiral bands in a positive feedback. These feedback mechanisms suggest that once a TC begins growing in size it is likely to continue to do so.

Although not tested here, the size of the initial disturbance likely also plays a role in TC size. Emanuel (1986) derived an analytical expression for the ratio of the RMW and extent of the outer wind field (his eq. 46) and notes that compensation will occur with changes in latitude or sea-surface temperature. Rotunno and Emanuel (1987) test these ideas with a numerical model, and conclude that the horizontal size of a TC is determined by the size of the initial disturbance. Recently, Wang (2010) concluded that initial vortex size plays is a more important factor in determining mature TC size than the environmental relative humidity, although the size of the initial disturbance and the environmental water vapor in the near-TC environment are related to one another. We concur that the size of the initial disturbance is an important factor in determining TC size, as the breadth of the cyclonic PV tower is closely tied to the size of the initial disturbance. However, in our study, we use an identical initial disturbance in each simulation, yet obtain disturbances that differ in size by a factor of 2. Our results are not inconsistent with the aforementioned, yet they highlight differences in outer-core precipitation due to environmental humidity as an additional factor.

5.1.1 Additional implications and future research directions

Environmental humidity is but one of several factors that could serve to regulate the spatial extent of precipitation with radius, and the outer-core latent heating need not be restricted to spiral bands. Research conducted on climate change and TCs indicates that tropospheric stability influences the amount of outer-core precipitation, with smaller TCs present in more stable environments. Although not investigated in detail, it is likely that differences in tropospheric stability influence observed TC sizes, although further analysis would be required to determine if observed differences in stability were large enough to influence precipitation and size. TC interaction with a frontal boundary or with an upper-level trough, topographic lift, and other mechanisms leading to asymmetry of the TC precipitation shield during extratropical transition (ET) could also affect the diabatic PV distribution and TC size. The noted tendency for TC wind-field expansion during ET (Jones et al. 2003) is consistent with our results.

The use of idealized modeling to test our initial hypotheses constitutes a first step towards a more comprehensive hypothesis test, with several avenues of future research possible. Additional idealized experiments could be performed to examine the sensitivity of TC size to environmental humidity at different altitudes; this information would hold operational significance because it would allow forecasters to predict TC size based on measured environmental humidity. It would be valuable to perform actual case studies to complement the idealized simulations presented here. This would also inform observational data collection in ways to optimize the accuracy of TC prediction in numerical models.

Observational data must be analyzed to corroborate these results, as analysis of observed TC size and the surrounding environments would provide an additional test of our hypothesis. If a link is found, then this suggests that examination of relative humidity fields from model analyses and forecasts could provide information about possible changes in the size of a TC wind field. Furthermore, satellite imagery could be used to monitor the extent of precipitation outside the storm core, which might facilitate anticipation of TC wind-field expansion. Interactions with fronts or mid-latitude troughs during ET could indicate that wind-field expansion is imminent if precipitation is observed or anticipated to increase in the outer core of the storm.

The apparent importance of diabatic PV generation in the outer rain bands indicates that a careful comparison of model heating and PV tendencies with observations should be undertaken in order to ensure that microphysical and dynamical processes are adequately represented there. Also, in order to accurately predict TC size it is important that models are run at a sufficient resolution to omit cumulus parameterization and properly resolve spiral rainbands and the associated diabatic PV production. Eyewall replacement cycles and associated intensity and size changes remain difficult to predict operationally. The presence of an eyewall replacement cycle in the 80RH simulation, along with other recent studies, suggests that environments which favor greater rainband activity may be more conducive to eyewall replacement cycles, as the precipitation, heating, and PV production at large radius tend to favor them. Therefore, in order to better predict eyewall replacement cycles in

operational NWP models, accurate initialization of the environmental moisture content may be important, along with sufficient resolution to accurately represent rainbands, diabatic heating, and PV production.

5.2 Climate change and TCs

The IPCC's Fourth Assessment Report (AR4; Solomon et al. 2007) concluded that most of the observed global mean temperature increase since the mid-twentieth century is very likely (defined as a probability of >90%) due to anthropogenic increases in greenhouse gas concentrations, and a continued increase in surface temperature (and SST) is projected by all general circulation models (GCMs) that employ increasing concentrations of carbon dioxide (CO_2) in the 21st century (Solomon et al. 2007). Given the close association between observations of SST and maximum TC intensity in the North Atlantic basin (Demaria and Kaplan 1994), it is anticipated that anthropogenic climate change could lead to an increase in TC intensity. Given the increasing vulnerability of the U.S. coastline to TCs as previously discussed, it is essential to investigate the impact that climate change will have on TCs, and to assess potential uncertainty.

In this study, the thermodynamic impact of anthropogenic climate change on maximum TC intensity was investigated; the impact of changes in wind shear was not considered. The methodology used here is a variation on previous techniques, utilizing analyzed data to represent the average environment in which current TCs form, GCM projections to assess 21st century changes in SST, air temperature, and moisture, and a high-resolution mesoscale model (WRF) to simulate idealized TCs. Previous work was extended in this study by utilizing a larger number of GCMs forced with 3 different greenhouse gas emissions scenarios to estimate climate change, which allowed for a detailed analysis of uncertainty. TC simulations featured higher resolution than in previous idealized downscaling studies, and the explicit convection simulations allowed for a more realistic representation of TC structure and analysis of TC structure changes in a future climate. The

high-resolution model output was used to investigate structural changes, and to explore the mechanism of future intensity changes.

Based on an ensemble of GCMs, the average large-scale changes in the environment over a subsection of the Atlantic MDR during the 21st century can be summarized as an increase in SST of ~1.0 C to ~3.5°C, near-surface atmospheric warming of slightly more than the SST increase, and tropospheric warming that increases with height with maximum warming of approximately double the SST increase typically found between 250–150 hPa. In each emissions scenario, there is large model-to-model variability, especially in the projections of upper tropospheric temperature change. This uncertainty is attributable to processes parameterized in GCMs, including convection and treatment of ozone, and other model attributes, including horizontal and vertical resolution. GCM projections indicate little change in tropospheric relative humidity, which combined with warming temperatures leads to increased water vapor content (in an absolute sense). For each GCM projection, larger SST increase is associated with more moistening and larger tropospheric lapse rate stabilization. Emissions scenarios with larger estimates of greenhouse gas emissions estimate larger increases in SST and tropospheric warming and moistening.

High-resolution TC simulations were performed using the WRF model with initial and boundary conditions derived from spatially and temporally averaged reanalysis data, and including an idealized incipient vortex. Control simulations were compared to otherwise identical runs, but with GCM-derived SST, temperature, and moisture changes added to the control initial and boundary conditions. WRF simulations with 6-km grid length were performed utilizing large-scale environments derived from current climate mean conditions with projected changes from individual GCMs, yielding a total of 78 simulations. WRF simulations with 2-km grid length were performed for a smaller sample of large-scale environments, owing to the larger computational cost associated with the higher resolution. These high-resolution simulations were performed with climate change projections from the 13-member ensemble mean of GCMs from each emissions scenario to investigate the sensitivity to emissions scenarios. In order to further analyze the impact of tropospheric

stabilization, simulations with projected changes from GCMs driven with the A1B emissions scenario that produced the least and most tropospheric stabilization were performed. Finally, to further isolate the role of specific climate changes, simulations were performed with no tropospheric stabilization (constant warming throughout the depth of the troposphere) and no stratospheric cooling (no temperature changes in the stratosphere).

Simulation results with 6-km grid spacing indicate an increase in TC intensity in 75 of the 78 future climate simulations relative to the control (Fig. 4.34). The bulk of the 6-km simulations exhibited an increased pressure deficit of 4-8, 8-12, or 12-16%, relative to the control simulation. Averaged over all simulations with 6-km grid spacing, future TCs had an increase in central pressure deficit of 9%. Future TC intensity increases were found to be sensitive to emissions scenario with average increases in central pressure deficit of 10, 11, and 5% found in future simulations with A1B, A2, and B1 emissions scenarios, respectively. The central pressure deficit increases in A1B and A2 simulations of 10 and 11% are similar but slightly less than the 14% found by Knutson and Tuleya (2004). Increases in future TC central pressure deficit of 11, 19, and 12% were found in simulations with 2-km grid spacing using the A1B, A2, and B1 emissions scenarios ensemble mean projected changes, or 13% averaged over all 2-km simulations (Table 4.2). This is slightly larger than found with 6-km simulations, although a larger number of simulations would be desirable in order to test the robustness of this result. Simulations with the least and most stabilization reached a similar maximum intensity, with increases in central pressure deficit of ~8 and 5%, respectively. Simulations with no tropospheric stabilization had an average increase in central pressure deficit of 28%, slightly more than double that found with an identical SST increase along with tropospheric stabilization. Stratospheric cooling was found to not impact TC intensity in the model simulations.

Overall, results presented here are consistent with previous studies and indicate a likely increase in the intensity of the strongest future TCs. Here, we speculate that the increased intensity is due to two separate mechanisms, the first being a change in the future thermodynamic efficiency. Calculated thermodynamic efficiency values were found to be

highly correlated to simulated TC intensity, illustrating the importance of the efficiency. The change in thermodynamic efficiency intensity found in the future simulations is linked to both projected changes in the atmosphere and ocean. Warmer inflow, due to increased SST, increases the thermodynamic efficiency, leading to more intense future TCs. Some of this increased efficiency is offset, however, by warming of the outflow, which in general is proportional to the amount of tropospheric stabilization (Table 4.4). Future weakening in a small number of future simulations indicates that an increase in tropospheric stability can completely negate the intensity increase that would occur due to a modest increase in SST, highlighting the importance of the balance between SST increase and tropospheric stabilization. The no-stable simulation illustrates the important role of tropospheric stabilization, in reducing the intensification that would occur due to SST warming alone by greater than 50%.

Increases in the future thermodynamic efficiency, however, are not able to fully explain the future intensity increases (Table 4.4). Also, a subroutine designed to provide estimates of MPI underestimates simulated intensity increases, further supporting the evidence that additional mechanisms in addition to thermodynamic effects may be leading to an increase in future TC intensity (Table 4.2). Future TCs feature greater rainfall than in the current climate, with the largest increase being found in the eyewall. This increase in inner-core rainfall is highly correlated to larger average PV, due to increased diabatic production (Fig. 4.30). This increase in future rainfall and PV also leads to future intensification relative to the current climate, and this mechanism is most effective in future simulations that featured the largest increase in rainfall. It is the combination of increased thermodynamic efficiency and increased rainfall and PV that leads to the simulated intensity increases.

Changes in TC structural characteristics were also investigated using high-resolution WRF simulations with 2-km grid spacing. As previously stated, rainfall increases are found in the future TCs; specifically, increases in average rainfall within 100-km of the TC center of approximately 19, 20, and 12% in simulations with A1B, A2, and B1 projected changes, respectively. These increases are comparable to the 18% found by Knutson and Tuleya

(2004), and demonstrate that the increase in rainfall is tied to projected increases in atmospheric water vapor. Overall, the increase in rainfall in future TC simulations is consistent with the greater intensity, despite the tropospheric stabilization seen in the GCM projections. This can be attributed dynamically to a stronger PV tower through greater diabatic PV production, and perhaps also to an increased precipitation mass sink effect (Lackmann and Yablonsky, 2004; Makarieva et al. 2009). Increases in rainfall are largest in the eyewall, while a decrease in outer-core precipitation was found, especially in simulations with 6-km grid spacing. Consistent with previous research on TC size, the reduction in outer-core precipitation was also associated with smaller TCs (relative to the control).

Analysis of the TC secondary circulation was performed in order to assess how CO₂ induced changes would impact the strength and location of updrafts, downdrafts, and radial inflow and outflow. Updrafts are of similar maximum strength in all simulations, but maximum updrafts are higher in altitude and updrafts extend higher in future simulations than in the control. These increases are likely associated with the increase in the height of the freezing level and tropopause, and also increased buoyancy due to higher water vapor content in future climate simulations. Outflow, while occurring at higher altitudes in the future simulations, is warmer than in the control simulation, partially offsetting the increased thermodynamic efficiency that would occur solely due to the increase in inflow temperature.

5.2.1 Additional implications and future research directions

The results here confirm that changes in SST and tropospheric temperature both play a roll in altering future TC intensity. Analysis of GCM projected temperature changes at the end of the 21st century reveals that the GCM spread increases with height in the troposphere, reaching a maximum just below the tropopause. The tropospheric warming influences TC outflow temperature, and is therefore an important control on future TC intensity changes. The large uncertainty in projections of upper tropospheric warming necessitates the use of a wide variety of climate change projections in order to span the range of current predictability

limits. Future analysis should focus on examining further the physical processes and associated representation in numerical models that are responsible for the GCM uncertainty. As computing power increases, GCM changes are made, and new emissions scenarios are constructed, evaluation techniques such as those used here should be performed in order to assess GCM uncertainty.

The result that future TCs are likely to increase in maximum intensity is not new, although the physical mechanisms responsible for this increase were analyzed in greater detail. The importance of future increases in TC rainfall in influencing PV structure and intensity indicates that it is essential for studies of this type to use high model resolution and omit cumulus parameterization in order to realistically simulate TC precipitation processes. Until GCM projections are performed using resolution that is high enough to realistically simulate TC precipitation processes, methods such as the idealized downscaling technique used here or other nesting techniques will be required in order to realistically simulate the physical processes responsible for future intensity change.

Future investigation could focus on addressing the uncertainty associated with several choices made regarding the specifics of the current study. Different regions of the Atlantic basin or other oceanic basins could be used for the spatial averaging region, and this could provide insight into the sensitivity of the results to this choice. In the present study changes in the tropical climate were evaluated at the end of the 21st century, while future studies may want to analyze different future periods. In the idealized context, a larger number of high-resolution TC simulations would be beneficial in further assessing model sensitivity. Finally, the study provided here is quite specific in its scope, and essentially provides insight into the intensity change of the most intense TCs due to changes in the tropical thermodynamic environment. Simulations of basin-wide TC activity can provide additional insight into changes in frequency, and also intensity over a wider spectrum of TCs. Studies of this type could again employ spatially and temporally averaged climate change projections as was done in this study.

REFERENCES

- Atkinson, G. D., 1971: Forecaster's guide to tropical meteorology. Tech. Rep. 240, Air Weather Service, Scott Air Force Base, IL 62225, 295 pp.
- Allan, R. P., V. Ramaswamy, and A. Slingo, 2002: Diagnostic analysis of atmospheric moisture and clear-sky radiative feedback in the Hadley Centre and Geophysical Fluid Dynamics (GFDL) climate models. *J. Geo. Res.*, **107**, 1 – 7.
- Bender, M. A., and Coauthors, 2010: Modeled impact of anthropogenic warming on the frequency of intense Atlantic Hurricanes. *Science*, **327**, 454 – 458.
- Bengtsson, L., M. Botzet, and M. Esch, 1996: Will greenhouse gas-induced warming over the next 50 years lead to higher frequency and greater intensity of hurricanes? *Tellus*, **48A**, 57 – 73.
- Bengtsson, L., K. I. Hodges, M. Esch, N. Keenlyside, L. Kornblueh, J.-J. Luo, and T. Yamagata, 2007: How may tropical cyclones change in a warmer climate? *Tellus*, **59A**, 539 – 561.
- Bister, M., 2001: Effect of peripheral convection on tropical cyclone formation. *J. Atmos. Sci.*, **58**, 3463–3476.
- Black, M. L., R. W. Burpee, and F. D. Marks, 1996: Vertical motion characteristics of tropical cyclones determined with airborne Doppler radial velocities. *J. Atmos. Sci.*, **53**, 1887 – 1909.
- Black, P. G., and Coauthors, 2007: Air-sea exchange in hurricane winds: Synthesis of observations from the Coupled Boundary Layer Air-Sea Transfer Experiment. *Bull. Amer. Meteor. Sci.*, **88**, 357–374.
- Blake, E. S., E. N. Rappaport, and C. W. Landsea, 2007: The deadliest, costliest, and most intense United States tropical cyclones from 1851 to 2006 (and other frequently requested hurricane facts). NOAA Tech. Memo NWS TPC-5, 45 pp.
- Bretherton, F. P., 1966: Critical layer instability in baroclinic flows. *Quart. J. Roy. Meteor. Soc.*, **92**, 325–334.
- Braun, S. A., and W.-K. Tao, 2000: Sensitivity of high-resolution simulation of Hurricane Bob (1991) to planetary boundary layer parameterizations. *Mon. Wea. Rev.*, **128**, 3941–3961.
- Bureau of Meteorology (1977): Report by Director of Meteorology on Cyclone Tracy, December 1974 Bureau of Meteorology, Melbourne, Australia, 82 pp.

- Camp, J. P., and M. T. Montgomery, 2001: Hurricane maximum intensity: past and present. *Mon. Wea. Rev.*, **129**, 1704–1717.
- Chan, J. C. L., and R. T. Williams, 1987: Analytical and numerical studies of the beta-effect in tropical cyclone motion. Part I: Zero mean flow. *J. Atmos. Sci.*, **44**, 1257–1265.
- Chen, Y. and M. K. Yau, 2001: Spiral bands in a simulated hurricane. Part I: Vortex Rossby wave verification. *J. Atmos. Sci.*, **58**, 2128–2145.
- Chen, Y., G. Brunet, and M. K. Yau, 2003: Spiral bands in a simulated hurricane. Part II: Wave activity diagnostics. *J. Atmos. Sci.*, **60**, 1239–1256.
- Cocks, S. B., and W. M. Gray, 2002: Variability of the outer wind profiles of Western North Pacific Typhoons: Classifications and techniques for analysis and forecasting. *Mon. Wea. Rev.*, **130**, 1989–2005.
- Cordero, E. C., and P. M. de F. Forster, 2006: Stratospheric variability and trends in models used for the IPCC AR4. *Atmos. Chem. Phys.*, **6**, 5369 – 5380.
- Covey, C., K. M. AchutaRao, U. Cubasch, P. Jones, S. J. Lambert, M. E. Mann, T. J. Phillips, and K. E. Taylor, 2003: An overview of results from the Coupled Model Intercomparison Project (CMPI). *Global Planet. Change*, **37**, 103 – 133.
- Davis, C. A. and L. F. Bosart, 2001: Numerical simulations of the genesis of Hurricane Diana (1984). Part I: Control simulation. *Mon. Wea. Rev.*, **129**, 1859–1881
- Davis, C., and L. F. Bosart, 2002: Numerical Simulations of the Genesis of Hurricane Diana (1984). Part II: Sensitivity of Track and Intensity Prediction. *Mon. Wea. Rev.*, **130**, 1100–1124.
- Davis, C. A., and K. A. Emanuel, 1991: Potential vorticity diagnostics of cyclogenesis. *Mon. Wea. Rev.*, **119**, 1929–1953.
- DeMaria, M., and J. Kaplan, 1994: Sea surface temperature and the maximum intensity of Atlantic tropical cyclones. *J. Climate*, **7**, 1324–1334.
- Dunion, J. P., and C. S. Velden, 2004: The impact of the Saharan air layer on Atlantic tropical cyclone activity. *Bull. Amer. Meteor. Soc.* **85**, 353–365
- Dunion, J. P., and C. S. Marron, 2008: A reexamination of the Jordan mean tropical sounding based on awareness of the Saharan air layer: results from 2002. *J. Climate*, **21**, 5242–5253.

- Dunnavan, G. M., and J. W. Diercks, 1980: An analysis of Super Typhoon Tip (October 1979). *Mon. Wea. Rev.*, **108**, 1915–1923.
- Emanuel, K. A., 1986: An air-sea interaction theory for tropical cyclones. Part I: Steady-state maintenance. *J. Atmos. Sci.*, **43**, 585–604.
- Emanuel, K. A., 1987: The dependence of hurricane intensity on climate. *Nature*, **326**, 483 – 485.
- Emanuel, K. A., M. Fantini, and A. J. Thorpe, 1987: Baroclinic instability in an environment of small stability to slantwise moist convection. Part I: Two-dimensional models. *J. Atmos. Sci.*, **44**, 1559–1573.
- Emanuel, K. A., 1988: The maximum intensity of hurricanes. *J. Atmos. Sci.*, **45**, 1143–1155.
- Emanuel, K. A., 1995: Sensitivity of tropical cyclones to surface exchange coefficients and a revised steady-state model incorporating eye dynamics. *J. Atmos. Sci.*, **52**, 3969 – 3976.
- Emanuel, K. A., 2005: Increasing destructiveness of tropical cyclones over the past 30 years. *Nature*, **436**, 686 – 688.
- Emanuel, K. A., R. Sundarajan, and J. Williams, 2008: Hurricanes and Global Warming: Results from Downscaling IPCC AR4 Simulations. *BAMS*, **89**, 347 – 367.
- Evans, J. L., B. F. Ryan, and J. L. McGregor, 1994: A numerical exploration of the sensitivity of tropical cyclone rainfall intensity to sea surface temperature. *J. Clim.*, 616 – 623.
- Fierro, A. O., R. F. Rogers, F. D. Marks, and D. S. Nolan, 2009: The impact of horizontal grid spacing on the microphysical and kinematic structures of strong tropical cyclones simulated with the WRF-ARW model. *Mon. Wea. Rev.*, **137**, 3717 – 3741.
- Forster, P. M. de F., and K. P. Shine, 2002: Assessing the climate impact of trends in stratospheric water vapor. *Geo. Res. Letters*, **29**, 1 – 4.
- Forster, P. M., G. Bodeker, R. Schofield, S. Solomon, and D. Thompson, 2007: Effects of ozone cooling in the tropical lower stratosphere and upper troposphere. *Geophys. Res. Lett.*, **34**, 1 – 5.
- Fovell, R. G., K. L. Corbosiero, and H.-C. Kuo, 2009: Cloud microphysics impact on hurricane track as revealed in idealized experiments. *J. Atmos. Sci.* **66**, 1764 - 1778.
- Frank, W. M., and W. M. Gray, 1980: Radius and frequency of 15 m s^{-1} (30 kt) winds around tropical cyclones. *J. Appl. Met.*, **19**, 219–223.

Fu, R., A. D. Del Genio, and W. B. Rossow, 1994: Influence of ocean surface conditions on atmospheric vertical thermodynamic structure and deep convection. *J. Clim.*, **7**, 1092 – 1108.

Garner, S. T., I. M. Held, T. Knutson, and J. Sirutis, 2009: The roles of wind shear and thermal stratification in past and projected changes of Atlantic tropical cyclone activity. *J. Climate*, **22**, 4723 – 4734.

Gentry, M. S., and G. Lackmann, 2010: Sensitivity of simulated tropical cyclone structure and intensity to horizontal resolution. *Mon. Wea. Rev.*, **138**, 688 - 704.

Goldenberg, S. B., et al., 2001: The recent increase in Atlantic hurricane activity: causes and implications. *Science*, **293**, 474 – 479.

Gualdi, S., E. Scoccimarro, and A. Navarra, 2008: Changes in tropical cyclone activity due to global warming: Results from a high-resolution coupled general circulation model. *J. Clim.*, **21**, 5204 – 5228.

Guinn, T. A., and W. H. Schubert, 1993: Hurricane spiral bands. *J. Atmos. Sci.* **50**, 3380–3403.

Haarsma, R. J., J. F. B. Mitchel, and C. A. Senior, 1993: Tropical disturbances in a GCM. *Clim. Dyn.*, **8**, 247 – 257.

Hack, J. J., 1994: Parameterization of moist convection in the National Centre for Atmospheric Research community climate model (CCM2). *J. Geophys. Res.*, **95**, 5551 – 5568.

Hausman, S. A., K. V. Ooyama, and W. H. Schubert, 2006: Potential Vorticity Structure of Simulated Hurricanes. *J. Atmos. Sci.*, **63**, 87–108.

Hence, D. A., and R. A. Houze, 2008: Kinematic structure of convective-scale elements in the rainbands of Hurricanes Katrina and Rita (2005). *J. Geophys. Res.* 113, D15108. doi:10.1029/2007D009429.

Henderson-Sellers, A., and coauthors, 1998: Tropical cyclones and global climate change: a post IPCC assessment. *BAMS*, **79**, 19 – 38.

Held, I. M., and B. J. Soden, 2006: Robust responses of the hydrological cycle to global warming. *J. Climate*, **19**, 5686 – 5699.

Hill, K. A., G. M. Lackmann, and A. Aiyyer, 2008: Model simulated changes in TC intensity due to global warming. *28th Conference on Hurricanes and Tropical Meteorology*, Orlando, Fl, Amer. Meteor. Soc., 7B.2.

- Hill, K. A., and G. M. Lackmann, 2009: Analysis of Idealized Tropical Cyclone Simulations using the Weather Research and Forecasting Model: Sensitivity to Turbulence Parameterization and Grid Spacing. *Mon. Wea. Rev.*, **137**, 745 – 765.
- Hill, K. A., and G. M. Lackmann, 2009: Influence of environmental humidity on tropical cyclone size. *Mon. Wea. Rev.*, **137**, 3294 – 3315.
- Holland, G. J., 1997: The maximum potential intensity of tropical cyclones. *J. Atm. Sci.*, **54**, 2519 – 1541.
- Hong, S.-H., and H.-L. Pan, 1996: Nonlocal boundary layer vertical diffusion in a medium-range forecast model. *Mon. Wea. Rev.*, **124**, 2322-2339.
- Hong, S.-H., et al., 2004: A revised approach to ice microphysical processes for the bulk parameterization of clouds and precipitation. *Mon. Wea. Rev.*, **132**, 103-120.
- Hoskins, B. J., M. E. McIntyre, and A. W. Robertson, 1985: On the use and significance of isentropic potential vorticity maps. *Quart. J. Roy. Meteor. Soc.*, **111**, 877–946.
- Hong, Y. -Y., and J.-O. J. Lim, 2006: The WRF single-moment 6-class microphysics scheme (WSM6). *J. Korean Meteor. Soc.*, **42**, 129 – 151.
- Houghton, J. T., G. J. Jenkins, and J. J. Ephraums, 1990: *Climate Change, the IPCC Assessment.* 365 pp., Cambridge Univ. Press, New York.
- Houze, R. A., S. S. Chen, B. F. Smull, W.-C. Lee, and M. M. Bell, 2007: Hurricane intensity and eyewall replacement. *Science*, DOI: 10.1126/science.1135650, 1235 – 1239.
- Irish, J. L., D. T. Resio, and J. J. Ratcliffe, 2008: The influence of storm size on hurricane surge. *J. Phy. Ocean.*, **38**, 2003 - 2013.
- Janjic, Z. I., 1990: The Step-Mountain Coordinate: Physical Package. *Mon. Wea. Rev.*, **118**, 1429-1443.
- Janjić, Z. I., 2002: Nonsingular implementation of the Mellor-Yamada Level 2.5 Scheme in the NCEP Meso model. *NCEP Office Note*, No. **437**, 61 pp.
- Jarvinen, B. R., C. J. Neumann, and M. A. S. Davis, 1984: A tropical cyclone data tape for the North Atlantic basin, 1886 – 1983: Contents, limitations, and uses. NOAA Tech. Memo. NWS NCH 22, National Hurricane Center, Miami, FL., 24 pp.
- Jiang, H., and coauthors, 2006: Validation of rain-rate estimation in hurricanes from the stepped frequency microwave radiometer: algorithm correction and error analysis. *J. Atmos. Sci.*, **63**, 252 – 267.

- Jones, S. and co-authors, 2003: The extratropical transition of tropical cyclones: Forecasting challenges, current understanding, and future directions. *Wea. Forecasting* **18**, 1052–1092.
- Jordan, C. L., 1958: Mean soundings for the West Indies area. *J. Met.*, **15**, 91–97.
- Kain, J. S., 2004: The Kain-Fritsch convective parameterization: an update. *J. App. Met.*, **43**, 170–181.
- Kalnay, E., and coauthors, 1996: The NCEP/NCAR 40-year reanalysis project. *BAMS*, **77**, 437 – 441.
- Kimball, S. K., M. S. Mulekar, 2004: A 15-year climatology of North Atlantic Tropical Cyclones: Part I: size parameters. *J. Climate*, **17**, 3555–3575.
- Kimball, S. K., and F. C. Dougherty, 2006: The sensitivity of idealized hurricane structure and development in the distribution of vertical levels in MM5. *Mon. Wea. Rev.*, **134**, 1987–2008.
- Kimball, S. K., 2006: A modeling study of hurricane landfall in a dry environment. *Mon. Wea. Rev.*, **134**, 1901–1918.
- Klotzbach, P. J., 2006: Trends in global tropical cyclone activity over the past twenty years (1986 – 2005). *GRL*, **33**, 1 – 4.
- Knaff, J. A., and R. M. Zehr, 2007: Reexamination of tropical cyclone wind-pressure relationships. *Wea. Forecasting*, **22**, 71–88.
- Knutson, T. R., and R. E. Tuleya, 1999: Increased hurricane intensities with CO₂-induced warming as simulated using the GFDL hurricane prediction system. *Climate Dyn.*, **15**, 503–519.
- –, – –, and Y. Kurihara, 1998: Simulated increase of hurricane intensities in a CO₂-warmed climate. *Science*, **279**, 1018–1020.
- –, R. E. Tuleya, W. Shen, and I. Ginis, 2001: Impact of CO₂-induced warming on hurricane intensities as simulated in a hurricane model with ocean coupling. *J. Climate*, **14**, 2458–2468.
- –, – –, 2004: Impact of CO₂-induced warming on simulated hurricane intensity and precipitation: Sensitivity to the choice of climate model and convective parameterization. *J. Climate*, **17**, 3477–3495.

Knutson, T. R., J. J. Sirutis, S. T. Garner, I. M. Held, and R. E. Tuleya, 2007: Simulation of the recent multidecadal increase of Atlantic hurricane activity using an 18-km-grid regional model. *Bull. Amer. Met. Soc.*, **88**, 1549 – 1565.

Knutson, T. R., J. J. Sirutis, S. T. Garner, G. A. Vecchi, and I. M. Held, 2008: Simulated reduction in Atlantic hurricane frequency under twenty-first century warming conditions. *Nat. Geosci.*, **1**, 359 – 364.

Knutson, T. R., J. L. McBride, J. Chan, K. Emanuel, G. Holland, C. Landsea, I. Held, J. P. Kossin, A. K. Srivastava, and M. Sugi, 2010: Tropical cyclones and climate change. *Nature Geoscience*, DOI:10.1038/NGE0779, 1 – 7.

Kossin, J. P., and W. H. Schubert, 2001: Mesovortices, polygonal flow patterns, and rapid pressure falls in hurricane-like vortices. *J. Atmos. Sci.* **58**, 2196–2209.

Lackmann, G. M., 2002: Cold-Frontal potential vorticity maxima, the low-level jet, and moisture transport in extratropical cyclones. *Mon. Wea. Rev.*, **130**, 59–74.

Lackmann, G. M., and R. M. Yablonsky, 2004: The importance of the precipitation mass sink in tropical cyclones and other heavily precipitating systems. *J. Atmos. Sci.*, **61**, 1674 – 1692.

Landsea, C. W., et al., 2006: Can we detect trends in extreme tropical cyclones. *Science*, **313**, 452 – 454.

Lin, Yuh-Lang, et al., 1983: Bulk parameterization of the snow field in a cloud model. *J. Climate and App. Met.*, **22**, 1065-1092.

Liu, K. S., and J. C. L. Chan, 2002: Synoptic flow patterns associated with small and large tropical cyclones over the Western North Pacific. *Mon. Wea. Rev.*, **130**, 2134–2142.

Lynn, B. H., R. Healy, and L. M. Druyan, 2009: Investigation of Hurricane Katrina characteristics for future, warmer climates. *Climate Research*, **39**, 75-86.

Manabe, S., R. J. Stouffer, M. J. Spelman, and K. Bryan, 1991: Transient response of a coupled ocean-atmosphere model to gradual changes of atmospheric CO₂. Part I: Annual mean response. *J. Clim.*, **4**, 785 – 818.

Marks, F. D. et al., 1998: Landfalling tropical cyclones: forecast problems and associated research opportunities. *Bul. Amer. Met. Soc.*, **79**, 305 – 323.

Matyas, C. J., and M. Cartaya, 2009: Comparing the rainfall patterns produced by Hurricanes Frances (2004) and Jeanne (2004) over Florida. *Southeast. Geog.*, **49**, 132 – 156.

- May, P. T., 1996: The organization of convection in the rainbands of tropical cyclone Laurence. *Mon. Wea. Rev.*, **124**, 807–815.
- May, P. T., and G. J. Holland, 1999: The role of potential vorticity generation in tropical cyclone rainbands. *J. Atmos. Sci.*, **56**, 1224–1228.
- Meehl, G. A., C. Covey, T. Delworth, M. Latif, B. McAvaney, J. F. B. Mitchell, R. J. Stouffer, and K. E. Taylor, 2007: The WCRP CMIP3 multi-model dataset: A new era in climate change research, *Bulletin of the American Meteorological Society*, **88**, 1383 – 1394.
- Merrill, R. T., 1984: A comparison of large and small tropical cyclones. *Mon. Wea. Rev.*, **112**, 1408–1418.
- Michaels, P. J., P. C. Knappenberger, and C. Landsea, 2005: Comments on “Impacts of CO₂-Induced Warming on Simulated Hurricane Intensity and Precipitation: Sensitivity to the Choice of Climate Model and Convective Scheme. *J. Clim.*, **18**, 5179 – 5182.
- Miller, B. I., 1958: On the maximum intensity of hurricanes. *J. of Met.*, **15**, 184-195.
- Molinari, J., S. Skubis, D. Vollaro, F. Alsheimer, and H. E. Willoughby, 1998: Potential vorticity analysis of tropical cyclone intensification. *J. Atmos. Sci.*, **55**, 2632–2644
- Möller, J. D. and M. T. Montgomery, 1999: Vortex Rossby waves and hurricane intensification in a barotropic model. *J. Atmos. Sci.*, **56**, 1674–1687.
- Möller, J. D. and L. J. Shapiro, 2002: Balanced contributions to the intensification of Hurricane Opal as diagnosed from a GFDL model forecast. *Mon. Wea. Rev.* **130**, 1866–1881.
- Montgomery, M. T., and R. J. Kallenbach, 1997: A theory for vortex Rossby waves and its application to spiral bands and intensity changes in hurricanes. *Quart. J. Roy. Meteor. Soc.*, **123**, 435–465.
- Moon, Y., and D. S. Nolan, 2010: The dynamic response of the hurricane wind field to spiral rainband heating. *J. Atmos. Sci.*, **67**, 1779 – 1805.
- Nolan, D. S., J. A. Zhang, and D. P. Stern, 2009: Evaluation of planetary boundary layer parameterizations in tropical cyclones by comparison of in situ observations and high-resolution simulations of Hurricane Isabel (2003). Part I: initialization, maximum winds, and outer-core boundary layer. *Mon. Wea. Rev.*, **137**, 3651 – 3674.

- Nolan, D. S., J. A. Zhang, and D. P. Stern, 2009: Evaluation of planetary boundary layer parameterizations in tropical cyclones by comparison of in situ observations and high-resolution simulations of Hurricane Isabel (2003). Part II: inner-core boundary layer and eyewall structure. *Mon. Wea. Rev.*, **137**, 3675 – 3698.
- Oouchi, K., J. Yoshimura, H. Yoshimura, R. Mizuta, S. Kusunoki, and A. Noda, 2006: Tropical cyclone climatology in a global-warming climate as simulated in a 20 km-mesh global atmospheric model: frequency and wind intensity analyses. *J. Meteor. Soc. Japan*, **84**, 259 – 276.
- Pielke, R. A., and C. W. Landsea, 1998: Normalized hurricane damages in the United States: 1925 – 95. *Wea. and Fcst.*, **13**, 621 – 631.
- Ramaswamy, V., and coauthors, 2001: Stratospheric temperature trends: observations and model simulations. *Reviews of Geophysics*, **39**, 71 – 122.
- Raymond, D. J., 1992: Nonlinear balance and potential-vorticity thinking at larger Rossby number. *Quart. J. Roy. Meteor. Soc.*, **118**, 987 – 1015.
- Rennick, M. A., 1977: The parameterization of tropospheric lapse rates in terms of surface temperature. *J. Atmos. Sci.*, **34**, 854 – 862.
- Reynolds, R. W., T. M. Smith, C. Liu, D. B. Chelton, K. S. Casey, and M. G. Schlax, 2007: Daily high-resolution-blended analyses for sea surface temperature. *J. Climate*, **20**, 5473 – 5496.
- Rogers, R. F., M. L. Black, S. S. Chen, and R. A. Black, 2007: An evaluation of microphysics fields from mesoscale model simulations of tropical cyclones. Part I: comparisons with observations. *J. Atmos. Sci.*, **64**, 1811 – 1834.
- Rotunno, R. and K. A. Emanuel, 1987: An air-sea interaction theory for tropical cyclones. Part II: Evolutionary study using a nonhydrostatic axisymmetric numerical model. *J. Atmos. Sci.*, **44**, 542–562.
- Santer, B. D., et al., 2006: Forced and unforced ocean temperature changes in Atlantic and Pacific tropical cyclogenesis regions. *PNAS*, **103**, 13905 – 13910.
- Santer, B. D., and Coauthors, 2008: Consistency of modeled and observed temperature trends in the tropical troposphere. *Int. J. Climatol.*, **10.1002/joc.1756**.
- Schubert, W. H., M. T. Montgomery, R. K. Taft, T. A. Guinn, S. R. Fulton, J. P. Kossin, and J. P. Edwards, 1999: Polygonal Eyewalls, Asymmetric Eye Contraction, and Potential Vorticity Mixing in Hurricanes. *J. Atmos. Sci.*, **56**, 1197–1223.

- Shapiro, L. J., and J. L. Franklin, 1999: Potential vorticity asymmetries and tropical cyclone motion. *Mon. Wea. Rev.* **127**, 124–131.
- Shapiro, L. J., and J. D. Möller, 2003: Influence of atmospheric asymmetries on the intensification of Hurricane Opal: Piecewise PV inversion diagnosis of a GFDL model forecast. *Mon. Wea. Rev.* **131**, 1637–1649.
- Sheets, R. C., 1969: Some mean hurricane soundings. *J. Applied. Met.*, **8**, 134–146.
- Sheets, R. C., 1990: The National Hurricane Center – Past, present, and future. *Wea. and Fcst.*, **5**, 185 – 232.
- Shen, W., R. E. Tuleya, and I. Ginis, 2000: A sensitivity study of the thermodynamic environment on GFDL model hurricane intensity: Implications for global warming. *J. Climate*, **13**, 109–121.
- Skamarock, W. C., J. B. Klemp, J. Dudhia, D. O. Gill, D. M. Barker, W. Wang, and J. G. Powers, 2007: A description of the advanced research WRF Version 2. *NCAR Technical Note*.
- Solomon, S., D. Qin, M. Manning. Z. Chen, M. Marquis, K.B. Averyt, M. Tigora, and H. L. Miller, Eds., 2007: *Climate Change 2007: The Physical Science Basis*. Cambridge University Press, 996 pp.
- Sobel, A. H., I. M. Held, and C. S. Bretherton, 2002: The ENSO signal in tropical tropospheric temperature. *J. Climate*, **15**, 2702 – 2706.
- Stoelinga, M. T., 1996: A potential vorticity-based study of the role of diabatic heating and friction in a numerically simulated baroclinic cyclone. *Mon. Wea. Rev.*, **124**, 849 – 874.
- Talgo, K. D., 2009: Tropical Atlantic vertical wind shear variability in a future climate. M.S. Thesis, Dept. of Marine, Earth, and Atmospheric Sciences, North Carolina State University, 97 pp.
- UNDP/BCPR, 2004: Reducing disaster risk: A challenge for development. United Nations Development Program, Bureau for Crisis Prevention and Recovery, 161 pp. [Available online at www.undp.org/bcpr/disred/rdr.html.]
- Vecchi, G. A., and B. J. Soden, 2007: Increased tropical Atlantic wind shear in model projections of global warming. *Geophys. Res. Lett.*, **34**, 1 – 5.
- Vecchi, G. A., and T. R. Knutson, 2008: On estimates of historical North Atlantic tropical cyclone activity. *J. Clim.*, **21**, 3580 – 3600.

Walsh, K. J. E., and B. F. Ryan, 2000: Tropical cyclone intensity near Australia as a result of climate change. *J. Climate*, **13**, 3029 – 3036.

Walsh, K. J. E., K.-C. Nguyen, and J. L. McGregor, 2004: Fine-resolution regional climate model simulations of the impact of climate change on tropical cyclones near Australia. *Clim. Dyn.*, **22**, 47 – 56.

Wang, X. and D.-L. Zhang, 2003: Potential vorticity diagnosis of a simulated hurricane. Part I: Formulation and quasi-balanced flow. *J. Atmos. Sci.* **60**, 1593–1607

Wang, Y., 2002a: Vortex Rossby waves in a numerically simulated tropical cyclone. Part I: Overall structure, potential vorticity, and kinetic energy budgets. *J. Atmos. Sci.*, **59**, 1213–1238.

Wang, Y., 2002b: Vortex Rossby waves in a numerically simulated tropical cyclone. Part II: The role in tropical cyclone structure and intensity changes. *J. Atmos. Sci.*, **59**, 1239–1262.

Wang, Y., 2008: How do outer spiral rainbands affect tropical cyclone structure and intensity? *J. Atmos. Sci.*, **66**, 1250 – 1273.

Webster, P. J., et al., 2005: Changes in tropical cyclone number, duration, and intensity in a warming environment. *Science*, **309**, 1844 – 1846.

Williams, E. and N. Renno, 1993: An analysis of the conditional instability of the tropical atmosphere. *Mon. Wea. Rev.*, **121**, 21 – 36.

Wu, C.-C., and K. A. Emanuel, 1995b: Potential vorticity diagnostics of hurricane movement. Part I: A case study of Hurricane Bob. *Mon. Wea. Rev.* **123**, 69–92.

Wu, C.-C., and K. A. Emanuel, 1995b: Potential vorticity diagnostics of hurricane movement. Part II: Tropical storm Ana (1991) and hurricane Andrew (1992). *Mon. Wea. Rev.* **123**, 93–109

Xu, K., and K. Emanuel, 1989: Is the tropical atmosphere conditionally unstable? *Mon. Wea. Rev.*, **117**, 1471 – 1479.

Xu, J., and Y. Wang, 2010: Sensitivity of the simulated tropical cyclone inner-core size to the initial vortex size. *Mon. Wea. Rev.*, in press.

Xu, J., and Y. Wang, 2010: Sensitivity of tropical cyclone inner-core size and intensity to the radial distribution of surface entropy flux. *J. Atmos. Sci.*, in press.

Zhang, C., 1993: Large-scale variability of atmospheric deep convection in relation to sea surface temperature in the tropics. *J. Clim.*, **6**, 1898 – 1913.

Zhang, Da-Lin, and X. Wang, 2003: Dependence of hurricane intensity and structures on vertical resolution and time-step size. *Advances in Atmospheric Sciences*, **20**, 711-724.